EXPERIMENTAL ANALYSIS OF THE FLOW AROUND A CYLINDER WITH A SQUARE CROSS-SECTION

August 2005

E.W.M. Roosenboom

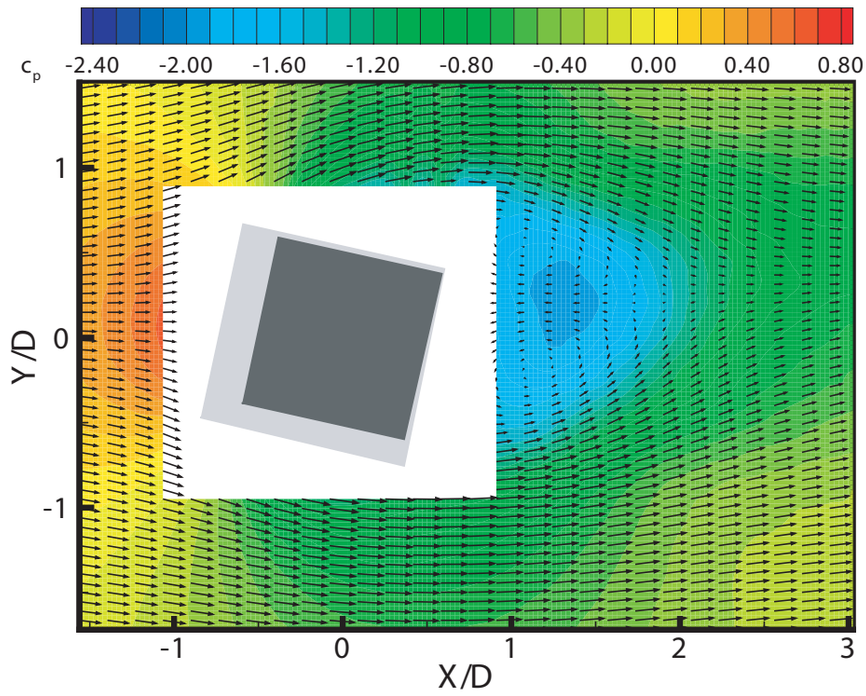

Aerodynamics

TU Delft

Faculty of Aerospace Engineering

Delft University of Technology

EXPERIMENTAL ANALYSIS OF THE FLOW AROUND A CYLINDER WITH A SQUARE CROSS-SECTION

by

Eric Wilhelmus Maria Roosenboom

born in Roermond, the Netherlands

B.Sc.
Delft University of Technology 2003

Submitted to the Department of Aerospace Engineering in partial fulfilment of the requirements for the degree of

Master of Science in Aerospace Engineering

at the

Delft University of Technology

August 2005

Signature of author: _____

Department of Aerodynamics
August 10, 2005

Certified by: _____

dr. F. Scarano
Thesis supervisor

Certified by: _____

dr.ir. B.W. van Oudheusden
Thesis supervisor

Accepted by: _____

Prof.dr.ir. P.G. Bakker
Chairman Aerodynamics Department

The Exam Committee consists of:

Prof.dr.ir. P.G. Bakker
dr. F. Scarano
dr.ir. B.W. van Oudheusden
dr.ir. L.L.M. Veldhuis

Abstract

Title:	Experimental analysis of the flow around a cylinder with a square cross-section
Author:	E.W.M. Roosenboom, © 2005
Contact:	eroosenboom@hotmail.com

The present work investigates the flow around a two-dimensional square section object at varying angles of incidence. The experimental approach employs Particle Image Velocimetry for the determination of the time-averaged velocity field and the unsteady large scale coherent variations (e.g. vortex shedding) as well as turbulent fluctuations. The angle of incidence is varied from 0° to 45° covering the entire range of possible wind directions. The investigation constitutes a further step within the ongoing research for the assessment of the quasi-steady theory for the low-frequency oscillation (galloping) phenomenon of bluff bodies.

A specific aspect of the set-up is the use of a transparent hollow model, which allows light transmission and minimizes internal total reflection. Above 10° incidence the flow may reattach on the lower surface and produce a separation bubble. Time-mean averaged velocity fields reveal that the near-wake length increases monotonically, peaking at 10°. Beyond, the distance from the vorticity centres to the nearest corner of the model drops significantly, caused by the shift of the separation point location. The vortex shedding is influenced hereby to a large extent. The flow organisation is further analysed with Proper Orthogonal Decomposition (POD) to investigate the unsteady flow structures associated with vortex shedding. The POD modes are used to reconstruct a low-order flow model that provides a phase reconstruction of the vortex shedding sequence for all angles of incidence.

In addition to the velocity field characterisation, a method to determine the mean (time-averaged) lift and drag coefficient of the model from PIV velocity data is proposed. The Reynolds-averaged momentum equations are employed to calculate the pressure gradient field, yielding subsequently the pressure field by means of a two-dimensional integration technique. The estimated pressure field is introduced in an integral momentum balance, which is solved on a contour around the model. The method has been successfully applied to the experimental data of the flow around a square cylinder. The force data show satisfactory agreement with reference data published in literature.

Table of Contents

List of Figures

List of Tables

Preface

This report describes an experimental investigation of the flow around a square cylinder and serves as a partial fulfilment for the degree of Master of Science in Aerospace Engineering at the Delft University of Technology, the Netherlands.

The current experimental investigation is a continuation of the research on bluff body aerodynamics and galloping conducted at the Delft University of Technology, started by dr.ir. B.W. van Oudheusden. The purpose of the current investigation is to acquire instantaneous velocity vectors and vorticity in order to accurately document the flow around a square cylinder at multiple angles of incidence using Particle Image Velocimetry. This should then enable a greater insight into the phenomena of the (unsteady) flow around bluff bodies and its related effect of galloping.

During the experiments and post-processing of the results several people from the Aerodynamics staff gave lots of tips and hints on specific problems encountered. Especially, I would like to thank from the Scientific staff dr.ir. B.W. van Oudheusden and dr. F. Scarano for their valuable theoretical and experimental advise on galloping and Particle Image Velocimetry. I also would like to thank ing. F.J. Donker Duyvis and P.J. Duyndam from the Technical staff for helping me with the practical wind tunnel and laser set-up. I also would like to thank N.P. van Hinsberg, for his cooperation during the first experimental campaign. And of course I would also like to thank everyone else who has supported me to complete this investigation.

Eric Roosenboom

Delft, August 2005

Chapter

1

Introduction

Aerodynamic research related to aeronautical applications generally involves the flow around streamlined bodies. There are however interesting phenomena that occur in the presence of non-streamlined bodies. These so-called bluff bodies exist almost anywhere because a body in general is not streamlined. Among many examples are buildings, bridges, bridge piers, chimneys, antennae, and islands. As a consequence, bluff body flow is also extensively studied in hydrodynamics and civil engineering. When these bluff bodies are introduced in a flow field, the flow forms a separated region. This separated flow will usually be unsteady and will create vortices and introduce fluctuating forces. In figure 1-1 an example of such vortices is clearly visible in the atmosphere behind Guadalupe Island (located about 200 *km* outside of the Mexican west coast).

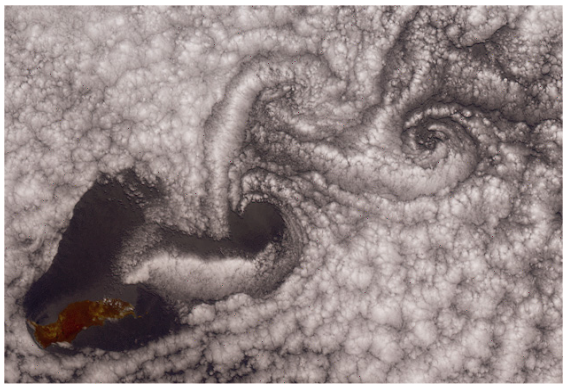

Figure 1-1: Atmospheric vortices in the wake of Guadalupe Island [Courtesy of NASA, MISR Team]

The fluctuating nature of this kind of flow is responsible for vibrations of structures. A distinction can be made in two types of vibration, Vortex induced vibra-

tion (VIV) and Flow induced vibration (FIV). In the vortex induced vibration vortices are shed at (or close to) the natural frequency of the structure causing the structure to respond [Williamson *et al*, 2004]. The flow-induced vibration is characterized by a low frequency oscillation, much lower than the vortex shedding frequency [Robertson *et al*, 2003]. Unsteady aerodynamic forces can lead to energy extraction from the flow. The extracted energy will amplify initial small displacements and/or rotations of the body when there is a negative aerodynamic damping. Regarding the flow around bluff bodies the typical type of flow-induced vibration is commonly referred to as galloping, it is similar to flutter in an aeroelastic analysis.

Galloping is a low frequency high amplitude vibration. This type of vibration can clearly be seen on a windy winter day when ice accretion on a power cable makes it aerodynamically unstable and thus susceptible to galloping. Because of the high amplitude motion, galloping can cause great damage to bridge decks or power cables. Ultimately such an oscillation can lead to the failure of a structure. One famous example is the failure of the "Tacoma Narrows Bridge" (figure 1-2), also known as 'Galloping Gertie', in Washington State in the US on November 7, 1940.

Figure 1-2: Tacoma Narrows Bridge failure due to galloping

Some measures can be taken to suppress or reduce the susceptibility of a structure to galloping. Bridge decks can for example be designed more aerodynamically, such that the wind has less influence on the structure. The introduction of taper in tall buildings disturbs the two-dimensionality of the flow and will reduce galloping. In the case of power cables special connectors can be used to suppress the effect of galloping. While contra measures are used widely, the theoretical background of these flows remains under investigation. The oscillations of the galloping of a structure can be estimated with a quasi-steady theory. This theory is widely used in galloping related cases, but experiments show deviations from this theory.

The essential assumption of the quasi-steady theory is that the results of experiments (or numerical predictions) on a static model at certain flow conditions may be used in the prediction of the dynamical oscillations of the same structure at the same flow conditions. This assumption is, however, at least questionable. In order to verify this assumption on which the quasi-steady theory is built an ongoing research is conducted at the Aerodynamics Department of the Faculty of Aerospace Engineering at the Delft University of Technology. Previous investigations on oscillating rectangular models are reported by Van Oudheusden in 1993, 1995 and 2000.

To enable an investigation of the quasi-steady assumption a database of static results has to be created. This database of results can then be used for a comparison with future experiments on an oscillating model. Van Hinsberg (2004) conducted Particle Image Velocimetry (PIV) experiments on a square prism at static conditions. Additionally a Proper Orthogonal Decomposition (POD) was used to create a low-order model of this type of flow, allowing a phase-resolved reconstruction of the vortex shedding. In the present work this investigation is continued and expanded. The flow around a square prism, a cylinder with a square cross-section, will be measured with PIV. Earlier studies confirmed that the flow was very dependent on the angle of incidence and only mildly on the Reynolds number (Luo *et al.*, 2005). Therefore in the present study the Reynolds number will be kept constant at about $2 \cdot 10^4$, based on a free stream velocity of 10 *m/s* and a model diameter of 30 *mm*. To study the effect of the angle of incidence, the model will be placed at various angles of incidence ranging from 0° to 45°. Between 0° and 15° the model will be measured every 2.5°; between 15° and 45° the model will be measured every 5°. The POD analysis will be applied to create low-order models of the investigated flows. Specific problems of the flow around a square prism can be contributed to the resulting aerodynamic force on this model. It was investigated how to obtain force data from the velocity field data acquired with PIV, using the control-volume approach. A two-dimensional integration of the Reynolds-averaged pressure gradient will be used to provide for the pressure in the integral momentum force equation, other terms being determined (indirectly) from the PIV results. This allows a calculation of the lift and drag coefficients at the measured angles of incidence.

The report is organized as follows. Chapter 2 introduces some specific aspects of bluff body flow. This type of flow is introduced with the flow around a circular cylinder. This is then extended to the flow around rectangular cylinders and in particular around a square cylinder. Some attention is given to the galloping theory. The experimental set-up is explained in chapter 3. The experiments are performed with Particle Image Velocimetry (PIV), a small introduction on the basic principle of this technique is provided. The initial set-up, as well as the further development, of the experiments is presented in detail. The results of the experiments are shown in chapter 4. First, a selection of statistical averaged results is presented. Secondly, the unsteady flow characteristics are determined by means of a Proper Orthogonal Decomposition (POD). Also, a low order representation of the flow can be made based on this POD analysis. In chapter 5 a method to derive the lift and drag coefficients from PIV data is given. Finally, the conclusions of

the experiments and the analysis are summarized in chapter 6. Also, some recommendations for improvement and further research are given.

The appendices deal with an in-depth explanation and/or a documentation of specific topics. A derivation of the classical galloping criteria is provided in Appendix A. Appendix B explains the optical properties of the two models used in the experiments. A full derivation of the expression for the Reynolds averaged pressure gradient and two integration methods to obtain the pressure field are presented in Appendix C. All the statistical and unsteady results are presented in Appendix D.

Chapter

2

Aspects of Bluff Body Flow

This chapter will deal with several aspects of general bluff body flow. The flow to be studied in the experiments is the flow around a square cylinder. This flow shares a great similarity with the flow around a circular cylinder. Since the flow around a circular cylinder is well documented some attention is given to this configuration first, before summarizing previous experiments and Computational Fluid Dynamics (CFD) results, which explain in more detail the flow around a square cylinder. This chapter concludes with an overview of the quasi-steady galloping theory and the identification of points that need investigation.

2.1 The flow around a circular cylinder

In any flow there are two basic sources for aerodynamic drag on an object: skin friction drag and pressure drag. Skin friction drag contributes most to the drag for a streamlined body. In a bluff body flow the dominating contribution is due to pressure forces because of large separation areas. When classifying bluff bodies a distinction can be made into bodies with sharp edges (squares, rectangles, etc.) and bodies with rounded edges (circular, elliptical, etc.).

The main difference between the two types of bodies is the location of the separation point. For bodies with sharp edges the separation point will stay in the same position, while for bodies with rounded edges the separation point will move alternately over the surface of the object. Both type of flows have a similar development of flow structures in the separated flow region. The flow around a circular cylinder for various Reynolds numbers is depicted in figure 2-1. Figure 2-1a shows a very viscous flow, so-called Stokes flow, where the Reynolds number is

typical below 4. Two stable vortices appear in the separated region for Reynolds numbers between 4 and 40, figure 2-1b.

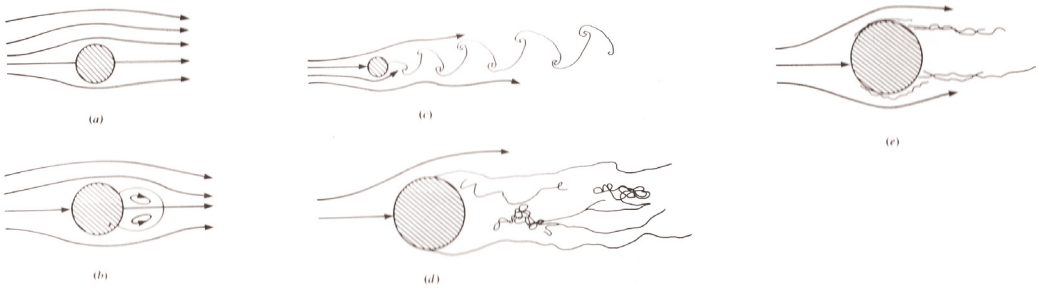

Figure 2-1: Various types of flow over a circular cylinder [Anderson, 1991]

When the Reynolds number is further increased the flow becomes unstable and vortices are being shed alternately from the cylinder, figure 2-1c. Such a vortex pattern is called a Karman vortex street. The vortex shedding frequency can be characterized with a dimensionless number, the Strouhal number, S (or St):

$$S = \frac{fD}{V} \tag{2.1}$$

where f the vortex shedding frequency, D a particular dimension of the body and V the velocity of the flow field.

For Reynolds numbers between 200 and 10^5 the Karman vortex street turns into a turbulent wake, see figure 2-1d. In the range of Reynolds numbers between 10^5 and $3 \cdot 10^6$, figure 2-1e, the flow separates on the forward surface but a transition to turbulent flow takes place and the flow is able to reattach at the backward surface. This particular effect causes a smaller wake and hence reduces the pressure drag on the cylinder.

The transition from laminar to turbulent flow depends on the Reynolds number as was pointed out in figure 2-1. These transitions can occur in different regions of the flow, see figure 2-2. For figure 2-2a-d the flow becomes gradually more turbulent as the Reynolds number is increased. The different types of transitions are:

a) Transition in the wake,
b) Laminar separated transition in the free shear layers,
c) Transition in the boundary layers, transition moves towards stagnation point,
d) All regions turbulent.

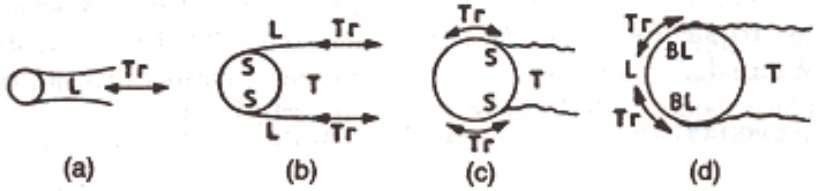

BL = boundary layer,
L = laminar,
T = turbulent,
Tr = transition,
S = separation

Figure 2-2: Transitions in disturbed regions [Zdravkovich, 1997]

2.1.1 Governing parameter: Reynolds number

The Reynolds number, *Re*, can be regarded as the ratio of inertia forces to viscous forces. It is defined as:

$$Re = \frac{\rho V l}{\mu} = \frac{V l}{\nu} \tag{2.2}$$

where ρ the density of the medium, V the velocity of the flow field, l a reference length of the body (for example the width), μ the viscosity and ν the kinematic viscosity.

The Reynolds number is the governing parameter for disturbance free flow around cylinders. Additional influencing parameters (which can become a governing parameter under certain conditions) are:

- Free stream turbulence
- Transverse or stream wise oscillations of the body
- Surface roughness
- Wall blockage and wall proximity
- End effects
- Aspect ratio and free end of the cylinder

2.1.2 Transition phases and eddies

During the experiments the Reynolds number will be around $20 \cdot 10^3$. Therefore the most important transition is the transition in the shear layers. This transition contains three phases:

1) Development of transition waves, $350\text{-}400 < Re < 1 \cdot 10^3\text{-}2 \cdot 10^3$
2) Formation of (alternating) transition eddies, $1 \cdot 10^3\text{-}2 \cdot 10^3 < Re < 2 \cdot 10^4\text{-}4 \cdot 10^4$
3) Burst to turbulence, $2 \cdot 10^4\text{-}4 \cdot 10^4 < Re < 1 \cdot 10^5\text{-}2 \cdot 10^5$

The formation of alternating transition eddies is a high-speed mode of eddy shedding and is characterized by two stages: formation and shedding. The formation of eddies occurs when the free shear layers behind the cylinder roll up at a fixed location. The fully-grown eddies start an eddy street due to alternating shedding.

This high speed eddy shedding depends on 4 parameters:

1. Distance between free shear layers
2. Strength of fully grown eddy
3. Thickness of shear layers
4. Entrainment into near wake.

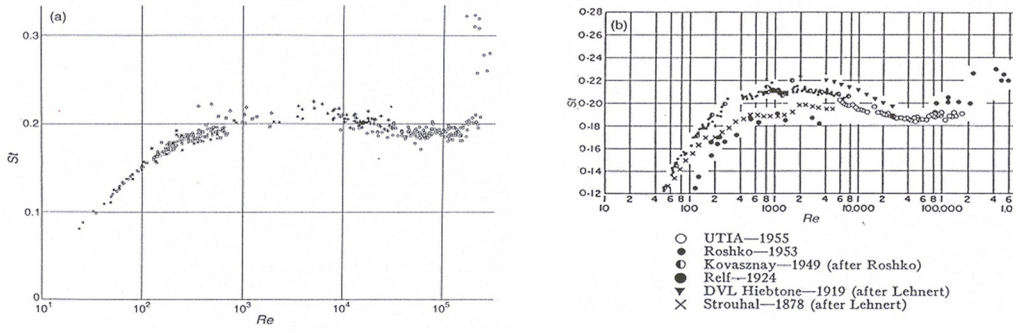

Figure 2-3: Compilation of *St* versus *Re* [Zdravkovich, 1997]

The distance between the free shear layers, or the width of the near-wake, is slightly smaller during the phase of the formation of eddies. The length of the eddy formation region is the longest here and the variation of the Strouhal number (figure 2-3) is related to the variation of the near-wake width. Vorticity generation and dissipation affect the strength of a fully-grown eddy. Both are similar in this region and the strength is thus constant. As the thickness of the free shear layers increases the shedding frequency is expected to decrease. The entrainment of the adjacent free stream into the wake affects the formation and shedding of eddies. At the end of the formation region, where the free stream crosses the wake axis, a large periodic entrainment can be seen (figure 2-4).

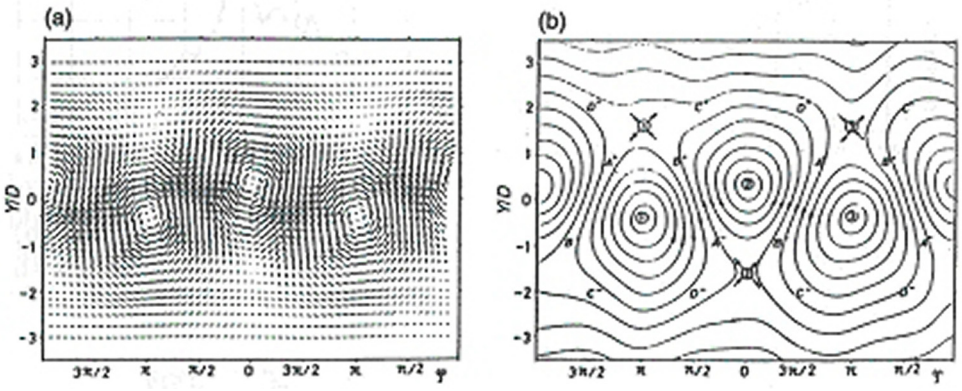

Figure 2-4: a) Velocity field, b) Streamlines at X/D = 8 and Re = $16 \cdot 10^3$ [Zdravkovich, 1997]

2.1.3 Entrainment streamlines

The point where two entrainment streamlines meet is a confluence point, each eddy has one confluence point. See for example the confluence point *S* in figure 2-5. Despite the fact that the Reynolds number is large ($14 \cdot 10^4$) similar eddies are present in figure 2-4 for $Re = 16 \cdot 10^3$. Both figures have a frame of reference, which moves with the position of the eddy centres. When the frame of reference is fixed to the cylinder no eddies or entrainment can be detected. In figure 2-5 entrainment streams are present as E_1 to E_4 in an averaged velocity field at the midpoint of the shedding cycle. The free shear layers are represented by the dotted lines.

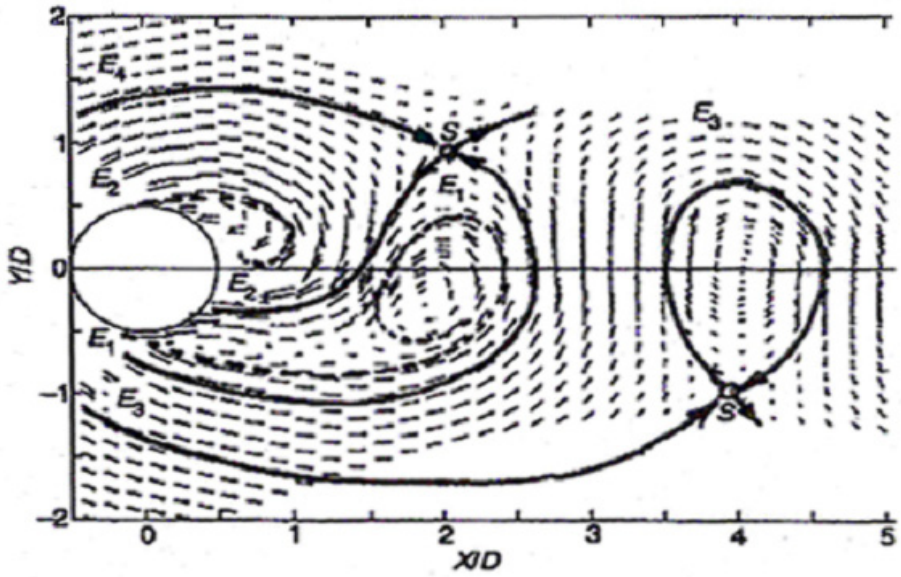

Figure 2-5: Instantaneous velocity field at $Re = 14 \cdot 10^4$, S-confluence point, E_1, E_2, E_3, E_4 - entrainment layers [Zdravkovich, 1997]

Samples of the velocity field at four stages of the first half of the shedding cycle are given in figure 2-6. Figure 2-6a shows an elongated eddy being split by the upper entrainment stream. The upper entrainment stream displaces and elongates the split eddies until a confluence point is formed at the bottom side of the near-wake, figure 2-6b. The split eddy is shed when it is fully engulfed by the upper entrainment stream, e.g. it is carried downstream by the flow. The width of the entrainment stream increases on the growing eddy (bottom of near-wake) and decreases on the opposite side (top), see figure 2-6c and d. When the half cycle is completed, the process of eddy shedding is repeated in a same manner with eddies being shed due to the bottom entrainment stream. These two related and opposite entrainment streams show an out of phase variation, which is responsible for the fluctuating lift force on the cylinder.

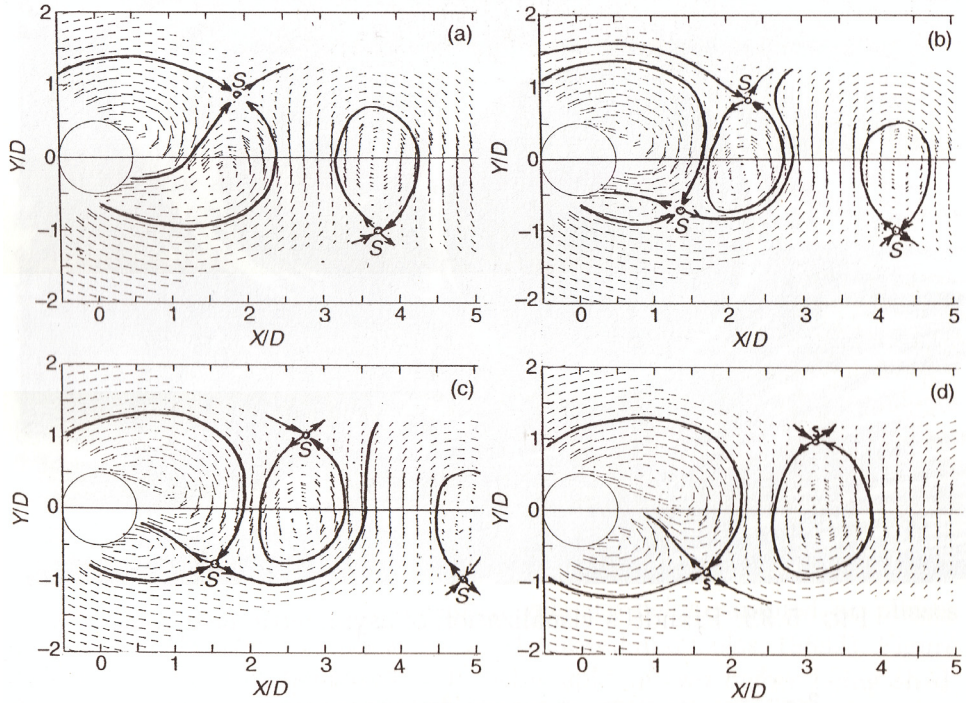

Figure 2-6: Four sequences of eddy shedding, a) -0.12, b) 0.00, c) 0.12, d) 0.25 of one shedding cycle at $Re = 14 \cdot 10^4$ [Zdravkovich, 1997]

A conventional way to interpret eddy shedding in the near-wake is to regard the flow as 'open' when viewed from upstream and as 'closed' when viewed from downstream. Both interpretations are given in figure 2-7. Notice that the confluence regions correspond to the cut-off of the free shear layer, the part regarded as 'closed'.

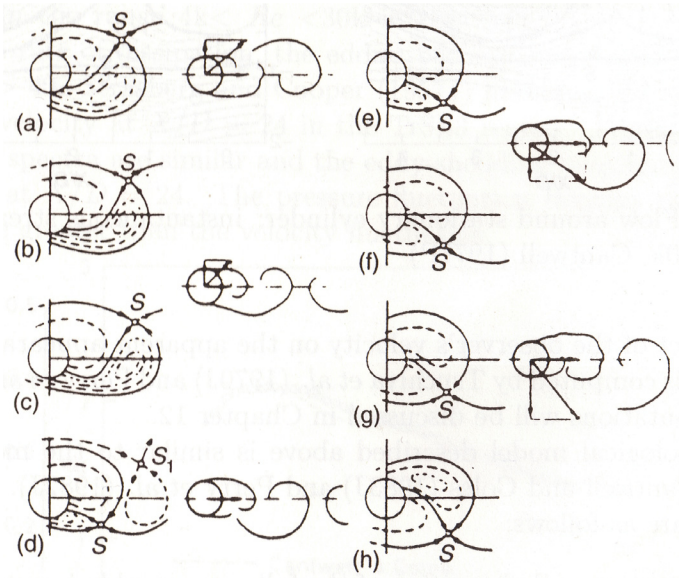

Figure 2-7: Comparison of Zdravkovich's sketches and Drescher's visualization [Zdravkovich, 1997]

2.2 Flow around rectangular cylinders

The discussion of flows around cylinders can now be extended to the class of rectangular cross-sections. The flow around a rectangular cylinder has a large similarity with the flow around a circular cylinder, but some notable differences are apparent, such as the effect of the afterbody and the angle of incidence.

2.2.1 Topology of rectangular cylinder flow

The aerodynamic characteristics of rectangular cylinders strongly depend on the absence, or presence, of reattachment of the shear layer in relation to the length to height ratio, b/h [a] of the cross-section. A distinction into three categories can be made:

1) Separated, $b/h < 2.8$
2) Intermittently reattached, $2.8 < b/h < 6.0$
3) Fully reattached, $b/h > 6.0$

From figure 2-8 it can be noted that the Strouhal number (*St*) will decrease with an increasing length to height ratio. Figure 2-9 shows numerically determined vorticity contours of various types of cross-sections [Shimida *et al.*, 2002]. Figure 2-9a-e shows the separated cross-sections in which a periodic and apparent vortex shedding is observed. Also observed is that the generation of vortices takes place at large distances from the cylinder for b/h up to 2. For $b/h = 2$ the vortex generation is the weakest of all cross-sections. Between $b/h = 2$ and 2.8 two frequency modes appear, which are determined from the Fourier spectrum of the fluctuating lift. This bimodal vortex shedding is accompanied by an occasional reattachment of the separated shear layer on the rear surface.

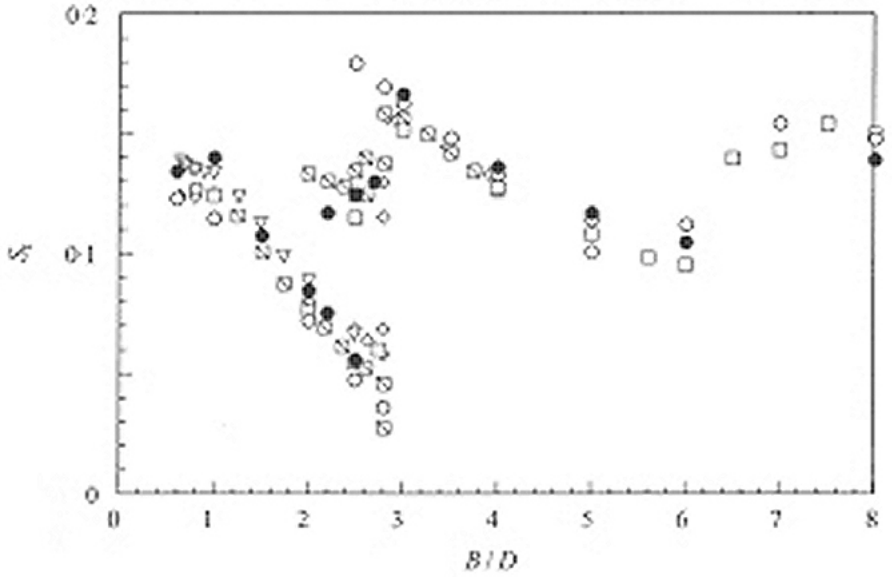

Figure 2-8: Variation of Strouhal number [Shimida *et al.*, 2002]

[a] Note that some of the figures use the equivalent notation B/H, or b/d, or B/D.

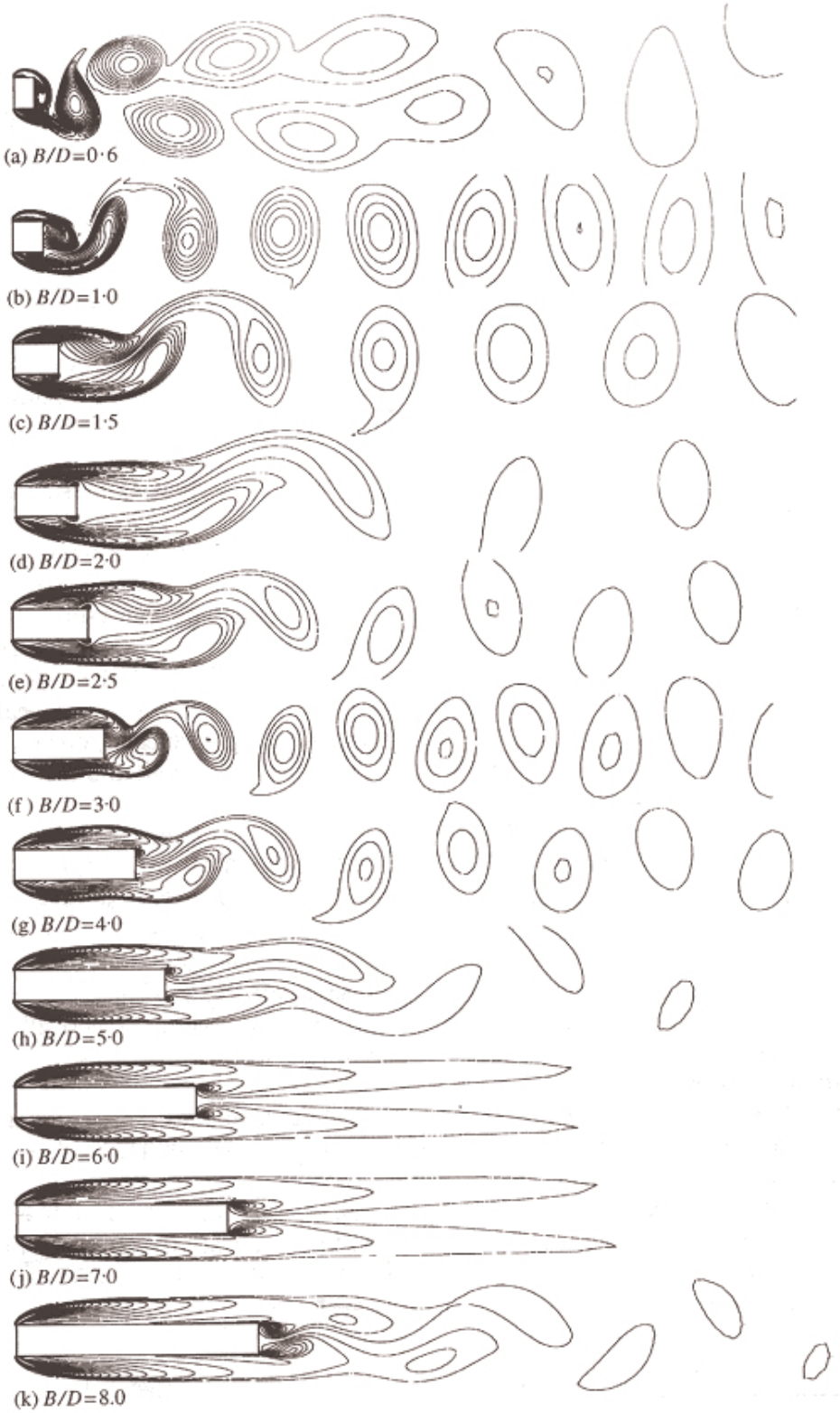

Figure 2-9: Instantaneous vorticity contours around rectangular cross-sections [Shimida *et al.*, 2002]

2.2.2 Influence of angle of incidence

A second distinction, the first being the alternating separation point, between the flow around a circular cylinder and a rectangular cylinder is the influence of the angle of incidence, α. Clearly a circular cylinder is line symmetric for every line passing through its origin and thus the flow around it will also be symmetrical, and similar at every angle of incidence. In contrast the flow around a rectangular cylinder at an angle of incidence is obviously not identical for all angles of incidence. See for example figure 2-10 where a sketch of the flow around a rectangular cylinder is given. From this sketch it can be noted that for some angles of incidence reattachment can occur.

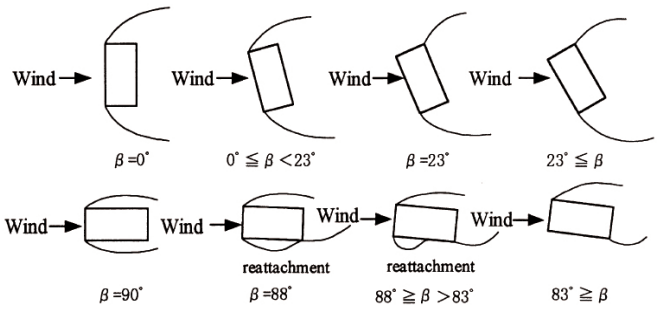

Figure 2-10: Assumed flow pattern around a rectangular prism [Matsumoto *et al.*, 1998]

Luo *et al.* [1994] conducted an experimental investigation to identify the effects of after body shape and the angle of incidence on the flow past several prismatic bodies. The tested prismatic bodies are a square cylinder, 2 trapezium cylinders and a triangular cylinder. Based on their definition of positive directions (figure 2-11), which are commonly defined in the opposite sense, the results for the lift coefficient and the drag coefficient are plotted in figure 2-12. The angle of incidence at which reattachment occurs happens to be the same angle at which the lift coefficient is at its maximum (its minimum negative value in standard notation) for every tested cross-section. At this position the drag coefficient is also at its minimum [Chen *et al.*, 1999]. When the cylinder is at positive angle of incidence (here: downwards) the flow will separate from both corners. The shear layer from the corner closest to the free stream flow will be also closest to the cylinder. This will result in a high suction on this side of the model and a higher pressure on the other side. The shear layer separating from the other corner will be further from the cylinder, resulting in a higher pressure. This will lead to a positive lift coefficient (note again that the angle of incidence is defined positive for a rotation counter clockwise).

Increasing the angle of incidence will ensure that the shear layer from the corner closest to the free stream moves closer to the cylinder. At a certain angle of incidence this shear layer will reattach on the cylinder, the lift coefficient is at its maximum at this position. Also a separation bubble is formed on this side of the model. When the angle of incidence is increased even further this separation bub-

ble will decrease in size. Simultaneously the pressure difference will decrease, and consequently the lift coefficient will decrease (increase in common notation). The influence of the angle of incidence and the occurrence of reattachment is thus similar to a change in the shape of the after body. So reattachment of the shear layer on the cylinder can occur at a certain angle of incidence and/or for a certain length to height ratio (see figure 2-9).

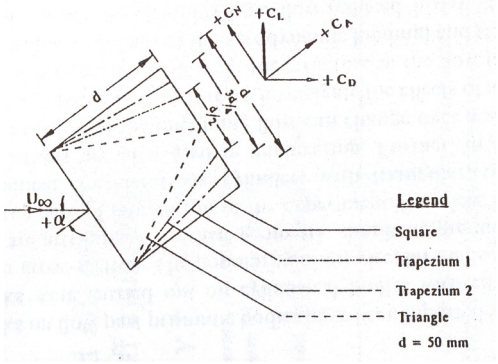

Figure 2-11: Dimensions of cross-sections and directions of positive quantities [Luo *et al.*, 1994] - *Note: Common positive directions are defined opposite of these definitions*

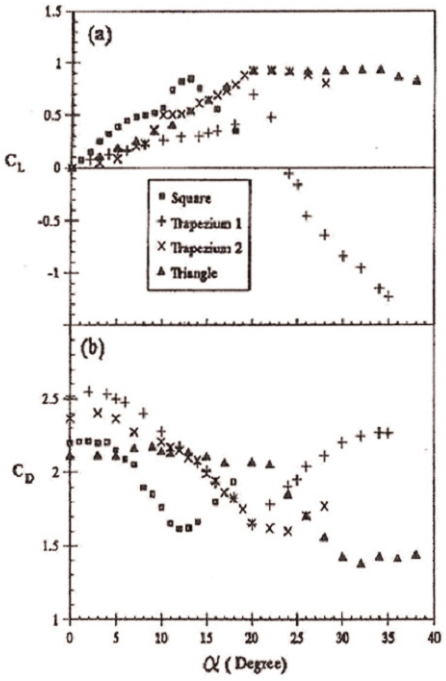

Figure 2-12: a) C_L versus α, b) C_D versus α [Luo *et al.*, 1994]

2.2.3 Bluff bodies subjected to galloping

The specific nature of bluff body flow is responsible for vibration of the structure. A distinction can be made in two types of vibration:

1. Vortex induced vibration (VIV),
2. Flow-induced vibration (FIV)

In the vortex induced vibration (VIV) vortices are shed at (or close to) the natural frequency of the structure causing the structure to respond [Williamson *et al.,* 2004]. The flow-induced vibration (FIV) is characterized by a low frequency oscillation, much lower than the vortex shedding frequency [Robertson *et al.*, 2003]. In the current research flow induced vibrations are of interest. Regarding the flow around bluff bodies the typical type of flow-induced vibration is commonly referred to as galloping, it is similar to flutter in an aero-elastic analysis.

Galloping is a low frequency high amplitude vibration, hence the name as it is similar to the motion of a galloping horse. This type of vibration can clearly be seen on a windy winter day when ice accretion on a power cable acts like a bluff body and thus becomes susceptible to galloping. Because of the high amplitude motion, galloping can also cause great damage to bridge decks or power cables.

2.2.4 Aerodynamic properties of rectangular cross-sections

A summary of properties for cross-sections with different length to height ratios, b/h, is given below [Parkinson, 1963]:

$0.375 \le b/h \le 0.683$
- No galloping from rest
- Vortex excited oscillation possible
- Strouhal number, wake width and drag coefficient nearly constant

$0.75 \le b/h \le 1.50$
- Galloping from rest
- Decreasing stationary amplitude at give wind speed for increasing b/h
- Behaviour like a square
- Strouhal number, wake width and drag coefficient decrease continuously

$1.725 \le b/h \le 3.00 \sim 4.00$
- Galloping from rest
- Decreasing stationary amplitude at give wind speed for increasing b/h
- Somewhere between 3.00 and 4.00 galloping from rest impossible (galloping from initial finite amplitude)
- Strouhal number, wake width and drag coefficient decrease continuously

$b/h \ge 4.00$
- No galloping
- When galloping stops, sudden increase in Strouhal number then for increasing b/h slow decrease, wake width and drag reach constant value for increasing b/h.

2.3 Description of classical (vertical) galloping

In order to predict galloping and its related properties, the commonly used theory is the quasi-steady theory [Blevins, 1990]. The two basic assumptions in the quasi-steady theory are that the dynamic effect of the oscillating motion can be approximated as if it was rectilinear and that there is an aerodynamic equivalent steady situation for each phase in the unsteady motion. The first implication of these assumptions is that any inertial or history effect is neglected and that only time-mean forces act on the structure, due to large separation between oscillation and vortex shedding frequencies. The second implication is that measurements on a static structure will be equivalent with an oscillating structure in a corresponding position.

Two forms of galloping exist, translational and rotational galloping. Translational galloping is a pure 1-DOF vibration, dominated by damping effects. The modelling of rotational galloping poses the additional aspect that both stiffness and damping effects are present [Van Oudheusden, 2000]. For translational galloping first order stiffness effects are absent and the modelling is simplified. The galloping curves (i.e. steady amplitudes as a function of wind speed) of translational and rotational galloping differ from each other in that for rotational galloping the limit-cycle amplitude tends to a constant value, whereas for translational galloping a linear asymptote is reached.

To provide insight in the dynamics behind galloping and its aerodynamic modelling, the stability criterion for a stable oscillation can be derived for the translational galloping case of 1-DOF damped mass-spring system. The followed derivation is similar to the derivation from Blevins [1990]. The expression for the vertical displacement can be used to address the stability of the damped mass-spring system. The displacement of the vibration is stable when (the exponential term in the solution, see equation (A.16) in Appendix A) the amplitude of the equation of motion decreases with time. This requires that the net damping should be larger than zero, or in terms of the vertical force component, C_y:

$$\left.\frac{\partial C_y}{\partial \alpha}\right|_{\alpha=0} < \frac{4m\omega_0\zeta_0}{\rho U_\infty D} \quad (stable) \tag{2.3}$$

where α the angle of incidence, m the mass of the model, ω_0 the natural frequency of the system, ζ_0 the structural damping of the system, ρ density of medium, U_∞ the free-stream velocity and D the side length of the model.

All terms on the right hand side of this strict inequality are positive and can be regarded as the structural damping component. It states that for a stable vibration the aerodynamic damping should be smaller than the structural component. The inequality is inversely dependent on the free stream velocity. For small velocities, the structural component is relatively large and galloping cannot occur, however when the velocity is increased, the ratio of the structural and aerodynamic component becomes smaller and galloping may occur.

The inequality for stable vibration can also be expressed in terms of the lift and drag coefficient and neglecting the structural component. Den Hartog first derived this inequality in the 1950's:

$$\left.\frac{\partial c_L}{\partial \alpha}\right|_{\alpha=0} + c_D > 0 \quad (stable) \tag{2.4}$$

An important feature related to galloping is that when the stability criterion is *not* fulfilled negative aerodynamic damping can occur, e.g. the net damping will be smaller than zero. From the above expression, it can be seen that, since C_D is always positive, a necessary requirement for galloping is the occurrence of a nega-

tive lift slope, $\partial c_L / \partial \alpha < 0$. This illustrates why galloping cannot occur on streamlined bodies with attached flow (wings for example), but only when flow separation occurs.

2.4 Research questions

Sustained oscillations (limit cycle solutions) are obtained where the negative aerodynamic damping just compensates the structural damping. Experimental rotational galloping curves for a rectangular cross-section show a large deviation from the quasi-steady theory [Van Oudheusden, 2000]. At different damping settings of an oscillator experiments tend to be over predicted for high damping settings. The experimental results are even more over estimated at low reduced wind speeds. For a square cross-section, on the other hand, the normalized aerodynamic amplitude curves were found to fall indeed onto a single curve, as predicted by the galloping theory [Van Oudheusden, 1995]. The observed discrepancies between experimental and theoretical galloping curves indicate a possible invalidity of the quasi-steady theory under certain conditions. It is one of the major motivations for the present quantitative visualisation study.

In order to investigate the above mentioned differentiations ongoing research is conducted at the Aerodynamics department of the faculty of Aerospace Engineering of the Delft University of Technology. The ultimate goal of the investigations is an explanation of the noted differences. For this it is necessary to assess the validity of the quasi-steady galloping theory. In the quasi-steady theory, it is assumed that the object is in a ‘steady’ position and that this position may be used to predict the galloping. It comes down to comparing an object at a steady position with one at a moving position, which resembles the galloping motion. The current research project will focus primarily on the establishment of an extensive database of steady measurements to which future measurements on a moving object can be compared.

Chapter

3

Experimental Arrangement

In the present study, the flow around the square cylinder is visualized with Particle Image Velocimetry (PIV). With this nonintrusive technique, instantaneous velocity vectors are obtained after post-processing of the acquired particle images. The experimental tests are performed in the W-tunnel, a low-speed open wind tunnel, of the Aerodynamics Department of Delft University of Technology. The basic experimental set-up is described in detail. This set-up is modified between measurement campaigns for different analysis purposes and practical reasons. The acquired results were also validated with a separate routine in order to minimize outliers.

3.1 Principles of Particle Image Velocimetry (PIV)

In contrast to many other experimental methods Particle Image Velocimetry (PIV) is a nonintrusive technique. There are no external objects, needed for measurement, inserted into the flow, leaving an undisturbed flow. PIV enables an indirect flow field velocity measurement. The general principal can be explained with the aid of figure 3-1. There are micrometric tracer particles introduced into the flow, subsequently illuminated within a light sheet at a given pulse time separation, t'- t. At each of these illumination pulses the light scattered by the particles is recorded by a digital imaging system. After spatial cross-correlation of the acquired images, the local displacement of the particles is known. The velocity is then evaluated by dividing the displacement with the known time separation. In the following paragraphs the general method of PIV for two-dimensional flows will be explained in more detail. Most of the information is extracted from Raffel *et al*. [1998].

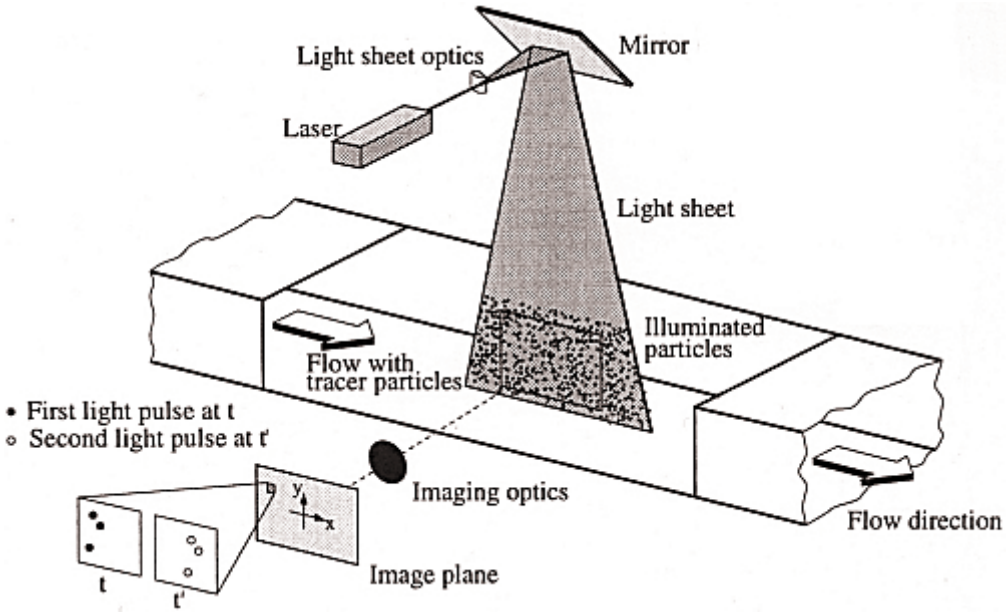

Figure 3-1: Experimental arrangement for particle image velocimetry in a wind tunnel [Raffel *et al.*, 1998]

3.1.1 Seeding and illumination

PIV is a nonintrusive method; nevertheless, generally small particles (seeding) have to be added to visualize the flow. These particles must (be able to) follow the flow medium, therefore large and heavy particles cannot be used. The difference in density between the seeding material and the medium sets another constraint on the size of the particles. To account for this difference the particles should have a small diameter. These constraints are clearly visible in an estimate for the velocity lag, $\vec{U}_s$, of a particle in a continuously accelerating fluid:

$$\vec{U}_s = d_p^2 \frac{\rho_p - \rho}{18\mu} \vec{a} \tag{3.1}$$

where d_p the particle diameter, ρ_p the particle density, μ the dynamic viscosity of the fluid and $\vec{a}$ the acceleration.

Equation (3.1) for the velocity lag is based on Stokes drag law and valid for spherical particles in an accelerating flow at a very low Reynolds number. At different flow conditions the equation can still be used to indicate the tendency for velocity lag of the flow. The velocity lag should be minimized for a particle to be able to follow the flow. Ideally, the particle density should equal the flow medium density. Otherwise, the particle diameter can be minimized.

However, this diameter cannot be too small because of light scattering properties. Light is not blocked by small particles, but according to Mie's scattering theory, spread in all directions (see figure 3-2). Small particles tend to scatter less and by using larger particles the scattered light intensity is increased.

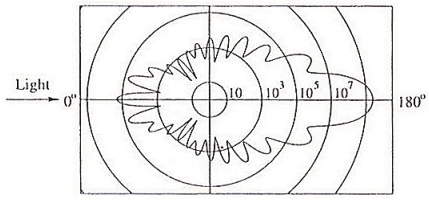

Figure 3-2: Light scattering by 1 μm oil particle in air [Raffel *et al.*, 1998]

So a balance has to be found for the size of the particles. The seeding material should be distributed evenly in the flow, and for open wind tunnels should be non-toxic. Appropriate seeding materials for gas flows are liquid based particles. The liquid will evaporate before entering the test section, leaving the tracer particles submerged into the flow.

In order to capture the seeding particles onto a recording device, they need to be illuminated by a high power energy source. Also the resulting light should be monochromatic and free of chromatic aberrations. Lasers possess these capabilities and are thus the most commonly used sources of light in PIV experiments. Laser light can easily be transformed, through a specific lens arrangement, into a thin light sheet. Several types of lasers are available but the most widely used solid-state lasers are Nd:YAG lasers. Nd:YAG stands for Neodym-Yttrium-Aluminum-Garnet. In this particular material neodym ions, Nd^{3+}, are incorporated in YAG crystals. The emission of light occurs after excitation of the material. The material is brought into a different energy level by transferring energy, generally by electromagnetic radiation. When the excited material drops back to its original energy state, stimulated emission of photons, e.g. light, results.

3.1.2 Particle image recording

The particle images are recorded onto the pixels of a camera. There are two distinct methods for recording PIV images:

Single Frame/Double-exposure records two exposures into one single image.

Double Frame/Single-exposure records one exposure into two images.

The former method introduces a directional ambiguity since it is not possible to distinguish which frame was recorded first. It is thus not possible, without any modifications, to track the direction of motion of the particles. This method was historically the first method that was used. In the last method the temporal order of the images is known, and thus also the direction of the particles. Two other advantages of the double frame/single-exposure recordings are:

- more flexibility in the pulse separation time range,
- higher signal-to-noise ratios in the correlation plane.

The optical properties of seeding particles that are to be recorded should be optimised with respect to their size in the image plane, e.g. the CCD (Charge-Coupled Device) sensors of a CCD camera. A CCD sensor is an electric sensor that converts light into an electric charge. One CCD sensor is equivalent to one pixel. The

intensity of the illuminated particles is read out from these sensors as a two dimensional array of grey intensity levels, the resulting images of the particles. One of the issues here is that light from a small particle is not imaged as a bright spot on the CCD. The particle is imaged on the CCD by using a lens, the objective in a camera, with a (to be) chosen aperture. The imaged is slightly blurred on the CCD. This effect is caused by diffraction of light when it passes a circular aperture. It is called Fraunhofer diffraction. The size of the diffraction limited minimum image diameter, d_{diff}, can be calculated with:

$$d_{diff} = 2.44 f_{\#} \left(M + 1\right) \lambda \tag{3.2}$$

where $f_{\#}$ the f-number, i.e. the ratio of the focal length of the camera and its aperture, M the magnification factor, i.e. the ratio of the image size and the object size, and λ the wavelength of the light. The particle image diameter, d_{τ}, can be estimated with:

$$d_{\tau} = \sqrt{\left(M d_p\right)^2 + d_{diff}^2} \tag{3.3}$$

where d_p is the (physical) particle diameter.

Equation (3.3) holds when lens aberrations can be neglected and the diffracted pattern can be described with a so-called Airy pattern. Note also that the first term under the square root can usually be neglected because the particle diameter is generally small, e.g. smaller than 50 μm.

There are two main reasons for optimising the particle image diameter. The first is that theoretically the error in velocity measurements is at its minimum for a particle image diameter of slightly more than 2 pixels. Secondly, the displacements of small particles can be biased towards integral values. This effect is called 'peak-locking'. It arises from the fact that when a particle is imaged fully within a pixel, the position of the maximum intensity cannot be determined adequately. 'Peak-locking' should always be avoided.

Another important imaging parameter that is affected by the lens aperture is the depth of field, δ_Z. This focal depth gives a measure for the focus of an image. Outside this focal depth images are blurred and it is to be ensured that the laser sheet is focused within this depth of field. The formula for δ_Z is given by:

$$\delta_Z = 2 f_{\#} d_{diff} \frac{\left(M + 1\right)}{M^2} \tag{3.4}$$

3.1.3 Image processing

So far it has been simply stated that the acquired images are to be post-processed to obtain the particle displacement, and the particle velocity accordingly. Several techniques are available to analyse images. The current experiments are analysed

with WIDIM, **Wi**ndow **D**eformation **I**terative **M**ultigrid [Scarano *et al.*, 1999], a post-processing tool developed in MATLAB. This tool is developed by Scarano and is continuously improved. This paragraph will give specific details on this tool. A contribution was made to this software package by introducing a graphical user interface (GUI). This GUI enables an easy way to create the necessary input-files for the WIDIM software package [Roosenboom, 2005].

The standard procedure to obtain the particle displacement by cross-correlation of two images is visualized in figure 3-3. Two sub regions of two images of one exposure are compared to produce a correlation peak, the single bright spot on the right in figure 3-3. The particles in the top-image move from their respective positions to those of the lower image. The single bright spot indicates that the particles move slightly to the bottom-right. After some inspection (e.g. identifying similar particles) of the images on the left this can be seen by the eye. The cross-correlation can be written in a discrete mathematical sense as follows:

$$S(x,y) = \sum_{i=-w}^{w} \sum_{j=-h}^{h} I(i,j) I'(x+i, y+j) \tag{3.5}$$

where a small region [-*w,w*]x[-*h,h*] of grey intensity values in I is linear shifted around, in i and j direction, in a larger region with grey intensities in I' to obtain a correlation peak S at the point (x,y).

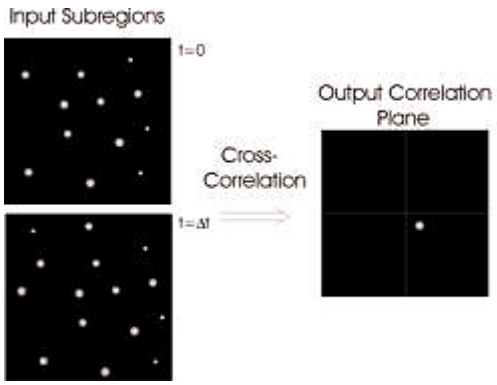

Figure 3-3: Two single exposure input subregions and the corresponding output cross-correlation plane. The location of the single bright correlation peak from the origin is the average displacement across the subregion. [Wernet, 1999]

Another consideration in PIV with respect to cross-correlation is that it is necessary to distinguish the cross-correlation peak from any measurement noise. Figure 3-4 shows a correlation peak R_D and the summation of the convolution of intensities, R_C, and fluctuating noise, R_F. To identify R_D as the correlation peak it should be larger than $R_C + R_F$. The signal-to-noise is thus defined as the ratio of R_D and $R_C + R_F$. The signal-to-noise ratio should already be considered in the set-up of the experiment. The signal-to-noise ratio should always be maximized, to reduce any measurement errors. To optimise the signal-to-noise one should look at a live preview of the cross-correlation of the flow so that any change of variables can be seen immediately. Key factors that need to be adjusted are the intensity of the laser, e.g. power, the laser sheet thickness, the overlap between the two lasers sheets and the time separation between laser pulses.

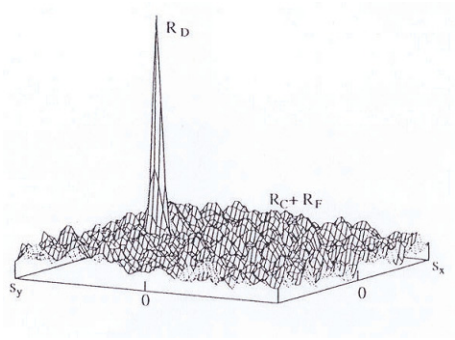

Figure 3-4: Composition of peaks in the cross-correlation function [Raffel *et al.*, 1998]

The distances, $\Delta\bar{x}$, in the sub regions for which the correlation function $S(x,y)$ produces the highest results are the particle displacements. The velocity field, $\bar{V}$, can then be determined according to:

$$\bar{V} = \frac{\Delta\bar{x}}{\Delta t} \tag{3.6}$$

where Δt the pulse separation time.

It can be remarked that dividing an image into equal sub regions (as is done in a standard approach in figure 3-3) has some disadvantages. Some of the particles present in the first region will move out of sight in the second image. This is called in-plane loss-of-pairs. Loss-of-pairs can also be due to out-of-plane motion because of three dimensionality of the flow or misalignment of the set-up. The negative effect of in-plane loss-of-pairs is minimized in the WIDIM software package by using a window offset to compute two interrogation windows. Figure 3-5 shows the principle of a window offset. The displacement δ is used to estimate the position of the grey rectangle. This can be improved by also taking into account the local displacement gradient, represented in figure 3-6.

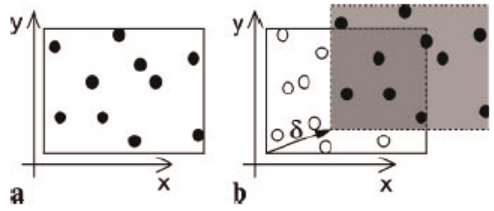

Figure 3-5: Principle of the window displacement [Scarano *et al.*, 1999]

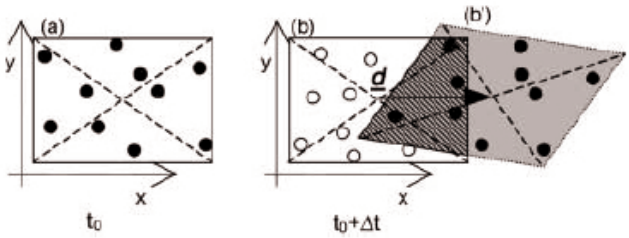

Figure 3-6: Schematic illustration of the image transformation due to in-plane motion. Particles follow the mean displacement *d* (translation) and the local displacement gradient [Scarano, 2002]

The window offset is not a priori known. Therefore an iterative method is employed where at every iteration step the sub regions are made smaller. The displacements found in these regions are then used as a predictor for the next itera-

tion step. A graphical interpretation is given in figure 3-7. When a final window size is reached, any next iteration is used to refine the computed data. WIDIM is therefore an iterative multigrid method that employs a window deformation. The iterative procedure of WIDIM enables also the possibility to validate the computed data at the end of every iteration, in contrast to non-iterative methods. It has the advantage that propagation of errors is reduced.

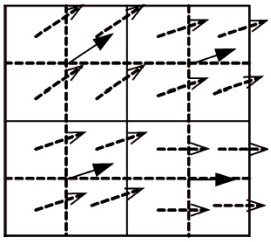

Figure 3-7: Application of an interrogation result (solid line arrows) to build a finer predictor (dotted line arrows) [Scarano *et al.*, 1999]

3.2 Experimental set-up

In the following sections a description of the experimental apparatus used in the present study is given. It gives a quantification of the aspects mentioned in the previous sections.

3.2.1 Wind tunnel and models

The experiments are performed in the open wind tunnel, W-tunnel, of the Aerodynamics Department of the Faculty of Aerospace Engineering of Delft University of Technology. The wind tunnel exit has an area of 0.4 x 0.4 m^2. A Perspex box with a cross-sectional area of 0.4 x 0.4 m^2 and a length of 0.4 *m* is installed at the exit to reduce the boundary effects of this exit. This Perspex box also allows optical access and an easy way to place calibration sheets. The maximum velocity that can be achieved with this wind tunnel is approximately 38 *m/s* (or 138 *km/h*). The wind tunnel has a low (~0.1%) turbulence intensity.

There are two models used in the experiments. Both models are cylinders with a square cross-section with a side length of 30 *mm* and a span of 345 *mm*. Taking into account the size of the model, the size of the wind tunnel section and the angles of incidence studied, it follows that the maximum blockage ratio during the experiments is about 10.6% at an angle of incidence of 45°. Note however that the effective blockage ratio is larger due to a displacement of the streamlines at the upper and lower surface of the model. The first model is the original model as used in previous visualisation PIV experiments [Van Hinsberg, 2004]. It is fully constructed of solid Perspex. However, this model produces relatively large shadow regions when crossed by the laser light sheet due to internal refraction and reflection effects (see Appendix B and Van Hinsberg [2004]). Since further experiments would involve static measurements where modest mechanical stiffness and strength of the model was required, it was decided to use a model with reduced shadow regions, a square cylinder with a hollow optical accessible area. In the following the differences between the two models will be explained. A detailed description of the optical properties of the two models is given in Appendix B.

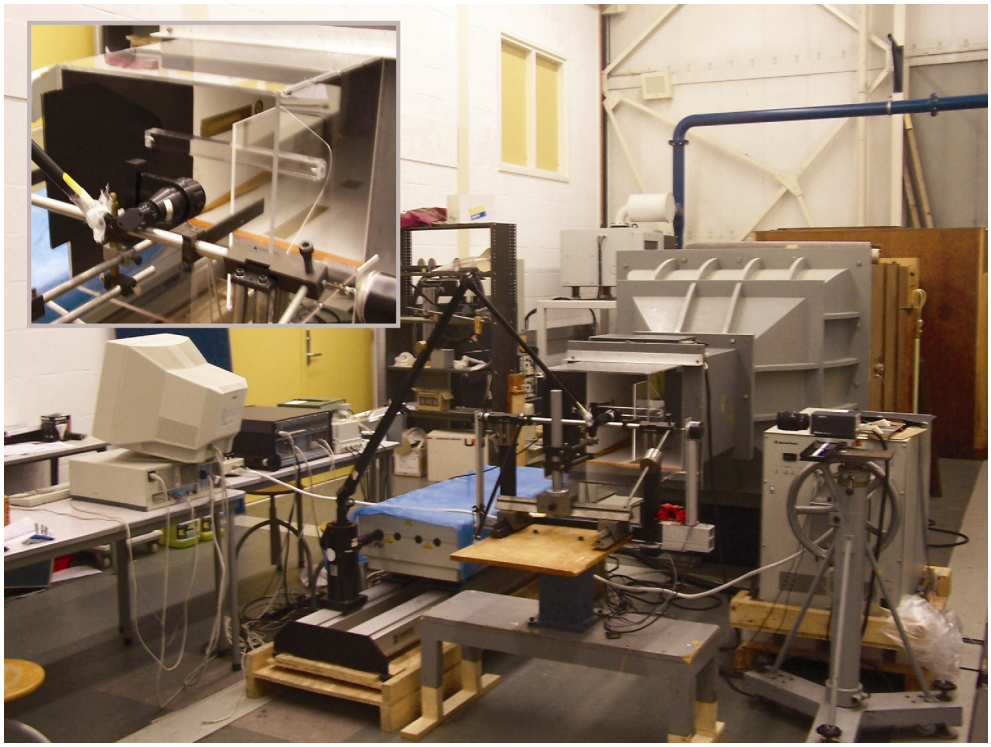

Figure 3-8: Wind tunnel and PIV set-up; inset shows a close-up of the full Perspex model and end-plates

The full cylinder is made of solid Perspex and has a square cross-sectional area of 30 x 30 mm^2 and a length of 345 *mm*. An overview of the wind tunnel and the full Perspex cylinder is given in figure 3-8. This model is attached to endplates and an oscillator frame originally developed for dynamic galloping investigations (as described in Van Oudheusden [1995] and [2000]). The endplates are connected to this oscillator frame through a hinge, which allows rotation of the model. In order to change the angle of incidence of the cylinder the model needs to be rotated about the hinge axis. This has the disadvantage that the model will move out of the field of view of the camera. Therefore, one must reposition the camera and/or move (!) the total oscillator frame. Thereafter calibration images have to be made and it has to be insured that the laser sheet is still aligned properly.

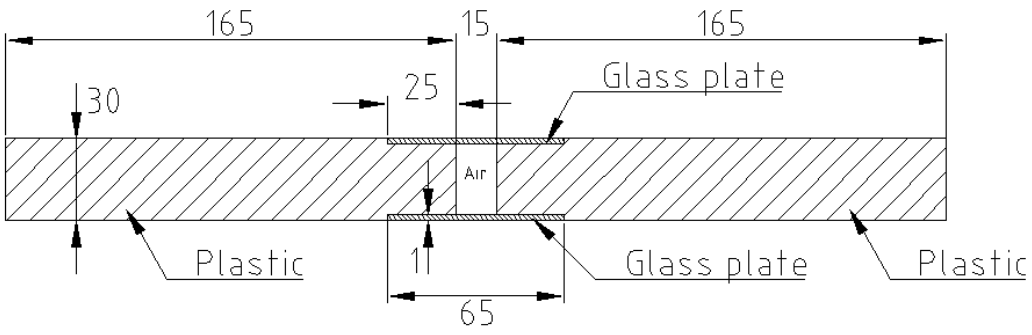

Figure 3-9: Cross sectional view of hollow glass model (all distances in *mm*)

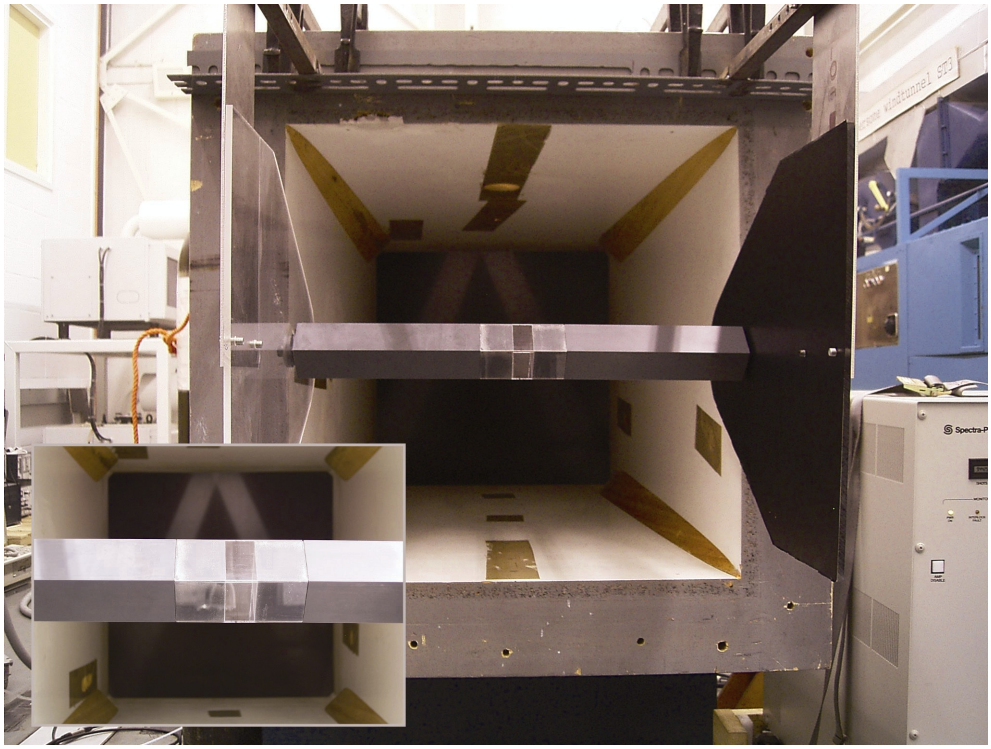

Figure 3-10: Hollow cylinder with endplates attached to wind tunnel; inset shows a close-up of the hollow cylinder

The hollow cylinder is constructed from two hard plastic parts with a constant square cross-section area of 30 x 30 mm^2 and a length of 165 *mm* (see figure 3-9). The two separate parts are connected by 4 thin glass plates, leaving an optical accessible (hollow) gap of 15 *mm* width in spanwise direction. The total length of the cylinder is (again) 345 *mm*. At the position where the glass is connected to the hard plastic parts the cross-sectional area of these parts is slightly reduced to provide a smooth surface. This construction greatly reduces the unwanted shadow stripe effects in comparison to the full Perspex model (see Appendix B). The hollow cylinder is connected to the endplates with adjustable screws. These endplates are *not* attached to the oscillating system but directly to wind tunnel by two metal parts. The oscillating system is not used because at this point in the measurement campaign it was determined that only static measurements would be carried out.

The direct connection to the endplates has also the advantage that the angle of incidence of the model can be changed by simply rotating the model, while keeping it in the field of view of the camera. There is no need to adjust the position of the camera and the experiments are not interrupted for movement of the oscillating system. The wind tunnel, metal sheets, the endplates and the hollow cylinder are shown in figure 3-10. The inset shows a close-up of the model with the hard plastic parts and the thin pieces of glass.

3.2.2 Flow seeding, illumination and imaging

The flow is seeded with a water based fog liquid, resulting in 1 μm oil particles after injection by a SAFEX™ Twin-fog “Double Power” fog-generator. The seed-

ing material is non-toxic and will remain in the wind tunnel hall for about 45 minutes. The flow (and seeding) is illuminated with a Spectra Physics™ Quanta-Ray PIV-400 double-cavity pulsed Nd:YAG laser. The wavelength of this laser is 532 *nm* (e.g. green light). The laser delivers an energy output of 400 *mJ* per pulse for a duration of 6 *ns*. Two types of cameras are used to record snapshots of the flow. These are a DANTEC™ HiSense PIV/PLIF CCD camera and a PCO™ SensiCam QE CCD camera, both equipped with a Nikon 60-mm focal length objective. Some of their properties are given in table 3-1.

Table 3-1: Properties of available CCD cameras

	Dantec	**PCO**
Resolution (*W* x *H, pixel*)	1280 x 1024	1376 x 1040
Storage (*bit*)	12	12
Pixel size (μm^2)	6.7 x 6.7	6.45 x 6.45
Used in case	A; B	A; C

3.2.3 Field of view configurations

This paragraph shows the evolution of the measurement configurations. In total three different measurement campaigns were performed. The first experiments focused on the wake behaviour of the flow, and two cameras were used simultaneously to obtain an increased (elongated) field of view. In the second measurements the focus was shifted to the reattachment of the vortices on the model and the model was viewed in close-up. In these two measurement series the angle of incidence was varied between 0° and 15°, at a step of 5°. In the final series of experiments a finer interval was chosen for varying the angle of incidence from 0° and 45°. These experiments were also performed in a batch-like situation and a vast amount of data was acquired. Some specific numbers and settings about the experiments are summarized in table 3-2. Table 3-3 shows theoretical calculated variables that can be derived from the settings in table 3-2 and the equations in paragraph 3.1. All experiments were performed at a free stream velocity of 10 *m/s* and consequently at a Reynolds number of $2 \cdot 10^4$ based on the model side length. Since earlier studies concluded that the flow was very dependent on the angle of incidence and only mildly on the Reynolds number (Van Hinsberg [2004], Luo *et al.* [2005]), only the angle of incidence is used in this parametric study.

In addition the maximum particle displacement, *s*, [in pixel] is determined to give a measure of the dynamic range:

$$s = V \cdot \frac{1}{S_c} \cdot \Delta t \tag{3.7}$$

where *V* the velocity in *m/s*, *Sc* the scale factor (*m/pixel*) and Δt (*s*) the pulse time separation.

Table 3-2: Settings during experiments

	Large view	Zoomed view	Multiple angles
Case	A	B	C
Type of model	Full Perspex	Full Perspex	Hollow
Number of cameras[a]	2	1	1
Magnification factor (-)	0.065	0.111	0.062
Scale factor (*mm*/*pixel*)	0.107	0.061	0.104
Focal number (-)	5.6 / 8[b]	11	11
Laser sheet thickness (*mm*)	~1	~1	~1
Total field of view (*W* x *H*)[c]	9 x 3	2.5 x 2	4.6 x 3.5
Reynolds number (-)	$2{\cdot}10^4$	$2{\cdot}10^4$	$2{\cdot}10^4$
Pulse separation (*μs*)	50	[20, 30]	[30, 50]
Frame rate (*Hz*)	3.3	3.3	3.3
Number of datasets per angle	1000	220	1000
Measured angles of incidence (°)	[0; 5; 10; 15]	[0; 5; 10; 15]	[0; 2.5; … ; 15; 20; 25; … ; 45]

[a] All measurements are two dimensional (2C)

[b] Different numbers due to difference in camera settings; Dantec camera has lowest value

[c] Normalized with model diameter, $D = 30$ *mm*

Table 3-3: Estimated imaging properties during measurements

	Large view	Zoomed view	Multiple angles
Particle image diameter (*pixel*)	1.20 / 1.72[a]	2.37	2.35
Minimum depth of field (*mm*)	20	31	90
Maximum pulse separation (*μs*)	50	30	50
Max. particle displacement (*pixel*)	5	5	5

[a] Different numbers due to difference in focal number; Dantec camera has lowest value

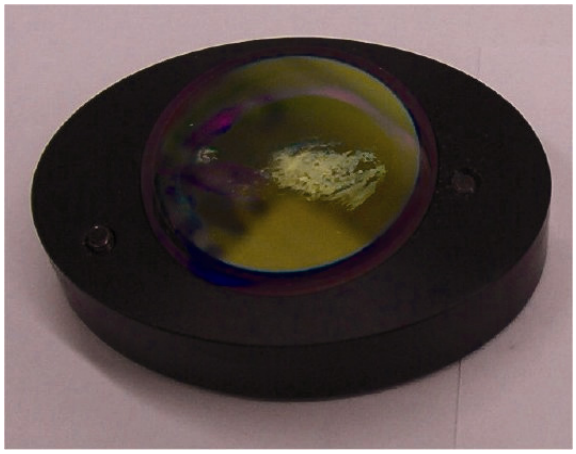

Figure 3-11: Mirror from laser arm with damaged coating

Not only was the evolution of the experiments influenced by the different goals of the experiments. The first experiments were greatly compromised by damaged mirrors in the laser arm. The second measurements were influenced hereby to less extent because the mirrors were cleaned and some mirrors were replaced. Before the third measurement series the laser arm was completely removed. A picture of one of the damaged mirrors can be seen in figure 3-11. The damage of the mirror is clearly visible. A schematic drawing of the Dantec laser arm is given in figure 3-12. This laser arm is (or was) used to provide a flexible way of introducing the light sheet into the flow. However, when the laser is (slightly) misaligned it will impinge on the circular rod of the laser arm. Since the laser has a high power the coating on the inside of the rod will, most likely, be damaged and tiny bits of dust will precipitate on the mirrors. The laser light will then burn these bits of dust into the mirrors. Also, after many operational hours seeding particles may protrude into the arm and be burned into the mirrors as well. It will speak for itself that the damaged mirrors reduce the quality of the acquired data.

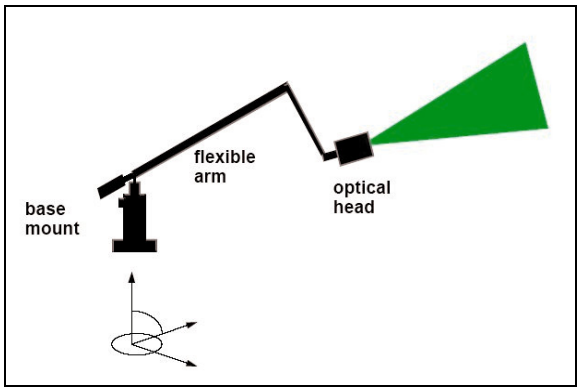

Figure 3-12: Sketch of the flexible Dantec laser arm [Dantec, 2000]

Samples of images acquired during the different measurement campaigns are shown in figure 3-13. From top to bottom images from the first, second and third campaigns are shown. The model is at an angle of incidence of 0° in the images on the left and at 15° in the images on the right. The most striking difference between the images is the level and quality of seeding. The final images show a uniform, and therefore optimal, distribution of seeding particles. It has been pointed out that in the first experimental campaign the mirrors inside the laser arm and laser head were damaged, resulting in poor illumination. The better illumination is also due to the increased focal number. Figure 3-13a and b were recorded with a focal number of 5.6, in the other images the focal number is 11. It was also found out during the third measurement campaign that the particles were more evenly distributed when the seeding generator was placed just outside the contraction room of the wind tunnel.

The fact that in figure 3-13 the (dark and light) stripes do not seem to emanate from the corners, is due to the perspective view. The view of the camera is partially blocked by the out of plane part of the model that is not in the plane of focus. This region is limited to the front and bottom side of the model and approxi-

mately 20% of the model side length. The crescent moon shaped white stripes in the top images are reflections of the end plate edges, which were in the field of view during these experiments.

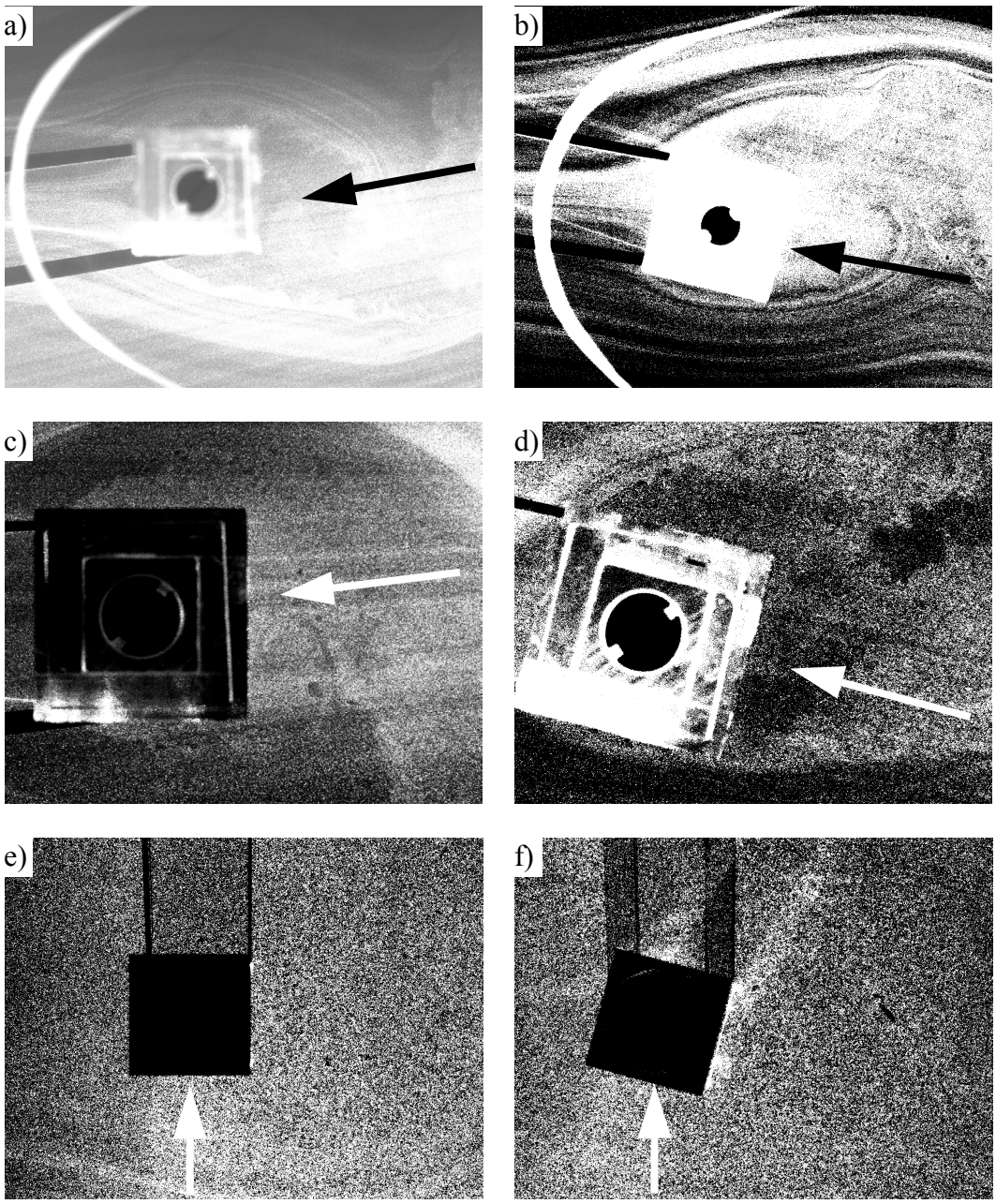

Figure 3-13: Shadow stripes emanating from model, the model is at an angle of incidence of 0° in the pictures on the left and at 15° in the pictures on the right, the flow is from left to right, arrows indicate the illumination direction; a)-d) full Perspex cylinder; e) and f) hollow cylinder

Large view for wake analysis, case A

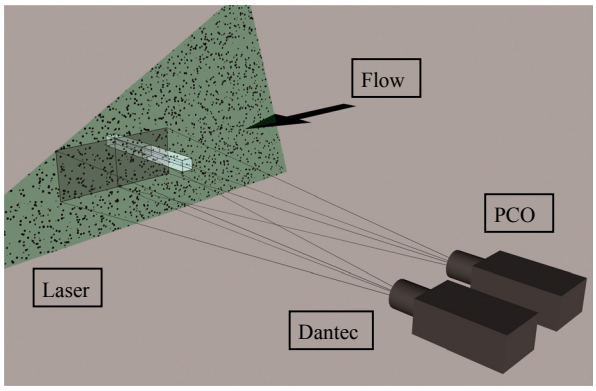

Figure 3-14: Sketch of experimental set-up with two camera's next to each other, case A

This experimental campaign uses two cameras to get a large field of view. The cameras are placed side by side to obtain a prolonged view of the wake. In these experiments the full Perspex model was used. The laser sheet was placed at a slight angle with respect to the flow direction. The laser sheet was aligned such that it crossed the middle of the model. A sketch of the set-up is given in figure 3-14. After the experiments it was found that the mirrors were damaged. The seeding was of low quality during the experiments and the focal number was set too low. All of this resulted in a low quality of the acquired data (low signal-to-noise ratio). It was even necessary to use a single pass during the cross-correlation.

Zoomed view for reattachment determination, case B

The second experimental campaign was used to acquire details of the reattachment of the flow on the model. Therefore one camera was used and it was placed closer to the laser sheet, with respect to the previous experiments. Also, to reduce the perspective error, the laser sheet was aligned more towards the side of the model. It was placed at about 80 *mm* of the side closest to the camera. It was assumed that at this position the two dimensionality of the flow was still valid. A schematic view of the set-up can be seen in figure 3-15. The mirrors and the laser head were cleaned before the measurements. This slightly improved the quality of the acquired data. The greatest improvement with respect to the previous experiments was the level of seeding. Also, setting the focal number of the camera to a higher number improved the situation.

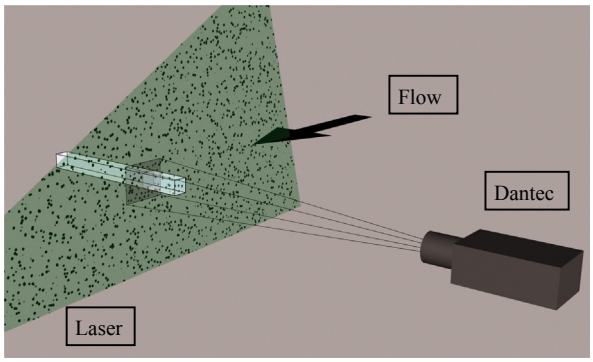

Figure 3-15: Sketch of experimental set-up for zoomed view, case B

High quality data at a wide range of angles, case C

The third and final experiments were used to obtain data for multiple angles. The measured angles were in the range between 0° and 45°. Between 0° and 15° at every 2.5° was measured; between 15° and 45° the interval was increased to 5°. The major modification with respect to the previous experiments was the change of the model. The hollow cylinder has a better light transmittance, as mentioned in Appendix B. Since the angle of incidence can now be modified by turning the model, it was fairly easy to prepare the wind tunnel set-up for the next set of an-

gles. The resulting dataset size was enlarged from 200 image pairs per angle to 1000 image pairs per angle. As a second improvement the flexible laser guide arm was also completely removed and replaced with a custom made optical system to create a laser sheet out of cylindrical and spherical lenses and an angle-reflecting element (prism). A sketch of the set-up is presented in figure 3-16. The better performance of the model and the improvement of the laser sheet quality also meant that the focal number could be increased. The resulting datasets are therefore of a good quality and should be able to serve as an extensive database for following measurement campaigns.

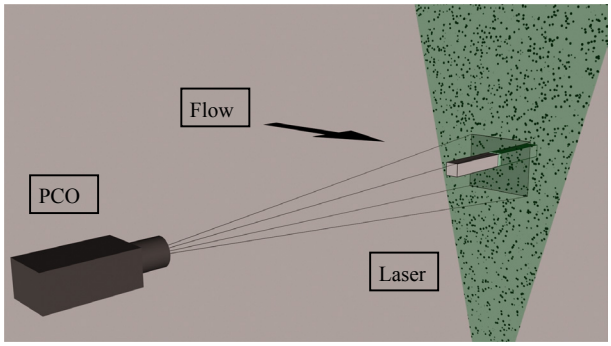

Figure 3-16: Sketch of experimental set-up with hollow cylinder, case C

3.3 Data post-processing

This paragraph describes the settings and equations used to obtain the instantaneous and time-averaged cross-correlation results. Also, a validation procedure is mentioned to minimize artefacts in the results.

3.3.1 Data analysis

The image pairs from the experiments are analysed with different settings, to improve the individual quality of the cross-correlation. These settings are summarised in table 3-4. It can immediately be noted that the settings for Case A yield coarse results. The results from Case B and C are defined on much finer grid. For illuminating reasons, mentioned in earlier in this chapter, the results from Case C are assumed to be the most accurate. The spatial resolution is estimated to be twice the grid spacing.

Table 3-4: Spatial properties of cross-correlation analysis

	Case A	Case B	Case C
Window size (*pixel* x *pixel*)	80 x 80	20 x 20	31 x 31
Overlap factor (%)	50	75	75
Number of datasets used	1000	220	1000
Grid spacing (*pixel*)	40	5	8
Grid spacing (*mm*)	4.3	0.3	0.84
Grid spacing (*D*)	0.14	0.01	0.03
Spatial resolution (*mm*)	8.6	0.6	1.7
Spatial resolution (*D*)	0.3	0.02	0.055

Despite the fact that the vortex shedding mechanism is predominantly a periodic phenomenon, interesting results can be derived from the time-mean flow. The sta-

tistical properties of the velocity field are derived after data processing of the images. To reduce propagation of errors due to outliers the statistical properties are based on an iterative averaging procedure until convergence has been reached.

The following statistical properties are derived for an dataset of N images. The mean velocity in x- and y-direction, respectively $\overline{u}$ and $\overline{v}$:

$$\overline{u} = \frac{\sum_{i=1}^{N} u_i}{N}, \quad \overline{v} = \frac{\sum_{i=1}^{N} v_i}{N} \tag{3.8}$$

Instead of plotting both the $\overline{u}$ and $\overline{v}$ velocity distributions, the magnitude of the velocity can be determined with:

$$|\vec{V}| = \sqrt{\overline{u}^2 + \overline{v}^2} \tag{3.9}$$

The mean velocity fluctuations u_{rms} and v_{rms}:

$$u_{rms} = \sqrt{\overline{u'^2}} = \frac{\sqrt{\sum_{i=1}^{N} \left(u_i - \overline{u}\right)^2}}{N}, \quad v_{rms} = \sqrt{\overline{v'^2}} = \frac{\sqrt{\sum_{i=1}^{N} \left(v_i - \overline{v}\right)^2}}{N} \tag{3.10}$$

And the Reynolds stress term $\overline{u'v'}$:

$$\overline{u'v'} = \frac{\sum_{i=1}^{N} \left(u_i - \overline{u}\right)\left(v_i - \overline{v}\right)}{N} \tag{3.11}$$

The normalized turbulence intensity, TI, is defined as:

$$T.I. = \frac{\sqrt{\overline{u'^2} + \overline{v'^2}}}{U_\infty} \tag{3.12}$$

The vorticity, ξ, of a two-dimensional velocity vector field can determined by:

$$\vec{\xi} = \frac{\partial \overline{v}}{\partial x} - \frac{\partial \overline{u}}{\partial y} \tag{3.13}$$

In the presented data all velocities have been scaled with the free stream velocity, U_∞, and dimensions with the cylinder side length, D, unless stated otherwise.

3.3.2 Data validation

After the filtering during the statistical analysis, there were still outliers present in the instantaneous and averaged velocity fields. These outliers compromised the computed pressure gradient and consequently the pressure field calculation (Chapter 5). The propagation of errors was too large. Instead of reanalysing the instantaneous data, a post-processing validation procedure was chosen. All the instantaneous data sets are read into memory and a histogram of the velocity distribution was created. Vectors in the instantaneous velocity field that were distinctively in the borders of the histogram are replaced by an average of surrounding vectors. The resulting instantaneous vector fields are then again time-averaged (with the original statistical averaging procedure). A similar procedure has currently been implemented in the post-processing software package AR-WIDIM 9.1.

A comparison of two statistical velocity fields is shown in figure 3-17. The red vectors are the original velocity vectors, the green vectors the new validated vectors. The original validation was not able to fully determine outliers in the corners of the dataset and near the position of the model. The new validation is better in these regions. It has to be noted, however, that the new validation still has small problems in replacing the vectors in the corners of the dataset. The results presented for the third measurement campaign (Case C) are based on the new validation of the datasets, as these were used extensively during the post analysis.

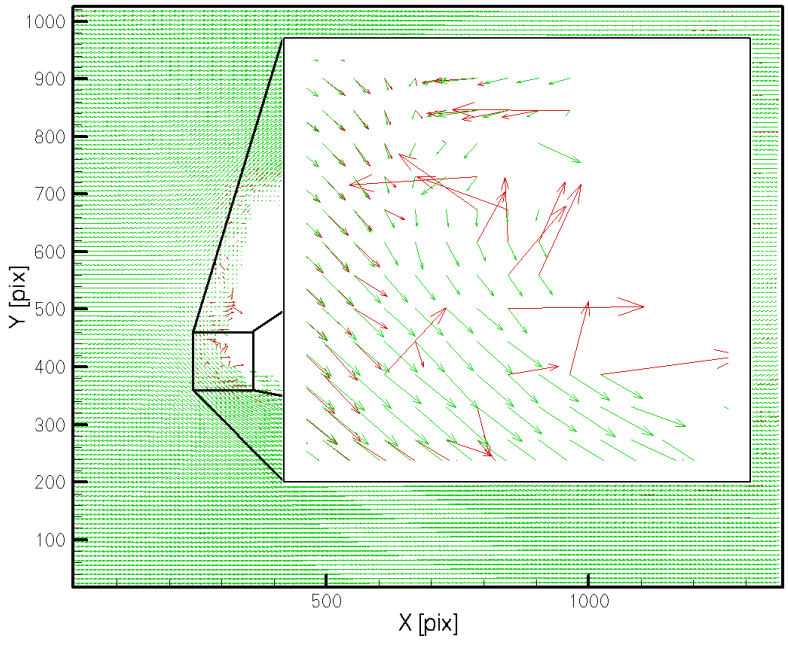

Figure 3-17: Comparison of two time-averaged velocity vector field plots before (red) and after (green) validation

A further check on the consistency of the velocity data is provided by investigating the divergence of the flow field. The divergence of a velocity field can be calculated with [Anderson, 1990]:

$$\nabla \cdot V = \frac{\partial \overline{u}}{\partial x} + \frac{\partial \overline{v}}{\partial y} + \frac{\partial \overline{w}}{\partial z} \tag{3.14}$$

For an incompressible flow, equation (3.14) should equal zero. The divergence is also a measure for the two-dimensionality of the flow, since in a two-dimensional flow no z-component of the velocity can be present. Figure 3-18 shows the divergence of a velocity field at an angle of incidence of 5°. The divergence of the velocity is approximately zero for most of the flow field. In three areas, the divergence deviates from zero. In the upper left corner the previously stated problem of bad vector replacement is clearly visible. The second area shows a contribution within the area influenced by the perspective view, introducing unreliable areas within the flow field. A third contribution can be found above the upper-right corner of the model and is due to shadow stripes emanating from this corner. Therefore, although the effect of the shadow stripes is greatly reduced by using the hollow cylinder model, still some influence is notable.

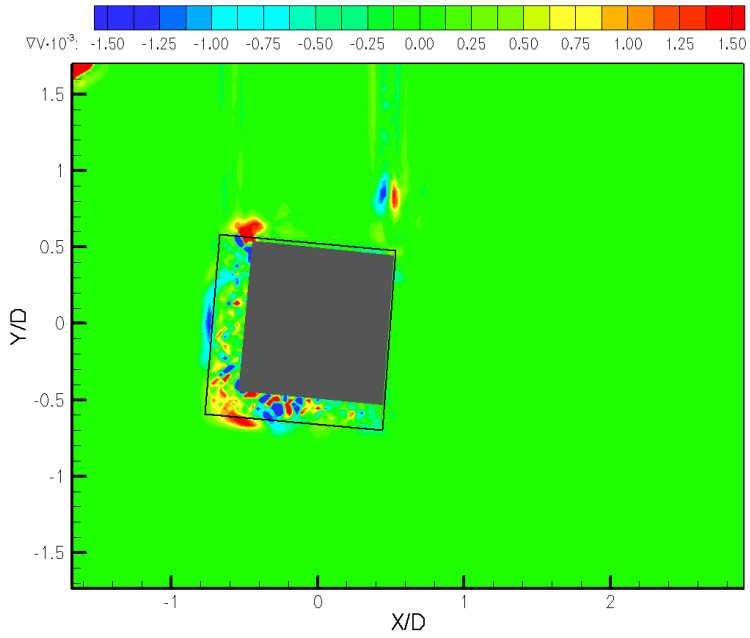

Figure 3-18: Divergence of velocity field at $\alpha = 5°$

Chapter

4

Flow Description

The results of the experimental visualization are presented in two sections. The first approach is a statistical description of the flow. Mean flow properties and turbulence are obtained from the experimental PIV data sets for each angle of incidence. The second approach is that of a phase-averaged reconstruction of the periodic flow component. For this the PIV results are first analysed with the Proper Orthogonal Decomposition (POD). This method returns the mean flow and the fluctuating part for every single flow configuration. The fluctuating part can be related to a specific phase angle of vortex shedding using a low-order flow representation.

4.1 Statistical flow characterisation

In this section, a selection of results will be presented to support the discussion of the most essential flow features and trends observed. The complete set of results of the statistical analysis is collected in Appendix D. The first experimental campaign was compromised by the low quality of the acquired data. During the second experimental campaign only 220 images were acquired. The final experimental campaign had the best quality of acquired data. The number of images per dataset acquired was 1000 and 13 different angles of incidence were measured. Unless stated otherwise, the results displayed here are taken from the final set of experiments, case C.

4.1.1 Flow topology

Typical time-averaged flow fields are plotted in figure 4-1a-d for angles of incidence of 0°, 10°, 12.5° and 30°, respectively. The regions affected due to the per-

spective view are not masked but are indicated by black lines enclosing the model. In these areas the streamlines on the lower side seem not affected by this region. The streamlines on the upper side (and the front side for 12.5°), however, are not well captured. For example in figure 4-1a a bubble appears to 'float' over the surface and in all images the streamlines seem to go through the model.

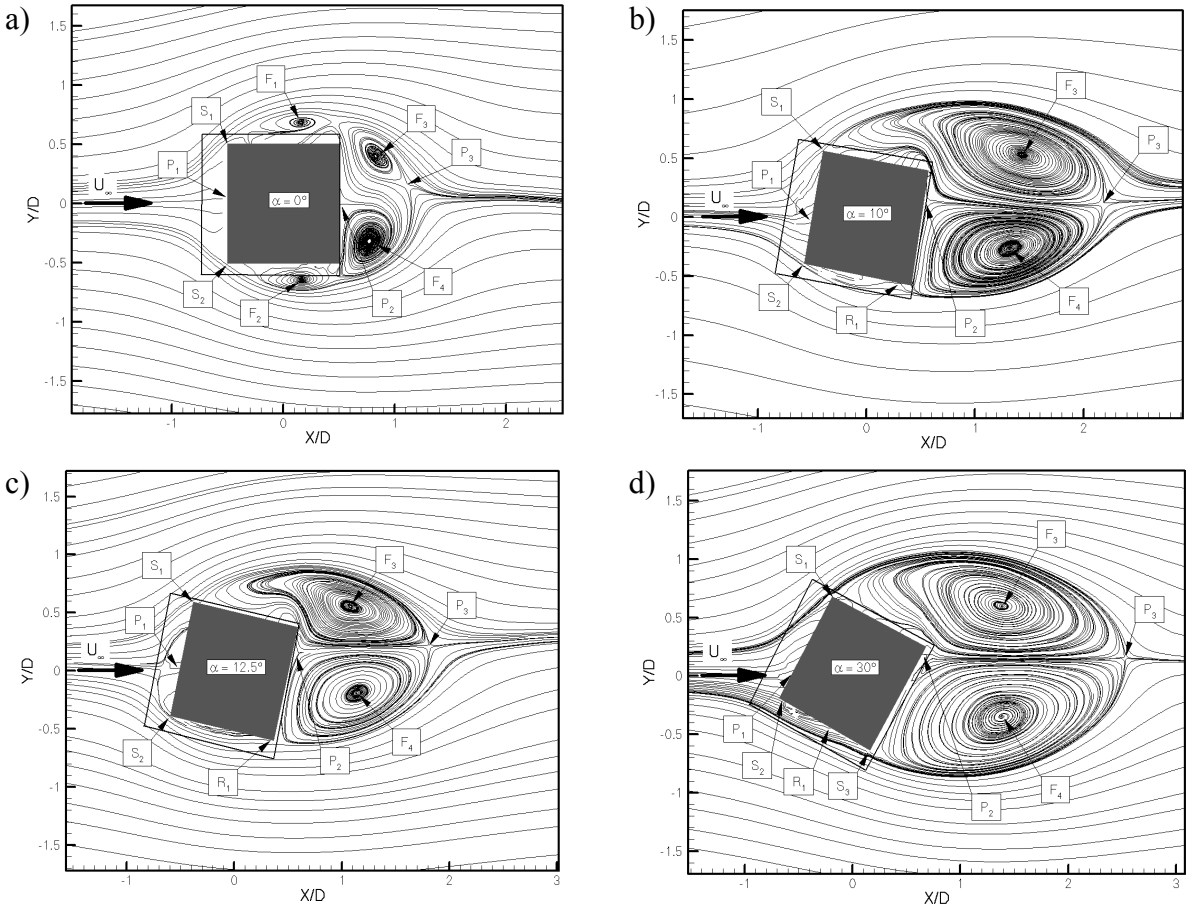

Figure 4-1: Topological overview of time-averaged flow types: a) $\alpha = 0°$, b) $\alpha = 10°$, c) $\alpha = 12.5°$, d) $\alpha = 30°$; P_1 and P_2 stagnation points, P_3 near-wake reattachment point, S_1 and S_2 separation points, F_1 to F_4 focal points, R_1 reattachment point

In figure 4-1 several topological points can be identified. Two points of stagnated flow, P_1 on the windward side, P_2 on the leeward side are present in all plots. Point P_3 identifies the position where the two separated bubbles on the back of the model meet, the near-wake length. The flow separates from the two separation points S_1 and S_2. For angles of incidence between 0° and 12.5° these points are the upper-left and lower-left corner points of the model. At 12.5 ° the flow just reattaches on the lower surface, indicate by R_1. In this particular case the flow separates immediately from this point. When the separated flow from the lower-left corner of the model reattaches on the lower surface a closed separation bubble is created. For increasing angles of incidence this bubble is shortened, as can be noted for 30° in figure 4-1d. The flow separates then from the lower-right corner of the model.

In the symmetrical case for 0° four regions with recirculation can be identified. Two recirculation regions are present on the upper and lower side of the model, with focal points F_1 and F_2, respectively and two regions at the back of the model forming the near-wake, with focal points F_3 and F_4. For increasing angles of incidence the two upper regions, F_1 and F_3, are joined together. At angles of incidence larger then 12.5° region F_2 forms the separation bubble. The only notable effect of region F_4, behind the lower right corner of the model, is a deformation in shape, in close relation with the orientation of the model. The region F_4 becomes stretched for increasing angles of incidence. The end of the regions F_3 and F_4 is defined as the near-wake length and indicated by the point P_3.

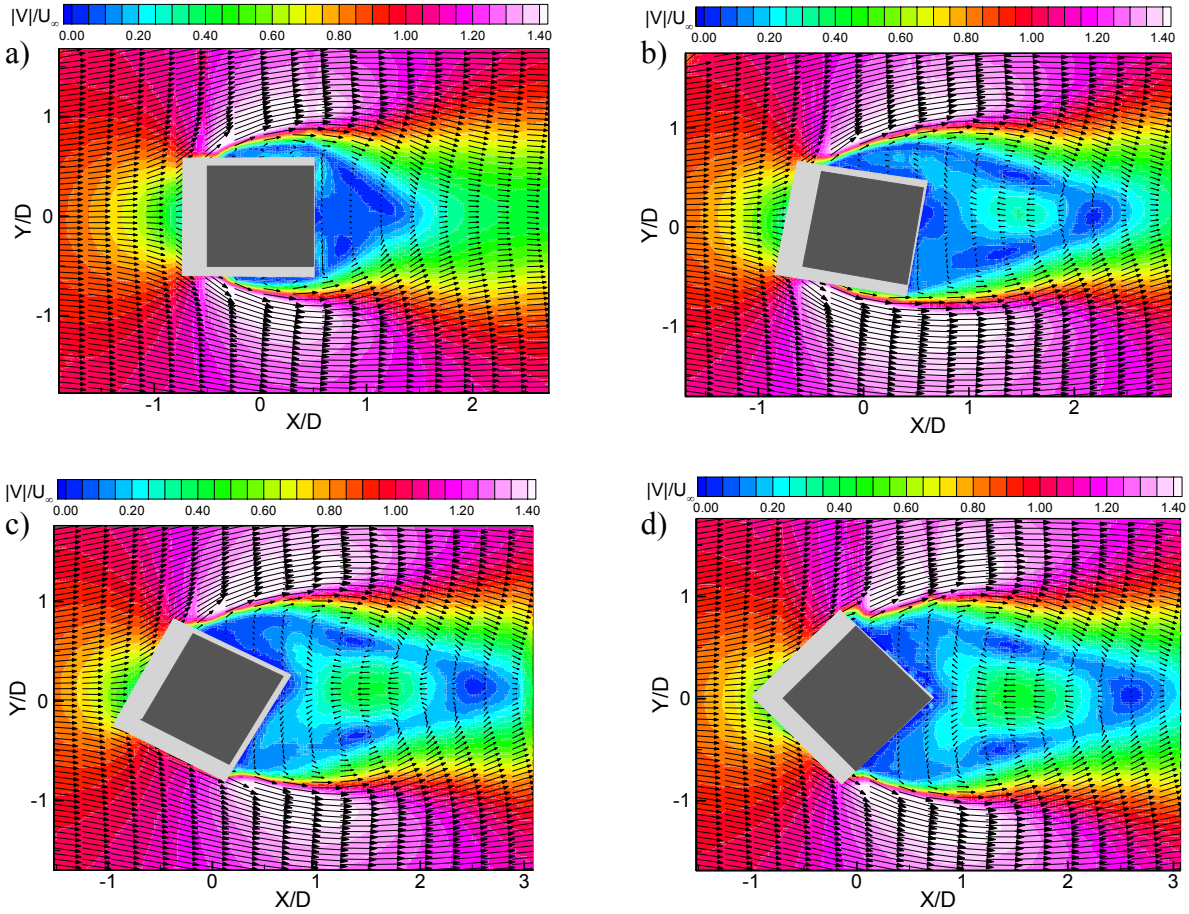

Figure 4-2: Velocity magnitudes; a) $\alpha = 0°$, b) $\alpha = 10°$, c) $\alpha = 30°$, d) $\alpha = 45°$

4.1.2 Flow regimes

Three different flow regimes can be identified in the flow around a square cylinder, as shown in figure 4-1. The first regime is characterized by separated flow from the windward corners, the second regime by a separation bubble on the full lower side and the third regime by separation from lower-right corner and a reattachment bubble on the lower windward side. Two other aspects can be used to indicate these flow regimes. In figure 4-2 plots of the velocity magnitude and in figure 4-3 the turbulence intensities are presented for angles of incidence of 0°, 10°, 30° and 45°.

The following aspects are present in the near-wake of the model. The magnitude of the velocity shows that low velocities are present in the near-wake for the symmetrical case of 0°. At increasing angles of incidence this region moves to the border of the near-wake and is limited to three distinguishable spots. The part in between these spots increases in size and in value with increasing angles of incidence.

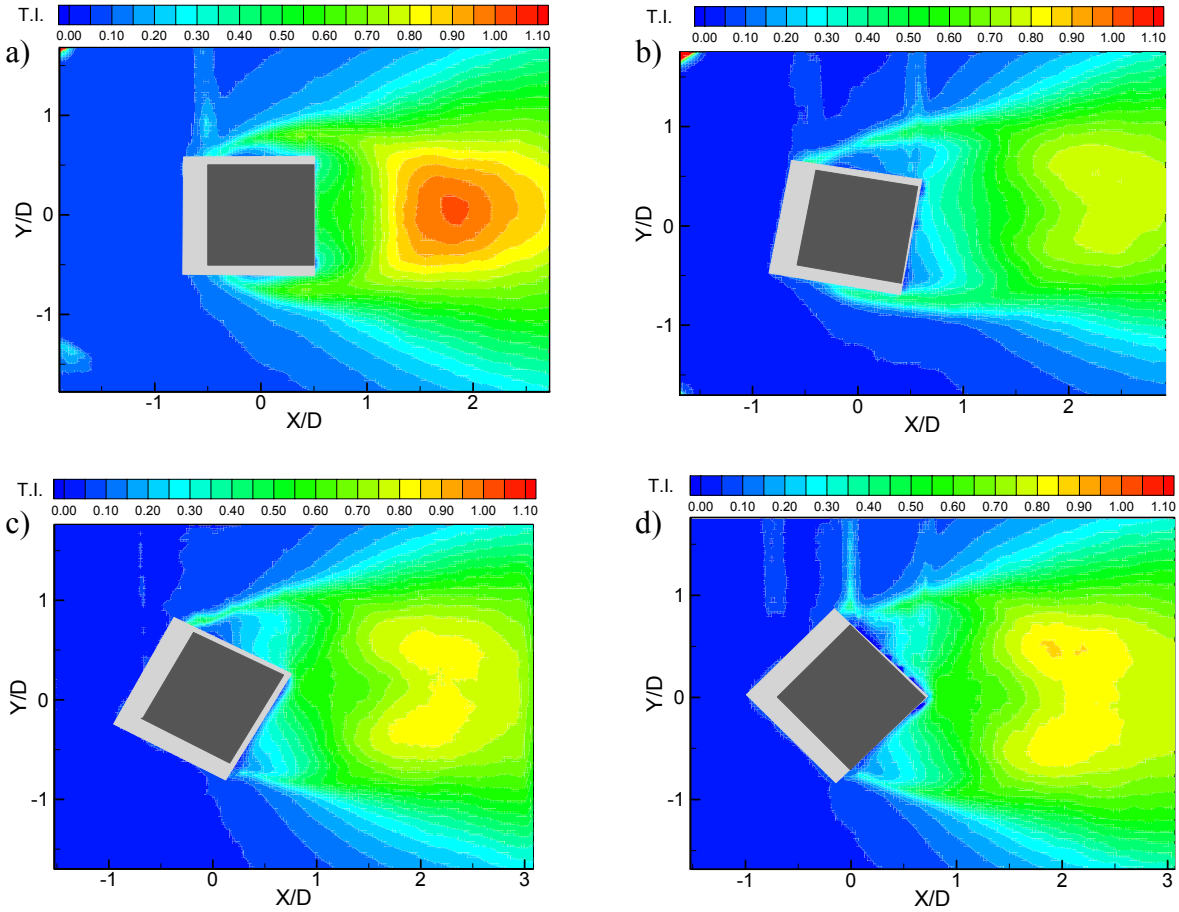

Figure 4-3: Normalized turbulence intensities; a) $\alpha = 0°$, b) $\alpha = 10°$, c) $\alpha = 30°$, d) $\alpha = 45°$

The turbulence intensity has a clearly identifiable region of the highest value for an angle of incidence of 0°. The turbulence intensities are not plotted on the same scale to distinguish these regions even more. It can also be remarked that the problem of the new validation is most notable in the upper left corner of the turbulence intensity plot at 10°, in figure 4-3b. A high value can be found in these areas, caused by the incorrect velocity vectors. After 0° the region with the highest value becomes slightly blurred and is finally split into two different regions, at 45°. This is most likely caused by the reduction of the vertical velocity fluctuation, v', at higher angles of incidence. The plots of the turbulence intensity show the added effect of the u and v fluctuations. As can be seen in figure 4-4 (and Appendix D), the u fluctuations have a maximum at off x-axis locations, while for the v fluctuations this is at the axis. It can also be noted that the turbulence intensities at lower angles of incidence are similar to the v fluctuations and at higher angles of inci-

dence more similar to the *u* fluctuations. Apparently, at small angles of incidence the *v* effects dominate and for larger angles the *u* effects. The horizontal position of the highest value of the turbulence intensity stays for all cases around X/D = 2.

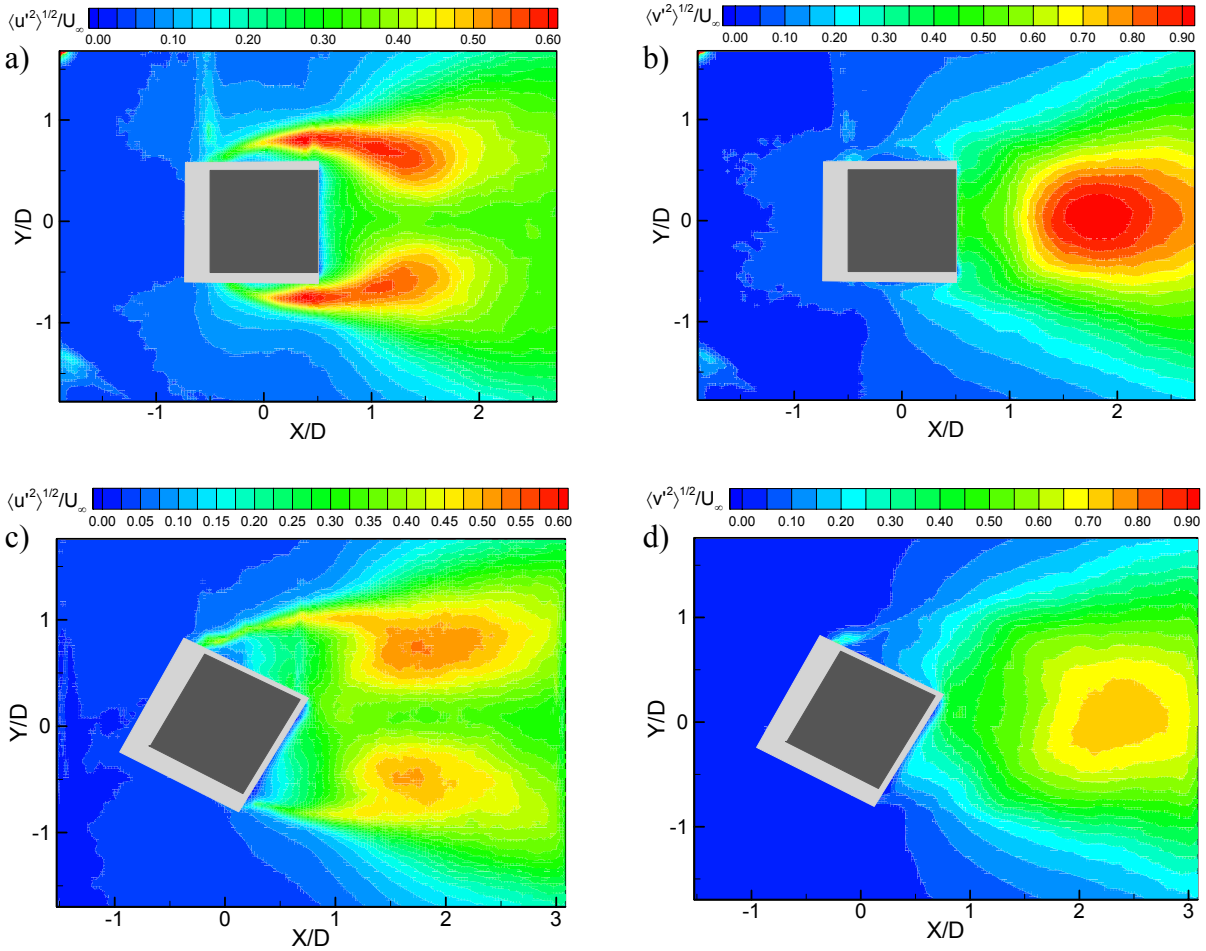

Figure 4-4: Horizontal, *u*', and vertical, *v*', velocity fluctuations for α = 0°, a) and b), and α = 30°, c) and d), respectively

4.1.3 Near-wake length

The position that defines the end of the near-wake, the points P_3 in the experiments, are presented in table 4-1. The value is the segment between the origin of the model and the (dimensionless) *x*-coordinate of the point P_3, X_3/D. These points are also visualised in figure 4-5. Also, previous experiments of Van Hinsberg [2004] are added for comparison. For Case B at 10° it was not possible to determine the exact position of the near-wake length because it was outside the field of view. This length is however slightly larger than 1.87. Case C and Van Hinsberg are close together. For an angle of incidence of 5° the datasets only match for Case B and Van Hinsberg. Two trend lines can be drawn through the data points. Trend line 1, the full line, connects the dataset of Case C where the near-wake length at 5° is replaced with the near-wake length of Case B. The trend line shows a local maximum at 10°.

Table 4-1: Values of dimensionless near-wake length, X_3/D

Angle of incidence (°)	0	2.5	5	7.5	10	12.5	15	20	25	30	35	40	45
Case A	1.06		1.09		1.85		1.80						
Case B	1.11		1.41		>1.87		1.83						
Case C	1.10	1.24	1.23	1.81	2.18	1.81	2.02	2.22	2.38	2.52	2.59	2.61	2.60

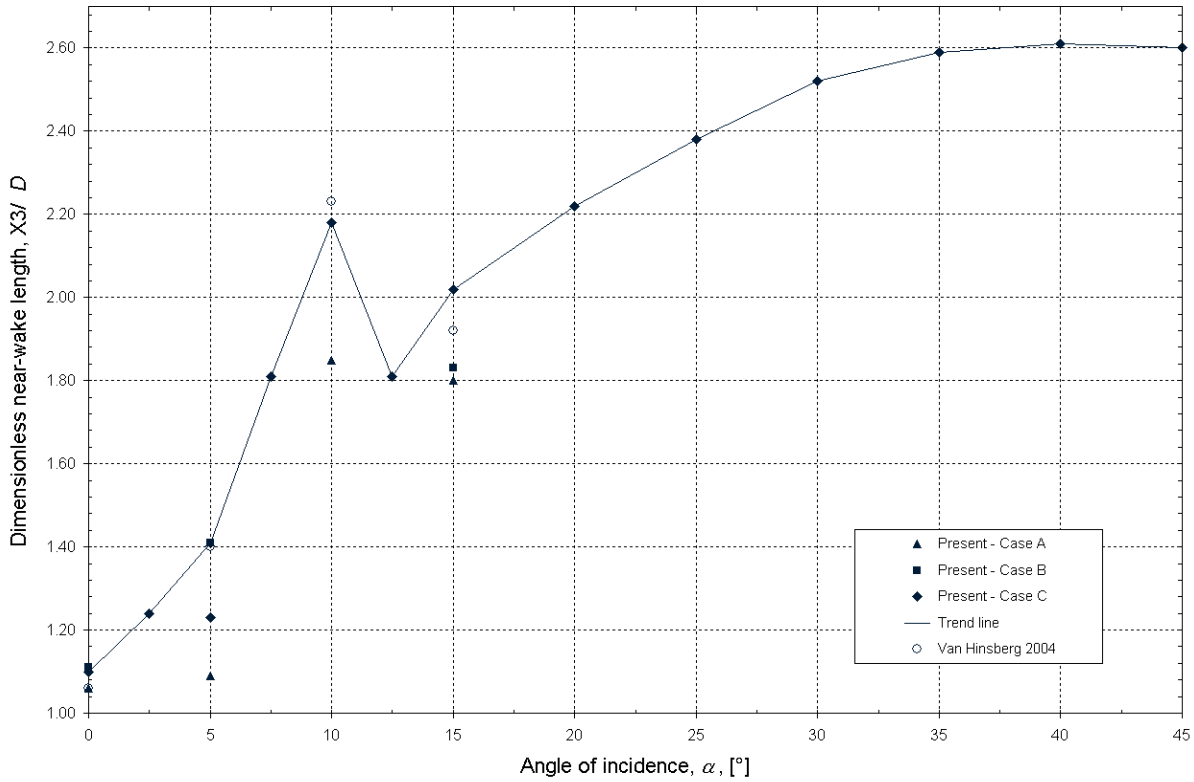

Figure 4-5: Near-wake length as function of angle of incidence

4.1.4 Velocity fluctuations

The maximum values of the mean horizontal and vertical velocity fluctuations *u*' and *v*' are visualized in figure 4-6 and figure 4-7, respectively. There is some difference between the results of Case B and C. The experiments from Case C are however considered more reliable. The maximum values of *u*' typically ranges between 45% and 65% of the free stream velocity, U_∞, while for *v*' this is between 75% and 95%. In both graphs, it is clear that with increasing angles of incidence the maximum values decrease and almost become constant, ~53% for the *u* fluctuations and ~75% for the *v* fluctuations. This may be caused by a weaker strength of the vortex shedding at high angles of incidence.

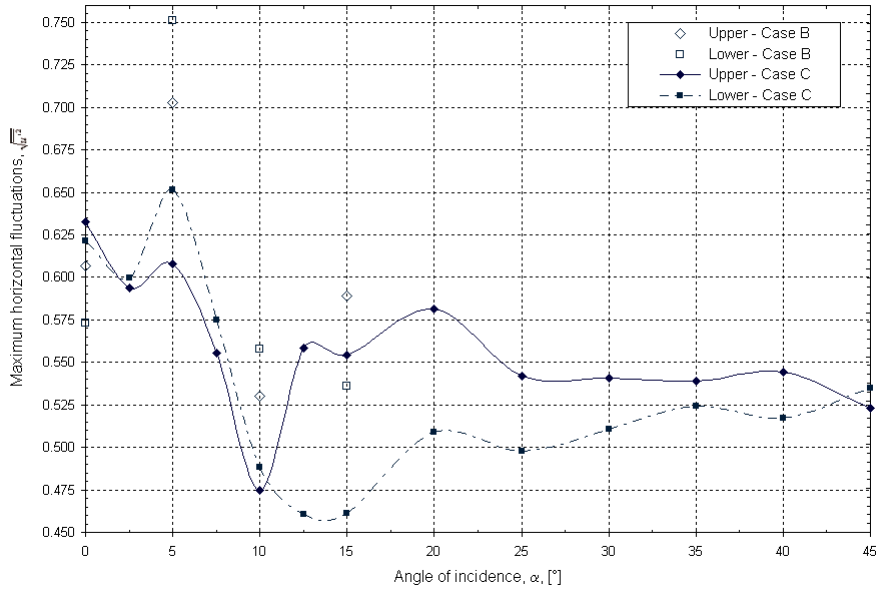

Figure 4-6: Maximum values of horizontal velocity fluctuations

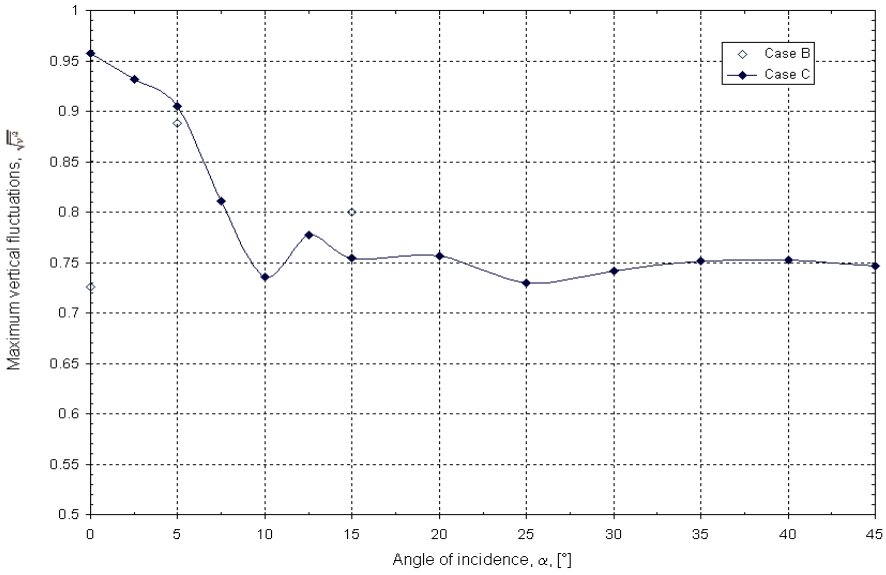

Figure 4-7: Maximum values of vertical velocity fluctuations

4.1.5 Vorticity

Regions of vorticity are present in the (time-averaged) bluff body flow around a square cylinder. A coloured contour plot, figure 4-8a, reveals that the minimum vorticity occurs on the upper side and the maximum value on the lower side. A contour plot with only contour lines (figure 4-8b) allows determining the positions of these minima and maxima. The positions of the upper and the lower vortices are plotted in figure 4-9.

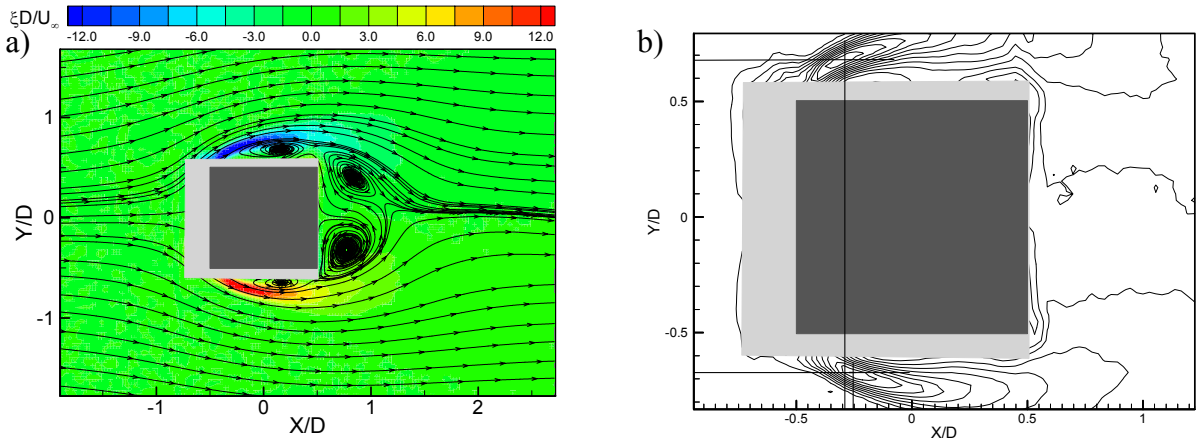

Figure 4-8: a) Contour plot of vorticity, b) location of vorticity centres

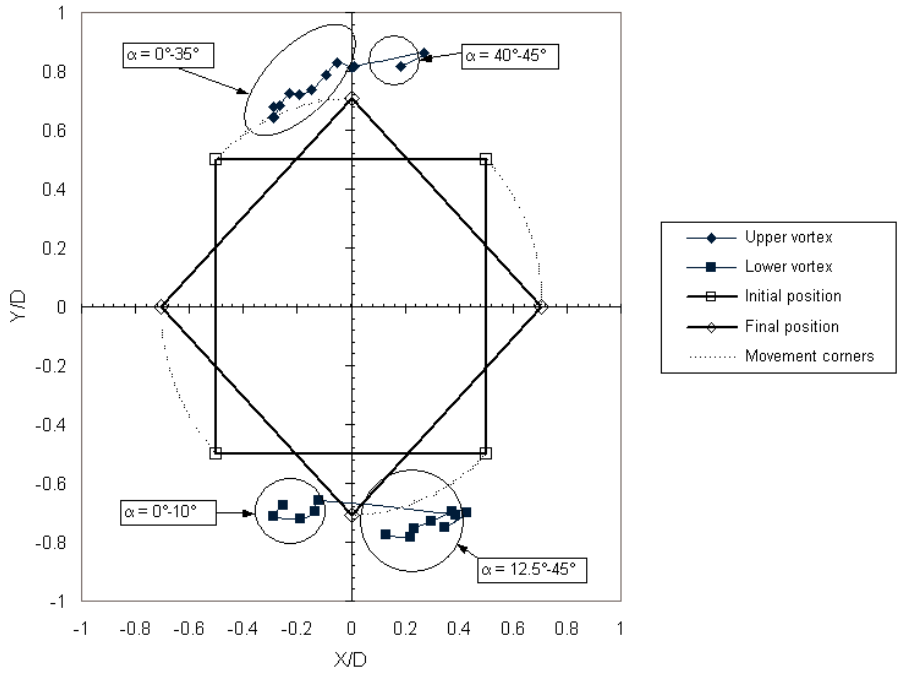

Figure 4-9: Location of vorticity centres with respect to model

The initial and final position of the model is also added to figure 4-9 to see the location of the vorticity maximum with respect to the model. The vorticity location of the flow separating from the upper left corner is always positioned slightly to the upper right of this corner. However, on the bottom side the position of the vorticity maximum is not locked at a certain point. A clear difference is notable when the angle of incidence changes from 10° to 12.5°. This change is related to the occurrence of shear layer reattachment. This is even more prominent when the specific locations of the maximum vorticity are related to the angles of incidence. Such representation is given in figure 4-10; the inset graph shows the distance from the position of the maximum vorticity to the nearest corner of the model. For angles of incidence between 0° and 10° this position is somewhere halfway below the lower side, and thus located to the right of the lower-left corner. At these angles the distance is largest. At 12.5° and 15° the location of the vorticity shifts to a

position below the lower-right corner, a clear identification that reattachment has occurred. The distance drops significantly. After 15° the distance remains nearly constant and the position of the maximum vorticity is slightly to the right of the lower-right corner.

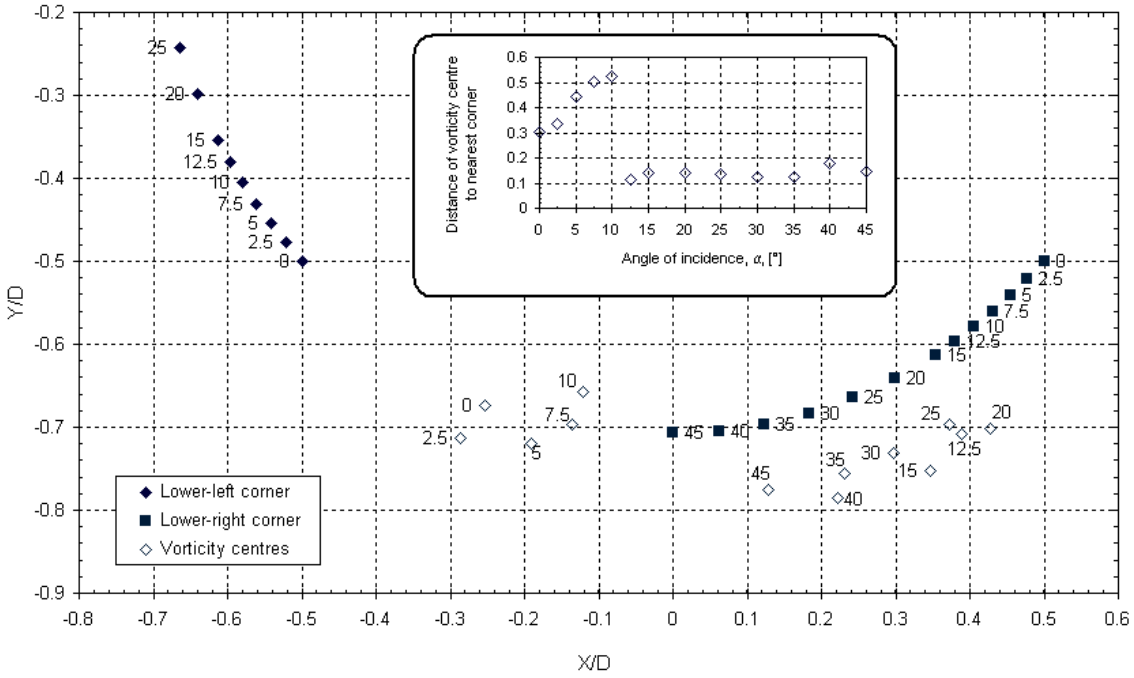

Figure 4-10: Specification of the location of vorticity centres at lower side of the model; inset shows the distance from these centres to the nearest corner of the model

4.2 *Unsteady flow characteristics*

So far, only the time-averaged results are discussed. These time-averaged results are based on instantaneous PIV measurements. The instantaneous results however do not show the same trend as the time-averaged results. The results of four instantaneous results at an angle of incidence of 0° are shown in figure 4-11. The four depicted results are randomly chosen from the available data. The four results differ from each other, and when the vector plots are compared to the time-averaged results of figure 4-2a none of them matches the time-averaged flow. Of course, the difference of the results is due to vortex shedding. Any of the PIV measurements will represent one particular instant of the phase of the vortex shedding. The time-averaged results represent then, when a large number (more than 200) of datasets is used, the mean flow and only incidentally will an instantaneous vector result be the same as the mean flow.

Because of the nature of vortex shedding it is interesting to have the information of the flow evolution in time. The current image acquisition rate of 3.3 *Hz* does not allow obtaining time-resolved results. The Strouhal number in the range of Reynolds numbers between 10^4 and $2{\cdot}10^4$ is reported to be (approximately) 0.13 [Okajima, 1982]. Under the current experimental conditions the vortex shedding

frequency, using equation (2.1), is about 43 *Hz*. To fully resolve this type of flow in time a system that can measure in the order of *kHz* would be required. Currently such systems exist. Cameras based on CMOS (Complimentary Metal Oxide Semiconductor) technology and high-speed lasers (Dioded pumped Nd:YAG) are required. Time-resolved systems are available from, among many, Dantec Dynamics, TSI or New Wave Research. Nevertheless, such a system is not available at the Aerodynamics Department. An alternative method to obtain phase-resolved information from randomly acquired PIV data sets is provided by the Proper Orthogonal Decomposition (POD) as it was applied to bluff body flow by Van Hinsberg [2004].

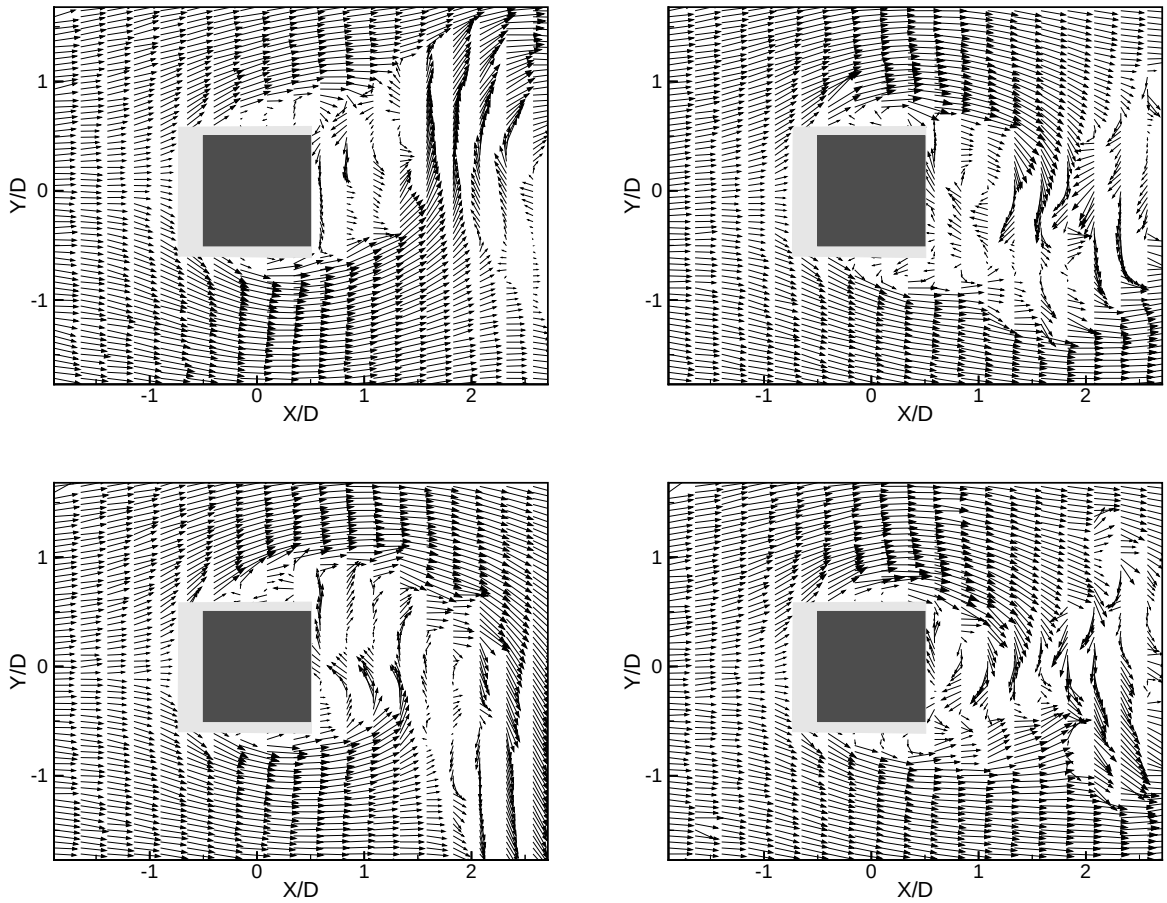

Figure 4-11: Four instantaneous PIV results at $\alpha = 0°$

4.2.1 Brief introduction to Proper Orthogonal Decomposition (POD)

The vortex shedding process is a regular large-scale process. An instantaneous flow property can be decomposed into a quasi-periodic component with small-scale turbulences according to Reynolds *et al.* [1970]:

$$u(\vec{x},t) = U(\vec{x}) + u'(\vec{x},t) = U(\vec{x}) + \tilde{u}(\vec{x},\varphi(t)) + u''(\vec{x},t) \tag{4.1}$$

where the instantaneous velocity u is decomposed into a mean velocity U and a

fluctuating component u', which can be further decomposed into a (quasi-) periodic $\tilde{u}$ and small-scale turbulences u''. The periodic component is characterised by a phase angle φ.

The coherent part of the velocity is given by the mean and periodic components, e.g. $U(\vec{x})+\tilde{u}(\vec{x},\varphi(t))$. The vortex formation and shedding process can be described with the coherent velocity. The coherent part of the flow can be obtained by phase averaging of the instantaneous velocity fields. The fluctuating part of a velocity field can be represented as a summation of normalized base functions, $\vec{\phi}_n$ multiplied with mode coefficients, a_n; the principle of the Proper Orthogonal Decomposition:

$$\tilde{u}(\vec{x},\varphi(t)) = \sum_{n=1}^{N} a_n(t)\vec{\phi}_n(\vec{x}) \tag{4.2}$$

where N the number of instantaneous velocity fields.

The coherent fluctuating velocity, equation (4.2), is split into a temporal part, the mode coefficients, and a spatial part, the normalized base functions. The normalized base functions are spatially orthogonal and the mode coefficients are uncorrelated in time:

$$\left\langle \vec{\phi}_i \cdot \vec{\phi}_j \right\rangle = \begin{matrix} 1, & i=j \\ 0, & i\neq j \end{matrix} \quad , \quad \overline{a_i a_j} = \begin{matrix} \lambda_i, & i=j \\ 0, & i\neq j \end{matrix} \tag{4.3}$$

where $\langle \ldots \rangle$ denotes spatial integration and $\overline{\ldots}$ denotes temporal averaging.

The normalized base functions are the POD eigenmodes and can be found with the two-point correlation matrix $C_{ij} = \overline{\tilde{u}(\vec{x}_i,t)\cdot\tilde{u}(\vec{x}_j,t)}$ from:

$$\boldsymbol{C}\vec{\phi}_n = \lambda_n \vec{\phi}_n \tag{4.4}$$

The total fluctuating energy is defined as the summation of all eigenvalues. As a consequence the contribution of a single eigenvalue to the total fluctuating energy reveals the dominant eigenmodes. The mode coefficients for a single instantaneous velocity field can be found from projecting the flow field onto the POD modes. A low-order reconstruction of the flow can be realized by representing the flow by only a few modes, for example only the first two modes in the case of convective dominated processes.

4.2.2 Properties of velocity modes

A summary of the symmetrical properties of the first 6 velocity modes is presented in table 4-2. The plots of the modes can be found in Appendix D. Only the

two symmetrical cases of 0° and 45° will show pure (anti-)symmetrical modes. At other angles of incidence, the symmetry is an indication how the modes are present in the flow, an anti-symmetrical mode has both positive *and* negative velocities whereas a symmetrical mode only has positive *or* negative velocities. The modes of the horizontal velocity (U) and the vertical velocity (V) appear in pairs as mentioned in Deane *et al*. [1991] and Noack *et al*. [2003]. Such is the case in the present POD analysis. The first two horizontal modes (U1 and U2) are always anti-symmetrical; the first two vertical velocity modes (V1 and V2) are always symmetrical. For some modes, it is not possible to determine their symmetrical property, probably due to a reduced correlation.

Table 4-2: Symmetry properties of first 6 velocity modes

Angle of incidence [°]	U1	U2	U3	U4	U5	U6	V1	V2	V3	V4	V5	V6
0	A	A	S	S	S	A	S	S	A	A	A	S
2.5	A	A	S	(S)	S	A	S	S	A	A	(A)	S
5	A	A	S	(S)	(S)	(A)	S	S	A	A	S	S
7.5	A	A	S	(S)	(A)	A	S	S	A	A	S	S
10	A	A	(S)	S	A	S	S	S	A	A	S	A
12.5	A	A	S	(S)	(A)	(A)	S	S	A	A	S	A
15	A	A	S	(S)	A	S	S	S	A	A	S	A
20	A	A	(S)	S	A	S	S	S	A	A	S	(A)
25	A	A	(S)	S	A	S	S	S	A	A	S	A
30	A	A	(S)	S	A	S	S	S	A	A	S	A
35	A	A	(S)	S	A	S	S	S	A	A	S	A
40	A	A	(S)	S	A	S	S	S	A	A	S	A
45	A	A	(S)	S	A	S	S	S	A	A	S	A

A: Anti-symmetric
S: Symmetric
(…): Unreliable

4.2.3 Eigenvalue spectra

The normalized eigenvalue spectrum for all angles of incidence of Case C is presented in figure 4-12 displaying how the fluctuation energy is distributed over the POD modes. Vortex shedding is a periodic phenomena as can be seen by the large values of the first two normalized eigenvalues with respect to higher order modes. The higher order modes are similar in their contribution; it is difficult in a POD analysis to distinguish specific modes. This explains why in table 4-2 the third and fourth horizontal unreliable velocity modes (U) sometimes are interchanged. The cumulative contribution of the (normalized) eigenvalues is plotted in figure 4-13 (note the logarithmic scale of the x-axis). The first six modes represent between 64% and 79% energy of the flow. Figure 4-14 shows the required number of eigenvalues to capture 80% and 90 % energy of the flow. This number increases at higher angles of incidence. Typically, 10-20 modes are required to cap-

ture 80% of the energy of the flow. Approximately 4 times more modes are needed to capture 90% of the flow instead of 80%.

The first two normalized eigenvalues capture the most prominent convective features of the periodic vortex shedding. Their values are not equal as can be seen in figure 4-15 and table 4-3. An interesting feature that can be observed is the significant change in the difference between the first two modes takes place between an angle of incidence of 10˚ and 15˚, whereas the difference for other angles of incidence gradually increases (indicated by the second order trend line). This difference is an indication that the nature of the periodicity of the vortex shedding is altered at angles of incidence between 10˚ and 15˚. The summation of the first two (normalized) eigenvalues is a measure for the energy in the periodic vortex shedding. Typically, between 52% and 72% of the energy is captured with these first two eigenvalues. In figure 4-15, it can be seen that this value gradually decreases, possibly an indication of reduced periodicity in the flow at higher angles of incidence.

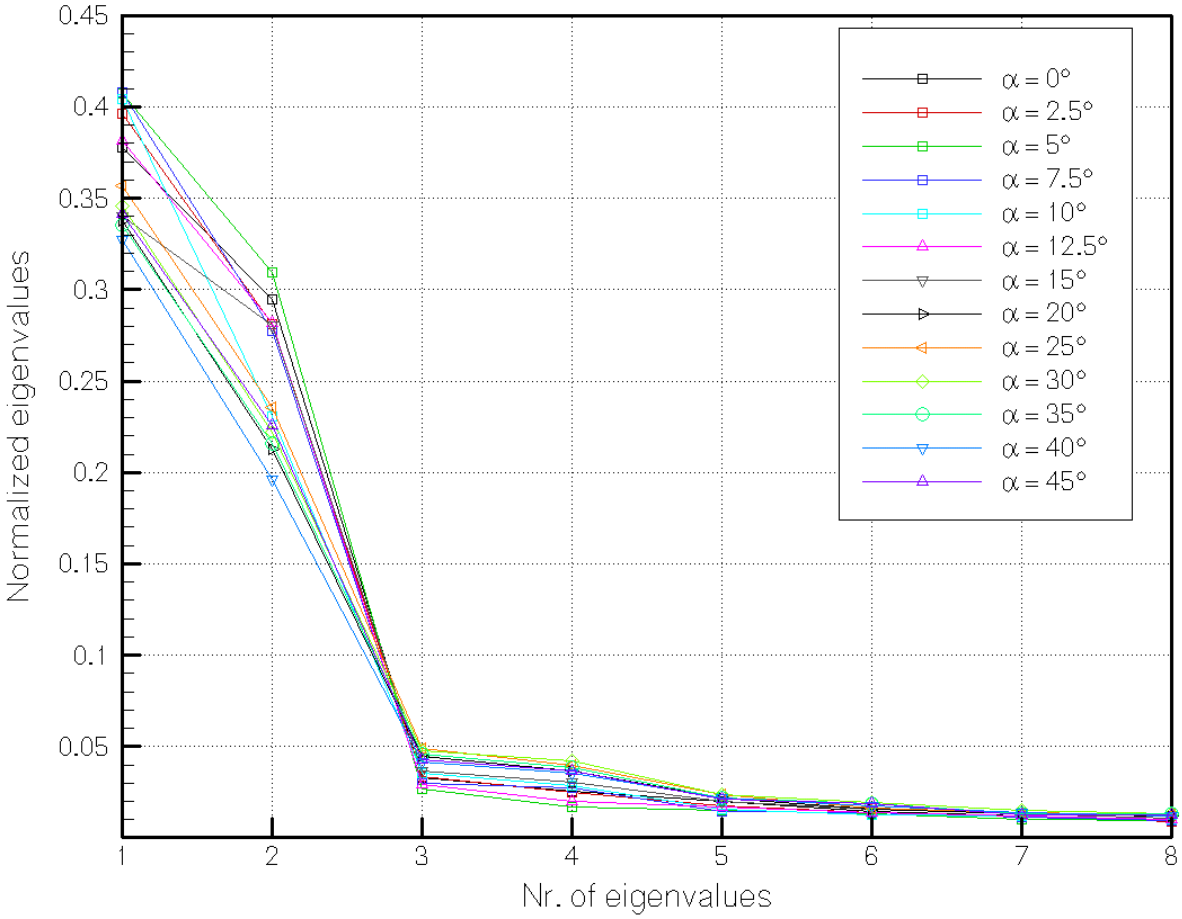

Figure 4-12: Eigenvalues spectrum

Table 4-3: Properties of first two normalized eigenvalues

Angle of incidence (°)	$\lambda_1 \Big/ \sum_{i=1}^{N} \lambda_i$	$\lambda_2 \Big/ \sum_{i=1}^{N} \lambda_i$	$(\lambda_1 - \lambda_2) \Big/ \sum_{i=1}^{N} \lambda_i$	$(\lambda_1 + \lambda_2) \Big/ \sum_{i=1}^{N} \lambda_i$
0	0.3778	0.2947	0.0830	0.6725
2.5	0.3964	0.2808	0.1156	0.6772
5	0.4072	0.3094	0.0979	0.7166
7.5	0.4081	0.2776	0.1305	0.6857
10	0.4040	0.2307	0.1734	0.6347
12.5	0.3816	0.2815	0.1001	0.6632
15	0.3400	0.2803	0.0597	0.6204
20	0.3379	0.2126	0.1252	0.5505
25	0.3566	0.2356	0.1210	0.5923
30	0.3459	0.2219	0.1240	0.5678
35	0.3353	0.2157	0.1196	0.5510
40	0.3272	0.1962	0.1310	0.5234
45	0.3414	0.2254	0.1159	0.5668

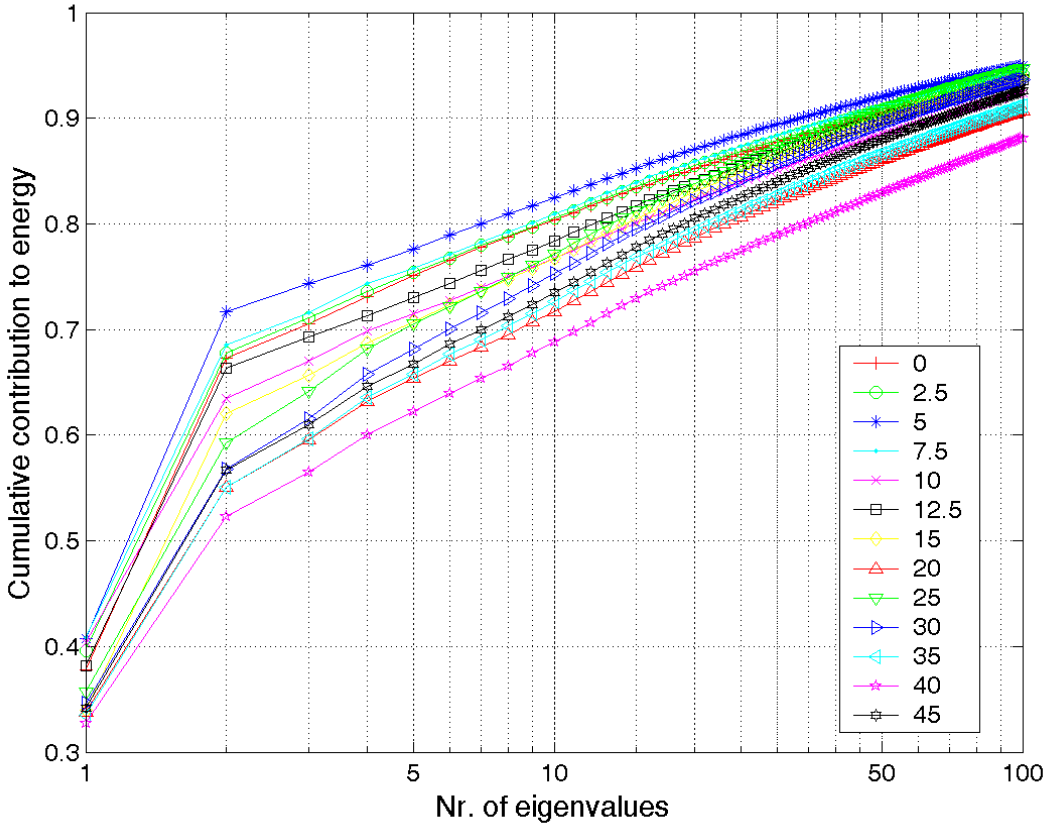

Figure 4-13: Relative contribution of number of eigenmodes to energy

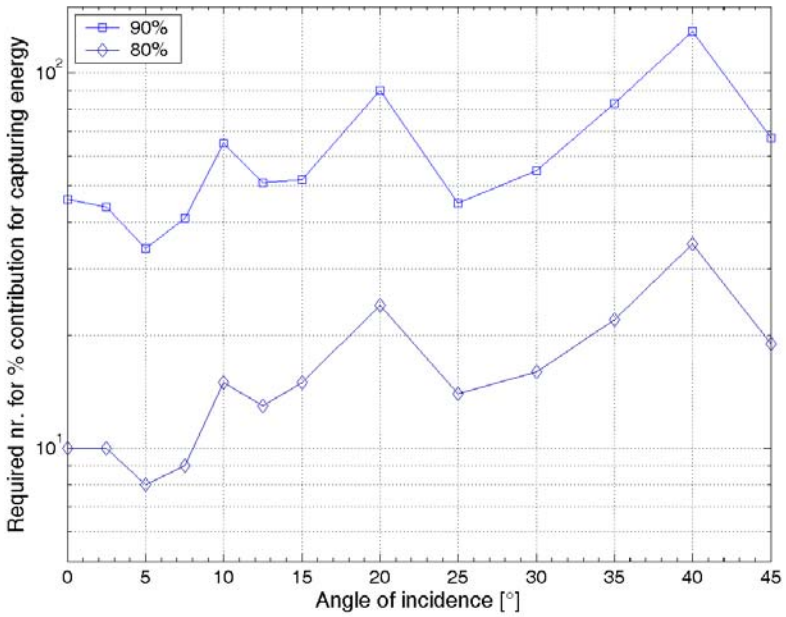

Figure 4-14: Number of eigenvalues needed for 80% and 90% contribution to energy

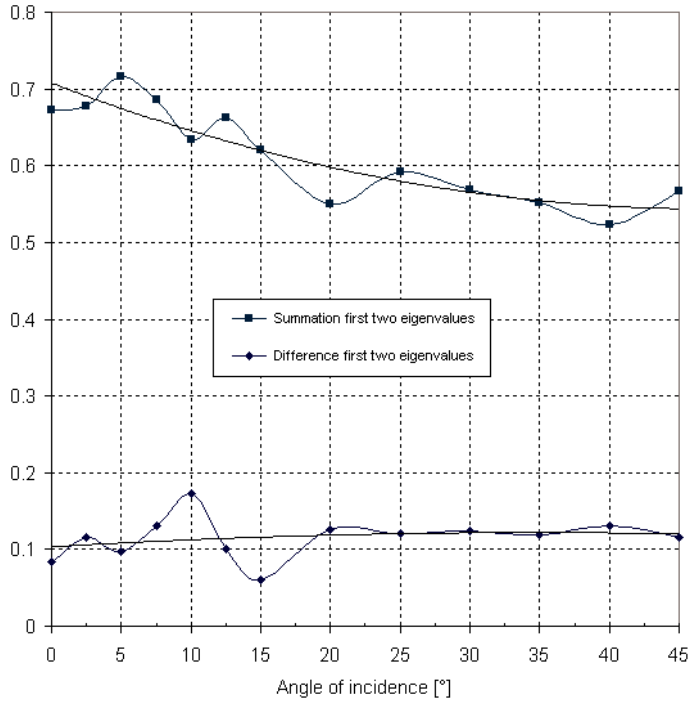

Figure 4-15: Properties of first two normalized eigenmodes

4.2.4 Low-order flow reconstruction using limited number of POD modes

The phase portraits of the first six normalized eigenvalues for an angle of incidence of 0˚ are presented in figure 4-16. The phase portraits of the first two eigenmodes of all angles of incidence are available in Appendix D. The phase portraits represent the correlation between two modes. Since the first two modes represent the periodic part of the flow, the correlation should ideally fall on a circle. For an angle of incidence of 0˚, this is indeed true, apart from some scatter in the correlation. However, from the phase portraits in Appendix D it can be noted that the correlation is lost after an angle of incidence of about 12.5˚. Figure 4-17 shows the mean velocities based on the POD analysis. The first two modes are presented in figure 4-18. The fluctuating velocities are calculated according to equation (4.5) and are given in figure 4-19.

$$\bar{\boldsymbol{u}}_{rms} = \sqrt{\overline{u'^2}} = \sqrt{\left(\sum_{i=1}^{6} a_i(t)\,\phi_i(\bar{\boldsymbol{x}})\right)^2} = \sqrt{\left(\sum_{i=1}^{6} a_i(t)\right)^2 \phi_i^2(\bar{\boldsymbol{x}})} = \sqrt{\sum_{i=1}^{6} \lambda_i \phi_i^2(\bar{\boldsymbol{x}})} \qquad (4.5)$$

4.2.5 Phase-resolved reconstruction

The dominant properties of the first two eigenmodes and the relative low contribution of the higher order values suggest that the coherent, phase-resolved component of the flow can be approximated with a low-order flow model. The low-order model contains only the mean and the first two modes:

$$u_{LOM}(\vec{x},\varphi) = U(\vec{x}) + \sqrt{2\lambda_1}\sin(\varphi)\cdot\vec{\phi}_1(\vec{x}) + \sqrt{2\lambda_2}\cos(\varphi)\cdot\vec{\phi}_2(\vec{x}) \qquad (4.6)$$

The low-order flow model from equation (4.6) excludes higher order harmonics of the coherent flow and the random turbulent motion. This exclusion is justified by the loss of correlation of the higher order harmonics (see figure 4-16).

Based on the correlation coefficients and the velocity modes the phase reconstructed flow for an angle of incidence at 0° is shown in figure 4-20. The other phase reconstructed snap shots are presented in Appendix D. The snapshots are phase-ordered from top to bottom.

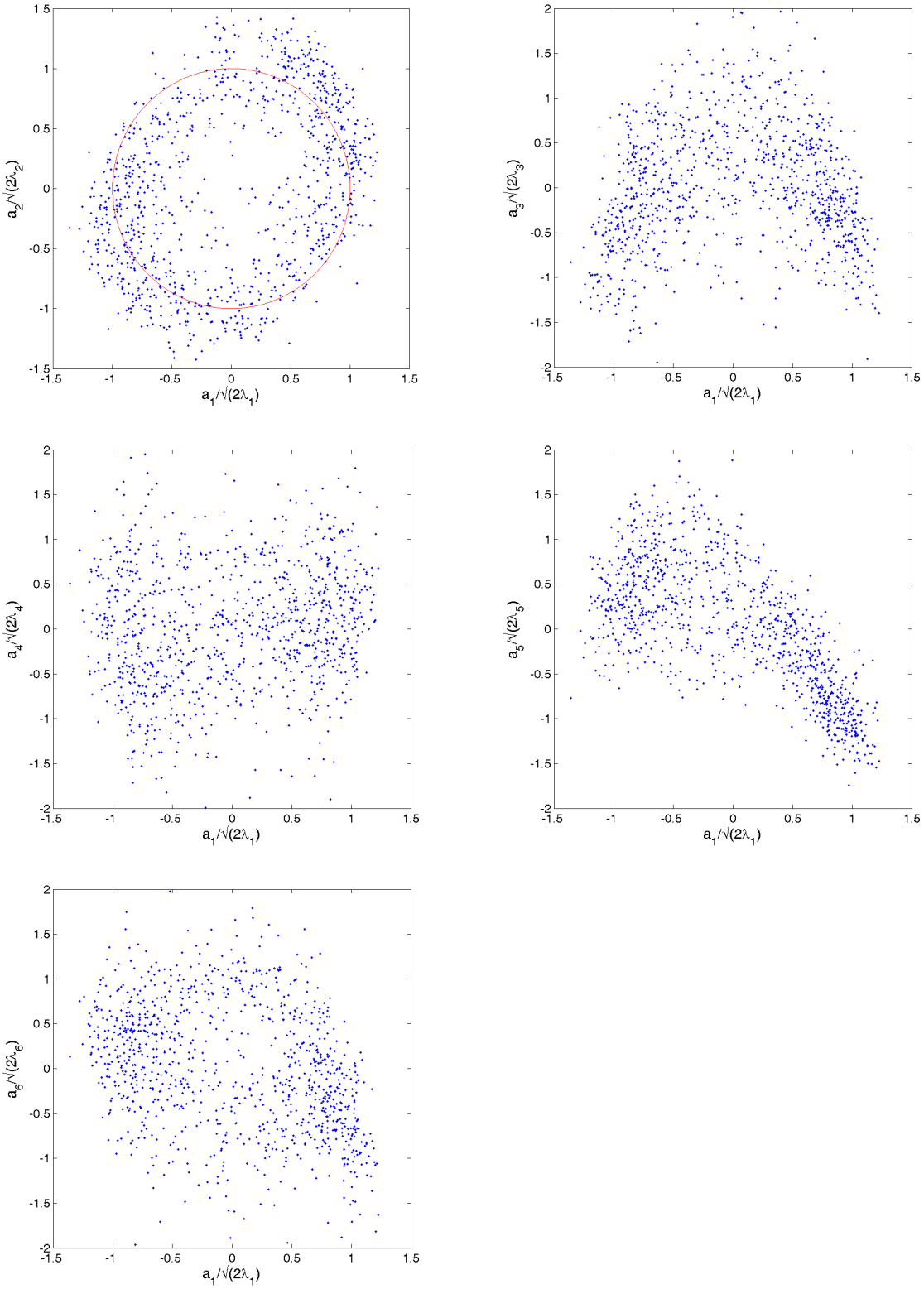

Figure 4-16: Phase portraits for α = 0°

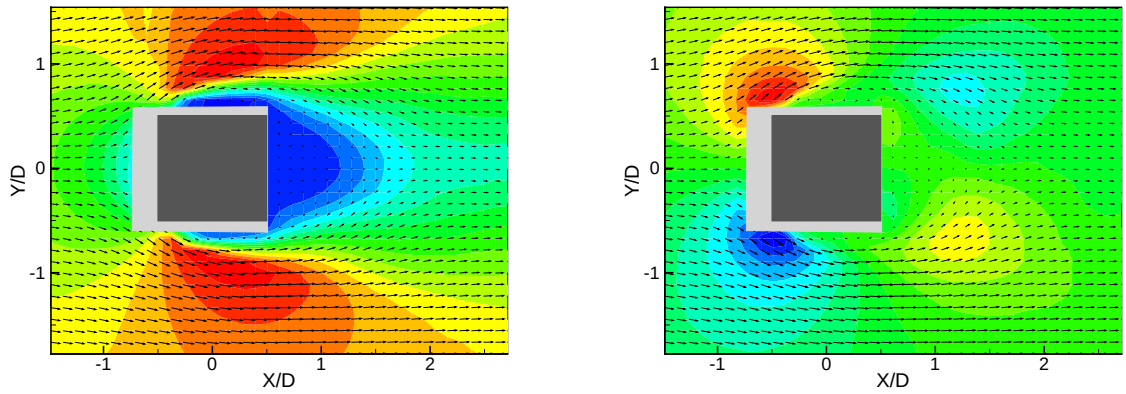

Figure 4-17: Mean velocities, left: *u* velocity, right: *v* velocity

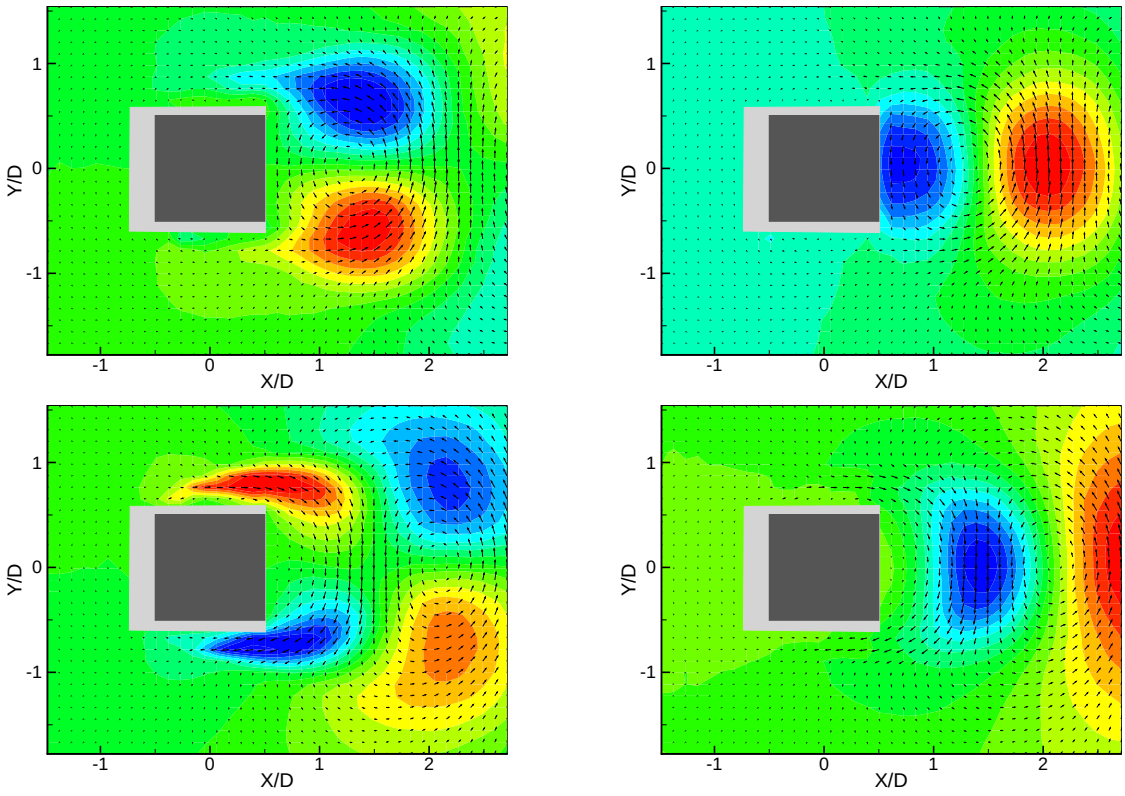

Figure 4-18: Coherent velocities, modes 1 and 2, left: *u* velocity, right: *v* velocity

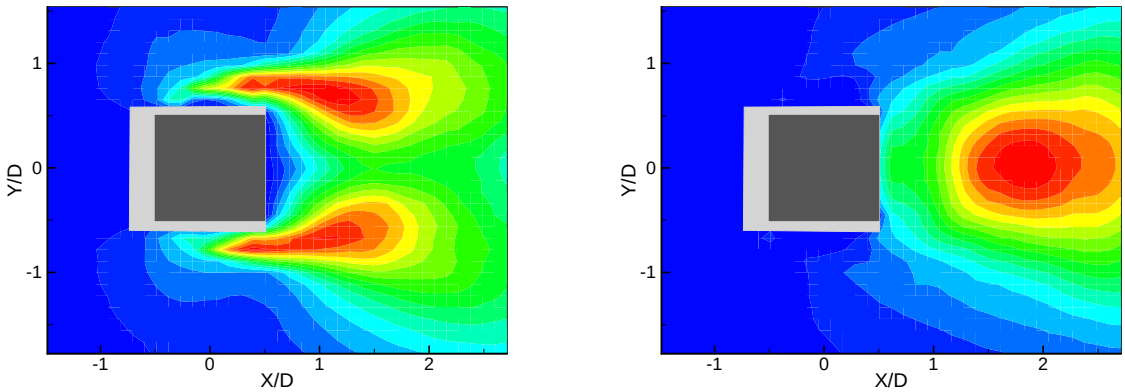

Figure 4-19: Fluctuating (random) velocities, left: *u* velocity, right: *v* velocity

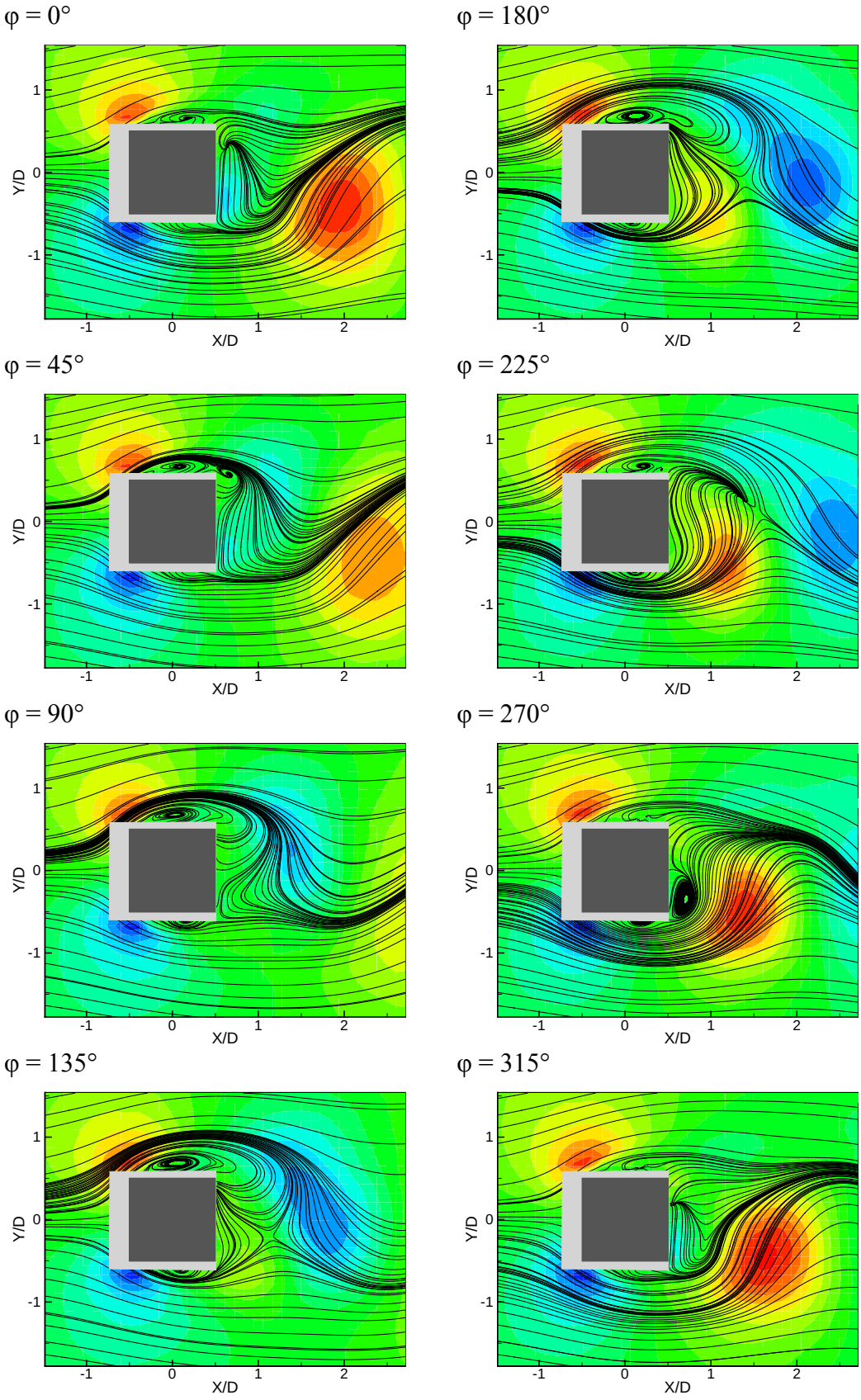

Figure 4-20: Snap shots of phase reconstructed flow at α = 0°

Chapter

5

Force Determination from Velocity Data

This chapter describes the approach to calculate the pressure fields as well as the lift and drag coefficient of the square cylinder at various angles of incidence from velocity data provided by the PIV experiments. The forces can be determined from the flow field around a body using a control-volume approach [Anderson, 1991]. This requires both the momentum flux and the pressure. The pressure cannot be measured directly by PIV, but with certain hypotheses can be computed using the momentum equation. In the present study with rotational flow regions evidently the Bernoulli equation cannot be used to approximate the pressure from the local value of the velocity. Therefore, a more complete approach is necessary, which also takes into account the viscous effects. The present chapter discusses several methods for the determination of the pressure field from local velocity data. Advantages and drawbacks are shown by means of comparison.

5.1 Force determination with integral momentum equation

The instantaneous value of the integral force, $\vec{F}(t)$, experienced by an object inserted in a flow on a fixed control volume S with an outer contour s and assuming incompressible flow field is related to the flow properties as (Anderson [1991] and Unal [1997]):

$$\vec{F}(t) = -\rho \iiint_S \frac{\partial \vec{V}}{\partial t} dS - \rho \iint_s (\vec{V} \cdot \vec{n}) \vec{V} ds - \iint_s p \vec{n} ds + \iint_s \vec{\vec{\tau}} \vec{n} ds \tag{5.1}$$

where $\vec{n}$ is the unit normal vector on the contour. The flow properties are the density, ρ, the velocity vector, $\vec{V}$, the pressure p and the viscous stress tensor, $\vec{\vec{\tau}}$. The

effect of the viscous stress tensor can in general be neglected if the control volume is sufficiently far from the body.

For a steady two-dimensional flow, using $\vec{F} = \begin{pmatrix} D & L \end{pmatrix}^T$ with in x-direction the (steady) drag D and in y-direction the (steady) lift L, $\vec{V} = \begin{pmatrix} u & v \end{pmatrix}^T$ and the outward unit normal vector defined as $\vec{n}ds = \begin{pmatrix} -dy & dx \end{pmatrix}^T$, the force equation can be explicitly written as:

$$\begin{pmatrix} D \\ L \end{pmatrix} = \rho \oint \begin{pmatrix} u^2 dy - uvdx \\ uvdy - v^2 dx \end{pmatrix} + \oint \begin{pmatrix} pdy \\ -pdx \end{pmatrix} \tag{5.2}$$

For an unsteady flow fluctuating terms can be introduced into equation (5.2) by means of Reynolds averaging with which the mean forces acting on the model for an unsteady flow are obtained as:

$$\begin{pmatrix} \overline{D} \\ \overline{L} \end{pmatrix} = \rho \oint \begin{pmatrix} \left(\overline{u}^2 + \overline{u'^2}\right) dy - \left(\overline{u}\,\overline{v} + \overline{u'v'}\right) dx \\ \left(\overline{u}\,\overline{v} + \overline{u'v'}\right) dy - \left(\overline{v}^2 + \overline{v'^2}\right) dx \end{pmatrix} + \oint \begin{pmatrix} \overline{p}dy \\ -\overline{p}dx \end{pmatrix} \tag{5.3}$$

The sign convention of the forces, angle of incidence, the free stream velocity and the coordinate system is given in figure 5-1.

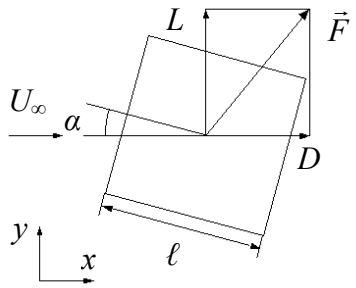

Figure 5-1: Coordinate system and direction of positive quantities

It can be noted from the mean force equation, equation (5.3), that in order to evaluate this expression the mean pressure, $\overline{p}$, is needed. The pressure field is not available with PIV experiments. It is also impossible to obtain the pressure field by applying the Bernoulli equation, since the flow under consideration has large regions of separated flow. However, the Navier-Stokes equation provides an equation for the pressure gradient. In principle, this pressure gradient can be integrated to provide the missing pressure field in the integral force equation. Before discussing an implementation of an integration method, several other methods are described to calculate the pressure field as can be found in literature.

5.2 Methods to determine the pressure field

Several methods are available for obtaining the force on a wind tunnel model. A broad division can be made into direct, indirect and advanced techniques. The di-

rect techniques are classical methods such as the force balance and pressure rakes. Indirect methods are based on solving the Navier-Stokes equations. Advanced techniques are a specific interpretation of existing techniques. A general description of a number of these techniques is given below. More methods are described in Norberg [2003], which also includes methods to estimate the fluctuating lift.

5.2.1 Direct methods

The direct methods provide an easy way of measuring the force on the wind tunnel model. Such methods are:

- *Force balance*: the model is directly connected to a force balance. This immediately returns the total force, which can be decomposed into lift and drag. Of course, there is no need to evaluate the pressure field using this method.
- *Static pressure taps*: holes in the surface of the model with static pressure tubes connected. The normal force is obtained by a spatial integration of the pressure on the surface.
- *Pressure probes*: also known as a pressure rake. A mechanism with multiple static and total pressure holes is traversed through the wake to obtain the total pressure losses in the wake. These pressure losses are related with the drag term due to viscosity. The spatial resolution is relatively coarse.

A major drawback of these methods is that any information of the structure of the wake is either not available (Force balance and Static pressure taps) or not fully resolved (Pressure probes, returns only mean values). These methods are also to some extent intrusive, as the model has to be properly attached to the force balance, or pressure probes have to be inserted in the wake quite close to the model. Moreover, the accuracy of the pressure measurement method decreases dramatically at low values of the dynamic pressure. Another drawback is that in order to be able to measure the forces or pressures additional instrumentation has to be installed.

5.2.2 Indirect methods

The current experimental investigation focuses on a detailed analysis of the flow around a bluff body. Force data alone is therefore insufficient. The current experimental analysis is conducted with PIV to obtain instantaneous velocity data. This enables a detailed description of the investigated flow. Using integral momentum relations it is, in essence, possible to acquire the (mean) force data on the model with PIV data. These integral relations, however, require the knowledge of the pressure field. This is complicated by the fact that the Bernoulli equation is not valid in a bluff body flow (e.g. it can not be used in the wake of the bluff body due to separation). Several methods have been employed by different researchers to obtain the pressure information.

The indirect methods can be classified into three groups based on the pressure field calculation:

1) *Full*: The pressure field is calculated throughout the computational domain. The force is evaluated using momentum integral equations,
2) *Partial*: Similar to the full pressure calculation but the pressure values are calculated only on the contour of the control volume,
3) *Circumvention*: The pressure field calculation is totally omitted by rewriting the Navier-Stokes equations such that the pressure is eliminated. The resulting force equations are in terms of velocity and vorticity.

Full Pressure Calculation

The method that is utilized in this report is based on a two dimensional integration of the pressure gradient field starting from a region where the static pressure is known (e.g. free stream). The pressure gradient field can be derived from the *x*- and *y*-momentum equations in an incompressible flow. The momentum equations are rewritten for the pressure gradient in *x*- and *y*-direction. The momentum equations are still valid in rotational flow. The momentum equations in non-conservative form for a two-dimensional flow are given in equation (5.4) [White, 1991]:

$$\begin{aligned}\frac{\partial u}{\partial t}+u\frac{\partial u}{\partial x}+v\frac{\partial u}{\partial y}&=-\frac{1}{\rho}\frac{\partial p}{\partial x}+\nu\left[\frac{\partial^2 u}{\partial x^2}+\frac{\partial^2 u}{\partial y^2}\right]\\ \frac{\partial v}{\partial t}+u\frac{\partial v}{\partial x}+v\frac{\partial v}{\partial y}&=-\frac{1}{\rho}\frac{\partial p}{\partial y}+\nu\left[\frac{\partial^2 v}{\partial x^2}+\frac{\partial^2 v}{\partial y^2}\right]\end{aligned} \tag{5.4}$$

These equations can be rewritten with the pressure gradients on the left hand side. By applying the Reynolds averaging technique and some algebraic manipulation the following set of equations is derived (the full derivation can be found in Appendix C):

$$\begin{aligned}\frac{\partial \overline{p}}{\partial x}&=\rho\left[-\overline{u}\frac{\partial \overline{u}}{\partial x}-\overline{v}\frac{\partial \overline{u}}{\partial y}-\frac{\partial \overline{u'^2}}{\partial x}-\frac{\partial \overline{u'v'}}{\partial y}+\nu\left\{\frac{\partial^2 \overline{u}}{\partial x^2}+\frac{\partial^2 \overline{u}}{\partial y^2}\right\}\right]\\ \frac{\partial \overline{p}}{\partial y}&=\rho\left[-\overline{u}\frac{\partial \overline{v}}{\partial x}-\overline{v}\frac{\partial \overline{v}}{\partial y}-\frac{\partial \overline{v'^2}}{\partial y}-\frac{\partial \overline{u'v'}}{\partial x}+\nu\left\{\frac{\partial^2 \overline{v}}{\partial x^2}+\frac{\partial^2 \overline{v}}{\partial y^2}\right\}\right]\end{aligned} \tag{5.5}$$

$$\underbrace{\qquad}_{Euler}\quad\underbrace{\qquad}_{Fluctuation}\quad\underbrace{\qquad}_{Viscous}$$

All the terms on the right hand side can be obtained by a PIV measurement with density, ρ, and viscosity, ν, taken as constants. On the right hand side of equation (5.5) three distinctive contributions can be identified. These are the Euler terms, the fluctuating terms and the viscous terms. After integration of the pressure gradient, the pressure can be inserted into the integral momentum equation to obtain the mean force acting on the model. The integration procedure and the force evaluation are explained in detail in the subsequent paragraphs. The remainder of this paragraph is devoted to alternative methods.

Another method available to calculate the full pressure field is based on solving a Pressure Poisson Equation (PPE). The PPE is obtained by applying the divergence operator on the incompressible Navier-Stokes equations (see Appendix C for a derivation). The function in Cartesian coordinates reads [Gurka *et al.*, 1999]:

$$\nabla^2 P = -\rho\left\{\left(\frac{\partial u}{\partial x}\right)^2 + 2\left(\frac{\partial u}{\partial y}\frac{\partial v}{\partial x}\right) + \left(\frac{\partial v}{\partial y}\right)^2\right\} + \left\{\frac{\partial^2}{\partial x^2}\left(\overline{u'^2}\right) + 2\frac{\partial^2}{\partial x \partial y}\left(\overline{u'v'}\right) + \frac{\partial^2}{\partial y^2}\left(\overline{v'^2}\right)\right\} \tag{5.6}$$

All terms in the PPE equation are available from, or can be derived from, PIV experiments. The PPE equation needs a boundary condition in order to obtain a solution. In general, the pressure gradient can be provided as a boundary condition.

$$\nabla p = -\rho\frac{\partial \vec{V}}{\partial t} + -\rho\left(\vec{V}\cdot\nabla\right)\vec{V} + \mu\nabla^2\vec{V} \tag{5.7}$$

Gurka *et al.* [1999] applied this method to the impinging flow on a flat plate and to a jet flow, both external flows without any interior object. Yoshioka *et al.* [1999] used this method to the turbulent separated flow over the backward-facing step. They assume an unrealistic zero pressure on the entire boundary and this needs to be further investigated. Fujisawa *et al.* [2005] solved the PPE equation for a circular cylinder with appropriate boundary conditions at a Reynolds number of 2000. Their results are close agreement with literature. Hosokawa *et al.* [2003] utilized this method for the evaluation of the pressure field of laminar flow around bubbles and single particles. The PPE in their case was not solved directly, but with a numerical solution algorithm (SOLA). This approach does not require explicit boundary conditions, but needs initial conditions as the method is based on a Newton-iteration method. At each iteration velocities are estimated from previous calculations.

The method of the PPE can prove itself viable but it needs to be validated for several other cases. It is not difficult to write a Poisson solver based on a successive-over-relaxation (SOR) for the numerical integration. However, the current investigated flow possesses a severe constraint on this method. Namely, the current experiments have an object inserted into the flow and special care has to be taken to implement the boundary conditions on this geometry. For the current experiments it is possible to prescribe a Dirichlet boundary condition on the left side of the domain (e.g. the pressure obtained according to the Bernoulli relation), a non-restrictive condition. The boundary condition on the object itself should be modelled with Neumann boundary conditions (e.g. the pressure gradient) along the circumference of the model. The boundary of a model is in general not aligned on grid points. A simple interpolation of the boundary conditions is not possible (when using Neumann boundary conditions) and one has to resolve to a more complex notation of tensor analysis to correctly implement these conditions [Van Kan *et al.*, 1993]. Such an approach is not adopted in this investigation, but may be of interest when a suitable Poisson solver is used.

Partial Pressure Calculation
The method of partial calculation of a pressure field is employed by Unal *et al.*, [1997]. The force is calculated using the integral momentum equation. The pressure terms are obtained by a numerical integration of the *x*- and *y*-momentum equations for the pressure gradient along the *x* and *y* surfaces of the contour. Their application shows a similar trend of the evolution of the lift-coefficient in time as transducer measurements. Deviations are related to low temporal and spatial resolution.

Circumvented Pressure Calculation
The integral momentum equations can be rewritten to circumvent the need for the explicit calculation of the pressure. Noca *et al.* [1999] derive closed-form equations for the evaluation of time-dependent forces on a body in an incompressible, viscous, rotational flow. The equations are rewritten such that only velocity and its gradients are needed for the calculation of the force. These data are readily available with PIV experiments. They derive three equations, which are: an "impulse equation", a "momentum equation" and a "flux equation". The first two equations require an evaluation of surface integrals over the boundary layer region next to the body, in a two-dimensional flow. In most experiments, this region cannot be fully resolved.

This restrictive condition is removed in the "flux equation", where only line integrals (in a two dimensional flow) are to be evaluated under the limiting condition that the flow field is divergence free, $\nabla \cdot u = 0$. In its time-dependent from this equation evaluates development of the force in time with data on an arbitrary contour (surrounding the body). The "impulse equation" and the "momentum equation" differ only by a vector relation. In all of the above formulations, the only measured quantity is the velocity; the vorticity is calculated from this velocity data. If the flow near the model yields spurious data (for example due to perspective errors in PIV experiments) the "flux equation" would give the most accurate result. The methods are applicable to flows, which are either highly resolved, or well accentuated (with large force coefficients). Tan *et al.* [2005] used the "flux equation" of Noca *et al.* [1999] to estimate the force on a circular cylinder using potential flow velocity data. They recognize the statement of Noca *et al.* [1999] that a contour should be chosen such that it is relatively close to the body. All the force formulations depend explicitly on a position vector, which may lead to errors for larger domains, or flows with low force coefficients.

5.2.3 Advanced methods

Two advanced techniques are available for obtaining the force information on a model. The first method involves the Direct Measurement of Vorticity (DMV). The second is based on the measurement of an acceleration field with PIV.

Direct Measurement of Vorticity (DMV)
Ruan *et al.* [2001] developed a method to measure the vorticity field directly instead of approximating it. The DMV method determines the vorticity from a correlation of the average angular displacement of rotation between two matched pat-

terns. This method is insensitive to velocity uncertainty as opposed to conventional vorticity methods. Only the particle image noise contributes to the measurement uncertainty. The DMV method neglects the deformation of image patterns and is therefore not suitable for high shear flows. An important feature of the DMV method is that correlated grey intensity levels are mapped from a Cartesian coordinate system to polar coordinate system.

They did not intend to use it for estimating the force on a model. This method can be used however in conjunction with the force relations from Noca *et al.* [1999] (see previous paragraph) to calculate the vorticity field with a lower uncertainty and thus a more reliable force prediction. Images would be analysed parallel with PIV and DMV to provide the velocity and vorticity fields. To provide for data around the model a three or four camera set-up could be employed. Two cameras are set-up for stereoscopic PIV that would capture the global flow field around the model. The third camera would be set-up such that the optical axis aligns with the centreline of the model to reduce perspective errors. To really minimize the effect actually a two-camera set-up to zoom in on the model is needed. The stereoscopic is used so that the cameras are not in each other's field of view. This third camera would focus primarily on the flow close to model and provide a necessary high resolution in this region (e.g. similar to the convention in CFD methods to decrease the cell size in the neighbourhood of a boundary). The resulting velocity and vorticity fields could then be inserted into the relations from Noca *et al.* [1999].

Planar accelerometry
Jakobsen *et al.* [1997] used a four CCD camera set-up to measure the acceleration in addition to the velocity; in principle a two-camera set-up would suffice. The measurement of the acceleration is necessary when The images from first two and the last two cameras were correlated to produce two velocity fields by conventional PIV analysis. These two velocity fields are then used to estimate the acceleration term based on an Eulerian approach. Using such a method leaves a first-order linear differential equation for the pressure. This method seems to be applicable to a wide range of flows.

5.3 Two dimensional pressure gradient integration

Two methods have been considered to integrate the pressure gradient field, the Conjugate Gradient Method and the Downstream Integration.

5.3.1 Conjugate Gradient Method

The Conjugate Gradient Method employed is the same as described in Elsinga [2003]. The application of the Reynolds averaged Navier-Stokes equations requires a second step to be performed to obtain the pressure field. This step encompasses the integration of the gradient field. The pressure field and the pressure gradient field are related as:

$$p = \int_S \nabla p \, dS \tag{5.8}$$

The pressure gradient field can be spatially integrated solving the system of equations:

$$D_{ij} p_i = g_i \tag{5.9}$$

where $\boldsymbol{D}$ a sparse matrix ($2N$ x N) with a second order accurate central differencing scheme, $\boldsymbol{p}$ a vector (N) containing the pressure values at each point and g a vector ($2N$) containing the pressure gradient values at every point in x- and y-direction. The system of equations, equation (5.9), is over specified and is solved in the least square sense using the Conjugate Gradient Method. The method used here is a (slight) modification of the method documented in Elsinga [2003].

The Conjugate Gradient Method is an iterative method at which at every iteration the following is derived:

step length: $$\beta^k = \left(\frac{\left| \bar{\bar{r}}^k \right|}{\left| \bar{\bar{D}} \bar{q}^k \right|} \right)^2$$

updated pressure: $$\bar{p}^{k+1} = \bar{p}^k + \beta^k \bar{q}^k$$

new residual: $$\bar{r}^{k+1} = \bar{\bar{D}}^T \left(\bar{g} - \bar{\bar{D}} \bar{p}^{k+1} \right)$$

coefficient: $$\alpha^k = \left(\frac{\left| \bar{r}^{k+1} \right|}{\left| \bar{r}^k \right|} \right)^2$$

new search direction: $$\bar{q}^{k+1} = \bar{r}^{k+1} + \alpha^k \bar{q}^k$$

The Conjugate Gradient Method is initialised with an uniform pressure field, $\bar{p}^k$, and $\bar{r}^k$ and $\bar{q}^k$ are defined as $\bar{r}^0 = \bar{q}^0 = \bar{\bar{D}}^T \bar{g}$. First the step length, β^k, in the search direction is calculated. The pressure is then updated in the direction of the vector q. The next step is to calculate the new residual for the updated pressure. The new residual is the old residual (e.g. the difference between the left- and right hand side of equation (5.9)) times the differential scheme matrix $\bar{\bar{D}}^T$. There is no error level defined for the residual since the Conjugate Gradient Method is bound to converge for finite dimensional problems. The final two steps consist of calculating a new coefficient, α^k, that is then used to determine the new search direction of the next iteration. Before the next iteration all the k+1 components are set to k. The boundary condition to initialise this procedure is the pressure, as determined by the Bernoulli pressure relation, in a single point on the left vertical side of the computational domain.

5.3.2 Downstream integration

The downstream integration approach is a modified version of the method documented in Baur *et al.* [1999]. The current method uses a Dirichlet condition on the inlet and the resulting pressure field is then reconstructed by a two-dimensional integration. The integration proceeds line by line in downstream direction. The integration process is an averaging over neighbouring points. For each line, there are two sweeps, from top to bottom and vice versa. The resulting pressure field is the average of the results of the two sweeps.

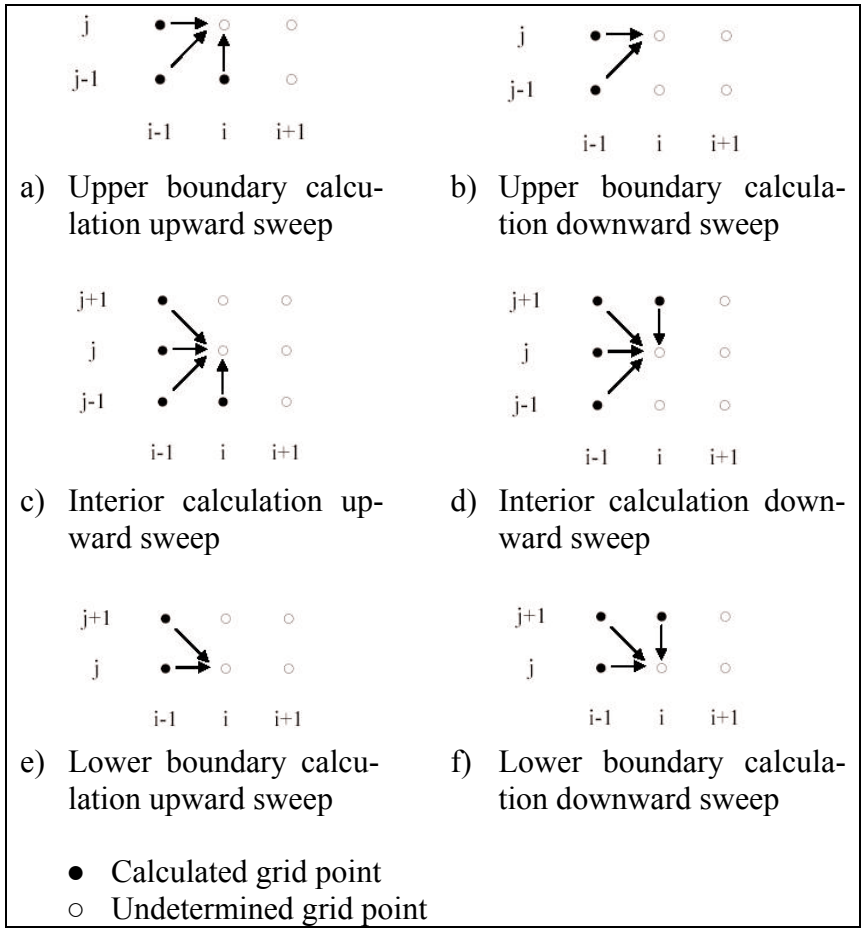

Figure 5-2: Pressure calculation at grid point (*i*,*j*) with upward and downward sweep

The method is visualized with integration directions in figure 5-2, which also illustrates how the integration on line *i* is determined, with pressures known from line *i*-1. The arrows indicate which grid points are used for the pressure determination at the point (*i*, *j*). The pressure from the previous calculated grid point, at the grid point (*i*, *j*-1) for the upward sweep or the grid point (*i*, *j*+1) for the downward sweep, is used as well as the results from the previous (downward or upward) sweep. At the lower boundary at the upward sweep and the upper boundary at the downward sweep only the results from the previous sweep are used. The pressure is then calculated according to:

$$p = \int \left(\frac{\partial p}{\partial x} dx + \frac{\partial p}{\partial y} dy \right) \tag{5.10}$$

This can be written in a discrete form for an interior grid point:

$$p(i,j) = \frac{p_1 + p_2 + p_3 + p_4}{4} \tag{5.11}$$

where the pressure p_1 to p_4 are evaluated by a second order Taylor series (using a trapezoid rule of integration):

$$p_1 = p(i-1, j+1) + \tfrac{1}{2}\left(\tfrac{\partial p}{\partial x}(i-1, j+1) + \tfrac{\partial p}{\partial x}(i,j) \right) dx + \tfrac{1}{2}\left(\tfrac{\partial p}{\partial x}(i-1, j+1) + \tfrac{\partial p}{\partial x}(i,j) \right)(-dy) \tag{5.12}$$

$$p_2 = p(i-1, j) + \frac{1}{2}\left(\frac{\partial p}{\partial x}(i-1, j) + \frac{\partial p}{\partial x}(i,j) \right) dx \tag{5.13}$$

$$p_3 = p(i-1, j-1) + \frac{1}{2}\left(\frac{\partial p}{\partial x}(i-1, j-1) + \frac{\partial p}{\partial x}(i,j) \right) dx + \frac{1}{2}\left(\frac{\partial p}{\partial y}(i-1, j-1) + \frac{\partial p}{\partial y}(i,j) \right) dy \tag{5.14}$$

$$p_4 = p(i, j-1) + \frac{1}{2}\left(\frac{\partial p}{\partial y}(i, j-1) + \frac{\partial p}{\partial y}(i,j) \right) dy, \quad \textit{upwards} \tag{5.15}$$

or,

$$p_4 = p(i, j+1) + \frac{1}{2}\left(\frac{\partial p}{\partial y}(i, j+1) + \frac{\partial p}{\partial y}(i,j) \right)(-dy), \quad \textit{downwards} \tag{5.16}$$

The number in the denominator in equation (5.11) equals the total number of points contributing to the pressure at the grid point (i, j). The pressure is thus an average of the neighbouring points to minimize any propagation of errors. At the upward sweep the denominator is 2 at the lower boundary and 3 at the upper boundary, and vice versa at the downward sweep. The denominator value is also dependent on the mask. A mask is created to take only into account the grid points that are outside the model. If during an upward and/or downward sweep no neighbouring points contribute to the pressure, the value of the pressure is not calculated and not used for any next calculation of the pressure.

5.3.3 Verification of integration methods

The two methods for the direct two-dimensional integration have been tested on an analytical function of two variables x and y reading as:

$$z = 1.5 + 0.05x - 6\frac{y-2}{2 + x^2 + (y-2)^2} \tag{5.17}$$

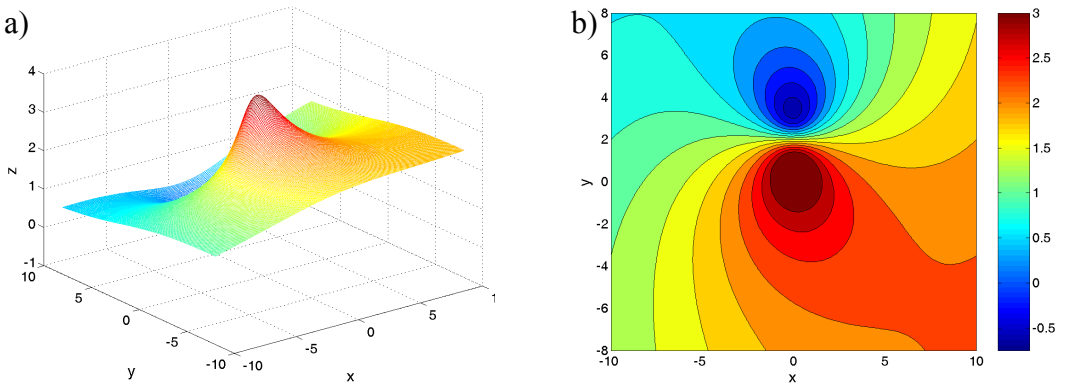

Figure 5-3: Analytical test function, a) Mesh plot, b) Contour plot

The integration of the gradient of this test function will be evaluated with the Conjugate Gradient Method and the downstream integration technique. The gradient field of the test function z, equation (5.17), will be calculated with the MATLAB function `GRADIENT`. The two methods will be compared in how they reproduce this test function. The test function z is visualized in a three dimensional sense in figure 5-3a and its accompanying contour plot in figure 5-3b. The function z will be defined on a grid with x-values ranging from -10 to +10 and y-values ranging from -8 to +8, with an equidistant stepsize of 0.1, leading to 201 by 161 grid points.

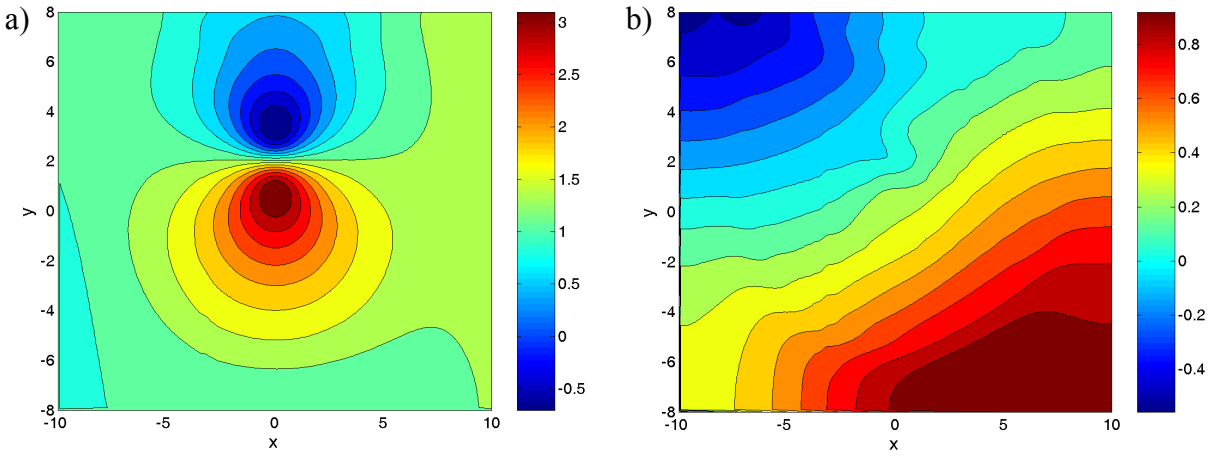

Figure 5-4: a) Contour plot of result of CGM method, b) Error

The results of the Conjugate Gradient Method applied on this test function are presented in figure 5-4a. The difference of the exact solution and the Conjugate Gradient Method is shown in figure 5-4b. It is clear that this method returns large differences in the solution, in order of 30% of the reference value. It seems that an approximated linear part of the solution is lost, the reason for this is not clear. Although one may conclude from this result that the Conjugate Gradient Method seems unsuitable for this kind of integration, it has to be mentioned that the Conjugate Gradient Method shows satisfying results for the symmetrical potential flow around a circular cylinder (see Appendix C).

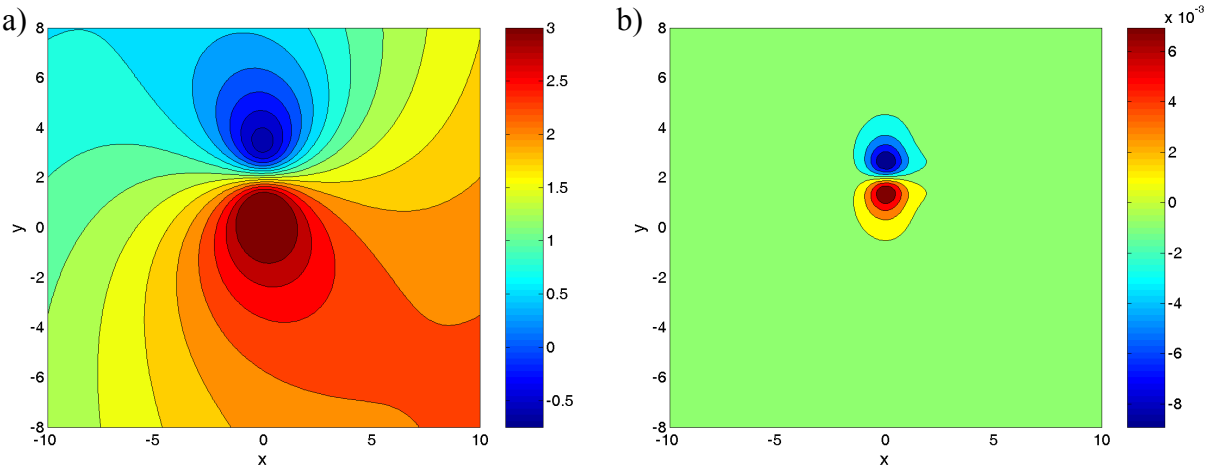

Figure 5-5: a) Contour plot of result of downstream integration, b) Error

The result obtained with the downstream integration method is given in figure 5-5a. The difference of the exact test function and the result of the downstream integration is given in figure 5-5b. It can immediately be concluded that this method approximates this test function with a small difference located at the regions of the largest gradients. The error is of the order 10^{-3} at the position where there is a large change in the gradient. Since the function is solved for discrete points, this error is ascribed to an insufficient spatial resolution for grid points in the neighbourhood of large gradients.

5.4 Critical parameters

When applying the procedure to the flow around a model, the numerical integration procedure is sensitive to a number of geometrical influences. One issue of the current method is that the solution is greatly affected by the size of the mask that covers the model and the adjoining region of unreliable velocity measurement. Another issue is that an increase of grid points will lead to a better converged solution, similar to (conventional) CFD methods.

5.4.1 Data mask

Already in the image processing procedure, a mask was included at the position of the model. In addition, a small area around the model was added to compensate for the lack of optical access due to perspective view. Consequently, within this mask there is no velocity data available. The first assumption during the downstream integration was to use the same mask. However, it turned out that there was a significant propagation of errors in the region just outside the mask. Also, due to flow separation there is a large difference in pressure gradients at the front corners of the model. These areas contribute the most to the error.

The propagation of errors can be minimized by introducing a mask distinctively larger than the model. Although this prohibits the pressure to be computed close to the body, it provides more reliable pressure data for the contour integration that yields the integral forces. A calculation of the potential flow around a circular cyl-

inder illustrates this effect. The large mask consists of 32 x 31 grid points and has a size of 1.6 x 1.6 *D*, where *D* is the diameter of the cylinder (set equal to 1). The small mask is equal to the cylinder, filling a circle of 19 x 19 grid points. Both masks are centred on the cylinder centre.

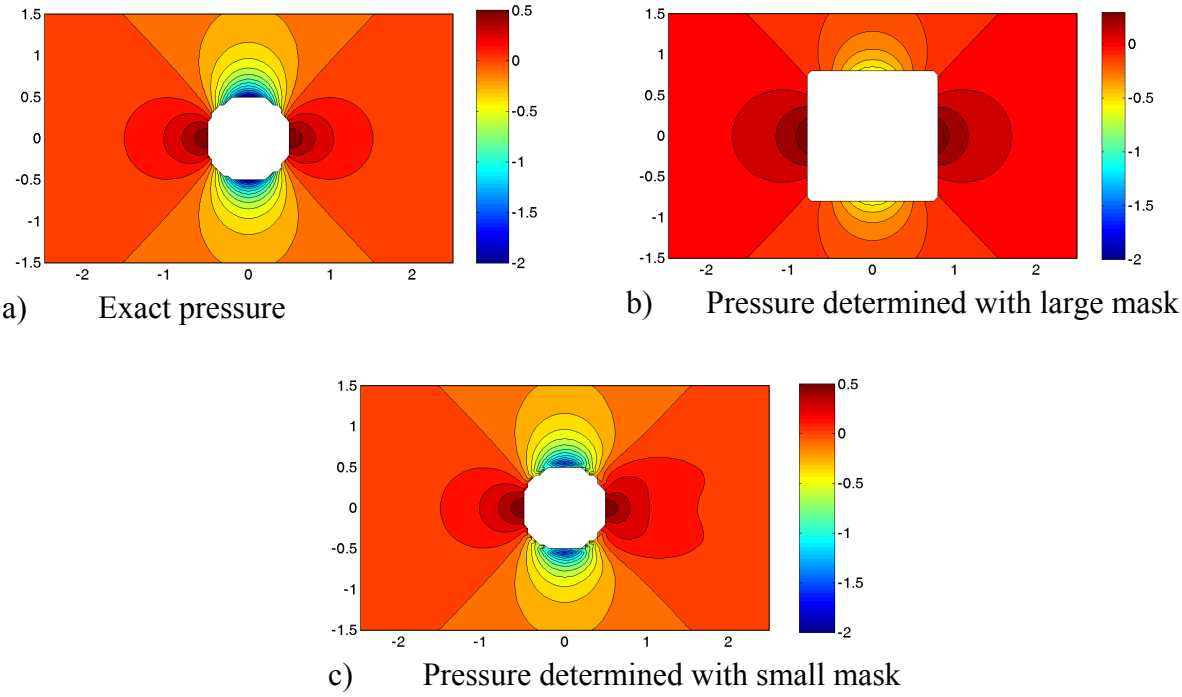

a) Exact pressure

b) Pressure determined with large mask

c) Pressure determined with small mask

Figure 5-6: Comparison of pressure calculations

Figure 5-6 shows the results for the potential flow with zero circulation where the approximated pressures with a large mask in figure 5-6b and a small mask in figure 5-6c are compared to the exact pressure, figure 5-6a. The difference of the calculated pressure values with the exact pressure are given in figure 5-7a and b for the large mask and the small mask, respectively. Figure C-4 (in Appendix C) shows the same effect for a potential flow calculation with circulation. At first glance (figure 5-6c), the results of the pressure calculation with the use of the small mask seem reasonable. However, close to model (figure 5-8) there is large difference between the calculated pressure and the exact pressure. The reason for this is most likely caused by the reliability of the pressure gradient. It might not be well estimated in the neighbourhood of a boundary. This difference is then propagated throughout the rest on the computational domain. When compared with the large mask, the differences are remarkably lower for the large mask.

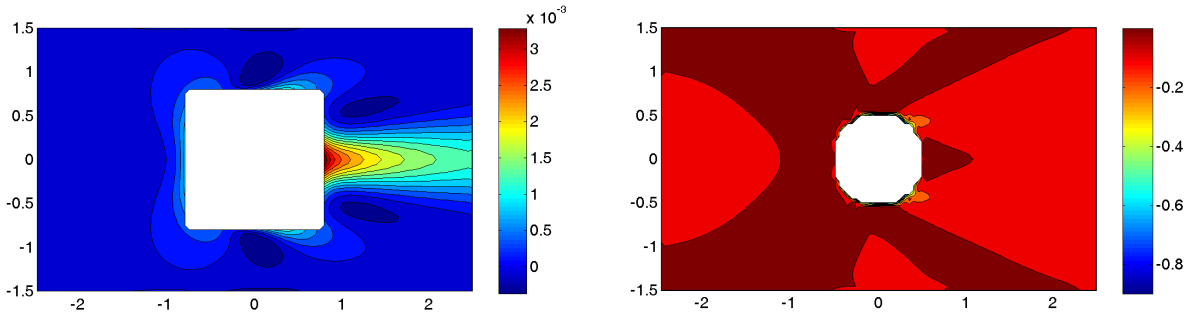

a) Large mask b) Small mask

Figure 5-7: Errors of pressure calculations, downstream integration

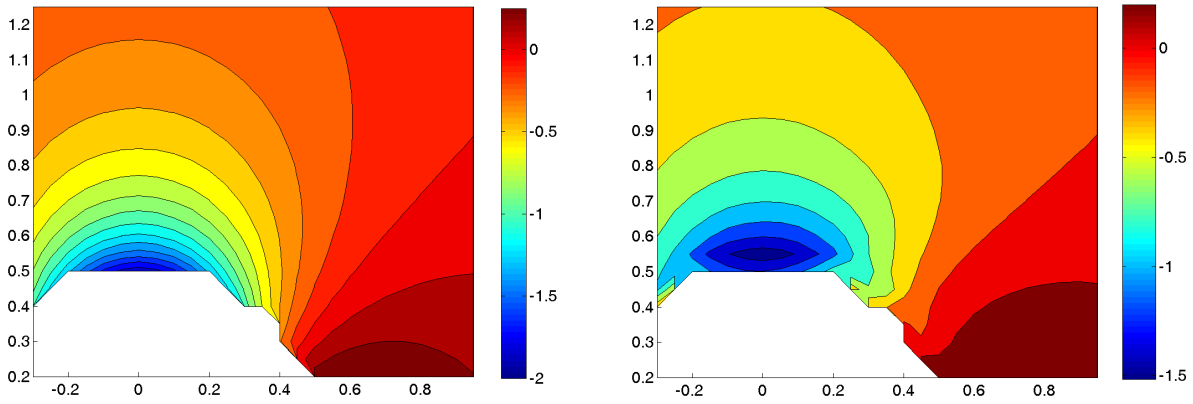

a) Exact pressure b) Calculated with small mask

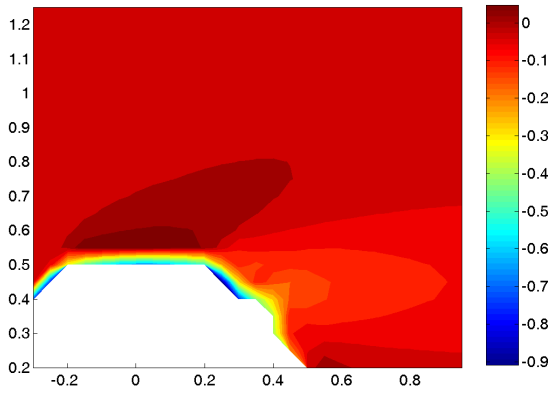

c) Error

Figure 5-8: Close-up of region around model using a small mask for potential flow with no circulation

5.4.2 Spatial resolution

One way to show the convergence of the method is to increase the number of grid points. For experiments this can be only be done by increasing the spatial resolution of the set-up but for the simulation this can varied by hand. The grid size encountered during the experiments is 126 x 168 $pixel^2$. To establish the effect on the solution the drag and lift coefficient are calculated for the potential flow

around a circular cylinder. In anticipation of the force calculation in the next paragraph, it can also be verified whether the force integral momentum is correctly implemented. The drag coefficient for this type of flow is zero (D'Alembert's paradox). The lift coefficient is zero for potential flow without circulation and for potential flow with circulation equals [Anderson, 1991]:

$$c_l = \frac{\Gamma}{RV_\infty} \tag{5.18}$$

where Γ the circulation and R the radius of the cylinder.

The values of the drag and lift coefficient are calculated for the potential flow around a circular cylinder with a radius of 0.5, a free stream velocity of 1 and circulation values of 0 and 5. So the drag and lift coefficient should all be 0, except for the case with circulation where the lift coefficient should equal 10. The drag and lift coefficient are calculated on the following grid sizes, 61 x 101 (Coarse grid) and 151 x 251 (Fine grid). The results of the calculation are given in table 5-1.

Table 5-1: Drag and lift coefficients calculated for potential flow around a circular cylinder with and without circulation

	c_d	c_l	c_d	c_l
Circulation	0		5	
Coarse grid	$2.90 \cdot 10^{-3}$	$-1.37 \cdot 10^{-4}$	$2.10 \cdot 10^{-3}$	10.0821
Fine grid	$6.30 \cdot 10^{-4}$	$-2.26 \cdot 10^{-7}$	$4.32 \cdot 10^{-4}$	10.0307
Exact	0	0	0	10

It appears that the theoretical values are well approximated. The small deviations are related to the calculation on discrete grid points and numerical integration errors. The values of the drag and lift coefficient are well approximated. An increased grid size (fine grid) shows a reduction of almost one order of magnitude in the error for the drag coefficient. An increased grid size shows also an improvement of the lift coefficient estimation. The error of the lift coefficient for the case with circulation is of the order 10^{-2}. The error is larger than the case without circulation.

5.5 Implementation of force calculation method

A schematic view of the integration area is presented in figure 5-9. The method is applied to validated data from which the upper eight pixel rows (the white area in the top of this figure) were eliminated. It turned out that in this region velocity outliers caused a large deviation in the computed pressure field. The contour line (solid black line) of the integration area is chosen 5 pixels within the outer left boundary of the image. This way border effects from the PIV experiments are minimized in the contour integral evaluation. The boundary condition for the

pressure is prescribed at the outer boundary of the image. The (size of the) mask is kept constant (at approximately 2 x 2 D) and always enclosing the model. The mask is illustrated by the white area surrounding the model in figure 5-9. The points ①, ②, ③ and ④ indicate the corners of the contour. The drag and lift coefficient are obtained by making the drag and lift dimensionless with $\frac{1}{2}\rho U_\infty^2 D$, where D is the length of one side of the square prism (U_∞ is 10 *m/s*, D is 30 *mm*).

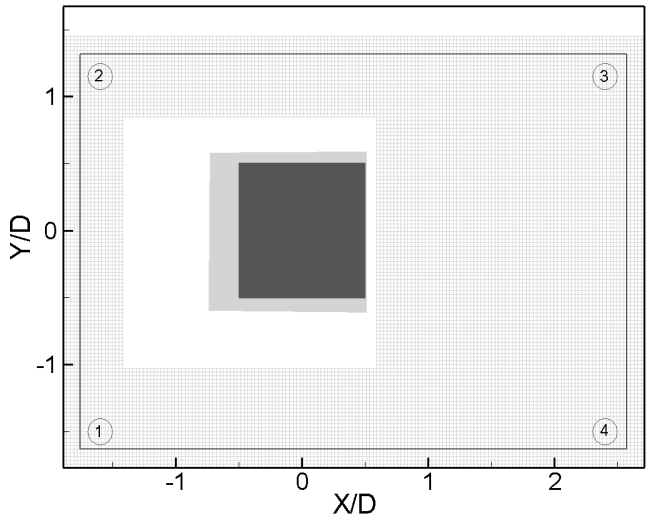

Figure 5-9: Schematic view of model (dark grey), perspective area (light grey), masked area (white area surrounding model), the skipped part (upper white area), the integration contour (black line) and the grid points (light grey mesh)

Two examples of the calculated pressure gradient are provided in figure 5-10 and figure 5-11 for the model at zero angle of incidence. Additionally, the contributions of the Euler, fluctuating and viscous terms are given as well (note the magnified scale for the viscous term), with the different terms as identified by equation (5.5). The first figure is based on the current dataset. It is based on the statistical procedure with which all present datasets were post-processed. The latter is based on an improved statistical procedure (which only recently has been added to the post-processing software WIDIM) with slightly coarser settings: a window size of 31 by 31 pixels and 50% overlap and only 500 (half of the dataset) image pairs are analysed.

The Euler terms take into account the front stagnation and the side acceleration of the flow. In the wake region the Euler terms show little contribution and in the shear layers account for pressure recovery of the flow. The fluctuating terms dominate the pressure gradient within the wake. A minimum in pressure is clearly visible at approximately $X/D = 1.2$. The pressure recovery by the Euler terms is counteracted in the shear layers by these fluctuating terms. As may be expected, the viscous terms do not add much to the pressure gradient and only show a small contribution in the shear layer. Due to the shadow stripe, the pressure gradient is slightly asymmetric. The results of the improved analysis are more symmetric, figure 5-11. The Euler terms of the pressure gradient are greatly affected by the shadow stripe emanating from the upper right corner of the model (figure 5-10). These terms are based on the velocity and the velocity gradient so the effect is dominating there. To a lesser extent is the effect visible in the contribution of the fluctuating terms.

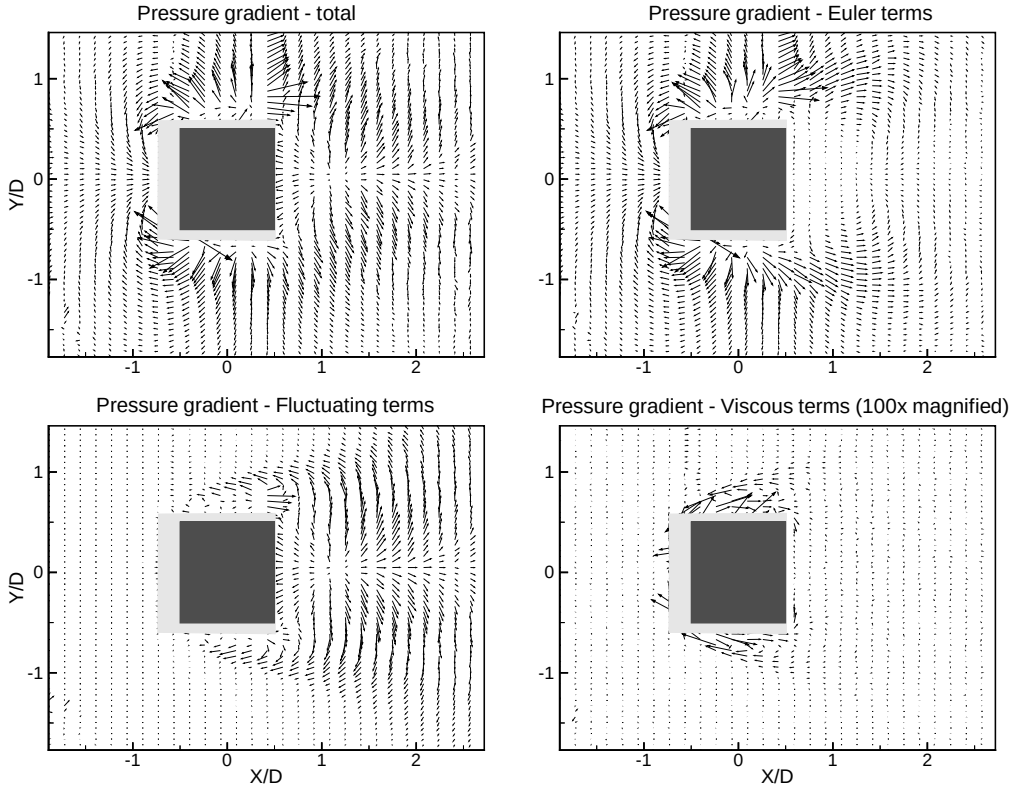

Figure 5-10: Contribution of terms to the pressure gradient using current statistical validation

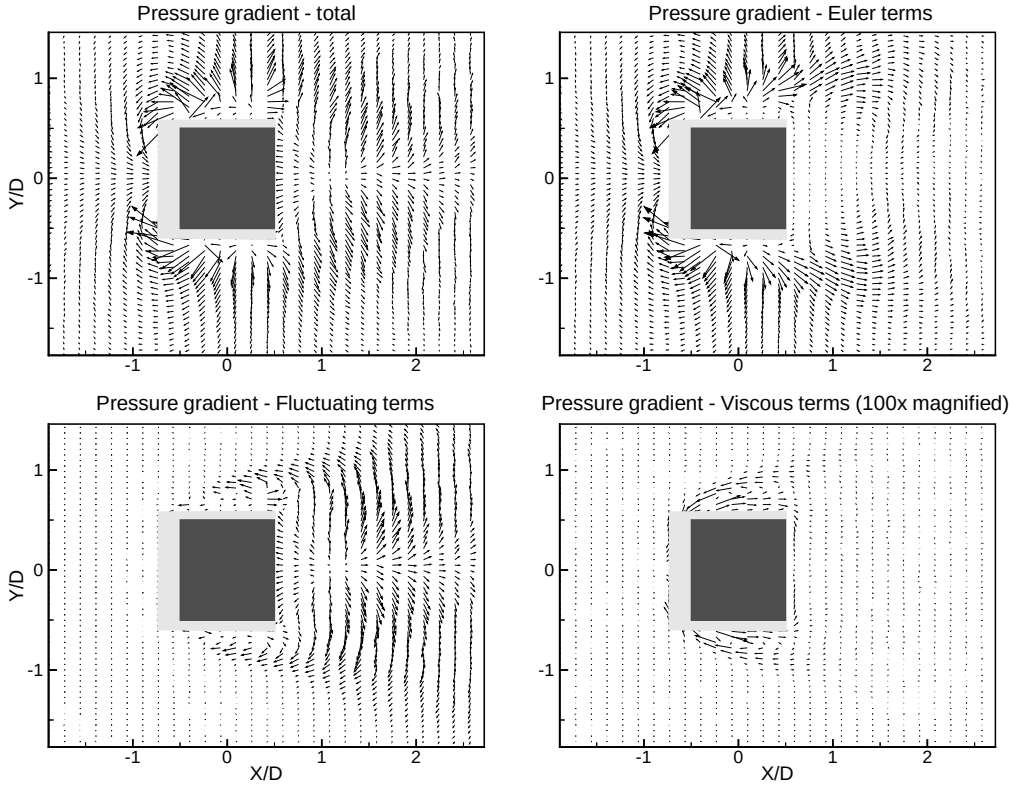

Figure 5-11: Contribution of terms to the pressure gradient using an improved statistical validation

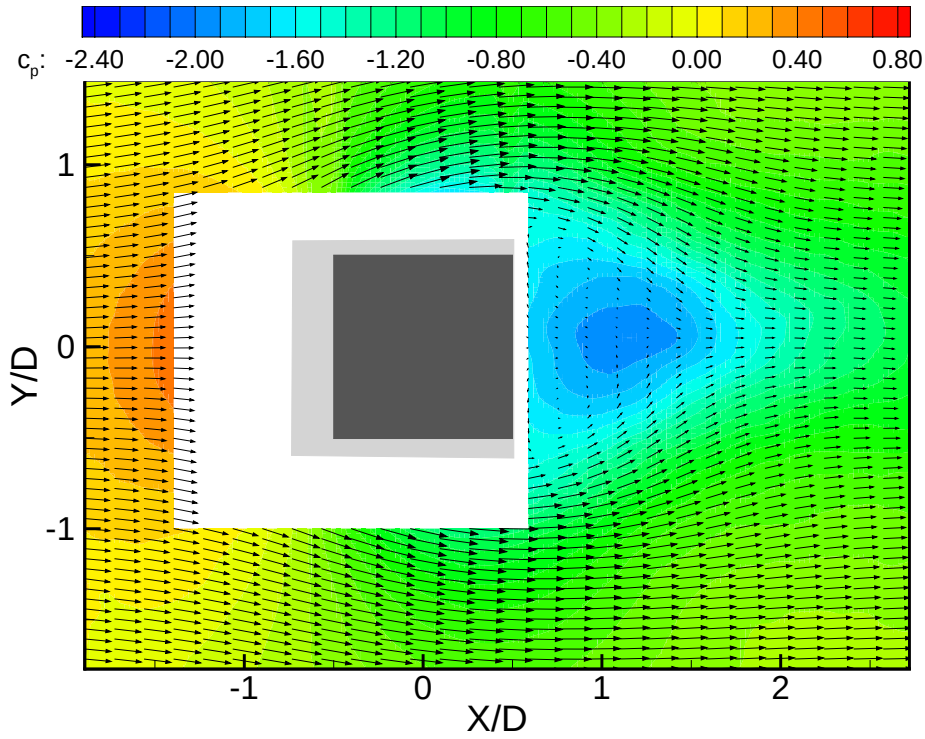

Figure 5-12: Pressure coefficient, c_p, at $\alpha = 0°$

Figure 5-12 presents the pressure coefficient distribution, c_p, for zero angle of incidence obtained with the 2D integration method. Due to the use of the mask, it is not possible to resolve the pressure coefficient in the region just around the model. The stagnated region therefore cannot be clearly determined. The minimum pressure behind the model is captured. Plots of the pressure coefficient for angles of incidence can be found in Appendix D.

In order to verify the assumptions of the pressure evaluation along the contour several methods are provided in figure 5-13. The following procedures are compared (the equations can be found in Appendix C):

- Bernoulli
- 'unsteady' Bernoulli
- 1D pressure integration (contour)
- 2D pressure integration (field)

All pressure calculations show good agreement outside the wake (front side and parts of the top side and bottom). The pressure field obtained by the Bernoulli and 'unsteady' Bernoulli equation show that these equations are not valid in the wake region, as may be expected. The 'unsteady' Bernoulli equation differs from the regular Bernoulli equation in such that the fluctuating velocity terms are added. This equation is therefore able to better predict the pressure near the shear layers, but this equation also deviates within the wake region. The integration of the pressure gradient along the contour was also calculated with a 1D integration. Since this integration can only be performed in one direction the end value of the integration is not the same as the start value. This corrected for by applying a linear

correction to the integrated pressure values. Even then, the 1D integration deviates from the 2D integration. The 2D integration is less sensitive as the 1D integration to outliers, since the pressure values are averaged over the neighbouring values. Therefore, the 2D integration seems the most reliable to predict the pressure field for the flow under consideration. Three regions with peaks appear along the contour. A small region of outliers causes the slight disturbance at the beginning of the integration contour. The two peaks on the topside of the model are due to the emanating shadow stripes. The pressure calculations of the all methods do not deviate behind these peaks.

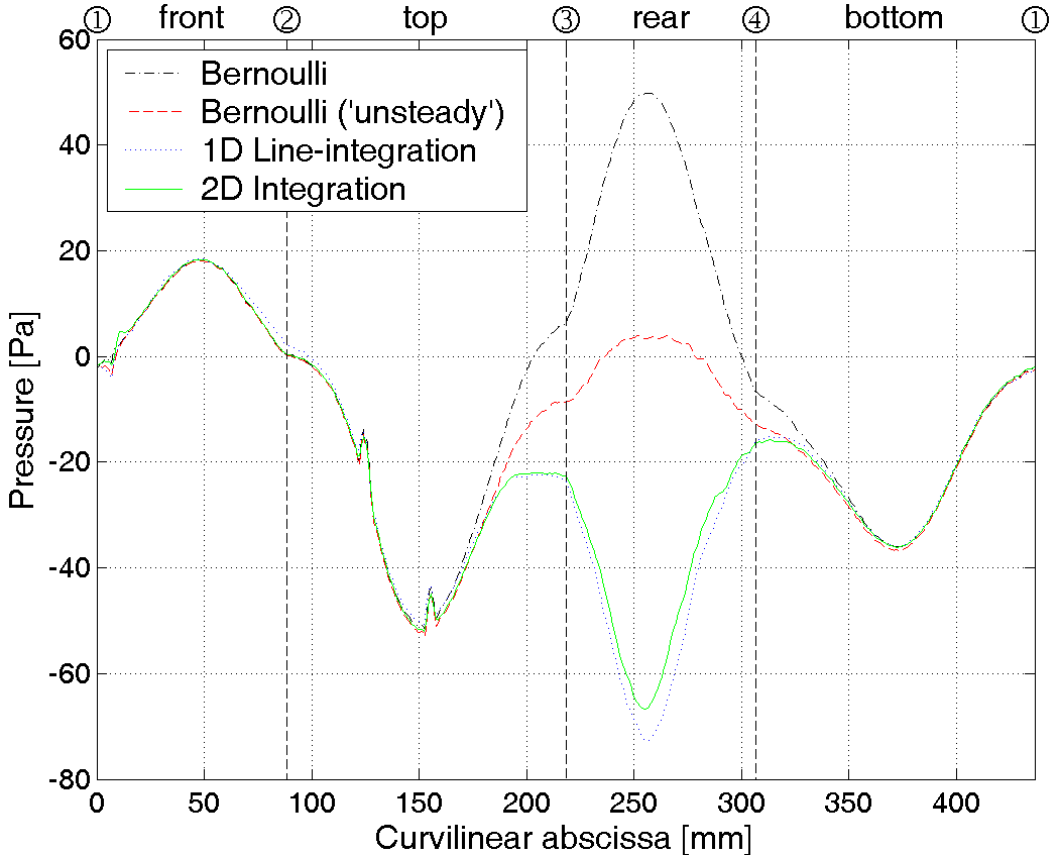

Figure 5-13: Comparison of several pressure computations along contour

5.6 *Discussion of results*

The method of the integral momentum force calculation is finally used to determine the drag and lift coefficient on the model. The obtained values of the drag and lift coefficient are presented in table 5-2. The calculated drag coefficient is shown in figure 5-14 compared to data from other researchers. The general trend of these results is recovered with the current method. However, the drag coefficient by the current method, red line/red dots, is overestimated in comparison with other results. An explanation for this deviation is the high blockage ratio during the experiments. The blocked area by the model is around 10%. The effective blockage ratio is even larger due to the displacement of the boundary layer. This would mean that the velocity over the model is more than 10% higher. Since an

aerodynamic force is scaled with the velocity squared, the drag would be estimated 21% higher. Cooper [1998] states that a continuing search for good wind tunnel corrections for bluff body experiments is still needed. Another deviation is the estimate for the occurrence of the minimum drag coefficient. All data suggest a minimum value of C_D between an angle of incidence of 12° and 13°, whereas the present method predicts a minimum value at angle of incidence of 10°.

The calculated lift coefficient is given in figure 5-15 together with results from other researchers. The lift coefficient, red line/red dots, shows a good agreement with other results. Similar to other data the minimum lift coefficient is predicted to occur an angle of incidence of 10°**.** The gradient of the lift coefficient is however not well estimated. Another issue is the deviation at zero angle of incidence where a non-zero (positive) value is calculated.

Table 5-2: Drag and lift coefficients (minimum values in boldface)

Angle of incidence (°)	Drag coefficient	Lift coefficient
0	2.1773	0.1344
2.5	2.0076	-0.4749
5	2.0899	-0.4825
7.5	2.0173	-0.6789
10	**1.8705**	-0.4274
12.5	1.9064	**-0.8256**
15	1.9807	-0.6948
20	2.1293	-0.3729
25	2.4273	-0.1188
30	2.4824	0.0446
35	2.5892	-0.0705
40	2.7978	-0.0148
45	2.9237	0.1060

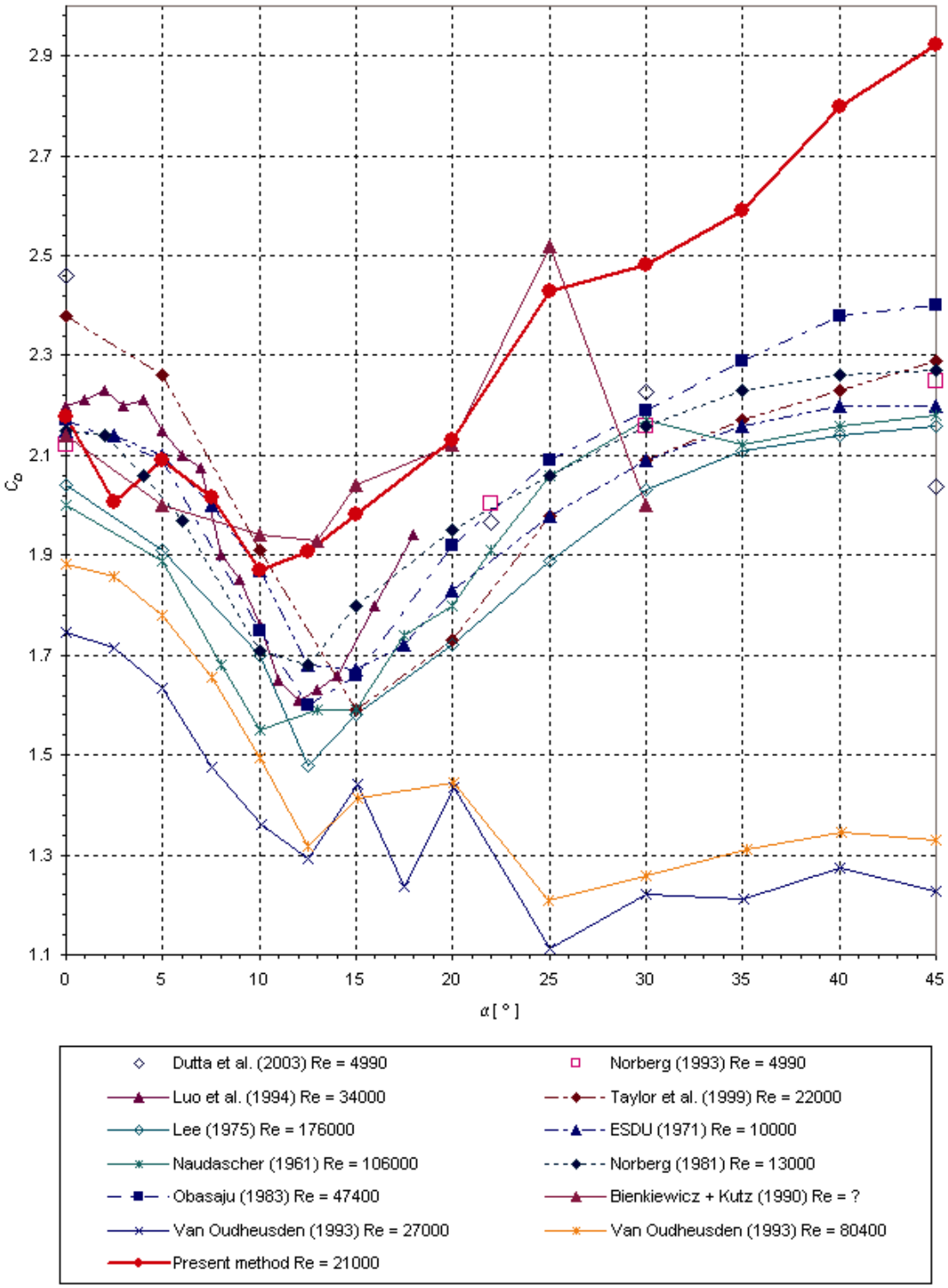

Figure 5-14: Drag coefficient, C_D, versus angle of incidence, α

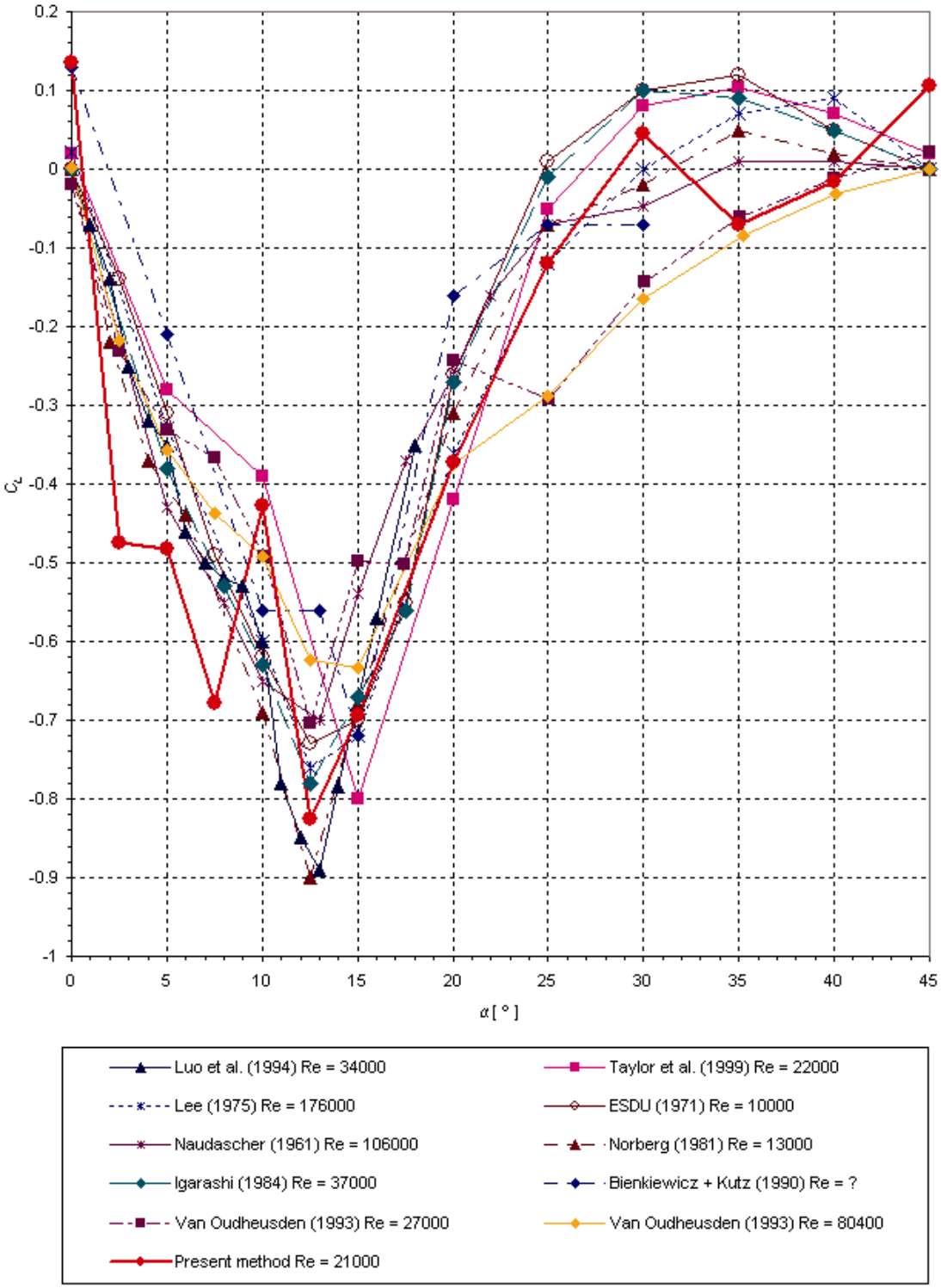

Figure 5-15: Lift coefficient, C_L, versus angle of incidence, α

Chapter

6

Conclusions and Recommendations

The main conclusions in the current investigation of the flow around a square cylinder are summarized in this chapter. Also, some aspects for future research on galloping and force determination are presented.

6.1 Conclusions

The flow around a bluff body exhibits large regions of separation. The separated flow can lead to vibrations of the bluff body, which can ultimately lead to the failure of the structure. Vibrations at frequencies lower than the natural frequency of the structure are referred to as galloping. Galloping is characterized by a large amplitude low frequency vibration. These vibrations can be described by a two-dimensional quasi-steady theory, in terms of negative aerodynamic damping. Typical properties of square prismatic cylinders are the occurrence of a negative lift coefficient, possible reattachment of the flow when the cylinder is placed at angles of incidence and a minimum lift and drag coefficient at an angle of incidence of approximately 12.5°.

An extensive database of steady measurements has been created as a first step in the verification of the quasi-steady assumptions. Three experimental campaigns were conducted on the flow around a square cylinder at different angles of incidence. All experiments were performed with Particle Image Velocimetry as a diagnostic technique. As a consequence an experimental model should provide optical access for laser light. Two different models were employed, a full Perspex model and a hollow model. Dark shadow regions were present in the instantaneous images of the flow when using the Perspex model, caused by the optical prop-

erties and the dimensions of the Perspex. A second model was created where the optical accessible area was constructed from thin Perspex parts, leaving the internal volume hollow. The shadow regions were reduced to small shadow lines. Consequently, the post-processing of the images provided better results.

The three experimental campaigns that were conducted, with a focus on:

Case A: the wake, field of view (FOV): 9 x 3 *D*,
Case B: a close-up of model, FOV: 2.5 x 2 *D*,
Case C: near-wake, FOV: 4.5 x 3.5 *D*.

All experiments were performed in the low speed open wind tunnel, W-tunnel, of the Aerodynamics Department of the Faculty of Aerospace Engineering of Delft University of Technology. The first two campaigns were performed with the full Perspex model, the last experiment with the hollow model. Both models had a side length of 30 *mm*. All measurements were performed at a Reynolds number of $2 \cdot 10^4$. Only four angles of incidence (0°, 5°, 10° and 15°) were investigated during the first two experiments. The database of angles of incidence was constructed during the final experiments (case C) where angles of incidence between 0° and 45° were measured. Between 0° and 15° every 2.5° was measured and between 15° and 45° every 5° was measured, resulting in 13 different angles of incidence. During Case C a total of 1000 snapshots was taken, for each configuration.

Several measures were taken to improve the quality of acquired data during the research period. The damaged mirrors in the laser head were replaced and cleaned (Case A and B) and finally the laser transmitting system was totally removed (Case C) and replaced with a custom made optical system to create a laser light sheet out of cylindrical and spherical lenses and angle reflecting element. The improvement was also partially due to an increase of the focal length of the camera and an optimisation of seeding level by placing the seeding generator outside of the contraction room of the wind tunnel. However, due to perspective view it is not possible to fully resolve the flow in a region 20% of the model length in front and below the model.

The acquired images are post-processed with the PIV software-package WIDIM. A user-interface has been provided to ease the creation of the necessary input-files (added as an annex to this report). After processing of the data, the resulting instantaneous velocity fields were statistical averaged by new method that exploited the properties of the histogram of instantaneous velocity distributions. With this method most of the previously undetected spurious vectors could be identified and replaced.

The different flow regimes that represent the flow around a square cylinder are clearly identified. In the symmetrical case at 0° flow separates from the windward corners and recirculation zones are formed. At increasing angles of incidence the flow can reattach on the lower side of the model. At 12.5° a separation bubble has been formed on the full length of bottom side of the model. The separation bubble captures the recirculation zone at the lower side of the model. The two upper re-

circulation zones are joined together. At angles of incidence larger than 12.5° the flow separates from the lower-right corner and the upper (left) corner. The separation bubble on the lower side is shortened. The lower recirculation zone at the back of the model is slightly increased in horizontal direction.

The near-wake, defined by the length of two recirculation zones at the leeward side of the model, increases with increasing angles of incidence and shows a local peak at 10°. Within the near-wake the magnitude of the velocity has a region with a maximum value. At increasing angles of incidence, this region increases and also the maximum value increases. A region of almost zero magnitude is present in the near-wake for 0°. This part is limited to spots to the border of the near-wake for increasing angles. These spots are reduced for increasing angles. The turbulence intensity remains fixed to a position of about 2. A single maximum is present at 0°. The turbulence intensity decreases for high angles of incidence. At 45° the single spot is split in two separate blobs.

The Proper Orthogonal Decomposition (POD) was applied to the datasets of Case C. This method returns the coherent velocity of the vortex shedding mechanism. This method orders eigenvalues according to their energy contribution. The convective features of the vortex shedding are captured with the first two eigenmodes. In particular, these two eigenmodes represent between 52 and 72% of the energy of the flow. When the eigenmodes of the horizontal velocity obtained by this method show are symmetric, the vertical eigenmodes are anti-symmetric and vice versa. The energy summation of the first two eigenmodes decreases at higher angles of incidence. In addition, the correlation of the phase portrait of the first two eigenmodes is reduced at higher angles of incidence. It might be an indication of a reduced periodicity of the flow. Using the mean velocity and the first two eigenmodes the flow, a low-order flow model can be constructed. This low-order flow model is phase-resolved and identifies the vortex shedding pattern at each angle of incidence.

The lift and drag coefficients are determined by an integral momentum approach. The pressure in this equation is provided by two-dimensional integration of the mean pressure gradient obtained from the Reynolds-averaged horizontal and vertical momentum equations. All parts in the equations are readily available with PIV experiments. The integration is initialized with a Bernoulli pressure on the inlet (Dirichlet conditions). The pressure at unevaluated grid-points is calculated by a Taylor series from already evaluated grid-points. The average pressure gradient of two neighboring grid-points is used to as the integration step. The pressure at a grid-point is determined by an average of all the contributions from the Taylor series.

In order to reduce errors in the pressure gradient integration, data masking has been applied. The area of data masking has to be distinctively larger than the model. Large pressure gradients near the corners of a model are most likely to contribute to the error and propagate into the flow field. Another way to reduce errors is to increase the grid size.

The procedure for the pressure integration and force determination from PIV data has been tested on an analytical test function and the potential flow around a circular cylinder. Subsequently these methods were applied to the experimental PIV data of the bluff body flow around a square cylinder. In all test cases shows the method a good agreement with the exact solution (analytical function and potential flow) or data from other researchers (bluff body flow). The trend of the drag coefficient, as predicted by others, is captured. However, it is overestimated and probably due to a high blockage ratio during the experiments (~10%). Both the trend and values of the lift coefficient predicted with the current method are in good agreement with other data. However, a positive value of the lift coefficient is predicted at zero degree of incidence whereas literature data suggest a zero value. The maximum of the lift coefficient is estimated at 10°.

6.2 Recommendations

- The experiments were primarily set-up to serve as a database to which future experiments could be compared. In order to fully validate the assumptions of the quasi-steady galloping theory, the flow around an oscillating cylinder should still be investigated.

- The current experimental set-up had a fairly high (>10%) blockage ratio of the model in the wind tunnel. The blockage ratio may cause the overestimation of the mean drag. To assess this statement the measurements, or a selection of angles of incidence, should be repeated in set-up with a lower blockage ratio, e.g. a smaller model or a larger wind tunnel.

- The hollow model used during the final experiments, Case C, might not be suitable for oscillating measurements. The connection of the thin Perspex plate is not torsionally stiff. It was possible during the current static experiments to fix both endplates at their respective positions and enforce the torsional stiffness by tightening screws. If both endplates are oscillating it has to be ensured that the two endplates cannot move with respect to each other.

- The integration method used in the estimation of the drag and lift coefficient was validated for two analytical cases, a test function and the potential flow around a circular cylinder. It was then successfully applied to the PIV measurements to obtain the mean lift and drag on the square cylinder model. To obtain the extent to which the current method is useful a comparison with several other methods should be made. The current method could for example be used for well-known benchmark results, such as the flow around a backward facing step or the flow around a NACA airfoil. These cases are studied widely and experimental and numerical data are readily available. Methods based on PIV data, that need comparison are the current method, the momentum relation from Noca *et al.* [1997] and the pressure Poisson equation method by Gurka *et al.* [1999]. In case of the flow around an airfoil, the methods could also be validated against conventional methods, such as the force balance or pressure rake. Note however that the measured lift with PIV data returns the sectional lift and a method such as the force balance the total

lift. A relation between the sectional and total lift is not known for the flow around a bluff body [Norberg, 2003].

- The integration with the Conjugated Gradient Method proved to give incorrect results when applied to current pressure gradient data. This method, however, has yielded good results in other papers. The implementation of the boundary condition and the numerical differential scheme may cause the deviation of the current application. A specific reason was not found. It may be worthwhile to investigate this behaviour for the Conjugate Gradient Method.

- In the present work only the mean lift and drag is determined. But the nature of vortex shedding, e.g. the alternating vortices, will also lead to an importance of fluctuating forces and pressures [Norberg, 2003]. For this the flow acceleration must be known, which cannot be obtained with the present experimental set-up and PIV equipment. A possible extension of the current method to unsteady flows could be achieved by using the low-order phase resolved flow. This low-order flow model is quasi-time resolved and might be used to provide an estimate for the acceleration term in the unsteady flow equations.

- Because of the nature of vortex shedding it is interesting to also have information of the flow evolution in time. The current image acquisition rate of 3.3 *Hz* does not allow obtaining time-resolved results, since under the current experimental conditions the vortex shedding frequency is about 43 *Hz*. To fully resolve this type of flow in time a system that can measure in the order of *kHz* would be required. Such systems would consist of cameras based on CMOS (Complimentary Metal Oxide Semiconductor) technology and high-speed lasers (Diode pumped Nd:YAG).

References

ANDERSON JR., J.D., *Fundamentals of Aerodynamics*, McGraw-Hill, Inc., 2nd edition 1991.

BAUR, T., KÖNGETER, J., *PIV with high temporal resolution for the determination of local pressure reductions from coherent turbulence phenomena*, 3rd International Workshop on Particle Image Velocimetry, Santa Barbara, USA, 16-18 September 1999.

BLEVINS, R.D., *Flow-induced vibration*, Krieger Publishing Company, New York, 2nd edition 1990.

CHEN, J.M., LIU, C.-H., *Vortex shedding and surface pressures on a square cylinder at incidence to a uniform air stream*, International Journal of Heat and Fluid Flow (1999) **20**, pp. 592-597.

COOPER, K., *Bluff-Body Blockage Corrections in Closed- and Open-Test-Section Wind Tunnels*, Wind Tunnel Wall Corrections, AGARD-AG-363, France, October 1998.

DANTEC, *FlowMap® Particle Image Velocimetry Instrumentation: Installation & User's guide*, Publication number 9040U3624, Skovlunde, Denmark, August 2000.

DEANE, A.E., KEVREKIDIS, I.G., KARNIADAKIS G.E., ORSZAGA S.A., *Low-dimensional models for complex geometry flows: Application to grooved channels and circular cylinders*, Physics of Fluids (1991) **10**, pp. 2337-2354.

ELSINGA, G.E., *Density measurements by means of schlieren methods, Assessment and application of Calibrated Color Schlieren and Background Oriented Schlieren*, Master Thesis, Delft University of Technology, April 2003.

FUJISAWA, N., TANAHASHI, S., SRINIVAS, K., Evaluation of pressure field and fluid forces on a circular cylinder with and without rotational oscillation using velocity data from PIV measurement, Measurement Science and Technology (2005) **16**, pp. 989-996.

GURKA, R., LIBERZON, A., HEFETZ, D., RUBINSTEIN, D., SHAVIT, U., *Computation of pressure distribution using PIV velocity data*, Proceedings of the Third International Workshop on PIV'99, Santa Barbara, USA, 16-18 September 1999, pp. 671-676.

HOSOKAWA, S., MORIYAMA, S., TOMIYAMA, A., TAKADA, N., *PIV Measurement of pressure distributions about single bubbles*, Journal of Nuclear Science and Technology (2003) **40**, pp. 754-762.

JAKOBSEN, M.L., DEWHIRST, T.P, GREATED, C.A., *Particle image velocimetry predictions of acceleration force within fluid flows*, Measurement Science and Technology (1997) **8**, pp. 1502–1516.

LUO, S.C., YAZDANI, MD.G., CHEW, Y.T., LEE, T.S., *Effects of incidence and afterbody shape on flow past bluff cylinders*, Journal of Wind Engineering and Industrial Aerodynamics (1994) **53**, pp. 375-399.

MATSUMOTO, M., ISHIZAKI, H., MATSUOKA, C., DAITO, Y., ICHIKAWA, Y., SHIMAHARA, A., *Aerodynamic effects of the angle of attack on a rectangular prism,* Journal of Wind Engineering and Industrial Aerodynamics (1998) **77&78**, pp. 531-542.

NOACK, B.R., AFANASIEV, K., MORZYNSKI, M., TADMOR, G., THIELE, F., *A hierarchy of low-dimensional models for the transient and post-transient cylinder wake*, Journal of Fluid Mechanics (2003) **497**, pp. 335-363.

NOCA, F., SHIELS, D., JEON, D., *A comparison of methods for evaluating time-dependent fluid dynamic forces on bodies, using only velocity fields and their derivatives*, Journal of Fluids and Structures (1999) **13**, pp. 551-578.

NORBERG, C., *Fluctuating lift on a cylinder: review and new measurements*, Journal of Fluids and Structures (2003) **17**, pp. 57-96.

OKAJIMA, A., *Strouhal numbers of rectangular cylinders*, Journal of Fluid Mechanics (1982) **123**, pp. 379-398.

PARKINSON, G.V., *Aeroelastic galloping in one degree of freedom*, First International Conference on Wind Effects on Buildings and Structures, Teddington, England, 26-28 June 1963.

RAFFEL, M., WILLERT, C., KOMPENHANS, J., *Particle Image Velocimetry: a practical guide*, Springer-Verlag, Heidelberg, 1998.

REYNOLDS, W.C., HUSSAIN, A.K.M.F., *The mechanics of an organized wave in turbulent shear flow. Part 3. Theoretical models and comparisons with experiments*, Journal of Fluid Mechanics (1972) **54**, part 2, pp. 263-288.

ROBERTSON, I., LI, L., SHERWIN, S.J., BEARMAN, P.W., *A numerical study of rotational and transverse galloping rectangular bodies*, Journal of Fluids and Structures (2003) **17**, pp. 681-699.

ROOSENBOOM, E.W.M., *AR-WIDIM 9.1 Configuration-File Editor Manual*, Aerodynamics Department, Faculty of Aerospace Engineering, Delft University of Technology, April 2005, unpublished.

RUAN, X., SONG, X., YAMAMOTO, F., *Direct measurement of the vorticity field in digital particle images*, Experiments in Fluids (2001) **30**, pp. 696-704.

SCARANO, F., RIETHMULLER, M.L., *Iterative multigrid approach in PIV image processing with discrete window offset*, Experiments in Fluids (1999) **26**, pp. 513-523.

SCARANO, F., *Iterative image deformation methods in PIV, Review article*, Measurement Science and Technology (2002) **13**, pp. R1- R19.

SHIMIDA, K., ISHIHARA, T., *Application of a modified k-ε model to the prediction of aerodynamic characteristics of rectangular cross-section cylinders*, Journal of Fluids and Structures (2002) **16**(4), pp. 465-485.

TAN, B.T., THOMPSON, M.C., HOURIGAN, K., *Evaluating fluid forces on bluff bodies using partial velocity data*, Journal of Fluids and Structures (2005) **5**, pp. 5-24.

UNAL, M.F., LIN, J.-C., ROCKWELL, D., *Force prediction by PIV imaging: a momentum-based approach (Special brief note)*, Journal of Fluids and Structures (1997) **11**, pp. 965-971.

VAN HINSBERG, N.P., *The visualisation of the unsteady separated wake flow around bluff-body cylinders (with rectangular cross-section) by means of Particle Image Velocimetry and Proper Orthogonal Decomposition*, Master Thesis, Delft University of Technology, August 2004.

VAN KAN, J., SEGAL, A., *Numerieke methoden voor partiële differentiaalvergelijkingen (Numerical methods for partial differential equations)*, Delftse Uitgevers Maatschappij, 1e druk, 1993 (in Dutch).

VAN OUDHEUSDEN, B.W., *Development of an Aeroelastic oscillator: Design and Initial Results of an Experimental Set-up; Report LR-746*, Delft University, Faculty of Aerospace Engineering, 1993.

VAN OUDHEUSDEN, B.W., *Investigation of Large-Amplitude 1-DOF Rotational Galloping; Report LR-794*, Delft University, Faculty of Aerospace Engineering, 1995.

VAN OUDHEUSDEN, B.W., *Aerodynamic Stiffness and Damping Effects in the Rotational Galloping of a Rectangular Cross-Section*, Journal of Fluids and Structures (2000) **14**, pp. 1119-1144.

WERNET, M.P., *Fuzzy logic enhanced digital PIV processing software*, 18th International Congress on Instrumentation in Aerospace Simulation Facilities (ICIASF), Toulouse, France, 14-17 June 1999.

WHITE, F.M., *Viscous Fluid Flow*, Mc-Graw-Hill, Inc., 2nd edition 1991.

WILLIAMSON, C.H.K., GOVARDHAN, R., *Vortex-induced vibrations*, Annual Review of Fluid Mechanics (2004) **36**, pp. 413-455.

YOSHIOKA, S., OBI, S., MASUDA, S., *Momentum transfer in the periodically perturbed turbulent separated flow over the backward-facing step*, Proceedings of the 1st in-

ternational symposium on turbulence and shear flow, Santa Barbara, USA, 12-15 September 1999, pp. 132-1326.

ZDRAVKOVICH, M.M., *Flow around circular cylinders Vol. 1: Fundamentals*, Oxford University Press, New York, 1997.

Appendix

A

Derivation of classical (vertical) galloping criteria

In order to predict galloping and its related properties, the commonly used theory is the quasi-steady theory. The two basic assumptions in the quasi-steady theory are that the dynamic effect of the oscillating motion can be approximated as if it was rectilinear and that there is an aerodynamic equivalent steady situation for each phase in the unsteady motion. The first assumption implies that any inertial or history effect is neglected and that only time-mean forces act on the structure, due to large separation between oscillation and vortex shedding frequencies. The second assumption implies that measurements on a static structure will be equivalent with an oscillating structure in a corresponding position.

Two forms of galloping exist, translational and rotational galloping. Translational galloping is a pure 1-DOF vibration, dominated by damping effects. The modelling of rotational galloping poses the additional aspect that both stiffness and damping effects are present. For translational galloping first order stiffness effects are absent and the modelling is simplified. The galloping curves (i.e. steady amplitudes as a function of wind speed) of translational and rotational galloping differ from each other in that for rotational galloping the limit-cycle amplitude tends to a constant value, whereas for translational galloping a linear asymptote is reached.

A.1 Equation of motion for 1-DOF model

To provide insight in the dynamics behind galloping and its aerodynamic properties the stability criterion for a stable oscillation will be considered only for the translational galloping case. One degree of freedom galloping of a cylinder with a square cross-section can be described with a damped mass-spring system as presented in figure A-1. The cylinder has a side length *D* and a mass *m*. The connected spring has a stiffness *k* and the damper a damping *c*. The definition of positive directions and the relation between velocities is depicted in the inset of this figure. Note that the plunge direction is defined positive downwards, as is common practice in flutter analysis. The following derivation is similar to the derivation from Blevins (1990).

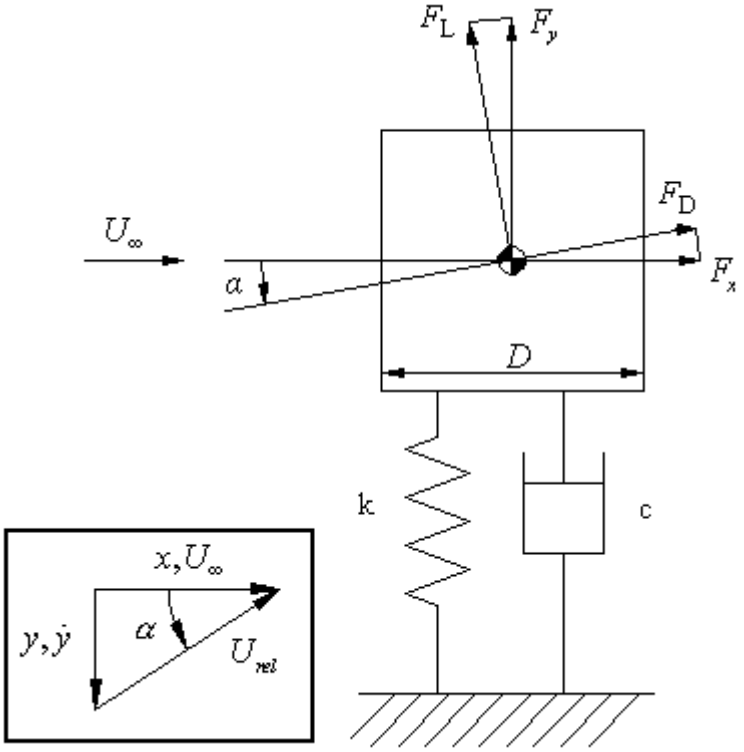

Figure A-1: One-degree of freedom damped mass-spring system to describe plunge galloping, inset shows positive directions and velocity relations

The equation of motion of this one degree of freedom system is given by:

$$m\ddot{y} + c\dot{y} + ky = F_y \tag{A.1}$$

Using conventional notation the damping can be written as $c = 2m\zeta_0\omega_0$, the stiffness as $k = m\omega_0^2$, where ζ_0 is the structural damping of the system and ω_0 the natural frequency of the system, and the force in (downward) *y*-direction as $F_y = \frac{1}{2}\rho U_\infty^2 D C_y$, where ρ is the density and C_y the vertical force coefficient.

From figure A-1 a relation can be derived for the vertical force:

$$F_y = -F_L \cos\alpha - F_D \sin\alpha \left(= \tfrac{1}{2}\rho U_\infty^2 D C_y \right) \tag{A.2}$$

where the lift force F_L and drag force F_D are defined as:

$$\begin{aligned} F_L &= \tfrac{1}{2}\rho U_{rel}^2 D c_L \\ F_D &= \tfrac{1}{2}\rho U_{rel}^2 D c_D \end{aligned} \tag{A.3}$$

Using Pythagoras to constitute a relation for the relative velocity gives:

$$U_{rel}^2 = \dot{y}^2 + U_\infty^2 \tag{A.4}$$

The angle of incidence can be formulated as:

$$\alpha = \arctan\left(\frac{\dot{y}}{U_\infty} \right) \tag{A.5}$$

Upon substitution of equation (A.3) and (A.4) into equation (A.2) the following formula for the vertical force component is obtained:

$$C_y = -\frac{U_{rel}^2}{U_\infty^2}\left(c_L \cos\alpha + c_D \sin\alpha \right) \tag{A.6}$$

A.2 Linearised simplifications

For small angles of incidence of incidence and neglecting any high powers of α, the formula for the angle of incidence can be simplified to:

$$\alpha \approx \frac{\dot{y}}{U_\infty} \tag{A.7}$$

This relation can be substituted into the relation for the relative velocity:

$$U_{rel} = \sqrt{U_\infty^2 + \dot{y}^2} \approx U_\infty \sqrt{1 + \alpha^2} \tag{A.8}$$

Expanding the obtained relation in a power series yields (again neglecting high order powers of α):

$$U_{rel} \approx U_\infty \tag{A.9}$$

The relation of the relative velocity can be used to simplify the vertical force

component, and also making use of $\cos\alpha \approx 1$ and $\sin\alpha \approx \alpha$:

$$C_y \approx -\left(c_L + c_D\alpha\right) \tag{A.10}$$

Note that at $\alpha = 0$, $C_y(0) = -c_L\big|_{\alpha=0}$.

The derivative of the vertical force component with respect to α is also useful:

$$\frac{\partial C_y}{\partial \alpha} = -\left(\frac{\partial c_L}{\partial \alpha} + c_D\right) \quad (\textit{for small } \alpha) \tag{A.11}$$

A power series of the vertical force component can be derived as:

$$C_y(\alpha) \approx C_y\big|_{\alpha=0} + \left.\frac{\partial C_y}{\partial \alpha}\right|_{\alpha=0} \alpha \tag{A.12}$$

Substituting the previously defined relations into the power series representation yields:

$$C_y = -c_L\big|_{\alpha=0} - \left.\frac{\partial C_y}{\partial \alpha}\right|_{\alpha=0} \frac{\dot{y}}{U_\infty} = -c_L\big|_{\alpha=0} - \left(\left.\frac{\partial c_L}{\partial \alpha}\right|_{\alpha=0} + c_D\right)\frac{\dot{y}}{U_\infty} \tag{A.13}$$

A.3 Galloping criteria

All these definitions can be substituted into the equation of motion, equation (A.1). The equation of motion is then a linearised equation that describes the stability of the system to small perturbations from an initial position:

$$m\ddot{y} + 2m\omega_0\left(\zeta_0 - \frac{\rho U_\infty D}{4m\omega_0}\left.\frac{\partial C_y}{\partial \alpha}\right|_{\alpha=0}\right)\dot{y} + m\omega_0^2 y = -\tfrac{1}{2}\rho U_\infty^2 D\, c_L\big|_{\alpha=0} \tag{A.14}$$

The terms between brackets can be interpreted as the net damping, ζ_T, of the plunge motion:

$$\zeta_T = \zeta_0 - \frac{\rho U_\infty D}{4m\omega_0}\left.\frac{\partial C_y}{\partial \alpha}\right|_{\alpha=0} \tag{A.15}$$

This net damping is the sum of the structural and aerodynamic damping.

The solution of the simplified equation of motion, equation (A.14), is given by:

$$y = \frac{\tfrac{1}{2}\rho U_\infty^2 D\, c_L\big|_{\alpha=0}}{m\omega_0^2} + A_y \mathrm{e}^{-\zeta_T\omega_0 t}\sin\left(\omega_0\sqrt{1-\zeta_T^2}\,t + \phi\right) \tag{A.16}$$

where A_y is an integration constant, t the time and ϕ the phase angle.

The expression for the vertical displacement, equation (A.14), can be used to address the stability of the damped mass-spring system in figure A-1. The displacement of the vibration is stable when the exponential term in equation (A.14) decreases with time. This implies that the net damping should be larger than 0, $\zeta_T > 0$, or in terms of the vertical force component:

$$\left.\frac{\partial C_y}{\partial \alpha}\right|_{\alpha=0} < \frac{4m\omega_0\zeta_0}{\rho U_\infty D} \quad (stable) \tag{A.17}$$

All terms on the right hand side of this strict inequality are positive and can be regarded as the structural damping component. It states that for a stable vibration the aerodynamic damping should be smaller than the structural component. The inequality is inversely dependent on the free stream velocity. For small velocities, the structural component is relatively large and galloping cannot occur, however when the velocity is increased, the ratio of the structural and aerodynamic component becomes smaller and galloping may occur.

The inequality for stable vibration can also be expressed in terms of the lift and drag coefficient, using equation (A.11) and neglecting the structural component. Den Hartog first derived this inequality in the 1950's.

$$\left.\frac{\partial c_L}{\partial \alpha}\right|_{\alpha=0} + c_D > 0 \quad (stable) \tag{A.18}$$

An important feature related to galloping is that when the stability criterion is *not* fulfilled negative aerodynamic damping can occur, e.g. the net damping will be smaller than zero, $\zeta_T < 0$. From the above expression, it can be seen that, since C_D is always positive, a necessary requirement for galloping is the occurrence of a negative lift slope, $\partial c_L / \partial \alpha < 0$. This illustrates why galloping cannot occur on streamlined bodies with attached flow (wings for example), but only when flow separation occurs.

Appendix

B

Optical properties of the Full Perspex and the hollow cylinder

Two types of models were utilized during the experiments. The first is a full Perspex model, the second a hollow model. The advantage of the second model is that shadow regions are reduced when the model is illuminated with a laser sheet. The next sections will explain this effect.

B.1 Full Perspex cylinder

Figure B-1 shows a sketch of the full Perspex cylinder, the original model used in the galloping experiments, illuminated with a straight bundle of light. The light enters the topside of the model at a light incidence angle of 15°. The light incidence angle, θ, is defined as the angle between the normal of a surface and the light rays. Consequently, the light hits the left side of the model at an angle of 75°. In the following it will be assumed that dispersion is negligible and that it therefore may be assumed that the refractive index, n, of Perspex is equal to 1.5. This assumption is only made to simplify the qualitative view of the light passing through the model. Indeed, at the wavelength of the laser light, 532 *nm*, (green light) the refractive index of Perspex is slightly more then the literature value of 1.5 at standard conditions (white light with a wave length of 538 *nm* and a temperature of 25 °C).

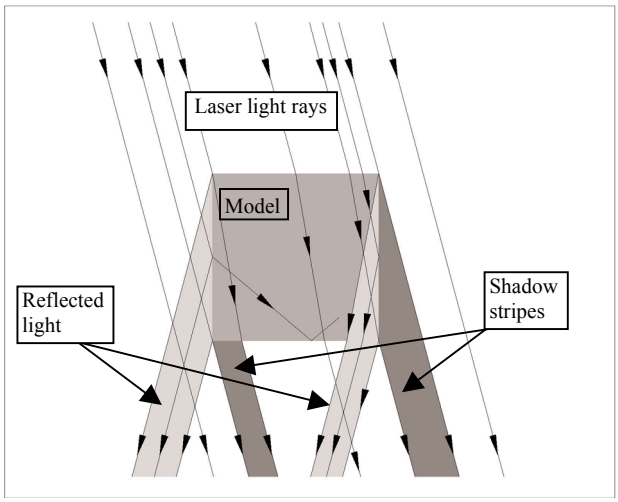

Figure B-1: Sketch of light passing through full Perspex cylinder

There are two shades of grey to indicate the behaviour of the light travelling through this model. The lightest shade is used to indicate reflected light; the darkest shade represents a shadow region. The middle shade of grey represents the full Perspex cylinder. Three typical features can be identified when light passes the model.

The first feature is light hitting the left side of the model. As mentioned, the light hits this surface at an angle of 75°. Since the light travels from a low-density area (air, n_{air} = 1.0) to a high-density area (Perspex) light is not only refracted but also reflected. The reflected light leaves the left side at the same angle as it hit the surface. The refracted light travels inside the model with a different angle. The refraction angle can be calculated with Snell's law:

$$n_1 \sin\theta_1 = n_2 \sin\theta_2 \tag{B.19}$$

where n the refractive index of the particular material, θ the light incidence angle and indices refer to the regions in front and behind the contact surface. It follows that the refracted angle for light travelling through the left side of the model is 40.1°. This light will impinge on the bottom surface of the full Perspex cylinder at an angle of (90° - 40.1° =) 49.9°. It will not pass through this surface because this angle is higher than the critical angle. The light will be totally internal reflected.

The second feature is identified as light passing through the upper surface and the bottom surface. These light rays are subjected to Snell's refraction law and it can be calculated that the angle of these light rays inside the model is equal to 9.9°. The shaded region in the lower left corner can now be explained. Light will pass unaltered just left from the lower left corner of the model. Light impinging on the left side of the model is reflected and light impinging on the upper surface is refracted. This leaves an area in the lower left corner where no light passes. This area will result in a dark stripe in the acquired images.

The third feature is identified as light that passes through the upper surface and after refraction impinges on the right side of the model. These light rays impinge at an angle higher than the critical angle and, thus, will be internally reflected. This will result in a light stripe from the right side of the model and in a shaded area.

B.2 Hollow cylinder

A model with thin surfaces can greatly reduce the influence of shadow stripes

emanating from the full Perspex cylinder. However, the light passing through such a hollow model is of a generally more complex nature as can be seen in figure B-2. To account for the more complex nature this figure is organized differently. On the left, one can see how the light would pass through the hollow cylinder. The middle shade of grey represents the hollow cylinder, light grey represents reflected light and the three dark grey areas at the bottom the (reduced) shadow stripes. Again light will have a light incidence angle of 15°, with respect to the upper surface.

The sketch on the left is composed out of the seven numbered possibilities on the right in figure B-2. The first three possibilities show how light will refract and reflect when it hits the left surface (with an angle of 75°). Light will reflect from the full left surface. Light refracted above the lower left corner of the model will pass (refracted) through the bottom surface. The part of light that is refracted in the lower left corner will be reflecting of the bottom surface. The third and fourth possibility show how light is internally reflected inside the vertical surfaces. A small part of light will travel in the same direction as the original illumination source. The other part of light will travel in a mirrored direction. Light that enters the upper surface of the model and, after refraction, just passes through the bottom surface is shown as the sixth possibility. The remaining part of light that travels through the upper surface and after refraction hits the right surface of the model is partially reflected and refracted. All these possibilities together identify the light travelling through the hollow cylinder as shown in the left part of figure B-2.

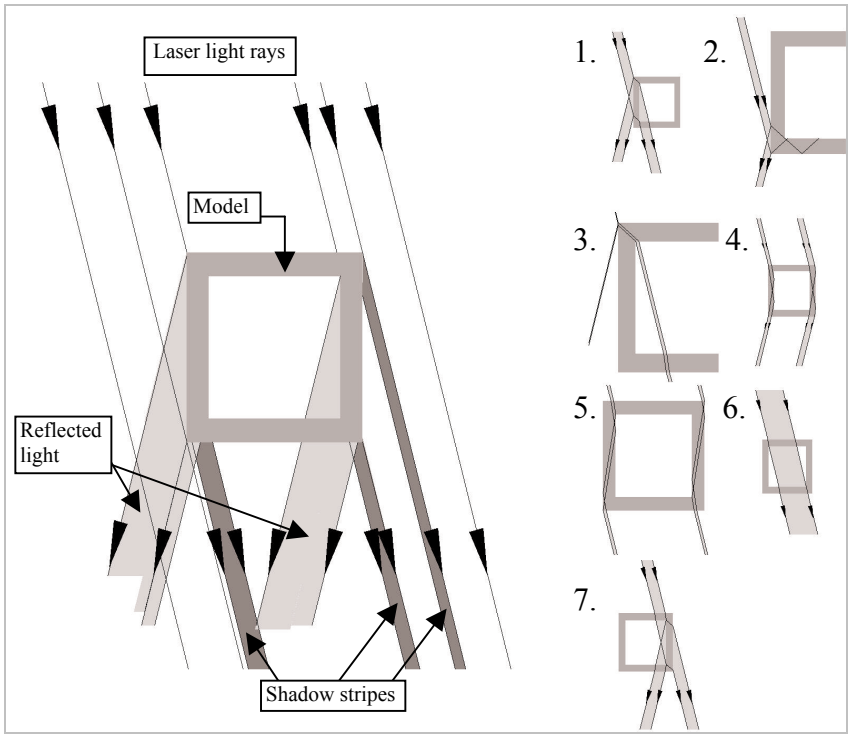

Figure B-2: Sketch of light passing through hollow cylinder

B.3 Comparison of both models

To show this effect of the reduced shadow stripes of the hollow model directly, the two models were both placed in the same flow. A cropped snapshot is given figure B-3a. An inverted image is displayed in figure A-3b. The hollow cylinder (in the lower left corner of the images) is clamped between the endplates; the full Perspex model was positioned by hand. As can be seen, the seeding was of low quality. This was due to the fact that a manual seeding apparatus was used. Both pictures were enhanced by manipulating with several options to improve the quality of the images. Since the two models are in a comparable situation, the significance of the shadow stripes can be seen. However, due to the poor quality of the images this distinction is not so obvious to see.

In these pictures the illumination comes from the bottom left corner and the flow is from right to the left. Distinct black stripes emanate from the hollow cylinder, white stripes in the right image. In the area between these stripes the seeding has the same level as just outside the stripes. Correlation is therefore possible in this area without any complication. From the corners of the full Perspex model (in the upper right corner of the images) grey shadow regions emanate. The seeding is not as visible as with the hollow model. The reason that this area is not fully dark is because background light entered the test section. The background light was minimized during the measurements. Because the seeding is not clearly visible in the shadow area of the full Perspex model it is difficult to obtain a reasonable correlation during the post-processing. It can be concluded that the hollow cylinder gives better optical properties that do not compromise the cross-correlation.

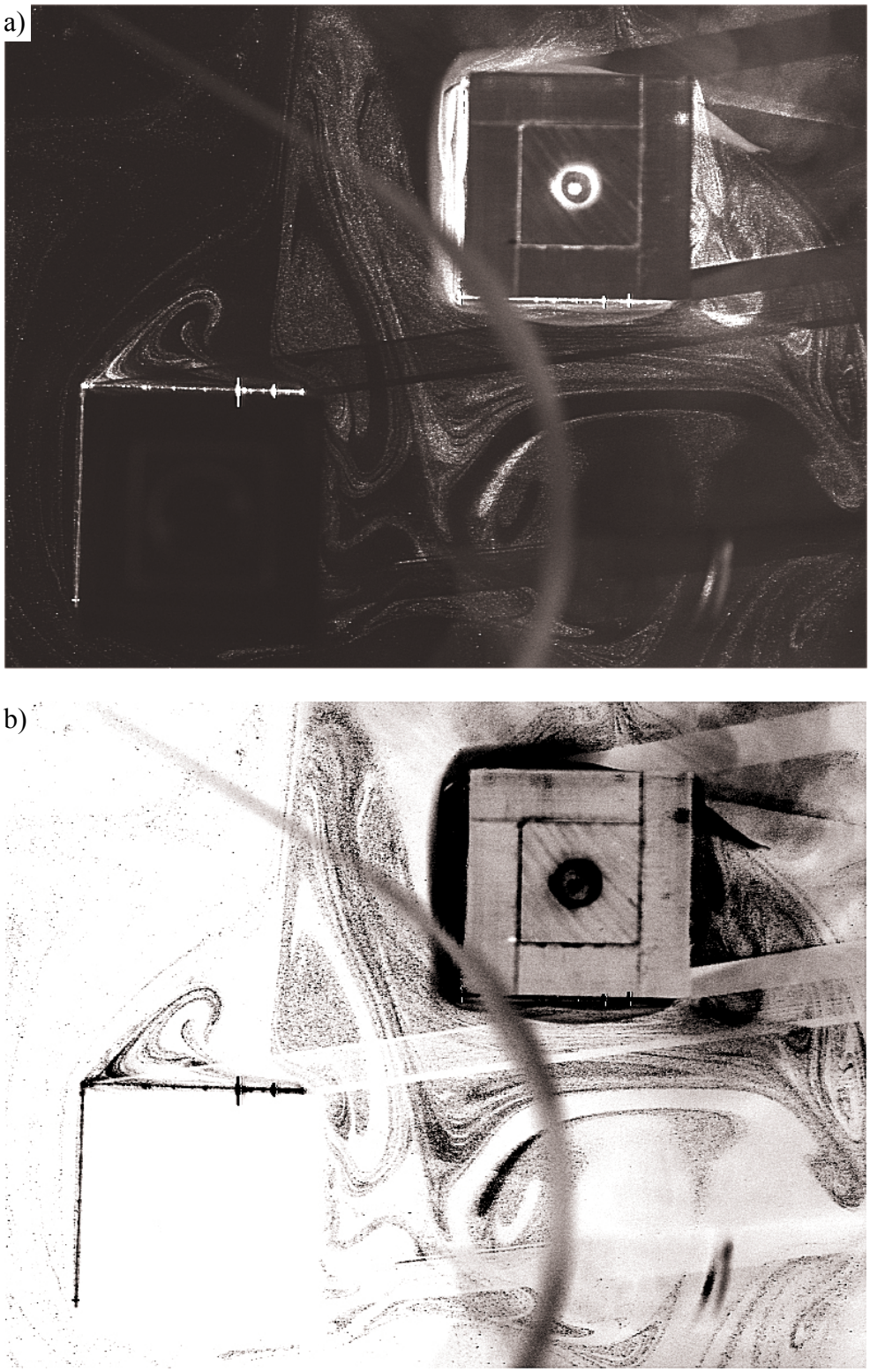

Figure B-3: Direct comparison of full Perspex and hollow cylinder; a) enhanced snapshot image, b) enhanced inverted snapshot image

Appendix

C

Validation of pressure calculation

In this appendix the derivation of the pressure gradient field will be given. The pressure gradient field is derived from the 2D Navier-Stokes equations. In order to be able to validate this derivation the pressure gradient based on the (non-lifting) potential flow around a circular cylinder is given. Starting with the full pressure field of this potential flow the pressure gradient field can be determined from the Bernoulli equation. The pressure gradient field is then integrated with the Conjugated Gradient Method to yield the pressure field. Finally, the integration is compared with the original pressure field as obtained with the Bernoulli equation.

C.1 Derivation of pressure (gradient) equations

The method used to determine the pressure gradient field from the PIV measure-

ments is a Reynolds averaging of the Navier-Stoke equations. In order to validate this method the pressure gradient field is also derived from the Bernoulli equation, which is essentially a simplification of the Navier-Stokes equation.

C.1.1 Pressure gradient field from Reynolds averaged Navier-Stokes-equations

The derivation will start with the 2D Navier-Stokes equations, the x- and y-momentum equations; see equation (C.1). These equations can be found in almost any textbook on aerodynamics, see for example White [1991].

$$\begin{cases} \dfrac{\partial u}{\partial t}+u\dfrac{\partial u}{\partial x}+v\dfrac{\partial u}{\partial y}=-\dfrac{1}{\rho}\dfrac{\partial p}{\partial x}+\nu\left[\dfrac{\partial^2 u}{\partial x^2}+\dfrac{\partial^2 u}{\partial y^2}\right] \\ \dfrac{\partial v}{\partial t}+u\dfrac{\partial v}{\partial x}+v\dfrac{\partial v}{\partial y}=-\dfrac{1}{\rho}\dfrac{\partial p}{\partial y}+\nu\left[\dfrac{\partial^2 v}{\partial x^2}+\dfrac{\partial^2 v}{\partial y^2}\right] \end{cases} \tag{C.1}$$

The spatial derivatives on the left hand side of equation (C.1) can be rewritten in conservative form:

$$\begin{cases} u\dfrac{\partial u}{\partial x}+v\dfrac{\partial u}{\partial y}=\dfrac{\partial u^2}{\partial x}+\dfrac{\partial uv}{\partial y} \\ u\dfrac{\partial v}{\partial x}+v\dfrac{\partial v}{\partial y}=\dfrac{\partial v^2}{\partial y}+\dfrac{\partial uv}{\partial x} \end{cases} \tag{C.2}$$

To see that this is correct expand the terms on the right hand side of equation (C.2) and note that the parts between brackets in equation (C.3) are equal to the continuity equation:

$$\begin{cases} \dfrac{\partial u^2}{\partial x}+\dfrac{\partial uv}{\partial y}=2u\dfrac{\partial u}{\partial x}+u\dfrac{\partial v}{\partial y}+v\dfrac{\partial u}{\partial y}=u\dfrac{\partial u}{\partial x}+v\dfrac{\partial u}{\partial y}+u\underbrace{\left(\dfrac{\partial u}{\partial x}+\dfrac{\partial v}{\partial y}\right)}_{=0} \\ \dfrac{\partial v^2}{\partial y}+\dfrac{\partial uv}{\partial x}=2v\dfrac{\partial v}{\partial y}+u\dfrac{\partial v}{\partial x}+v\dfrac{\partial u}{\partial x}=u\dfrac{\partial v}{\partial x}+v\dfrac{\partial v}{\partial y}+v\underbrace{\left(\dfrac{\partial u}{\partial x}+\dfrac{\partial v}{\partial y}\right)}_{=0} \end{cases} \tag{C.3}$$

Equation (C.1) then turns into:

$$\begin{cases} \dfrac{\partial u}{\partial t}+\dfrac{\partial u^2}{\partial x}+\dfrac{\partial uv}{\partial y}=-\dfrac{1}{\rho}\dfrac{\partial p}{\partial x}+\nu\left[\dfrac{\partial^2 u}{\partial x^2}+\dfrac{\partial^2 u}{\partial y^2}\right] \\ \dfrac{\partial v}{\partial t}+\dfrac{\partial uv}{\partial x}+\dfrac{\partial v^2}{\partial y}=-\dfrac{1}{\rho}\dfrac{\partial p}{\partial y}+\nu\left[\dfrac{\partial^2 v}{\partial x^2}+\dfrac{\partial^2 v}{\partial y^2}\right] \end{cases} \tag{C.4}$$

The variables *u*, *v* and *p* are assumed to be build from a mean value, $\overline{(...)}$, and a fluctuating part, $(...)'$, the so-called Reynolds notation (see Reynolds [1972]):

$$\begin{cases} u = \overline{u} + u' \\ v = \overline{v} + v' \\ p = \overline{p} + p' \end{cases} \tag{C.5}$$

The following properties of the Reynolds notation can be used: $\overline{f+g} = \overline{f} + \overline{g}$, $\overline{\overline{f}} = \overline{f}$ and $\overline{f'} = 0$. The previous properties imply the following statement: $\overline{\overline{f} + f'} = \overline{\overline{f}} + \overline{f'} = \overline{f}$.

Equation (C.4) can now be averaged:

$$\begin{cases} \overline{\dfrac{\partial u}{\partial t} + \dfrac{\partial u^2}{\partial x} + \dfrac{\partial uv}{\partial y}} = \overline{-\dfrac{1}{\rho}\dfrac{\partial p}{\partial x} + \nu\left[\dfrac{\partial^2 u}{\partial x^2} + \dfrac{\partial^2 u}{\partial y^2}\right]} \\ \overline{\dfrac{\partial v}{\partial t} + \dfrac{\partial uv}{\partial x} + \dfrac{\partial v^2}{\partial y}} = \overline{-\dfrac{1}{\rho}\dfrac{\partial p}{\partial y} + \nu\left[\dfrac{\partial^2 v}{\partial x^2} + \dfrac{\partial^2 v}{\partial y^2}\right]} \end{cases} \tag{C.6}$$

First the notation of equation (C.5) is inserted in equation (C.6) and one can then apply the Reynolds properties to equation (C.7):

$$\begin{cases} \dfrac{\partial \overline{\overline{u} + u'}}{\partial t} + \dfrac{\partial \overline{\left(\overline{u} + u'\right)^2}}{\partial x} + \dfrac{\partial \overline{\left(\overline{u} + u'\right)\left(\overline{v} + v'\right)}}{\partial y} = -\dfrac{1}{\rho}\dfrac{\partial \overline{\overline{p} + p'}}{\partial x} + \nu\left[\dfrac{\partial^2 \overline{\overline{u} + u'}}{\partial x^2} + \dfrac{\partial^2 \overline{\overline{u} + u'}}{\partial y^2}\right] \\ \dfrac{\partial \overline{\overline{v} + v'}}{\partial t} + \dfrac{\partial \overline{\left(\overline{u} + u'\right)\left(\overline{v} + v'\right)}}{\partial x} + \dfrac{\partial \overline{\left(\overline{v} + v'\right)^2}}{\partial y} = -\dfrac{1}{\rho}\dfrac{\partial \overline{\overline{p} + p'}}{\partial y} + \nu\left[\dfrac{\partial^2 \overline{\overline{v} + v'}}{\partial x^2} + \dfrac{\partial^2 \overline{\overline{v} + v'}}{\partial y^2}\right] \end{cases} \tag{C.7}$$

The temporal derivatives of *u* and *v* vanish completely, because the first statement in equation (C.8) implies that the mean value does not vary in time and the second statement follows from the Reynolds properties:

$$\frac{\partial \overline{\left(\overline{u} + u'\right)}}{\partial t} = \underbrace{\frac{\partial \overline{u}}{\partial t}}_{=0} + \underbrace{\frac{\partial \overline{u'}}{\partial t}}_{=0}, \quad \frac{\partial \overline{\left(\overline{v} + v'\right)}}{\partial t} = \underbrace{\frac{\partial \overline{v}}{\partial t}}_{=0} + \underbrace{\frac{\partial \overline{v'}}{\partial t}}_{=0} \tag{C.8}$$

The expanded quadratic terms can be written as:

$$\begin{cases} \overline{\left(\overline{u}+u'\right)^2} = \overline{\left(\overline{u}^2 + 2\overline{u}u' + u'^2\right)} = \overline{u}^2 + 2\overline{u}\underbrace{\overline{u'}}_{=0} + \overline{u'^2} \\ \overline{\left(\overline{v}+v'\right)^2} = \overline{\left(\overline{v}^2 + 2\overline{v}v' + v'^2\right)} = \overline{v}^2 + 2\overline{v}\underbrace{\overline{v'}}_{=0} + \overline{v'^2} \end{cases} \tag{C.9}$$

The cross product of the *u* and *v* velocity can be turned into the following equation (note the appearance of the Reynolds stress term $\overline{u'v'}$):

$$\overline{\left(\overline{u}+u'\right)\left(\overline{v}+v'\right)} = \overline{u}\,\overline{v} + \overline{u}\underbrace{\overline{v'}}_{=0} + \overline{v}\underbrace{\overline{u'}}_{=0} + \overline{u'v'} \tag{C.10}$$

An interesting fact of equation (C.9) and (C.10) is that the end result is the summation of the product of mean terms and fluctuating terms (e.g. products of mean and fluctuating terms are left out).

The Reynolds properties applied to the right hand side of equation (C.7) lead to a cancellation of the fluctuating terms.

Using the above observations equation (C.7) can be written as:

$$\begin{cases} \dfrac{\partial\left(\overline{u}^2 + \overline{u'^2}\right)}{\partial x} + \dfrac{\partial\left(\overline{u}\,\overline{v} + \overline{u'v'}\right)}{\partial y} = -\dfrac{1}{\rho}\dfrac{\partial \overline{p}}{\partial x} + \nu\left[\dfrac{\partial^2 \overline{u}}{\partial x^2} + \dfrac{\partial^2 \overline{u}}{\partial y^2}\right] \\ \dfrac{\partial\left(\overline{u}\,\overline{v} + \overline{u'v'}\right)}{\partial x} + \dfrac{\partial\left(\overline{v}^2 + \overline{v'^2}\right)}{\partial y} = -\dfrac{1}{\rho}\dfrac{\partial \overline{p}}{\partial y} + \nu\left[\dfrac{\partial^2 \overline{v}}{\partial x^2} + \dfrac{\partial^2 \overline{v}}{\partial y^2}\right] \end{cases} \tag{C.11}$$

Expanding all of the terms on the left hand side of equation (C.11) leads to:

$$\begin{cases} 2\overline{u}\dfrac{\partial \overline{u}}{\partial x} + \dfrac{\partial \overline{u'^2}}{\partial x} + \dfrac{\partial \overline{u}\,\overline{v}}{\partial y} + \dfrac{\partial \overline{u'v'}}{\partial y} = \overline{u}\underbrace{\left(\dfrac{\partial \overline{u}}{\partial x} + \dfrac{\partial \overline{v}}{\partial y}\right)}_{=0} + \overline{u}\dfrac{\partial \overline{u}}{\partial x} + \overline{v}\dfrac{\partial \overline{u}}{\partial y} + \dfrac{\partial \overline{u'^2}}{\partial x} + \dfrac{\partial \overline{u'v'}}{\partial y} \\ \dfrac{\partial \overline{u}\,\overline{v}}{\partial x} + \dfrac{\partial \overline{u'v'}}{\partial x} + 2\overline{v}\dfrac{\partial \overline{v}}{\partial y} + \dfrac{\partial \overline{v'^2}}{\partial y} = \overline{v}\underbrace{\left(\dfrac{\partial \overline{u}}{\partial x} + \dfrac{\partial \overline{v}}{\partial y}\right)}_{=0} + \overline{u}\dfrac{\partial \overline{v}}{\partial x} + \overline{v}\dfrac{\partial \overline{v}}{\partial y} + \dfrac{\partial \overline{v'^2}}{\partial y} + \dfrac{\partial \overline{u'v'}}{\partial x} \end{cases} \tag{C.12}$$

In equation (C.12) $\dfrac{\partial \overline{u}}{\partial x} + \dfrac{\partial \overline{v}}{\partial y} = 0$ can be regarded as an averaged continuity equation. This assumption is correct when the velocity field is on average 2D.

Substituting equation (C.12) into equation (C.11) and bringing the pressure gradient in x- and y-direction to the left hand side finally leads to the following equations:

$$\frac{\partial \overline{p}}{\partial x} = \rho\left[-\overline{u}\frac{\partial \overline{u}}{\partial x} - \overline{v}\frac{\partial \overline{u}}{\partial y} - \frac{\partial \overline{u'^2}}{\partial x} - \frac{\partial \overline{u'v'}}{\partial y} + \nu\left\{\frac{\partial^2 \overline{u}}{\partial x^2} + \frac{\partial^2 \overline{u}}{\partial y^2}\right\}\right] \tag{C.13}$$

and,

$$\frac{\partial \overline{p}}{\partial y} = \rho\left[-\overline{u}\frac{\partial \overline{v}}{\partial x} - \overline{v}\frac{\partial \overline{v}}{\partial y} - \frac{\partial \overline{v'^2}}{\partial y} - \frac{\partial \overline{u'v'}}{\partial x} + \nu\left\{\frac{\partial^2 \overline{v}}{\partial x^2} + \frac{\partial^2 \overline{v}}{\partial y^2}\right\}\right] \tag{C.14}$$

Equation (C.13) and equation (C.14) represent the averaged pressure gradient in respectively the x- and y-direction.

All the terms on the right hand side of equation (C.13) and equation (C.14) are directly available, or can be derived, from PIV measurements. The averaged pressure gradient field allows for a reconstruction of the pressure field around any object submerged in a flow because the functions for the pressure gradient field are directly derived from the Navier-Stokes equations. Therefore, the derived functions for the pressure gradient field are also valid in an irrotational flow.

C.1.2 Pressure gradient field determined with Bernoulli equation

The pressure field of an inviscid, incompressible and irrotational flow can directly be obtained from the Bernoulli equation:

$$p = p_\infty + \tfrac{1}{2}\rho\left(U_\infty^2 - \left(u^2 + v^2\right)\right) \tag{C.15}$$

The pressure gradient field is obtained by differentiating equation (C.15) with respect to x and y:

$$\frac{\partial p}{\partial x} = -\rho u\frac{\partial u}{\partial x} - \rho v\frac{\partial v}{\partial x} \tag{C.16}$$

$$\frac{\partial p}{\partial y} = -\rho u\frac{\partial u}{\partial y} - \rho v\frac{\partial v}{\partial y} \tag{C.17}$$

C.1.3 Pressure field with unsteady Bernoulli equation

The Navier-Stokes equation with constant ρ and μ, and neglecting gravitational body forces is:

$$\rho\frac{\partial \vec{V}}{\partial t} + \rho\left(\vec{V}\cdot\nabla\right)\vec{V} = -\nabla p + \mu\nabla^2\vec{V} \tag{C.18}$$

Two vector identities can be used to rewrite the Navier-Stokes:

$$\nabla \times (\nabla \times \vec{V}) = \nabla (\nabla \cdot \vec{V}) - \nabla^2 \vec{V} \tag{C.19}$$

and

$$(\vec{V} \cdot \nabla)\vec{V} = \nabla \left(\tfrac{1}{2} \vec{V}^2 \right) - \vec{V} \times (\nabla \times \vec{V}) \tag{C.20}$$

Firstly, the two vector identities can be simplified by assuming an incompressible flow, $\nabla \cdot \vec{V} = 0$, and by introducing the vorticity vector, $\vec{\xi} = \nabla \times \vec{V}$, yielding:

$$\nabla^2 \vec{V} = \nabla \times \vec{\xi} \tag{C.21}$$

and

$$(\vec{V} \cdot \nabla)\vec{V} = \nabla \left(\tfrac{1}{2} \vec{V}^2 \right) - \vec{V} \times \vec{\xi} \tag{C.22}$$

These simplifications substituted into the Navier-Stokes equation leads to the following:

$$\rho \frac{\partial \vec{V}}{\partial t} + \nabla \left(p + \tfrac{1}{2} \vec{V}^2 \right) = \rho \vec{V} \times \vec{\xi} - \mu \nabla \times \vec{\xi} \tag{C.23}$$

To illuminate the contribution of the shear layers equation (C.23) can be Reynolds-averaged. To show the extent of the shear-layer contribution also zero vorticity is assumed. Equation (C.23) is then *only* valid outside the wake region. This will lead to the following relation for the pressure:

$$\overline{p} + \tfrac{1}{2} \rho \left(\overline{u}^2 + \overline{v}^2 + \overline{u'^2} + \overline{v'^2} \right) = p_\infty + \tfrac{1}{2} \rho U_\infty^2 \tag{C.24}$$

C.1.4 Pressure Poisson Equation (PPE)

Starting from the Navier-Stokes equation, equation (C.18), yet another pressure equation can be obtained by taking its divergence:

$$\nabla \cdot \left(\rho \frac{\partial \vec{V}}{\partial t} \right) + \nabla \cdot \left(\rho (\vec{V} \cdot \nabla)\vec{V} \right) = \nabla \cdot (-\nabla p) + \nabla \cdot \left(\mu \nabla^2 \vec{V} \right) \tag{C.25}$$

This equation can be simplified by remarking that:

$$\nabla \cdot \left(\rho \frac{\partial \vec{V}}{\partial t} \right) = \rho \frac{\partial}{\partial t} (\nabla \cdot \vec{V}) = 0 \tag{C.26}$$

and

$$\nabla \cdot \left(\mu \nabla^2 \vec{V} \right) = \mu \nabla^2 (\nabla \cdot \vec{V}) = 0 \tag{C.27}$$

Using these simplifications the Pressure Poisson Equation is obtained:

$$\nabla^2 p = -\nabla \cdot \left(\rho (\vec{V} \cdot \nabla) \vec{V} \right) \tag{C.28}$$

Or Cartesian coordinates:

$$\nabla^2 p = -\rho \left\{ \left(\frac{\partial u}{\partial x} \right)^2 + 2 \frac{\partial u}{\partial y} \frac{\partial v}{\partial x} + \left(\frac{\partial v}{\partial y} \right)^2 \right\} \tag{C.29}$$

After Reynolds-averaging the following equation is obtained:

$$\nabla^2 \overline{p} = -\rho \left\{ \left(\frac{\partial \overline{u}}{\partial x} \right)^2 + 2 \frac{\partial \overline{u}}{\partial y} \frac{\partial \overline{v}}{\partial x} + \left(\frac{\partial \overline{v}}{\partial y} \right)^2 \right\} + \frac{\partial^2}{\partial x^2} \overline{u'^2} + 2 \frac{\partial^2}{\partial x \partial x} \overline{u'v'} + \frac{\partial^2}{\partial y^2} \overline{v'^2} \tag{C.30}$$

Equation (C.30) can be solved by a Poisson solver. However, this second order equation needs a boundary condition. The boundary condition can be provided by the pressure gradient form the Navier-Stokes equation:

$$\nabla p = -\rho \frac{\partial \vec{V}}{\partial t} + -\rho (\vec{V} \cdot \nabla) \vec{V} + \mu \nabla^2 \vec{V} \tag{C.31}$$

C.2 *Methods applied to the non-lifting potential flow around a circular cylinder*

The non-lifting potential flow around a circular cylinder can be considered as the summation of a uniform flow and a doublet (Anderson, 1991). The corresponding stream function is (usually) expressed in polar coordinates:

$$\psi = U_\infty r \sin\theta \left(1 - \frac{R^2}{r^2} \right) \tag{C.32}$$

The stream function can also be expressed in Cartesian coordinates:

$$\psi = U_\infty y \left(1 - \frac{R^2}{x^2 + y^2} \right) \tag{C.33}$$

The velocities *u* and *v* in respectively x- and y-direction for the circular potential flow are derived as follows:

$$u = \frac{\partial \psi}{\partial y} = U_\infty \left(1 + \frac{R^2 \left(y^2 - x^2 \right)}{\left(x^2 + y^2 \right)^2} \right) \tag{C.34}$$

$$v = -\frac{\partial \psi}{\partial x} = -2U_\infty \frac{R^2 xy}{\left(x^2 + y^2\right)^2} \tag{C.35}$$

The derivatives of the *u* and *v* velocities in x- and y-direction can also be found:

$$\frac{\partial u}{\partial x} = 2U_\infty R^2 x \frac{\left(x^2 - 3y^2\right)}{\left(x^2 + y^2\right)^3} \tag{C.36}$$

$$\frac{\partial u}{\partial y} = 2U_\infty R^2 y \frac{\left(3x^2 - y^2\right)}{\left(x^2 + y^2\right)^3} \tag{C.37}$$

$$\frac{\partial v}{\partial x} = 2U_\infty R^2 y \frac{\left(3x^2 - y^2\right)}{\left(x^2 + y^2\right)^3} = \frac{\partial u}{\partial y} \tag{C.38}$$

$$\frac{\partial v}{\partial y} = -2U_\infty R^2 y \frac{\left(3x^2 - y^2\right)}{\left(x^2 + y^2\right)^3} = -\frac{\partial u}{\partial x} \tag{C.39}$$

C.2.1 Pressure gradient field obtained with Reynolds averaged Navier-Stokes equations

When any fluctuations and second order effects are neglected in the non-lifting potential flow around a circular cylinder then equation (C.13) and equation (C.14) simplify to:

$$\frac{\partial p}{\partial x} = -\rho u \frac{\partial u}{\partial x} - \rho v \frac{\partial u}{\partial y} \tag{C.40}$$

$$\frac{\partial p}{\partial y} = -\rho u \frac{\partial v}{\partial x} - \rho v \frac{\partial v}{\partial y} \tag{C.41}$$

If one evaluates these equations with (the appropriate derivatives of) equation (C.34) and equation (C.35) (with respect to x and y), the pressure gradient in x- and y-direction can be found as:

$$\frac{\partial p}{\partial x} = 2\rho U_\infty^2 R^2 x \frac{3y^2 - x^2 + R^2}{\left(x^2 + y^2\right)^3} \tag{C.42}$$

$$\frac{\partial p}{\partial y} = 2\rho U_\infty^2 R^2 y \frac{y^2 - 3x^2 + R^2}{\left(x^2 + y^2\right)^3} \tag{C.43}$$

C.2.2 Pressure gradient field obtained with Bernoulli equation

Equation (C.15) fully written out returns:

$$p = p_\infty - \tfrac{1}{2}\rho U_\infty^2 R^2 \frac{R^2 + 2\left(y^2 - x^2\right)}{\left(x^2 + y^2\right)^2} \tag{C.44}$$

By differentiating equation (C.44) to respectively x and y, one obtains the pressure gradient in x- and y-direction as:

$$\frac{\partial p}{\partial x} = 2\rho U_\infty^2 R^2 x \frac{3y^2 - x^2 + R^2}{\left(x^2 + y^2\right)^3} \tag{C.45}$$

$$\frac{\partial p}{\partial y} = 2\rho U_\infty^2 R^2 y \frac{y^2 - 3x^2 + R^2}{\left(x^2 + y^2\right)^3} \tag{C.46}$$

First note the interesting fact that equation (C.42) is similar to equation (C.45) and that equation (C.43) is similar to (C.46). This could be expected because the assumptions in deriving equation (C.42) and equation (C.43) are the same as in the derivation of the Bernoulli equation. Also note that one could first differentiate equation (C.34) and equation (C.35) to x and y and then enter the results in equation (C.16) and equation (C.17) to obtain the same results.

C.3 Comparison of pressure fields

The pressure gradient field for the first method, 'Pressure gradient field obtained with Reynolds averaged Navier-Stokes equations', is calculated with equation (C.13) and equation (C.14). The gradient is determined with the MATLAB-function `GRADIENT` and the fluctuating terms (denoted by primes) and the viscous part (between curly brackets) are both neglected in the present pressure field determination. The pressure gradient fields for the second method, 'Pressure gradient field obtained with Bernoulli equation' are calculated with equation (C.16) and equation (C.17). All the pressure gradient fields are integrated with the Conjugated Gradient Method. The boundary condition used is an uniform pressure field and equal to zero. The resulting pressure fields are thus in fact the dynamic pressure fields. The results of the integration are presented in figure B-2. As can be seen in this figure gives the method 'Pressure gradients from Reynolds averaged Navier-Stokes-equations' satisfactory results for the application of the method to the circular potential flow.

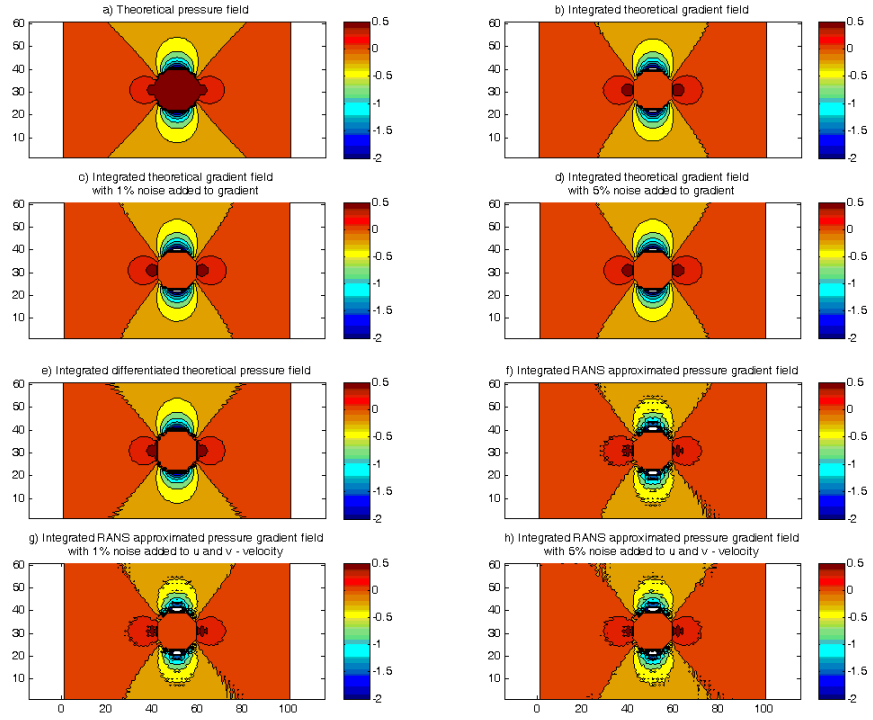

Figure C-1: Comparison of integrated pressure fields with Conjugate Gradient Method

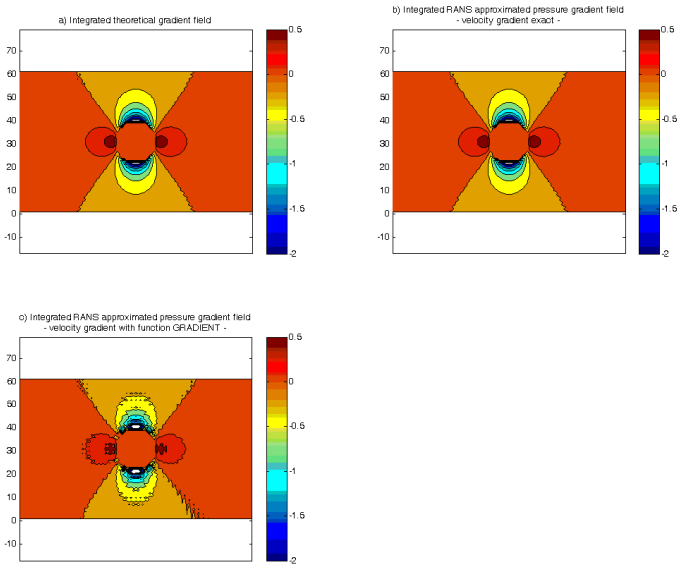

Figure C-2: Comparison of integrated pressure fields with different velocity gradient calculations

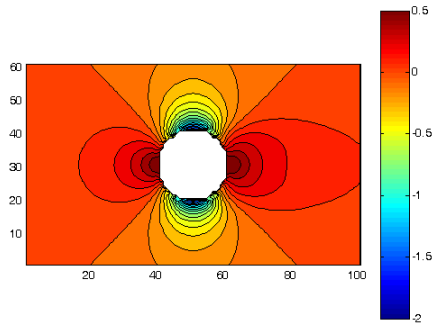

Figure C-3: Integrated pressure with 2D integration (small mask)

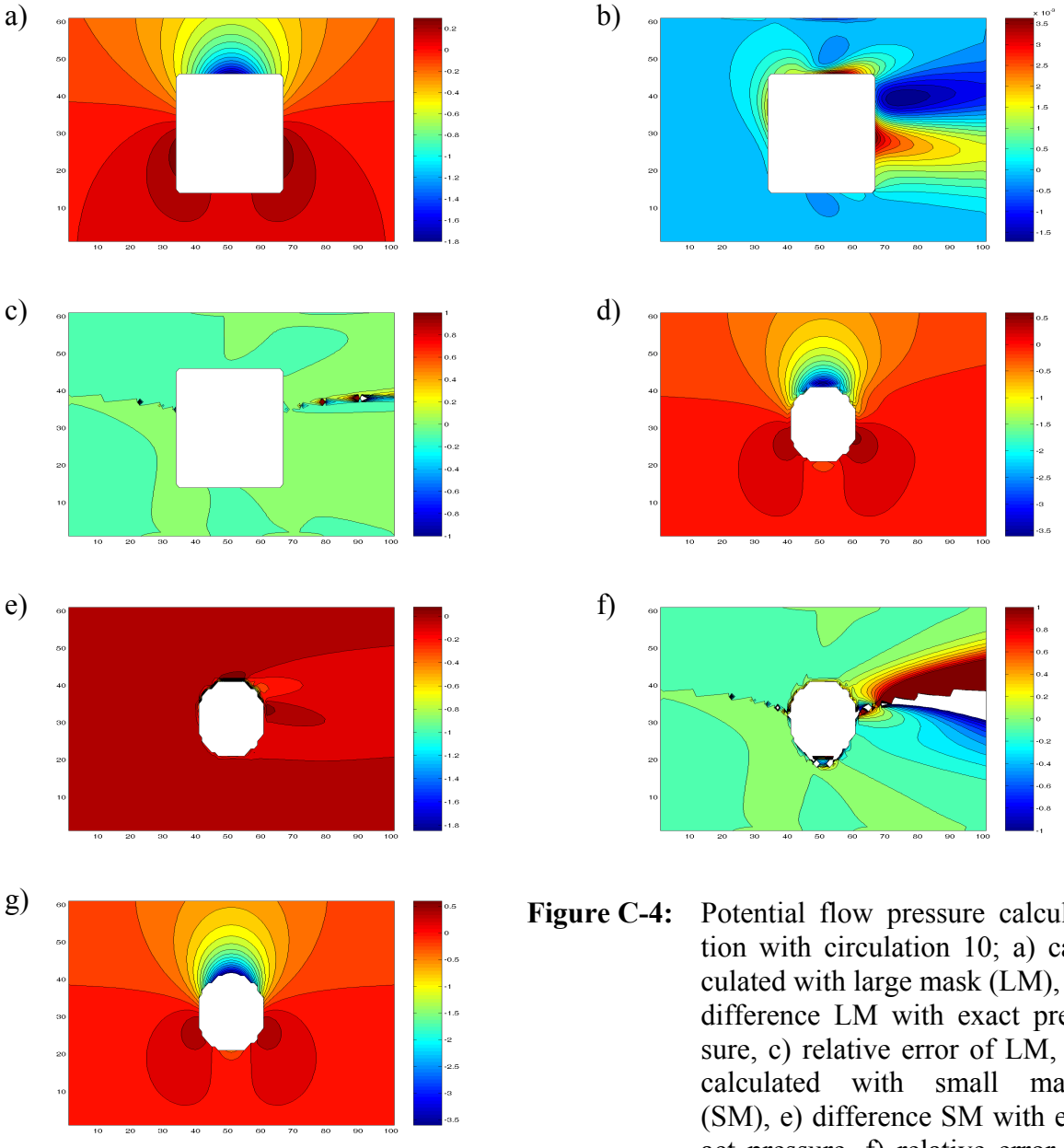

Figure C-4: Potential flow pressure calculation with circulation 10; a) calculated with large mask (LM), b) difference LM with exact pressure, c) relative error of LM, d) calculated with small mask (SM), e) difference SM with exact pressure, f) relative error of SM, g) exact pressure

Appendix

D

Compilation of Results

All the results of the three experimental campaigns are presented in this appendix. The first paragraph lists the statistical averaged results, the second paragraph images and snapshots of the Proper Orthogonal Decomposition analysis. The third paragraph contains the pressure coefficients determined with the 2D integration method. The statistical results are all made dimensionless with the free stream velocity, U_∞, of 10 *m/s*. For the first campaign, case A, the plotted statistical results are contour plots of the *U* velocity, the vorticity ξ, the velocity fluctuations *u'*, in *x*-direction, the velocity fluctuations *v'*, in *y*-direction, the Reynolds stress term, *u'v'* and the turbulence intensity. For case B and C the magnitude of the velocity is plotted instead of the *U*-velocity. The statistical results for each angle of incidence are plotted on separate pages.

D.1 Statistical results

D.1.1 Case A

Angle of incidence: 0°

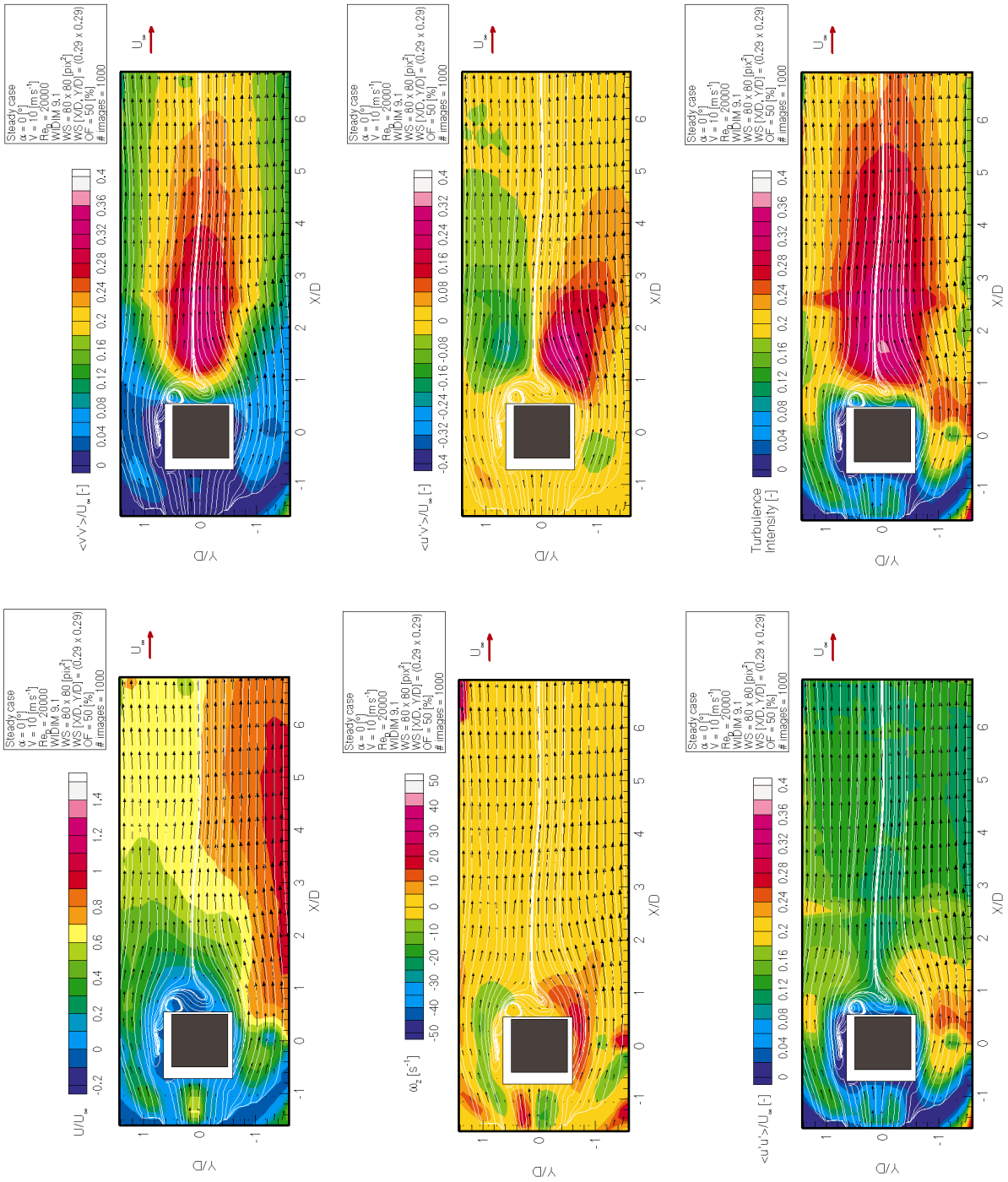

Angle of incidence: 5°

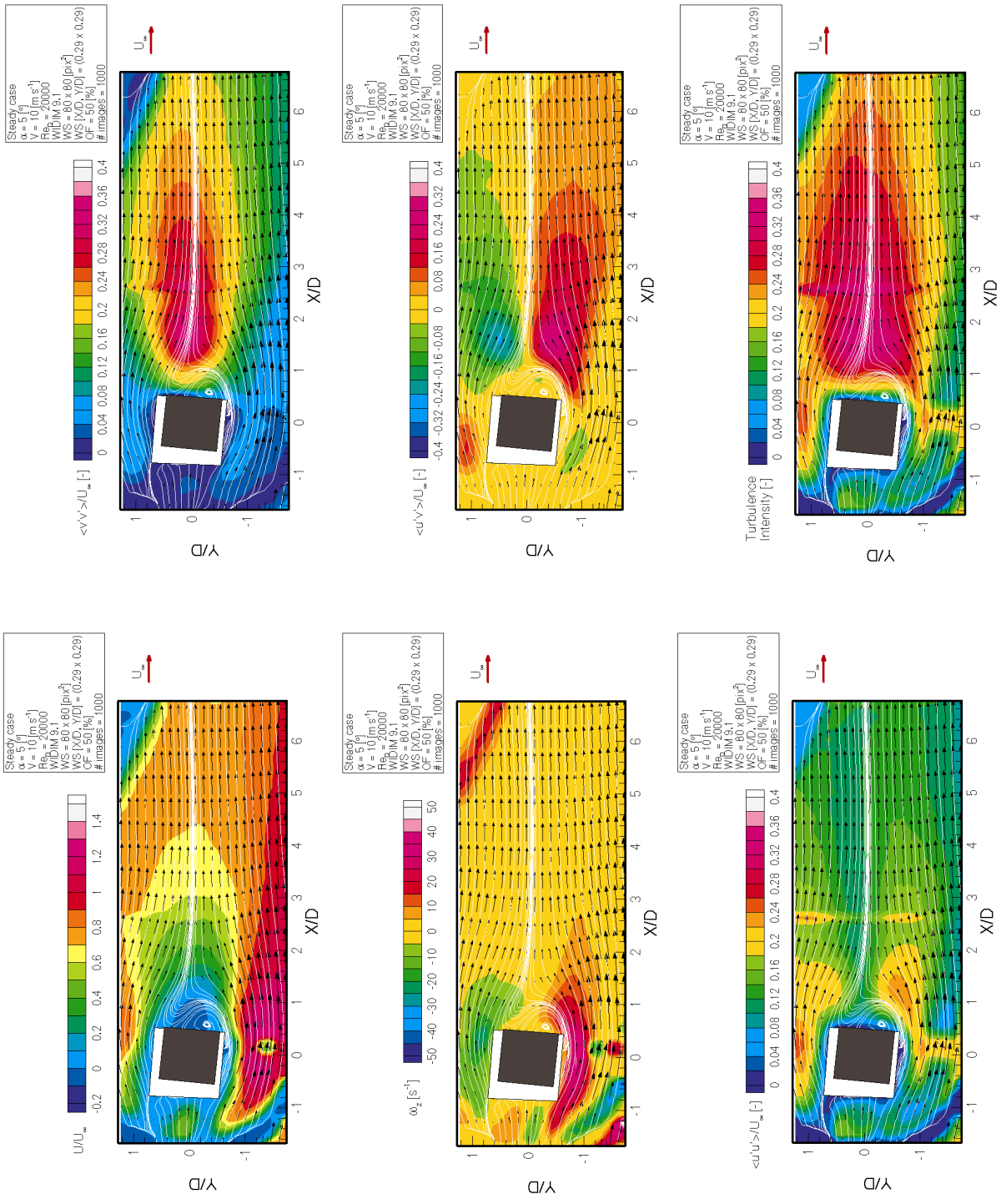

Angle of incidence: 10°

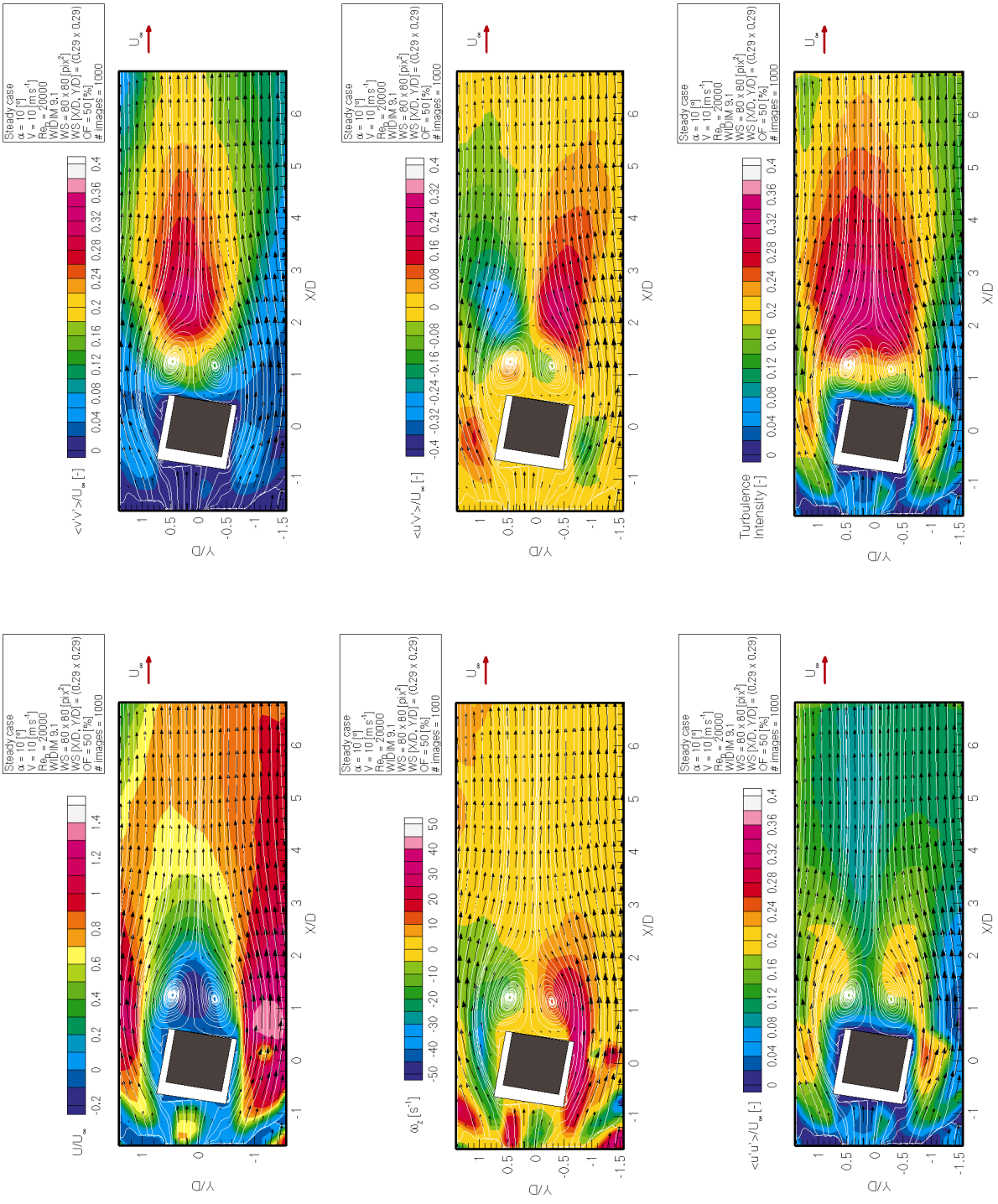

Angle of incidence: 15°

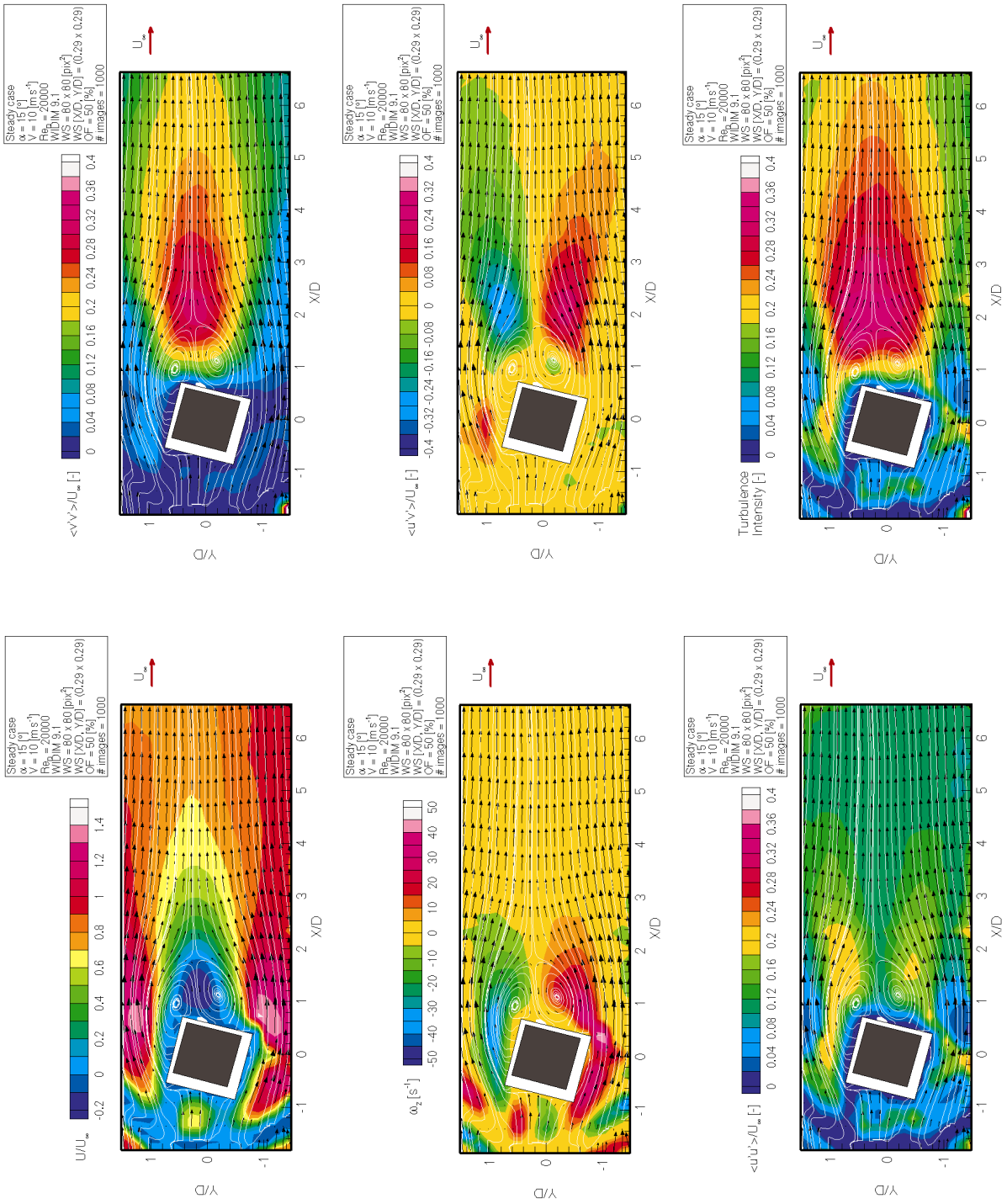

D.1.2 Case B

Angle of incidence: 0°

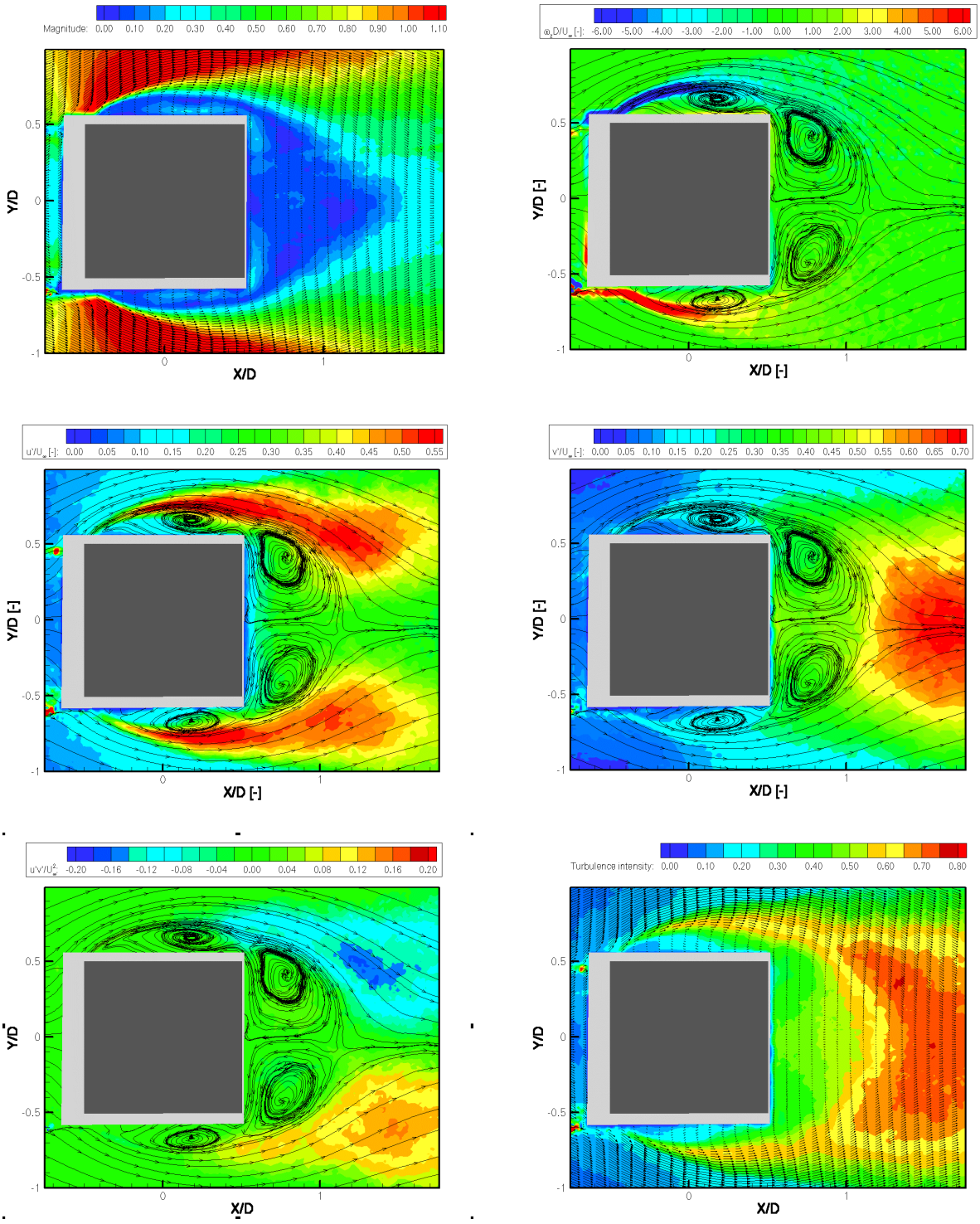

Angle of incidence: 5°

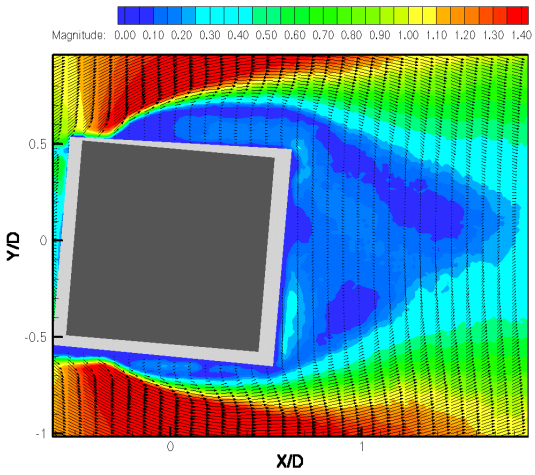

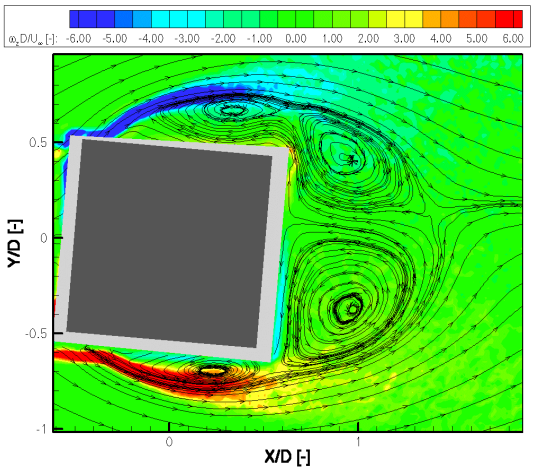

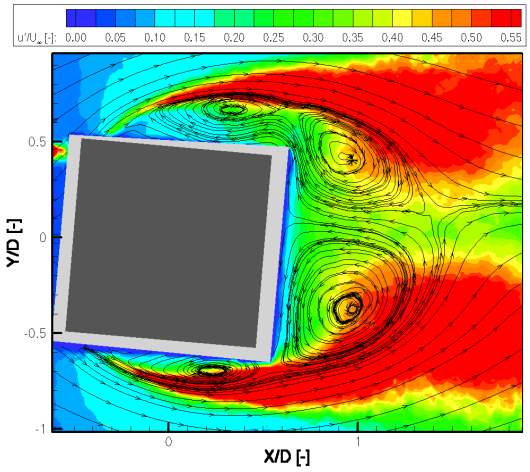

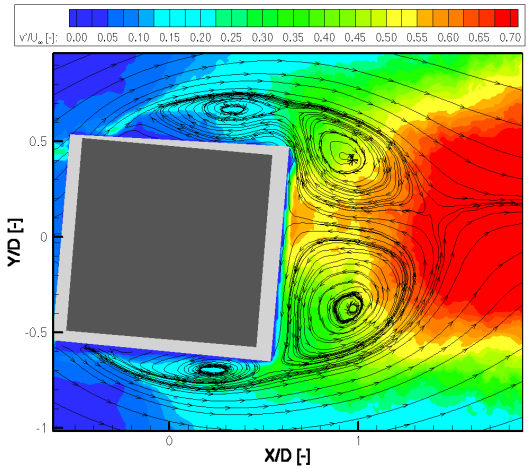

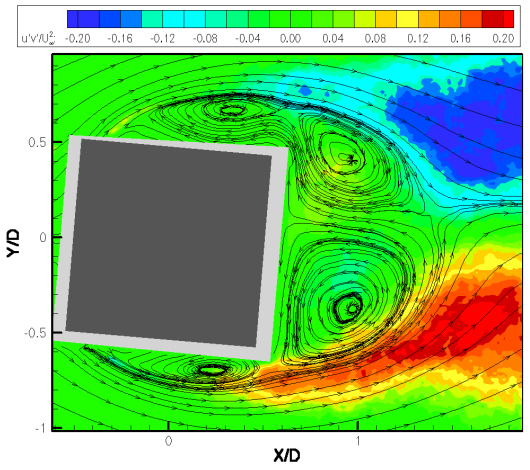

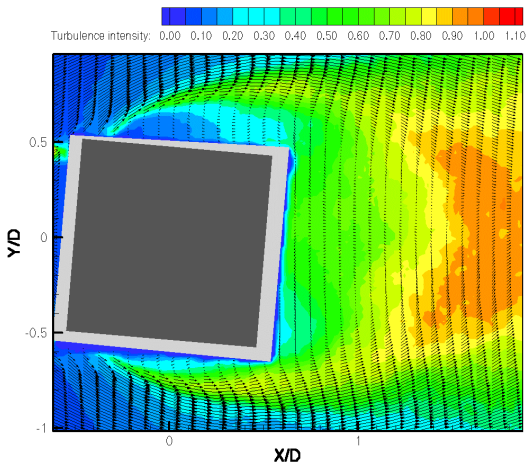

Angle of incidence: 10°

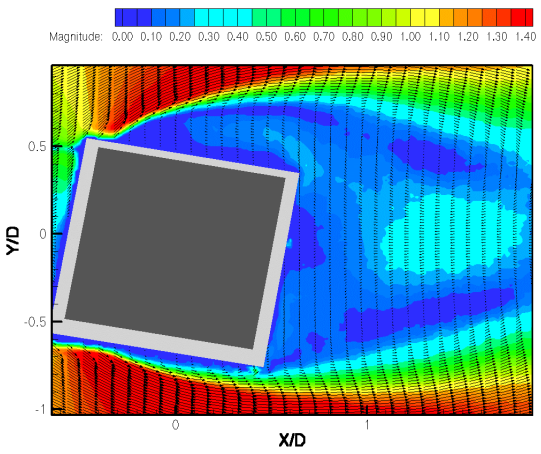

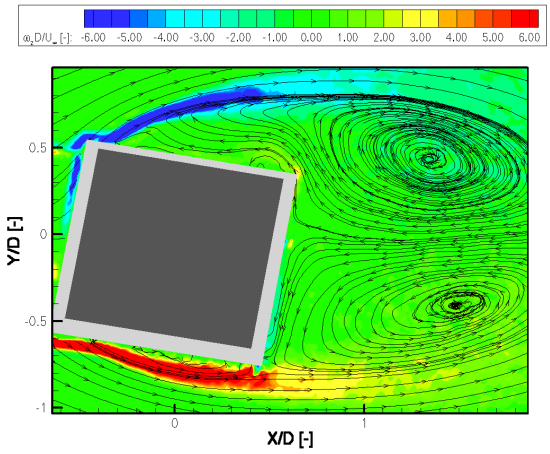

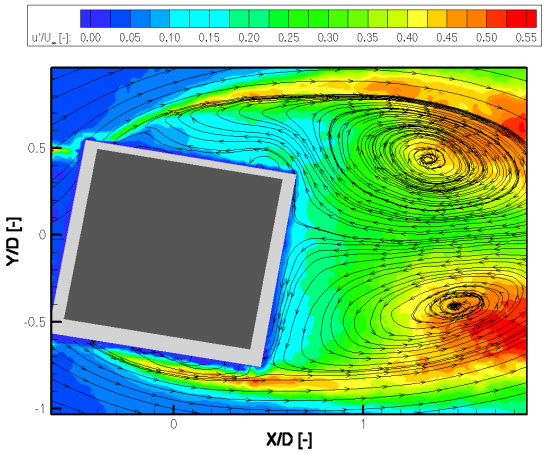

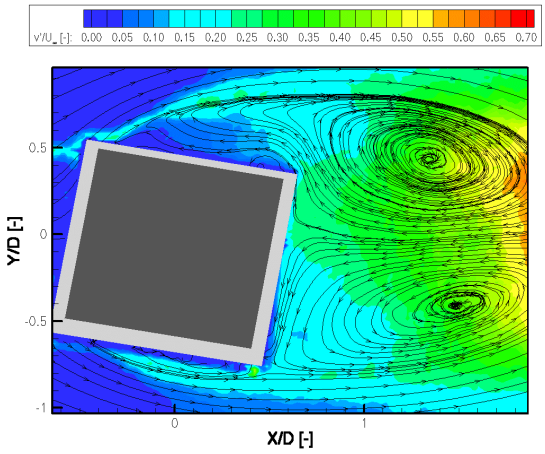

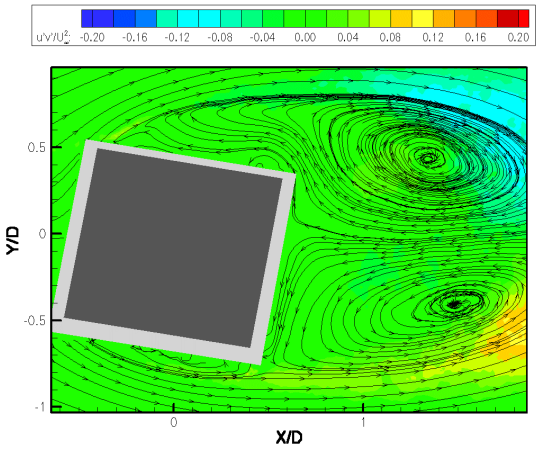

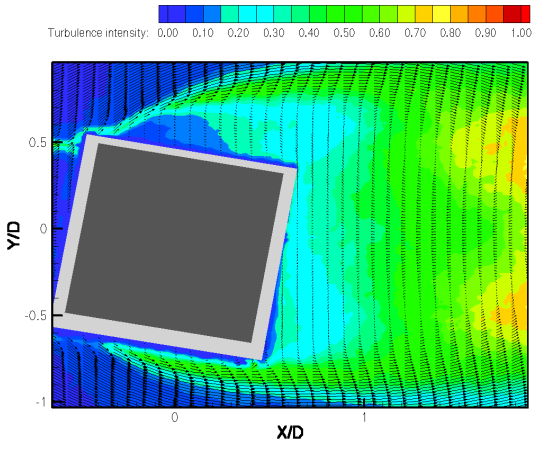

Angle of incidence: 15°

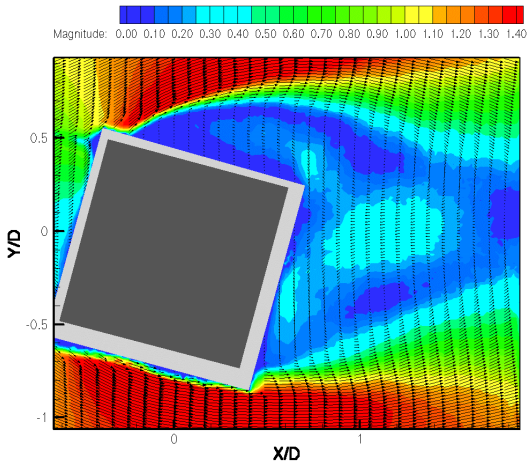

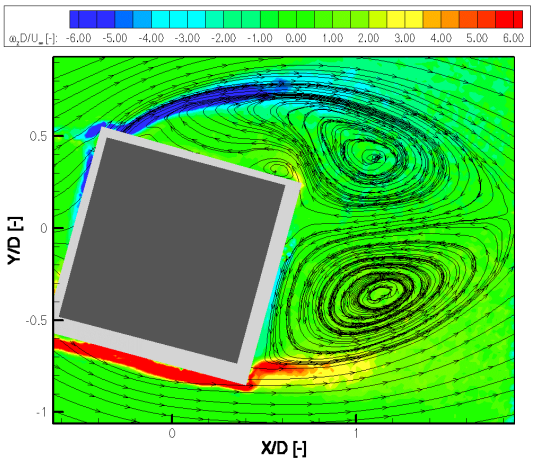

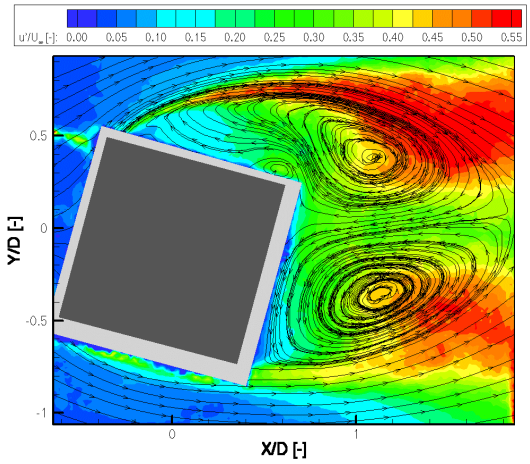

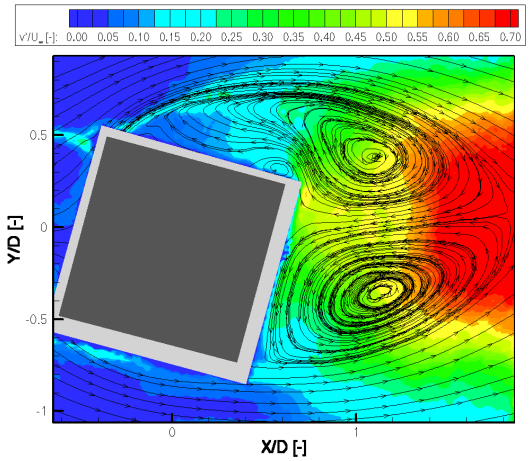

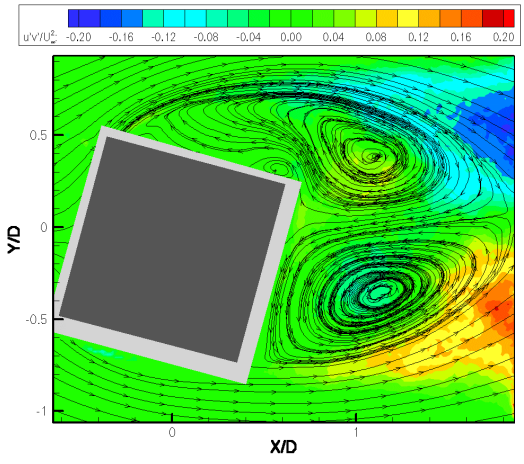

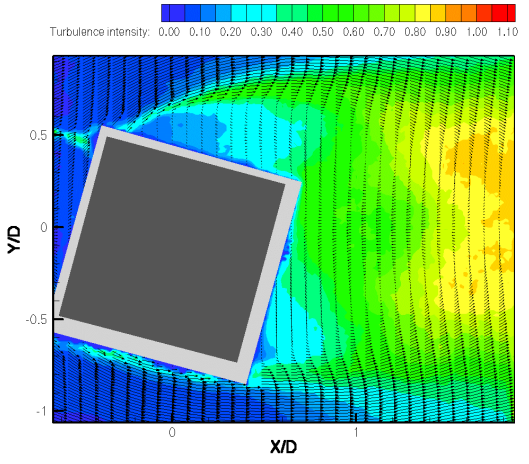

D.1.3 Case C

Angle of incidence: 0°

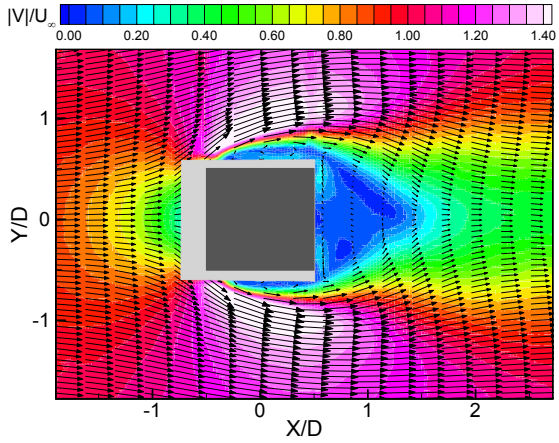

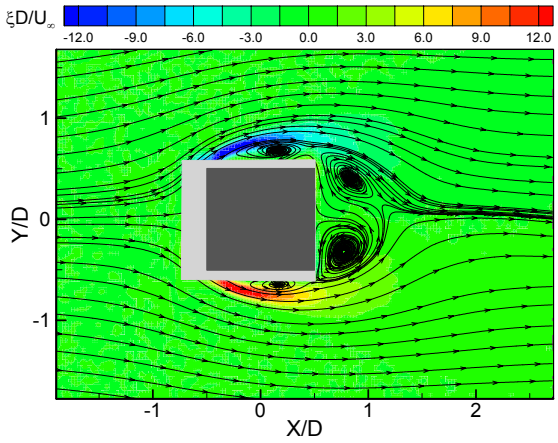

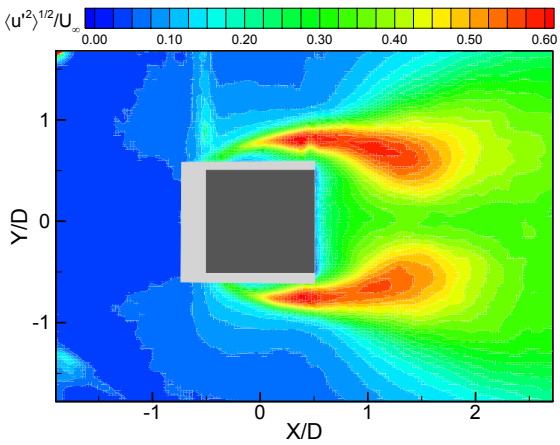

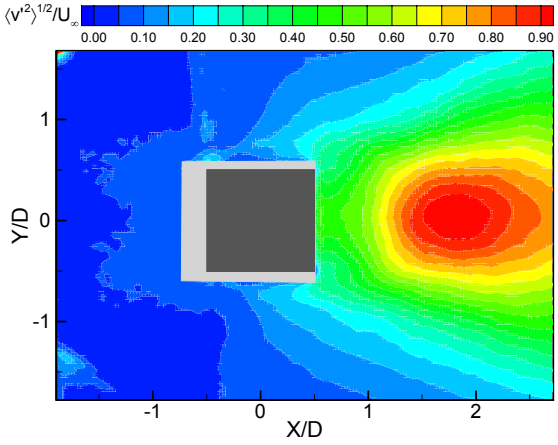

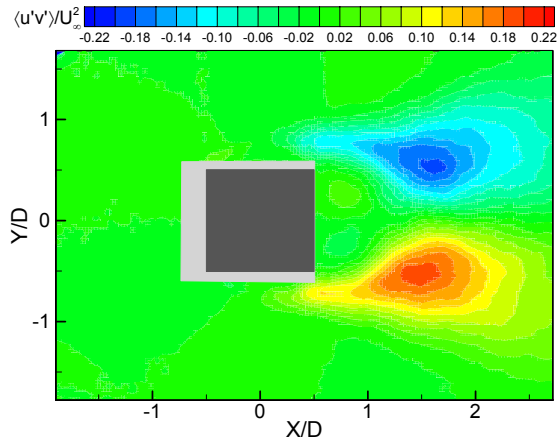

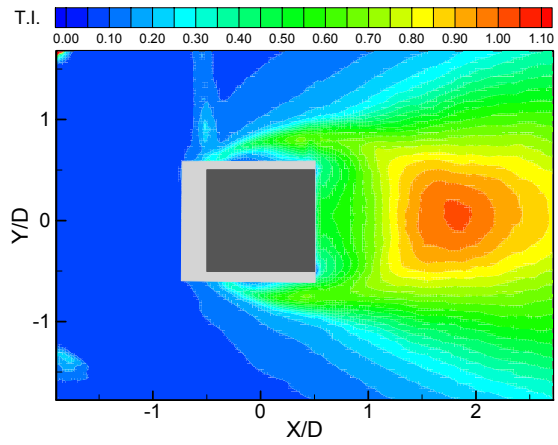

Angle of incidence: 2.5°

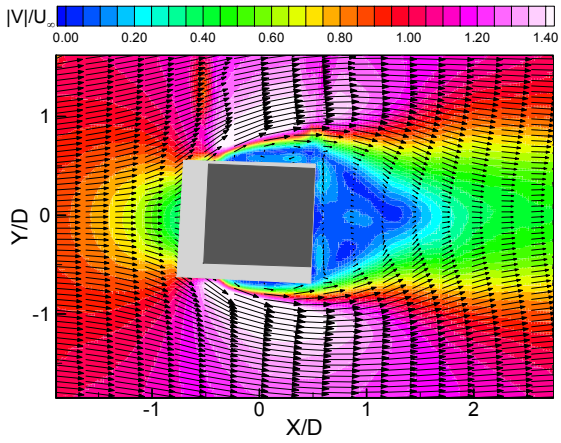

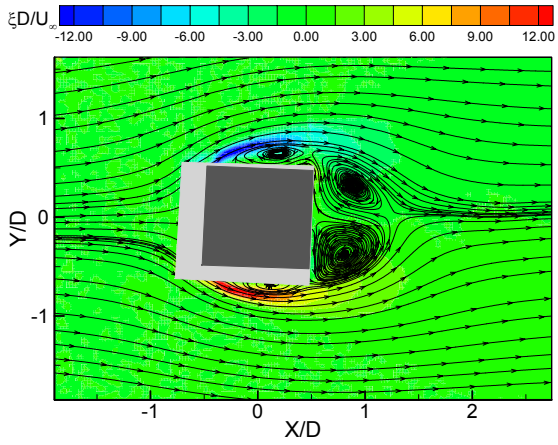

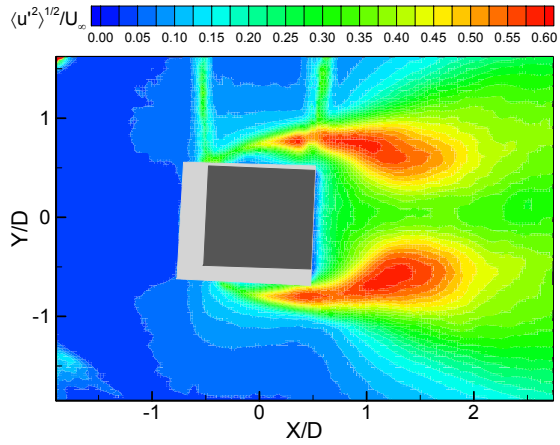

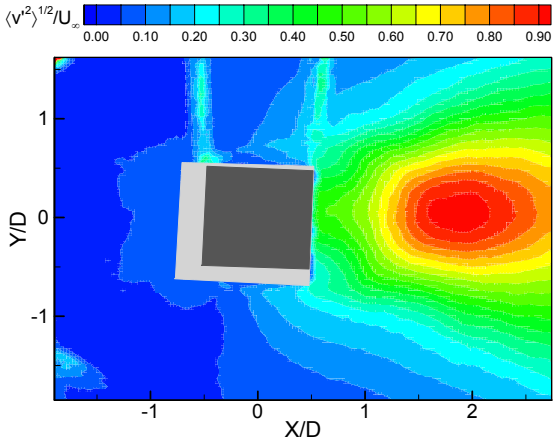

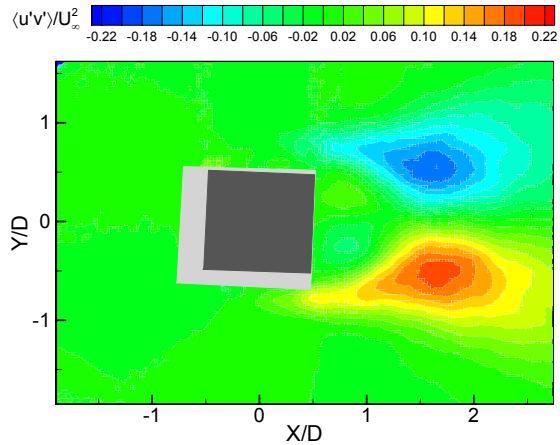

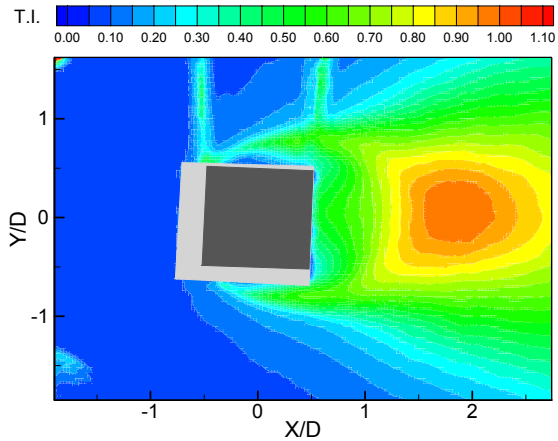

Angle of incidence: 5°

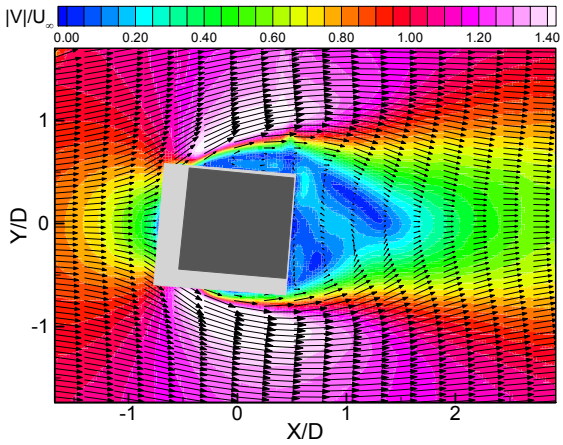

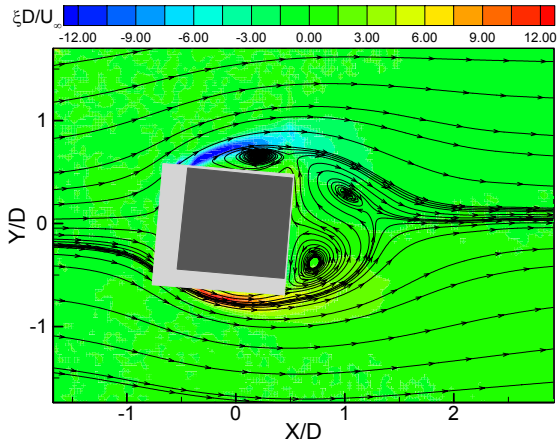

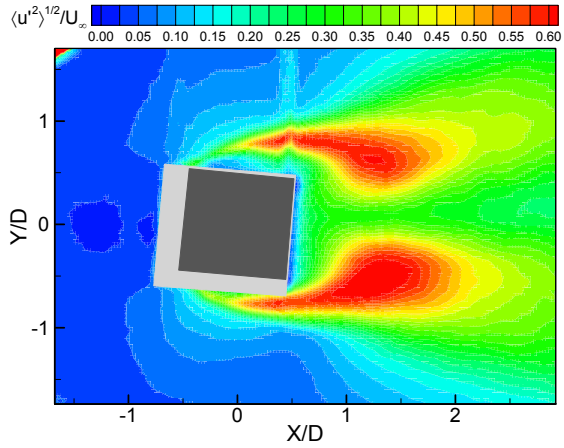

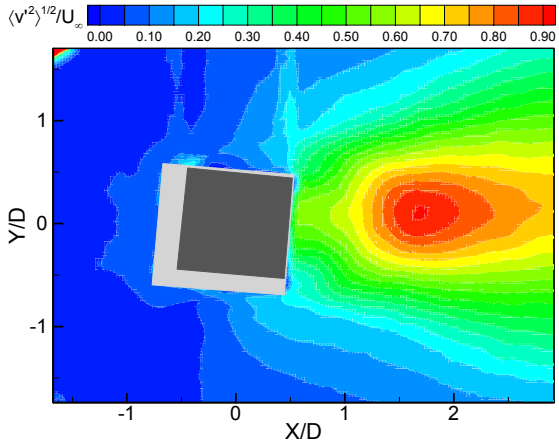

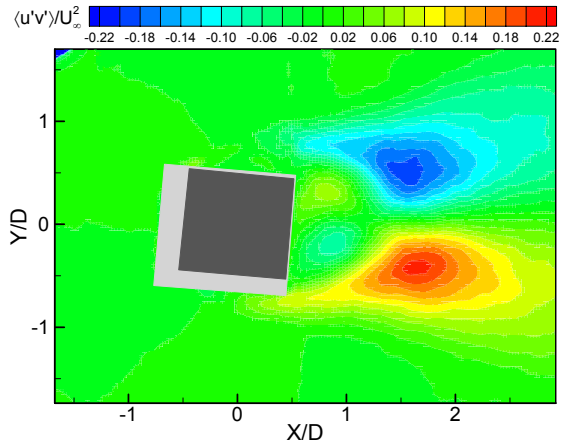

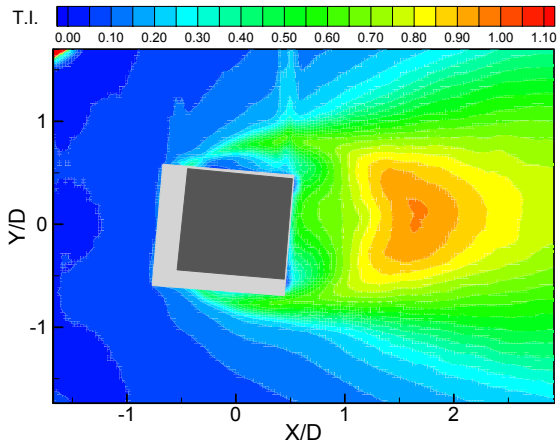

Angle of incidence: 7.5°

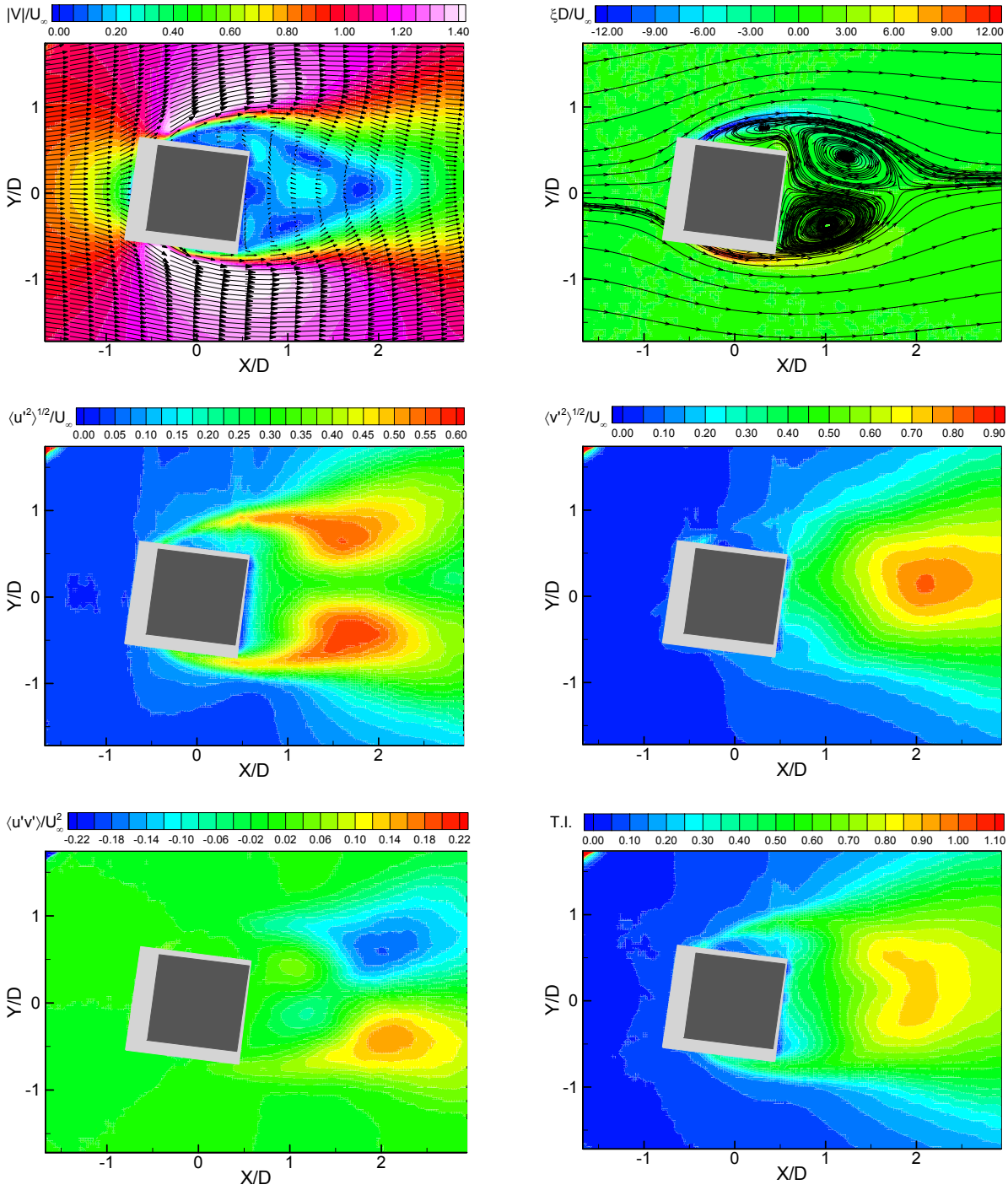

Angle of incidence: 10°

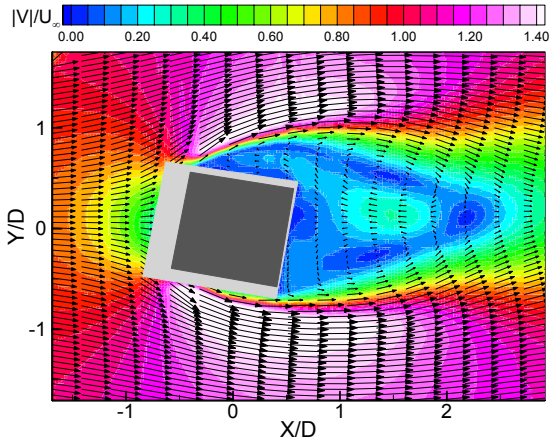

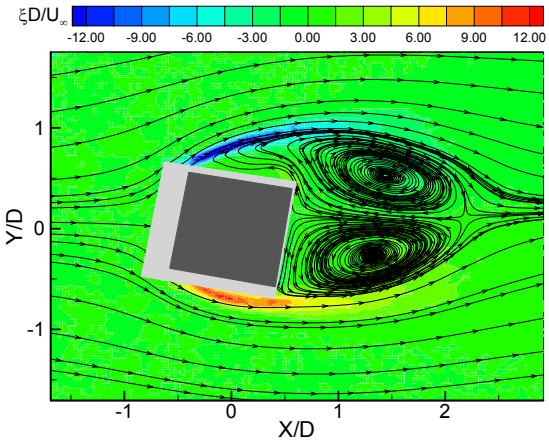

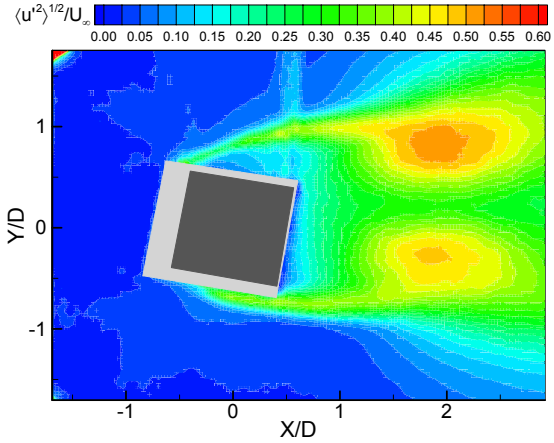

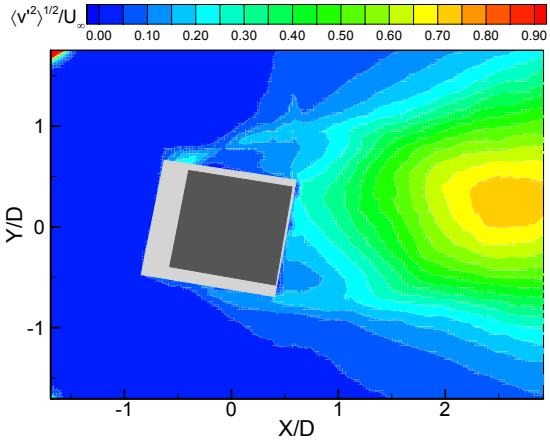

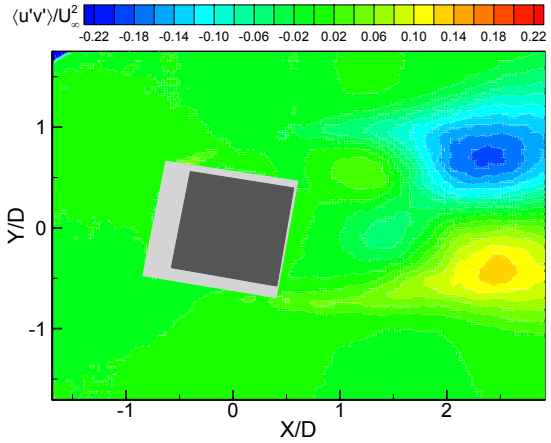

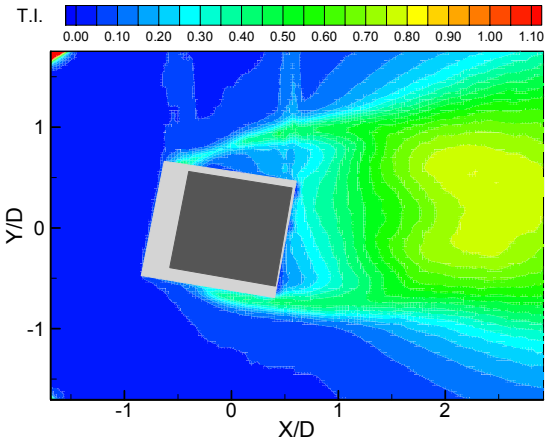

Angle of incidence: 12.5°

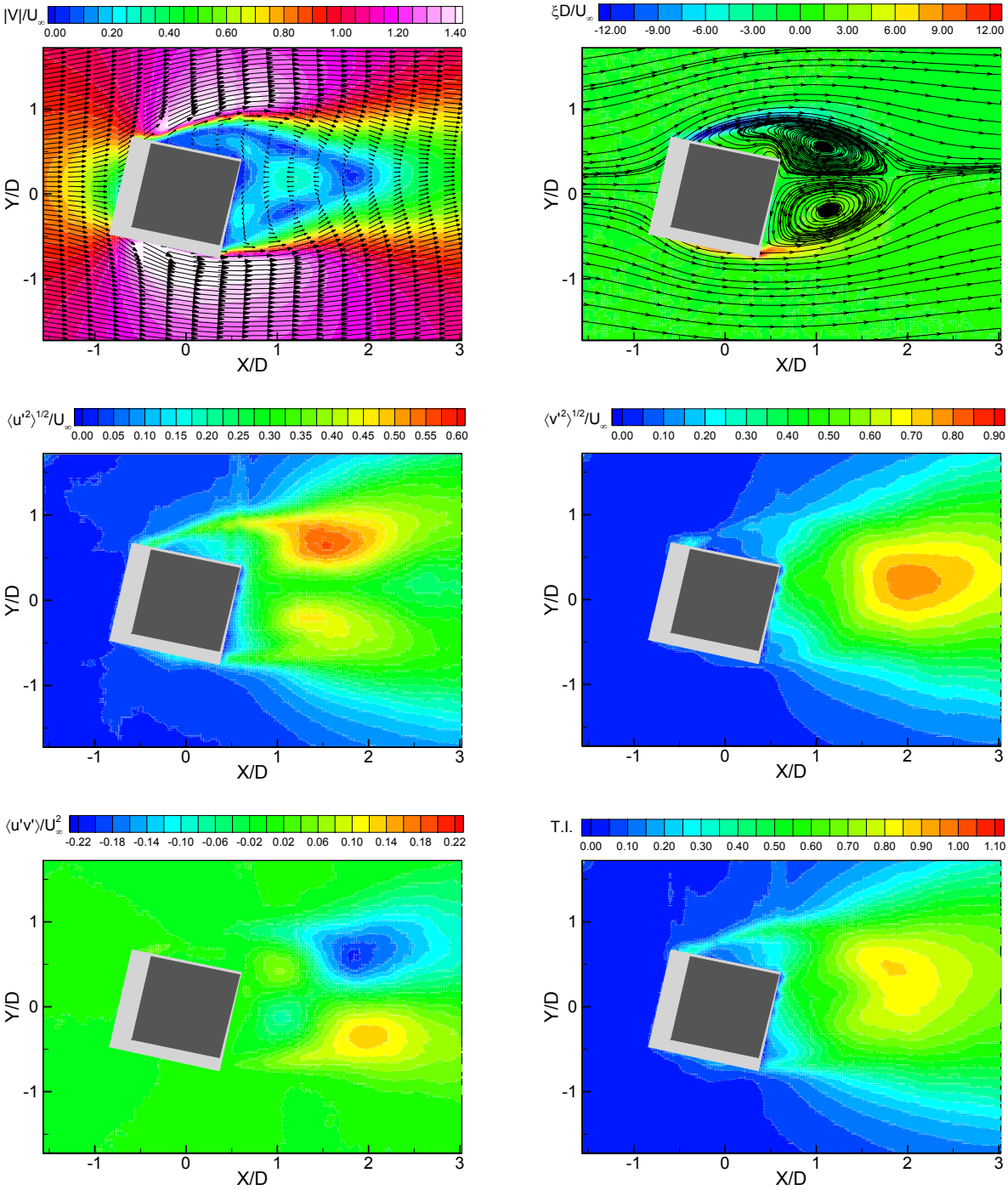

Angle of incidence: 15°

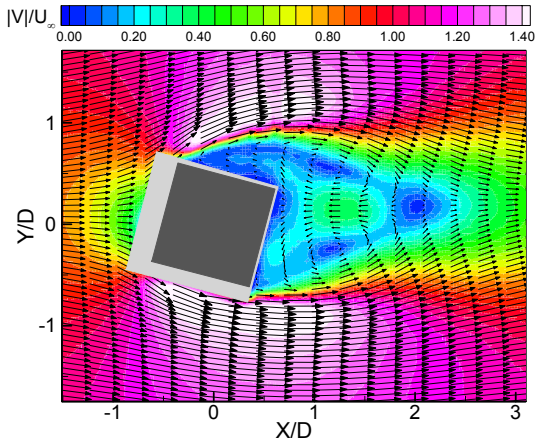

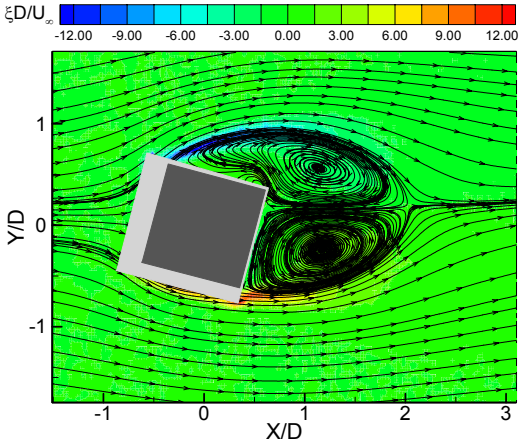

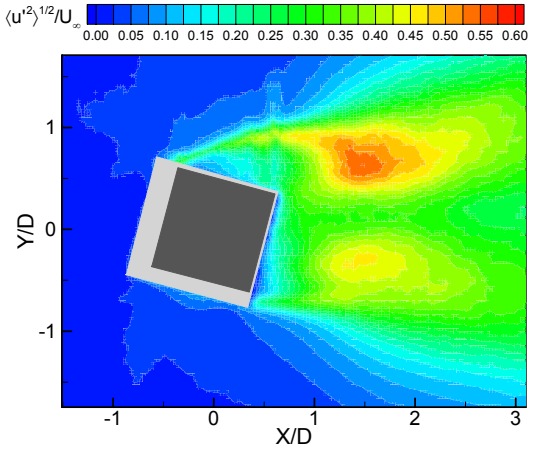

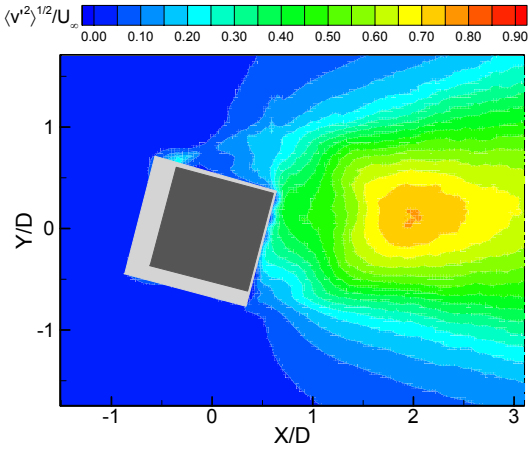

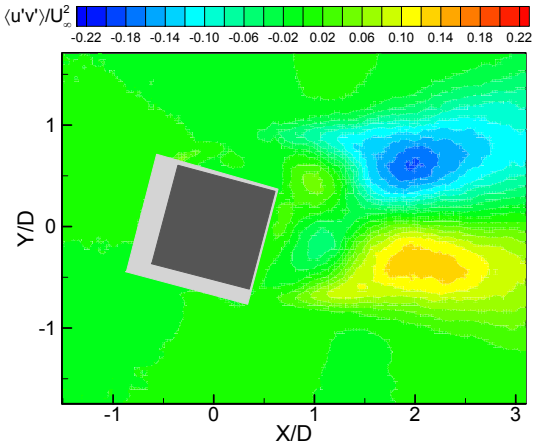

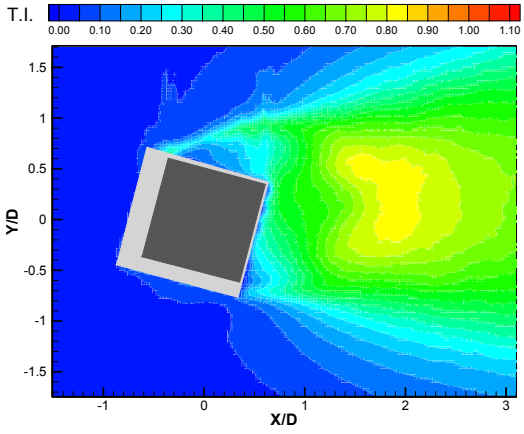

Angle of incidence: 20°

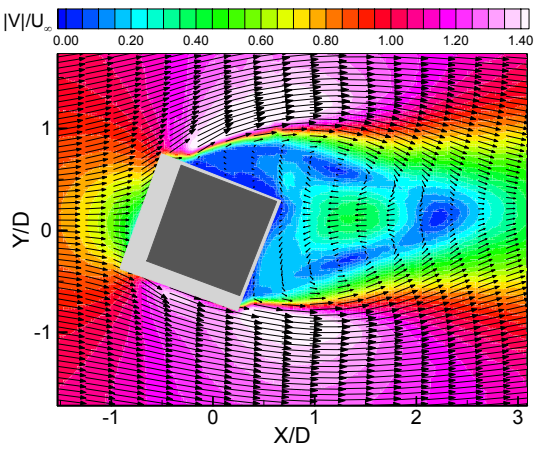

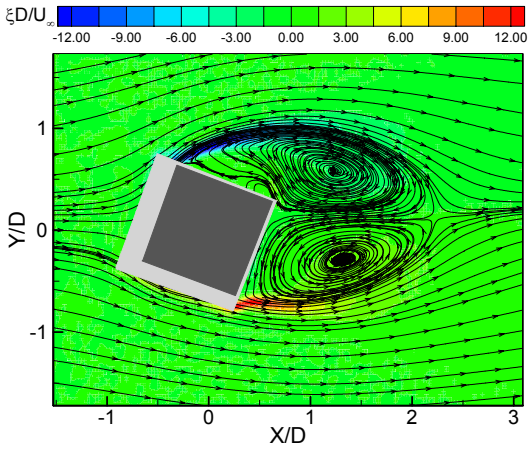

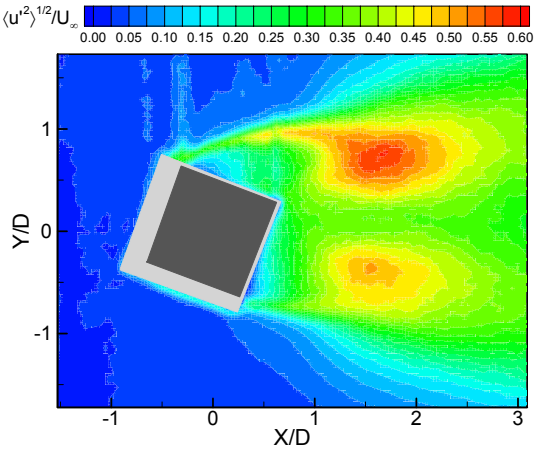

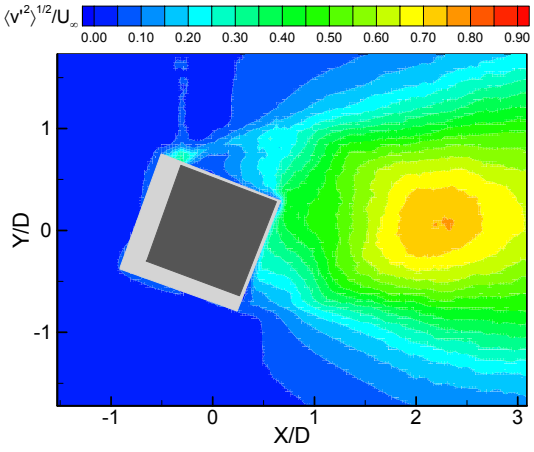

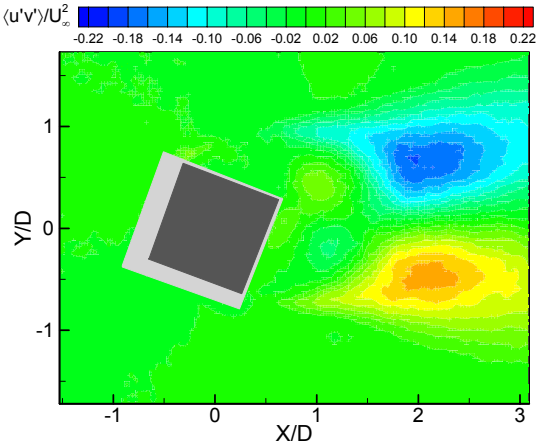

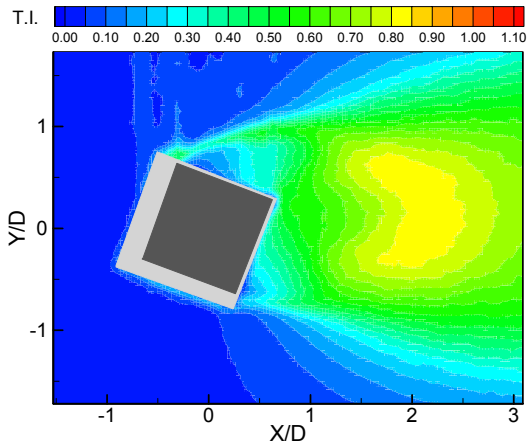

Angle of incidence: 25°

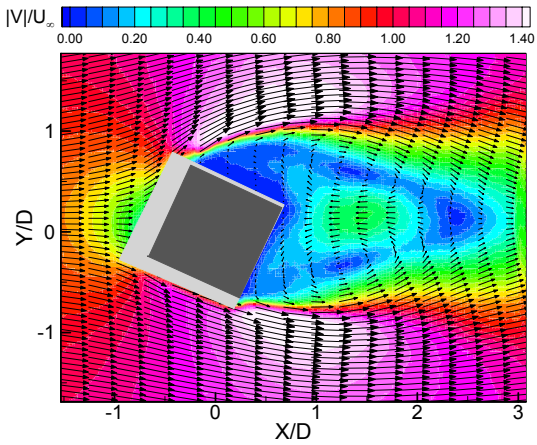

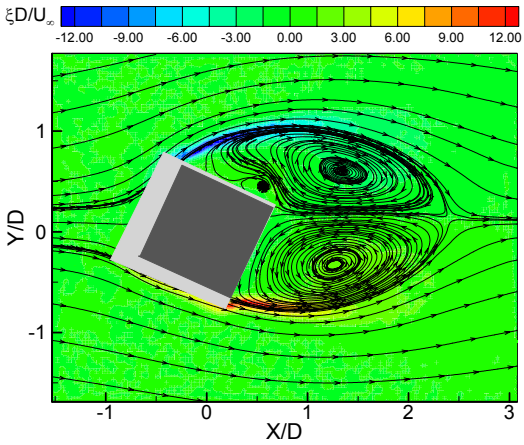

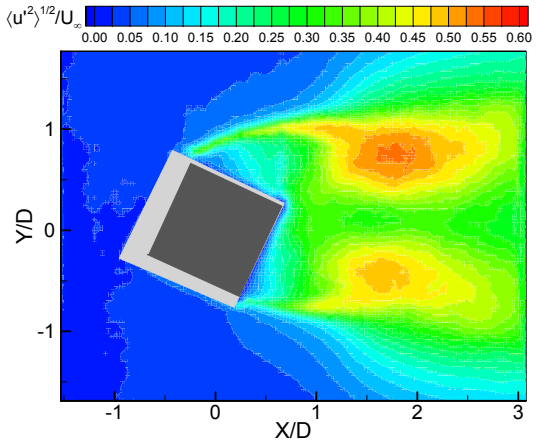

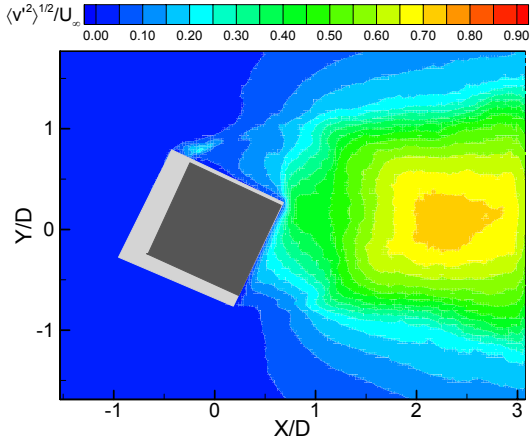

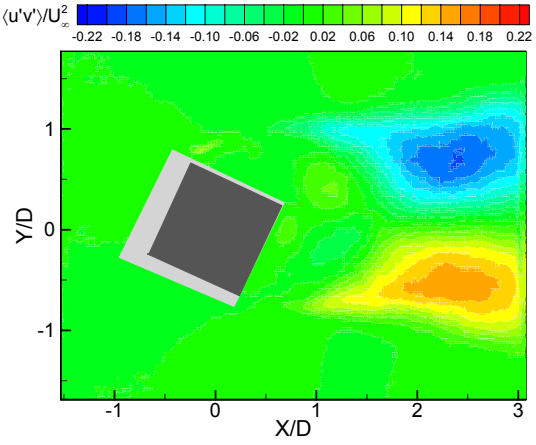

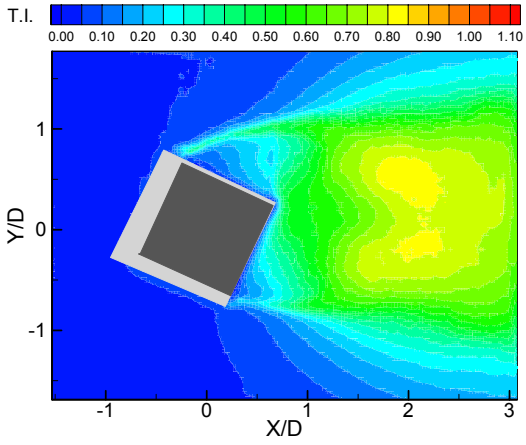

Angle of incidence: 30°

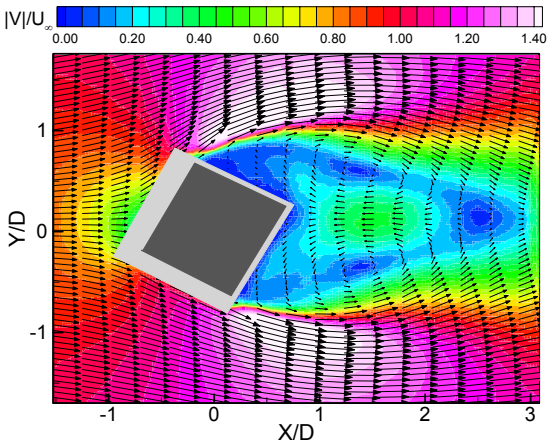

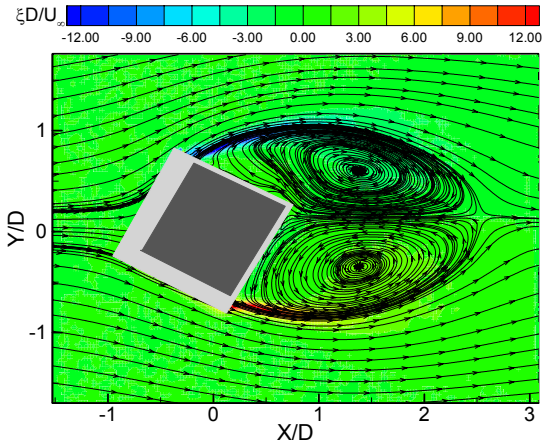

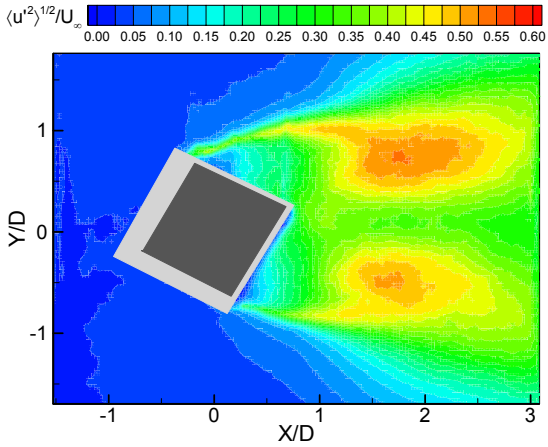

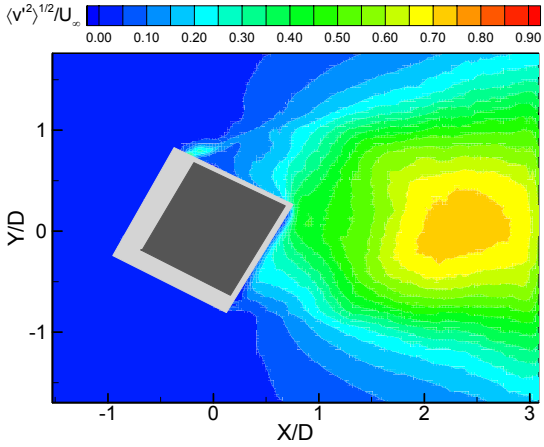

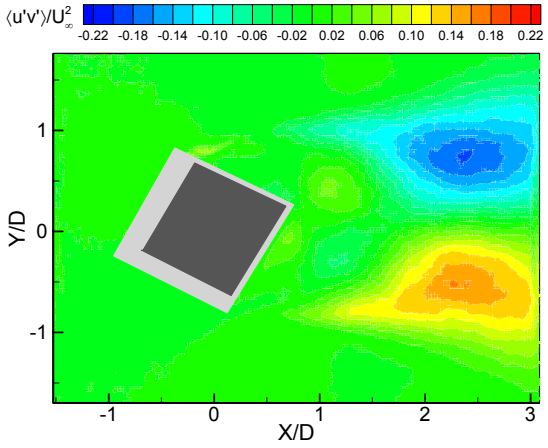

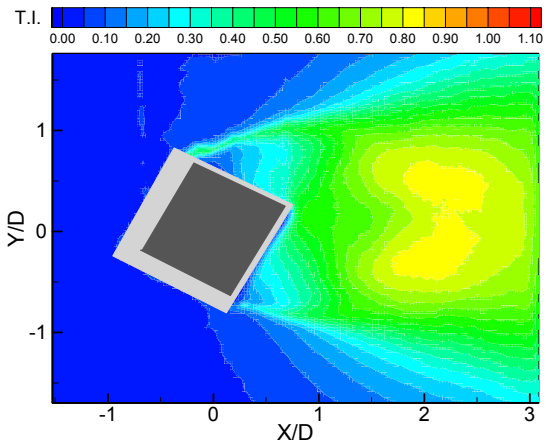

Angle of incidence: 35°

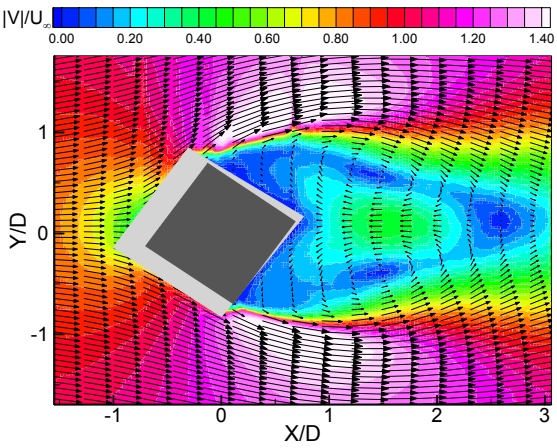

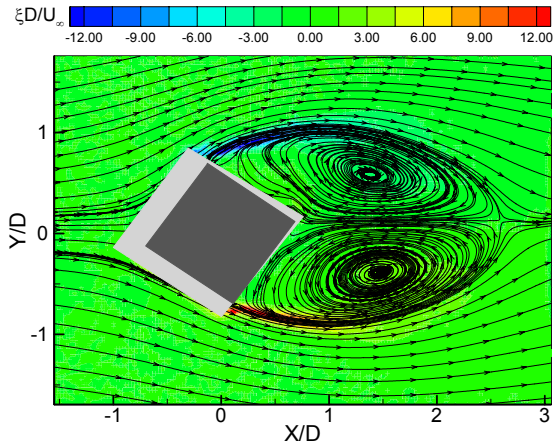

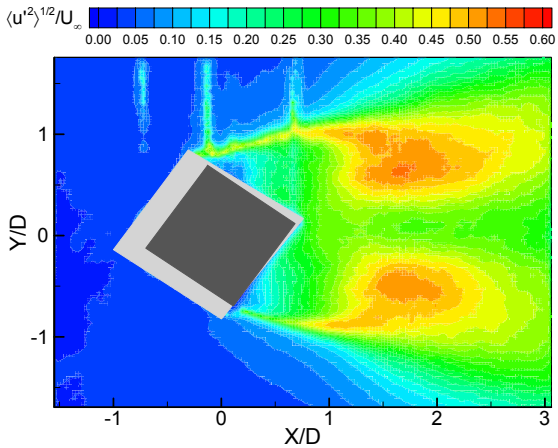

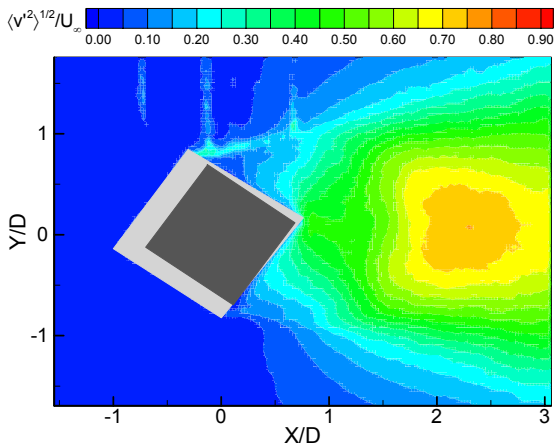

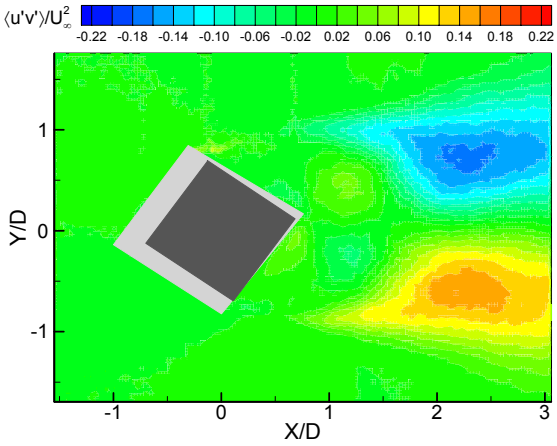

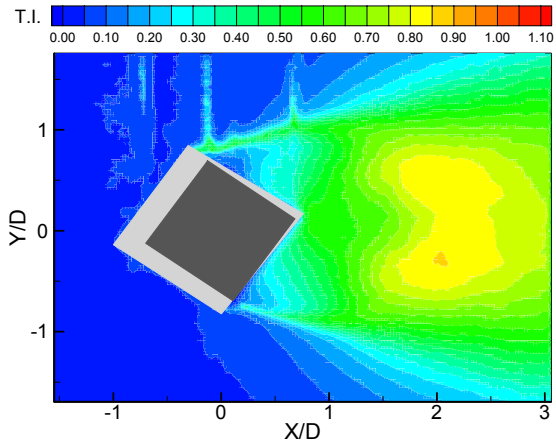

Angle of incidence: 40°

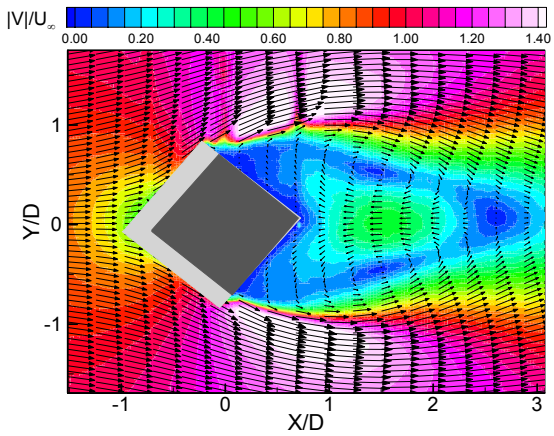

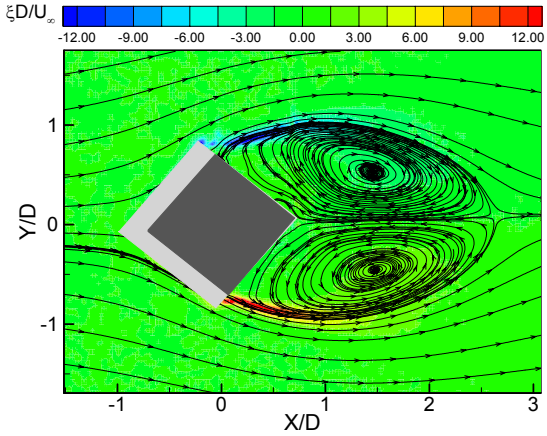

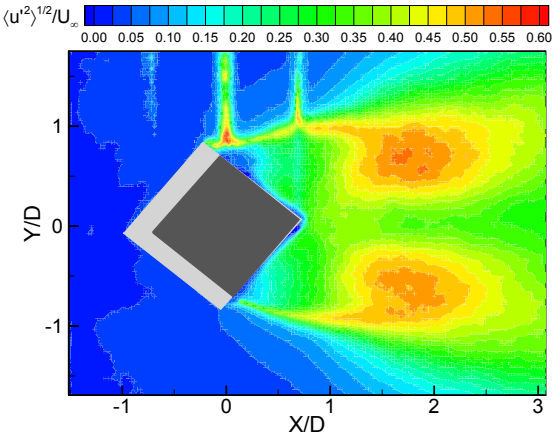

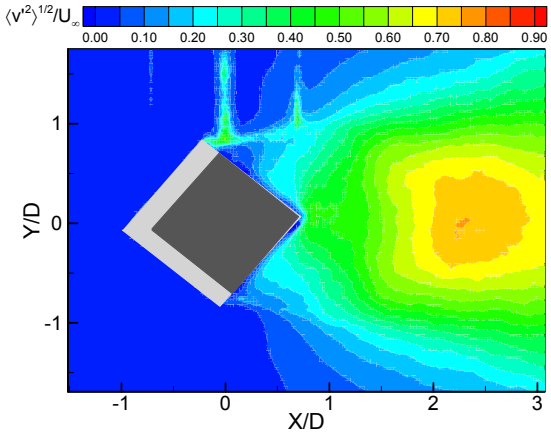

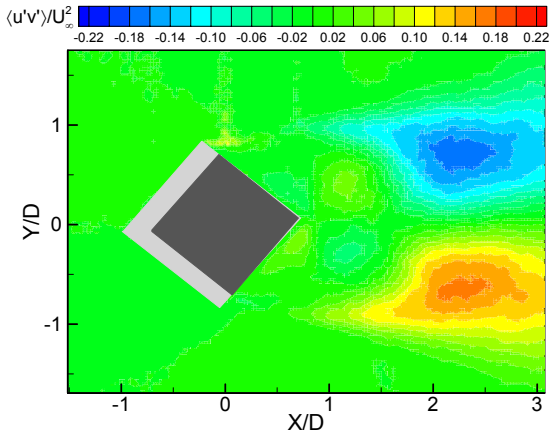

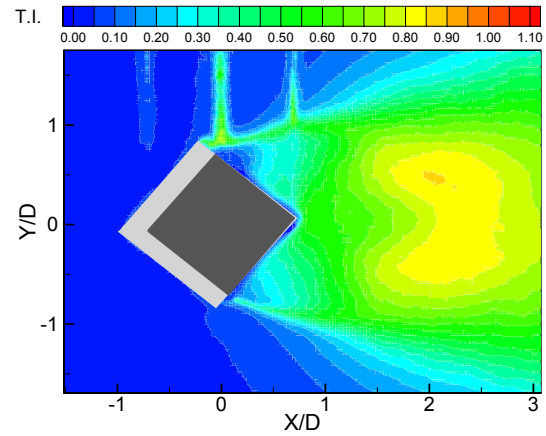

Angle of incidence: 45°

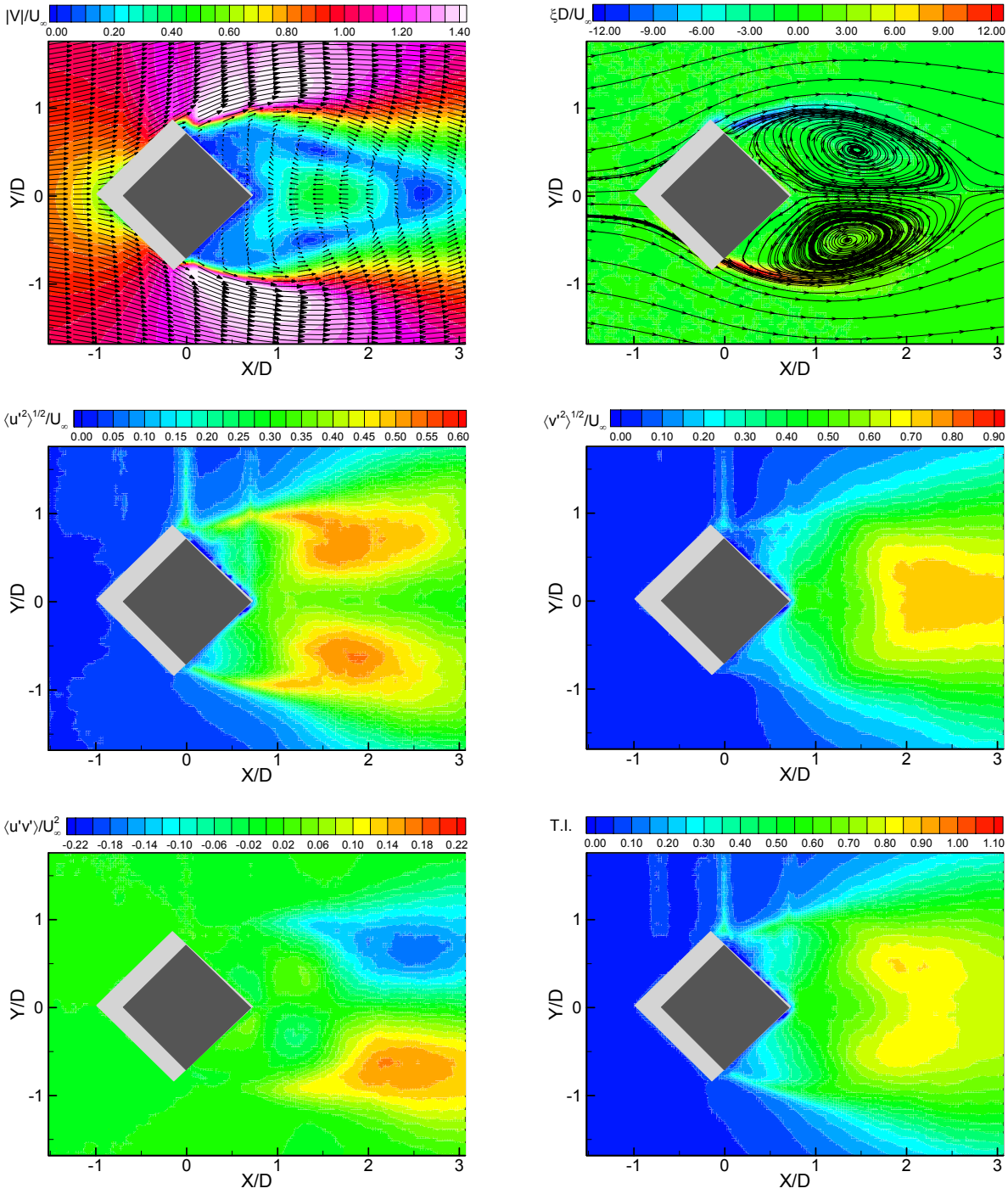

D.2 Unsteady flow analysis (Case C only)

D.2.1 Proper Orthogonal (POD) Modes

Angle of incidence: 0°

u1

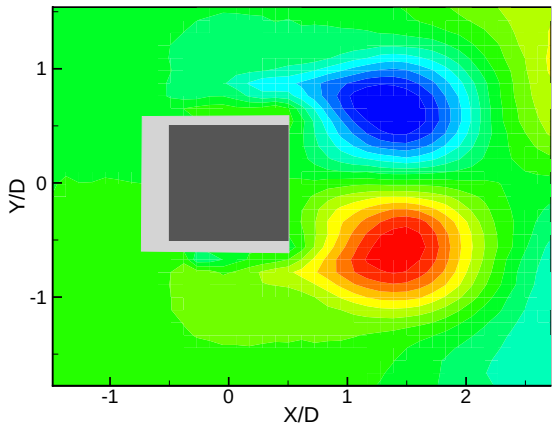

v1

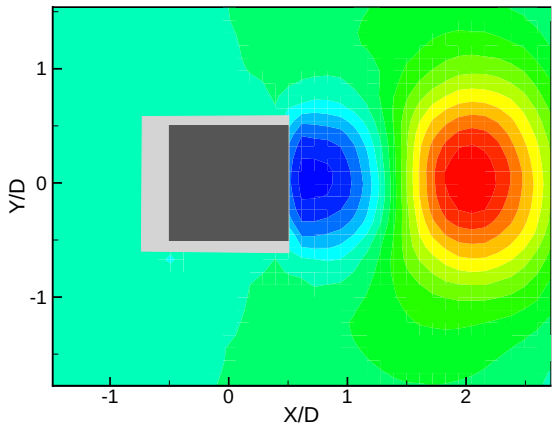

u2

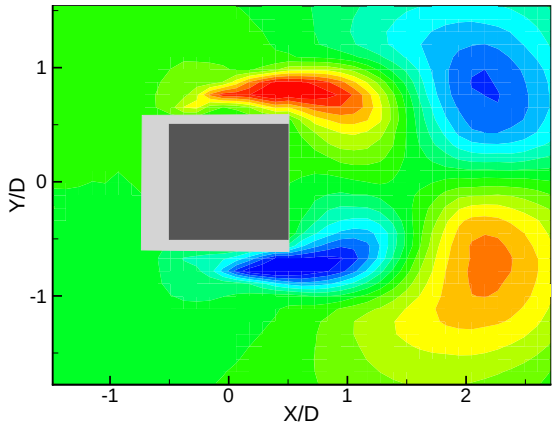

v2

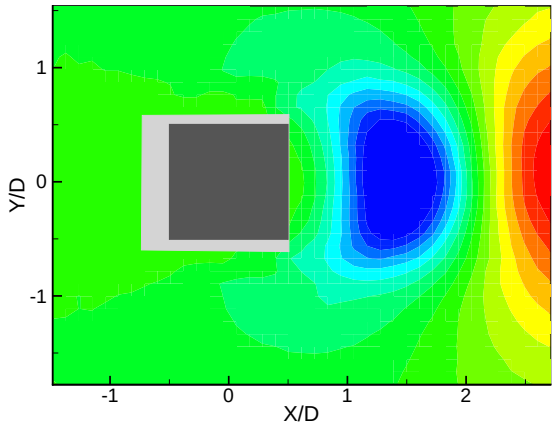

u3

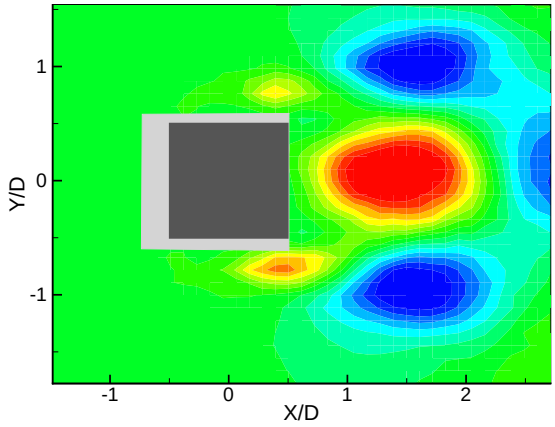

v3

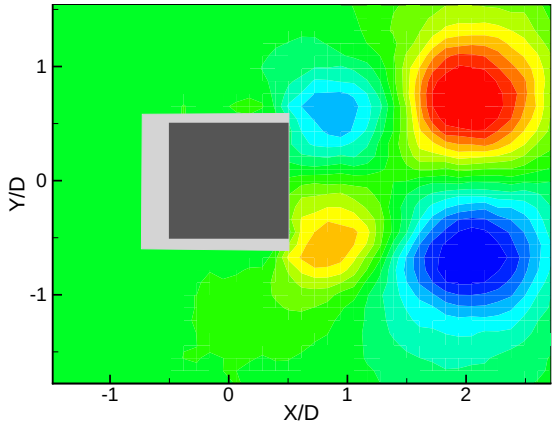

u4

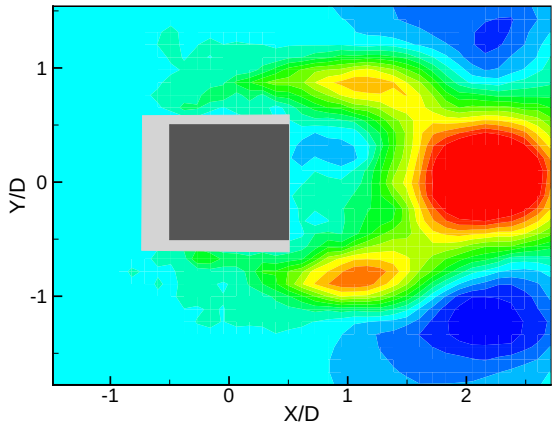

v4

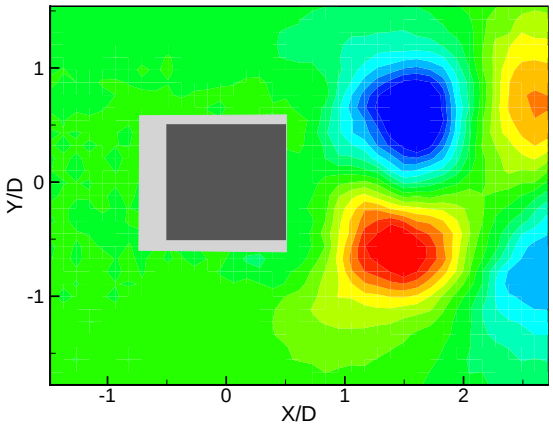

u5

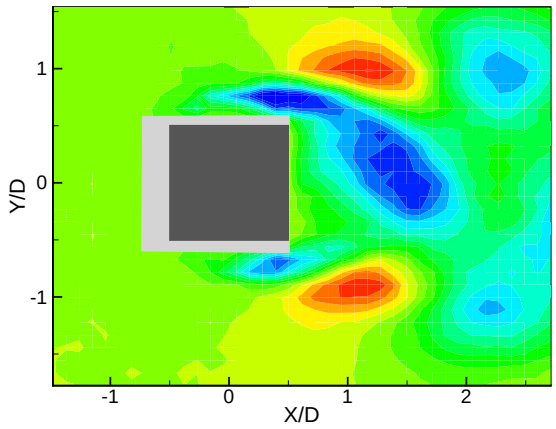

v5

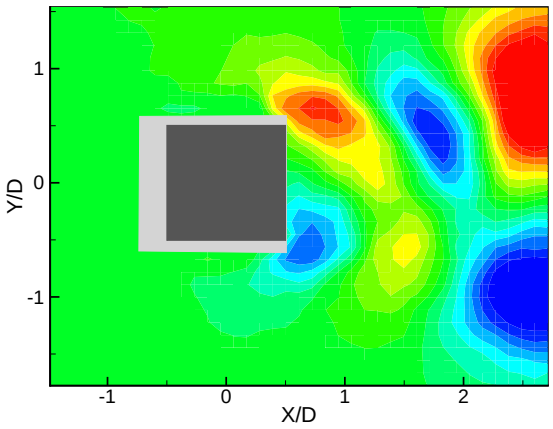

u6

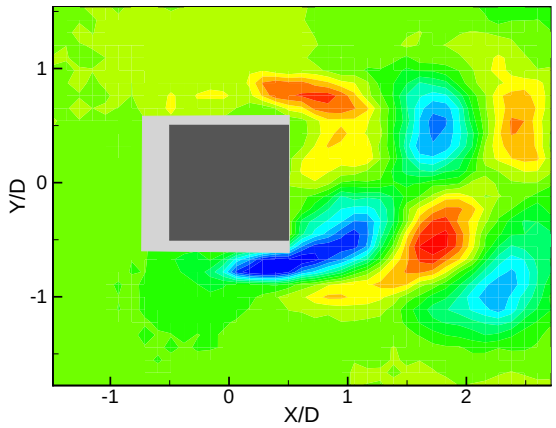

v6

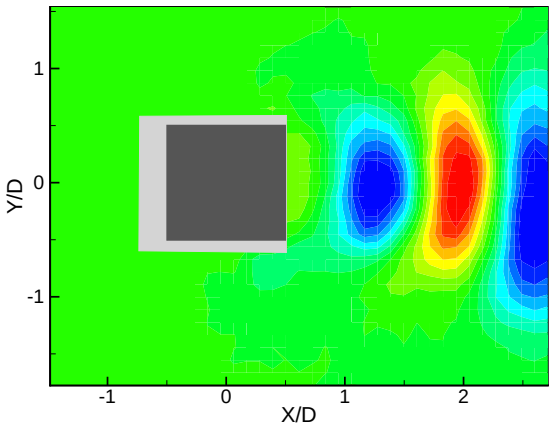

Angle of incidence: 2.5°

u1

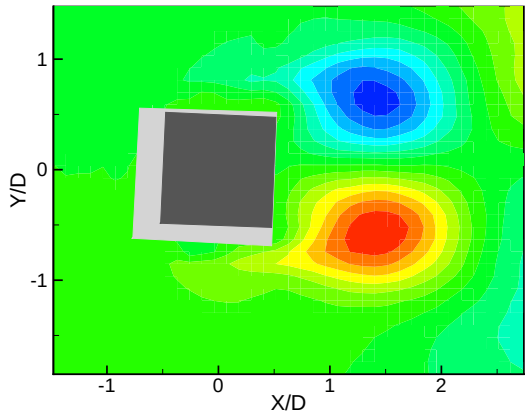

v1

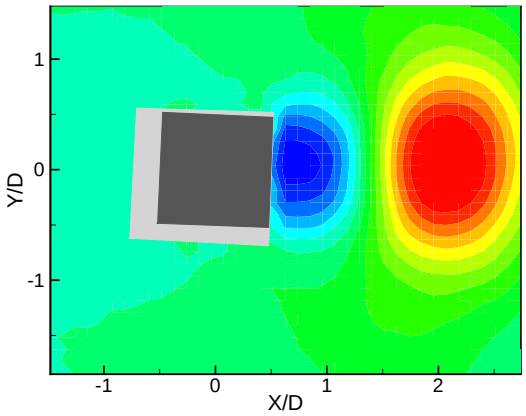

u2

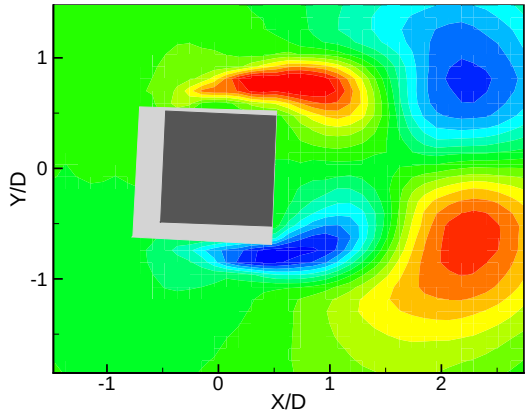

v2

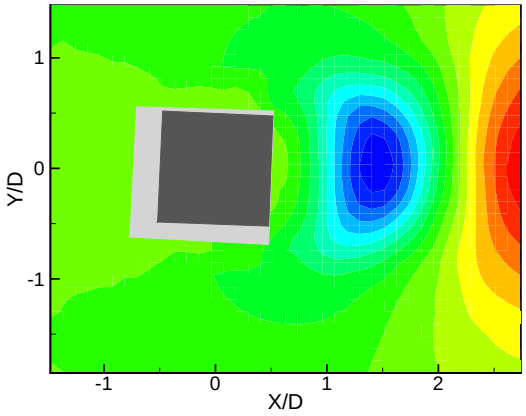

u3

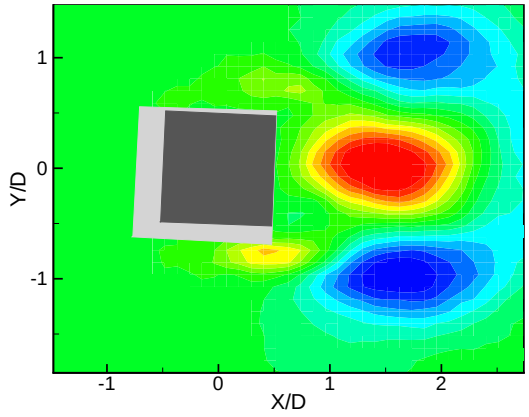

v3

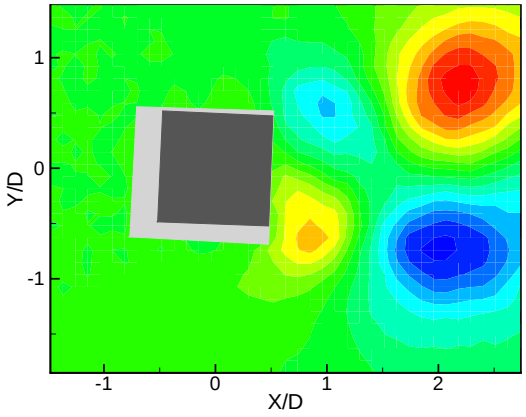

u4

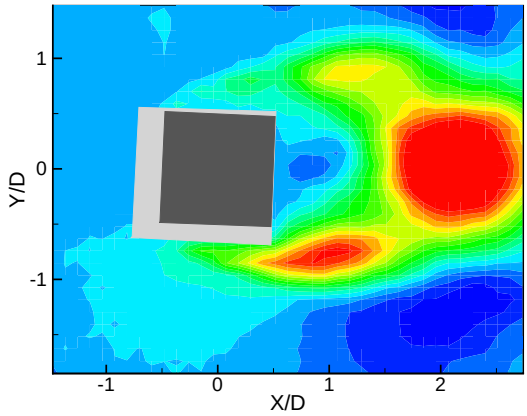

v4

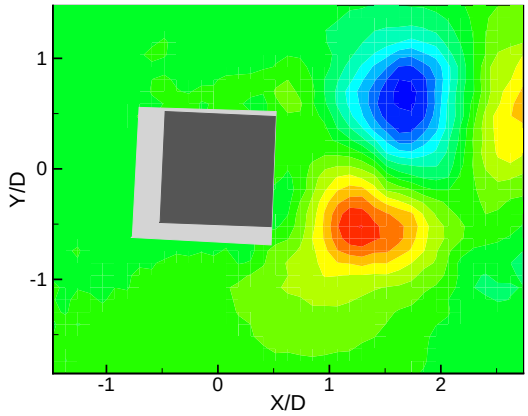

u5

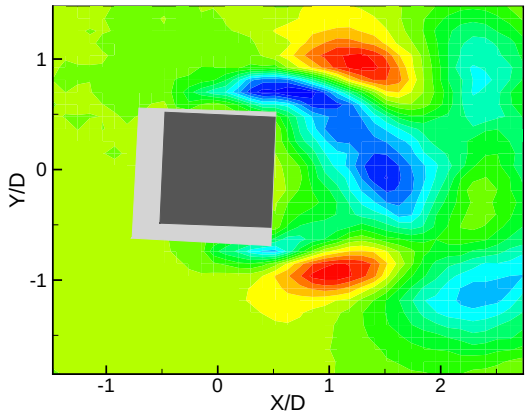

v5

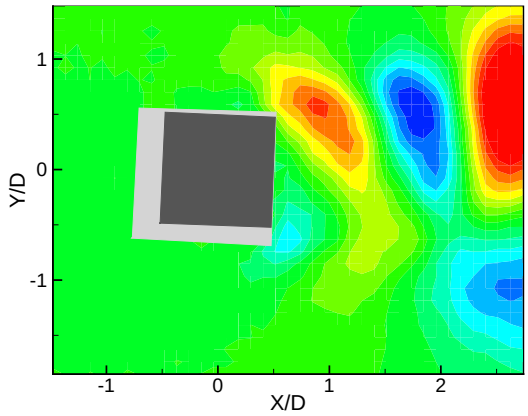

u6

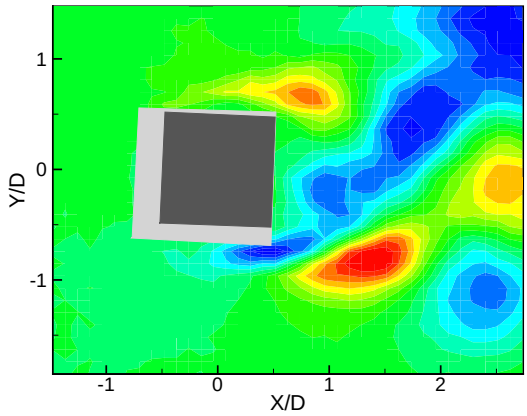

v6

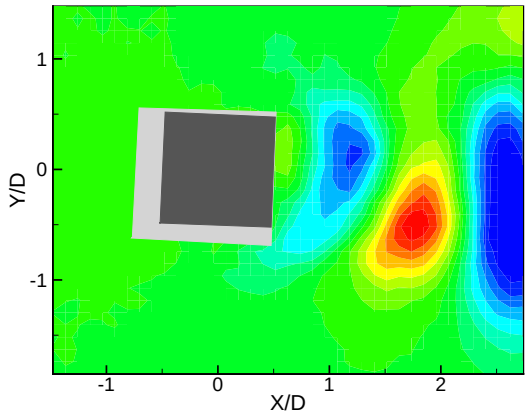

Angle of incidence: 5°

u1

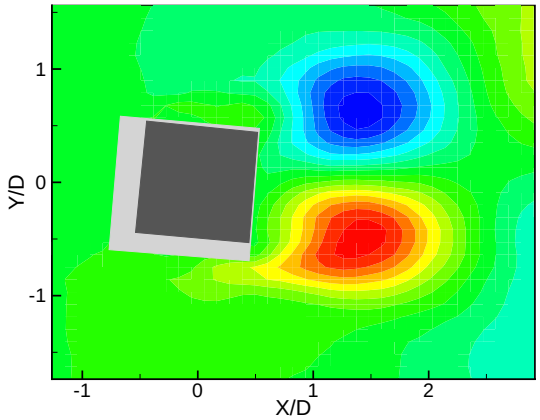

v1

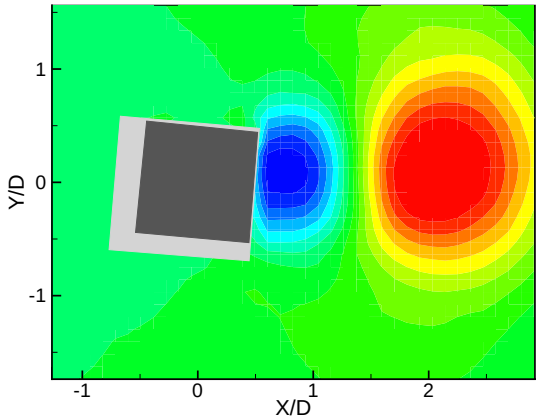

u2

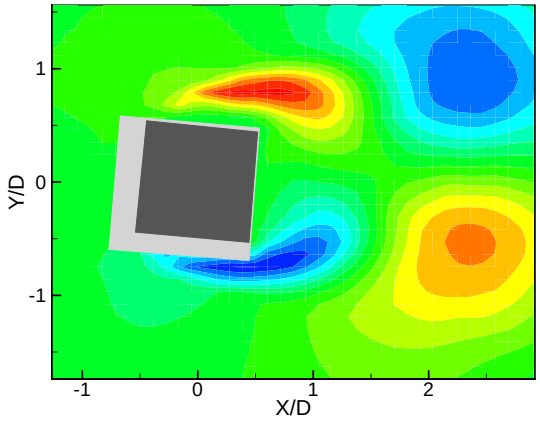

v2

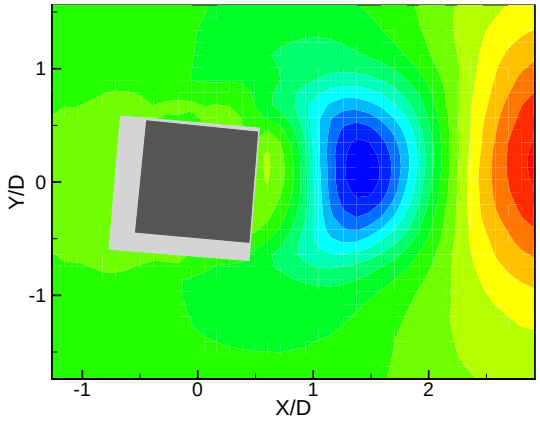

u3

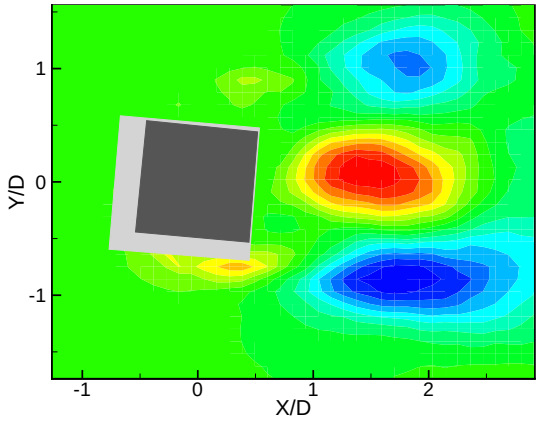

v3

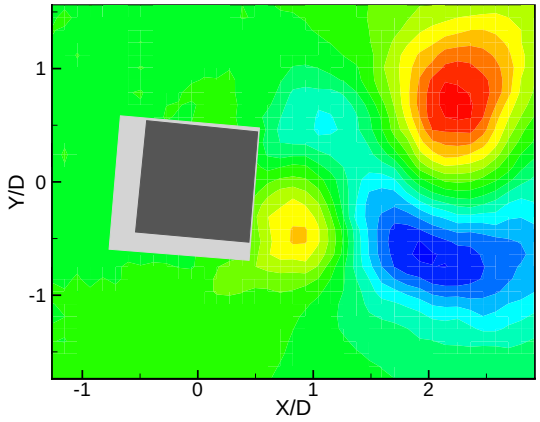

u4

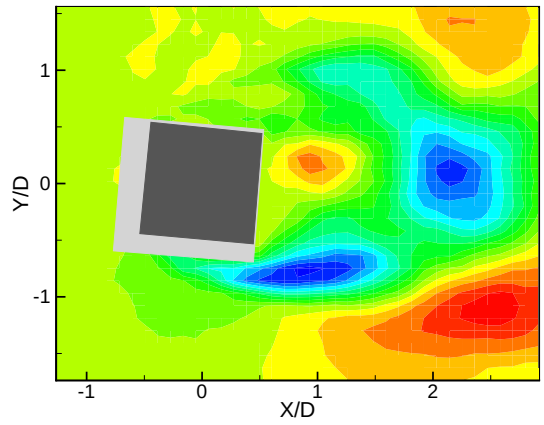

v4

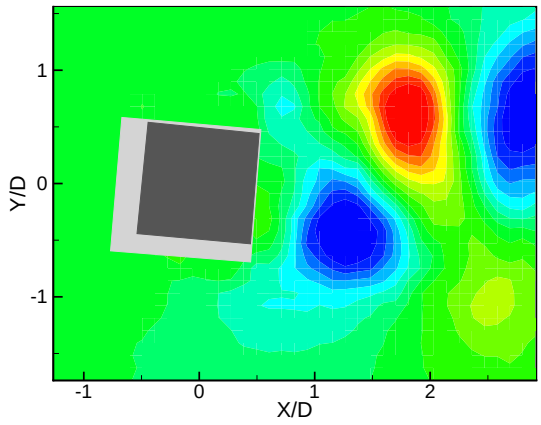

u5

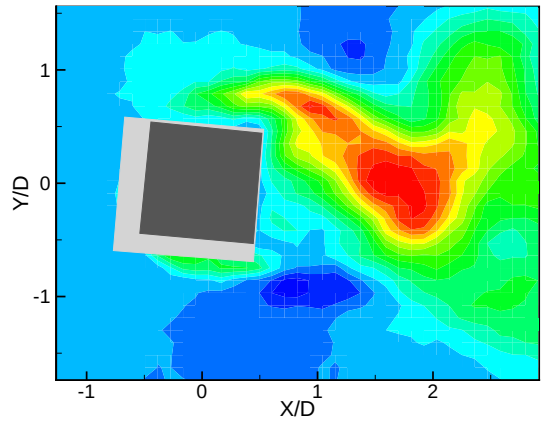

v5

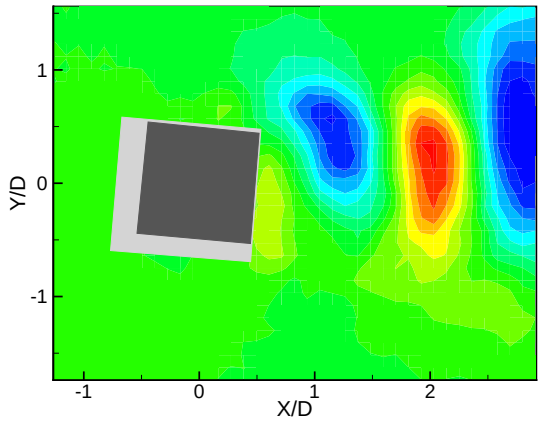

u6

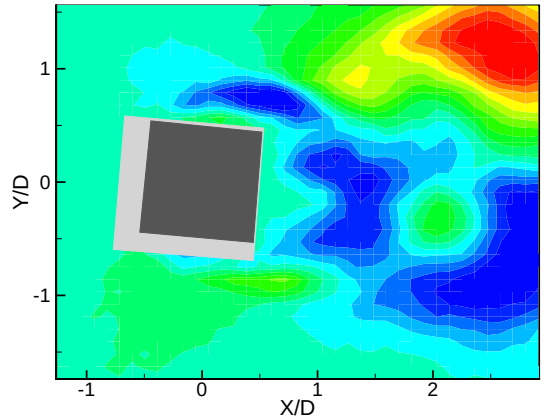

v6

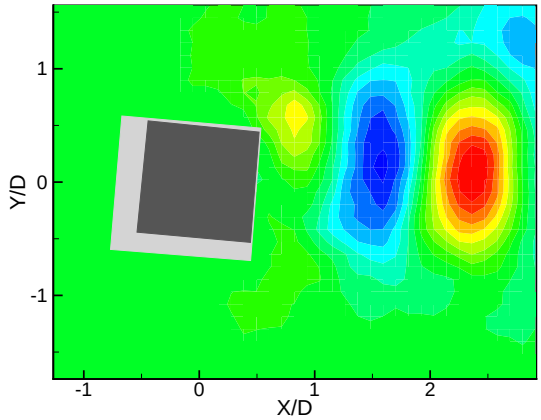

Angle of incidence: 7.5°

u1

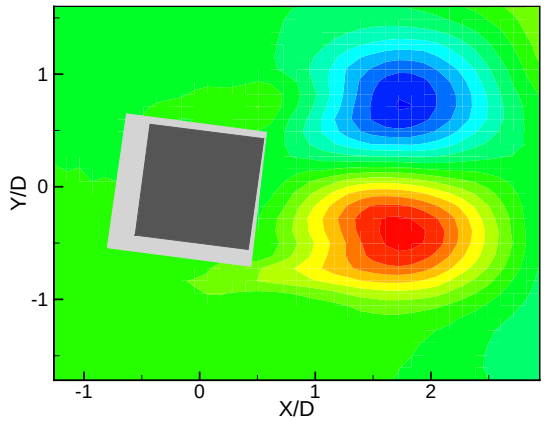

v1

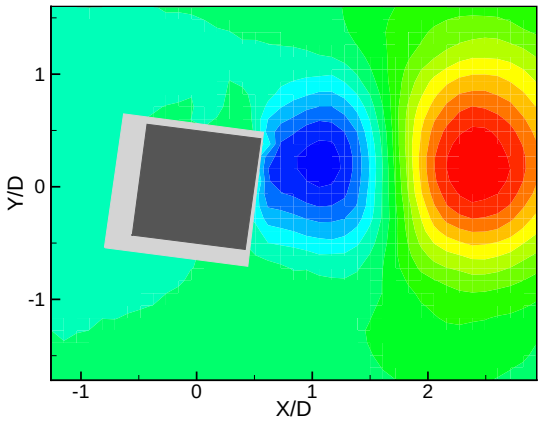

u2

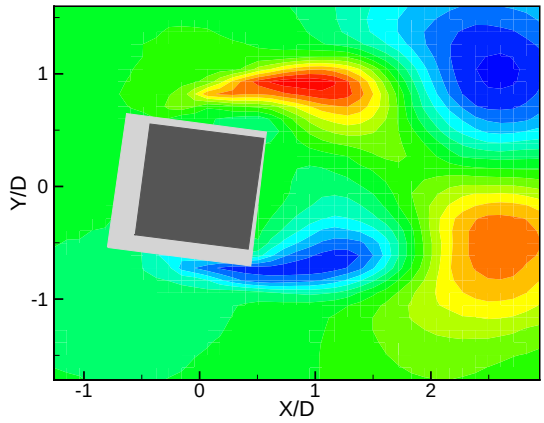

v2

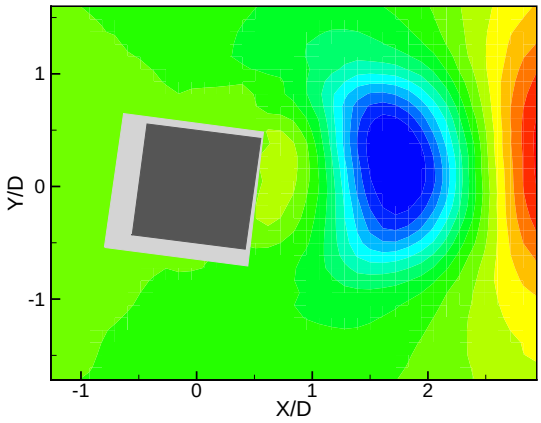

u3

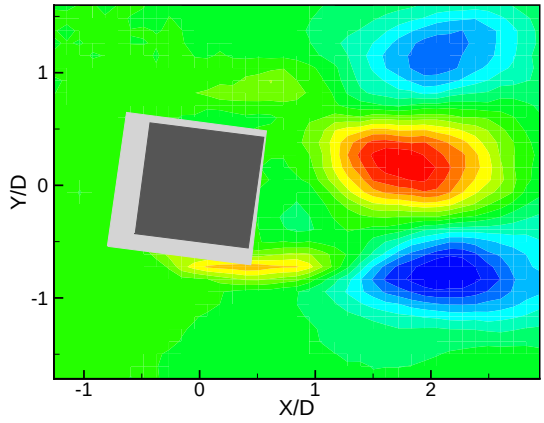

v3

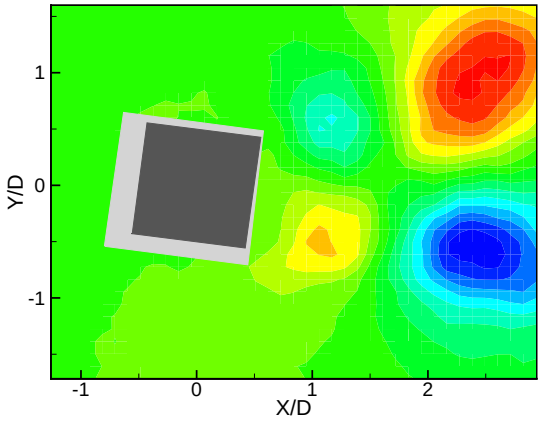

u4

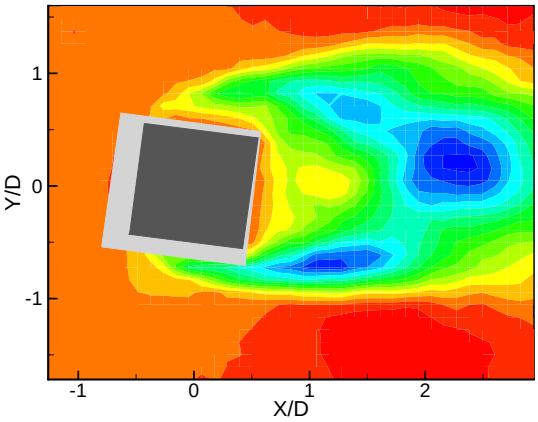

v4

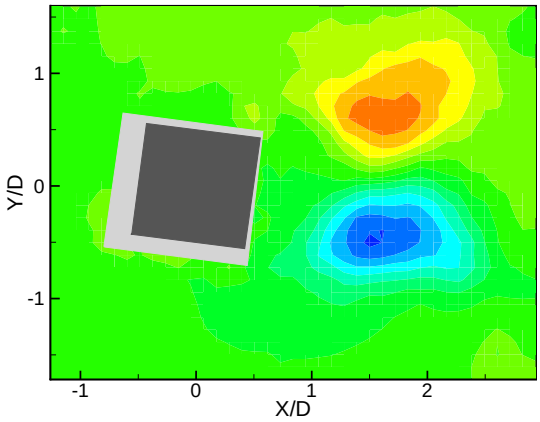

u5

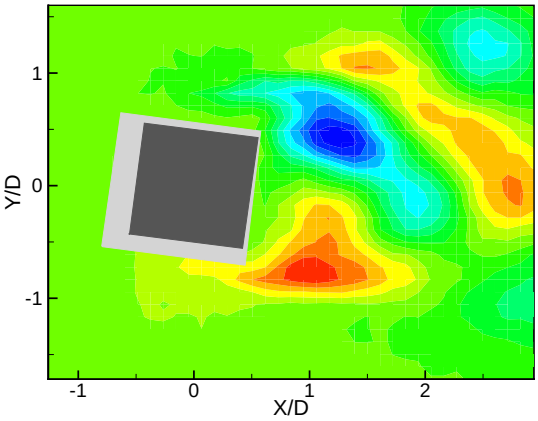

v5

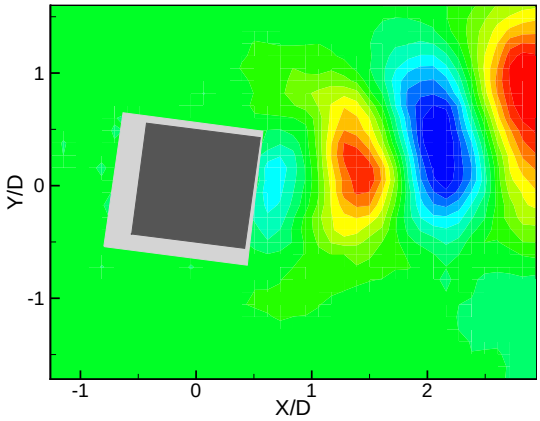

u6

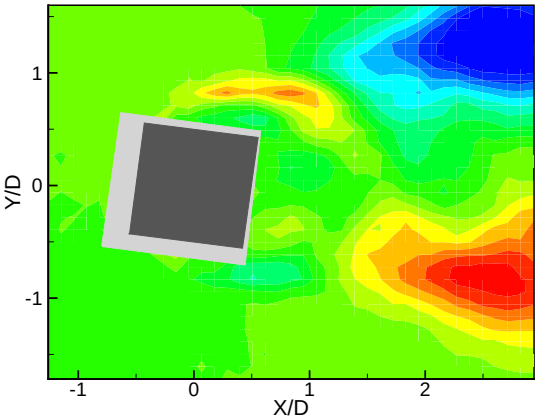

v6

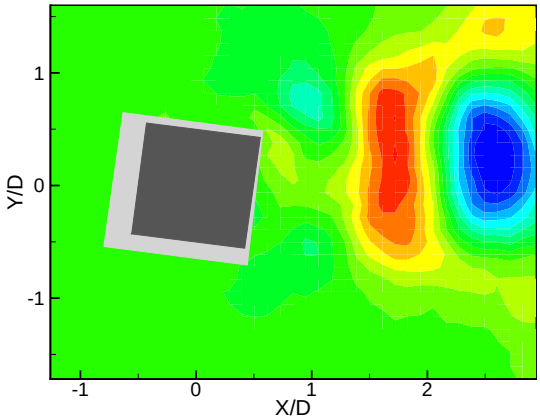

Angle of incidence: 10°

u1

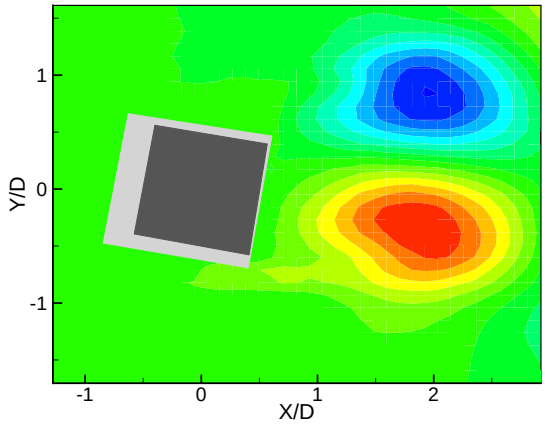

v1

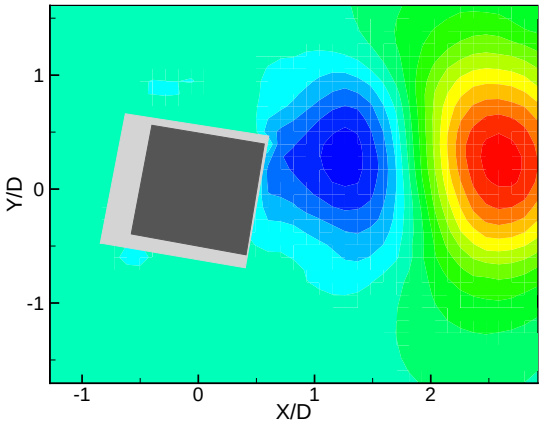

u2

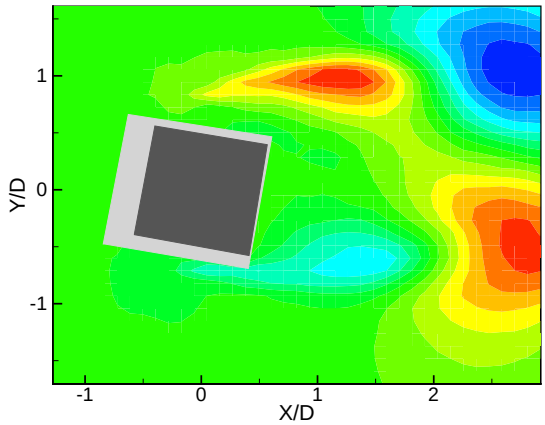

v2

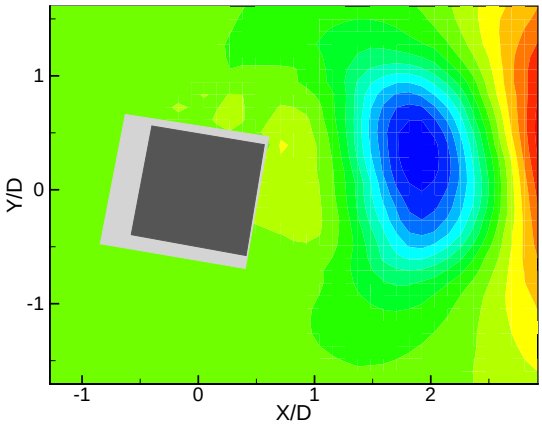

u3

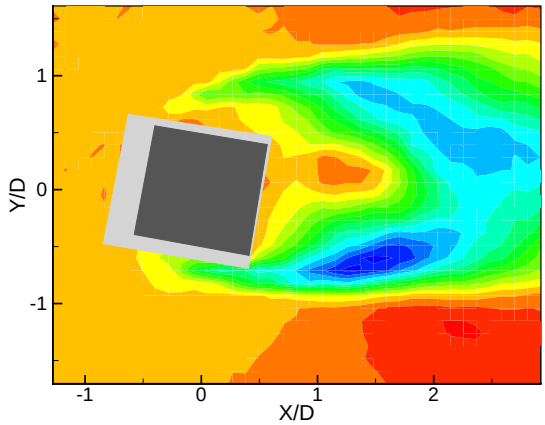

v3

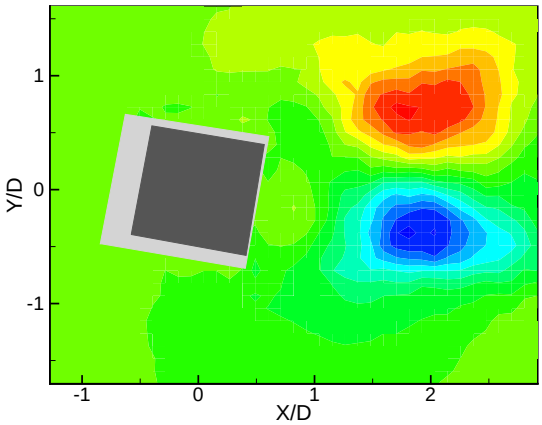

u4

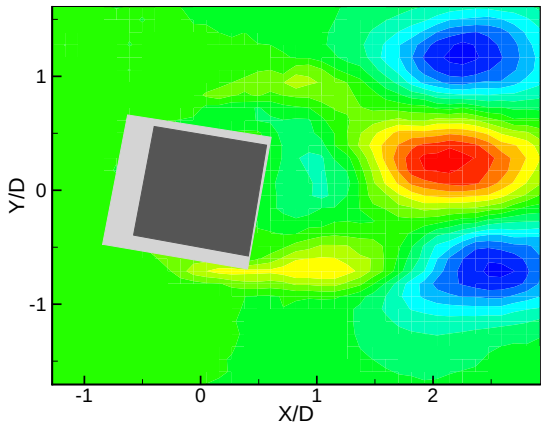

v4

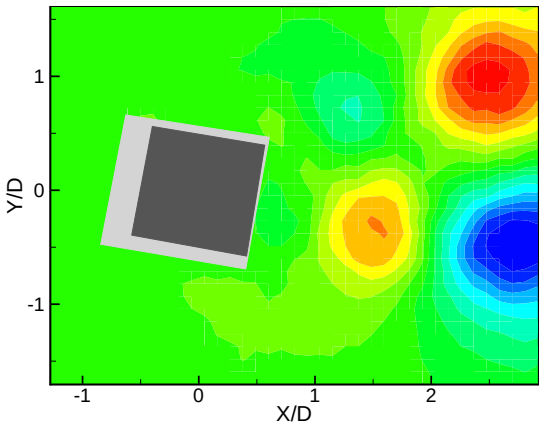

u5

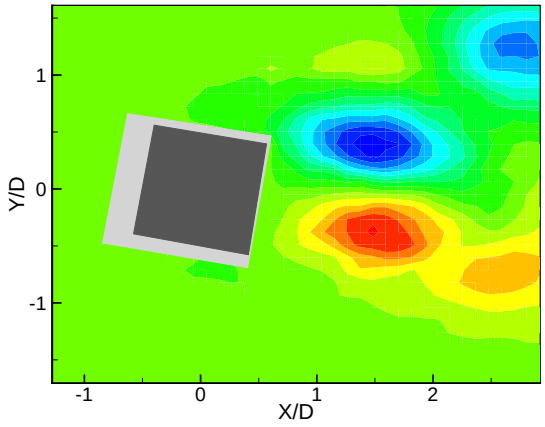

v5

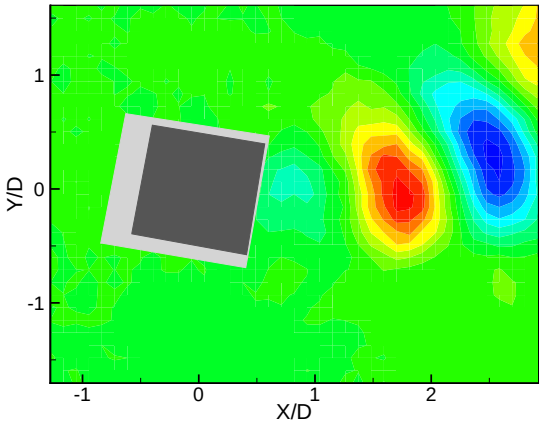

u6

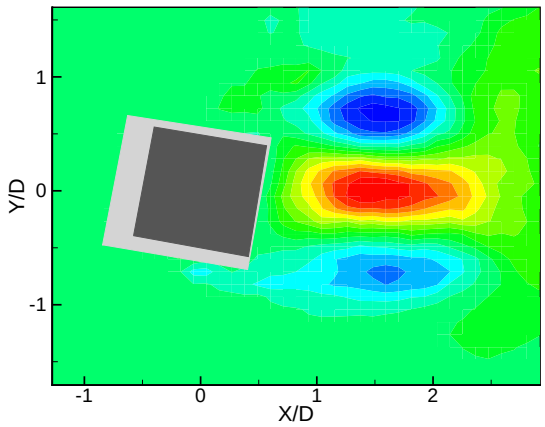

v6

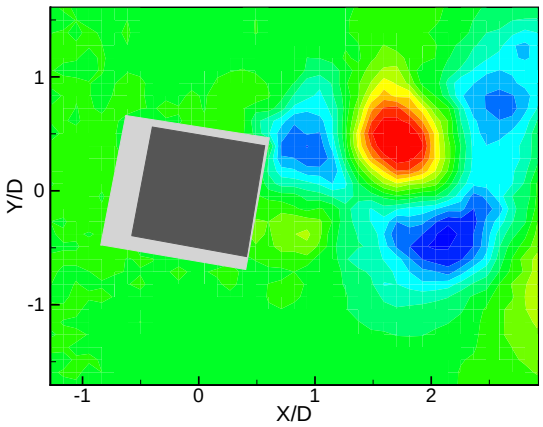

Angle of incidence: 12.5°

u1

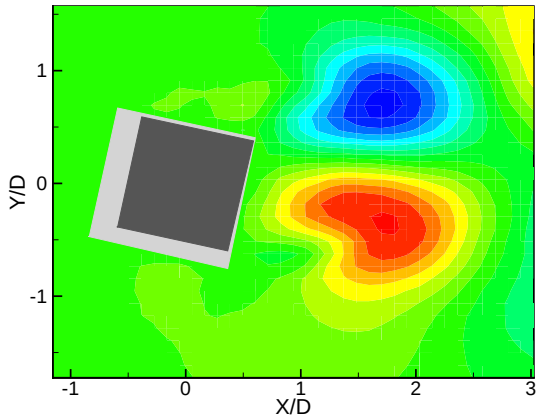

v1

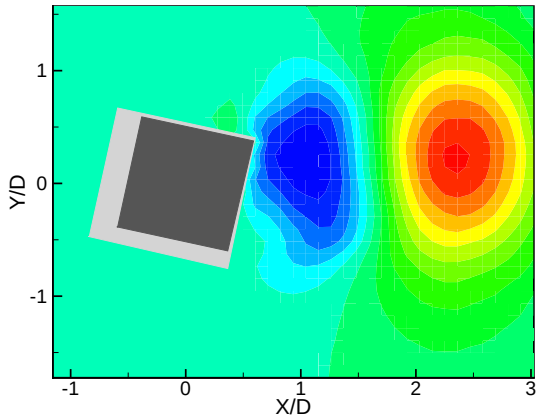

u2

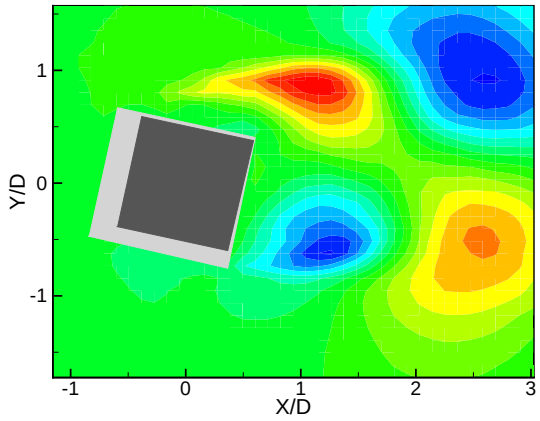

v2

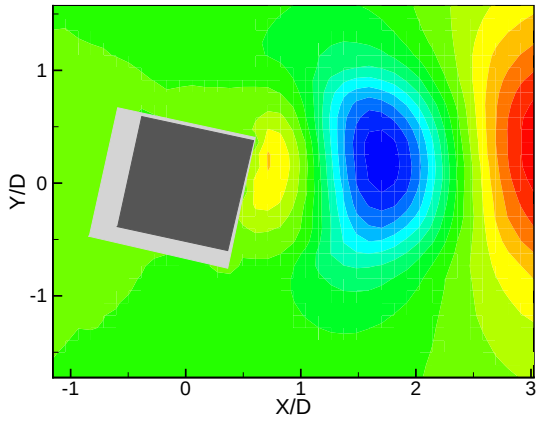

u3

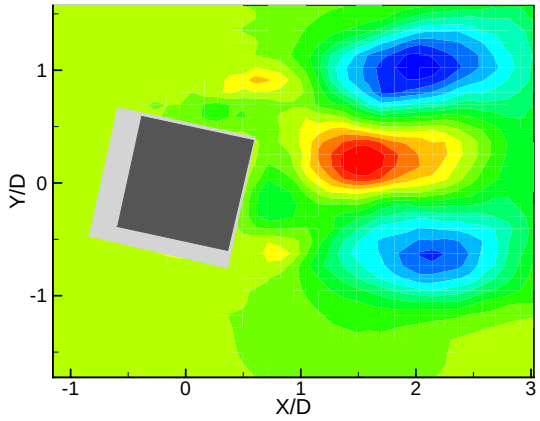

v3

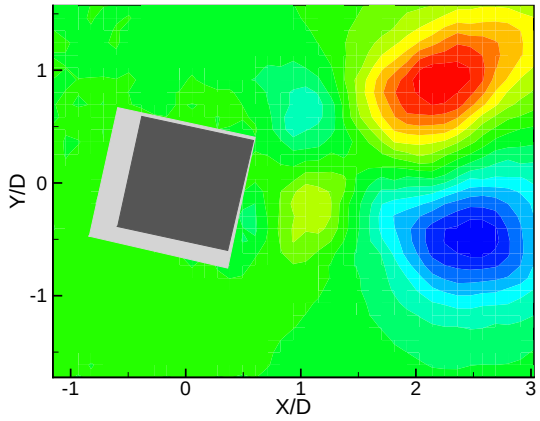

u4

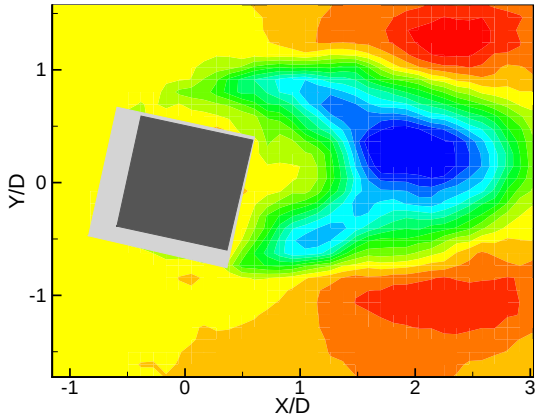

v4

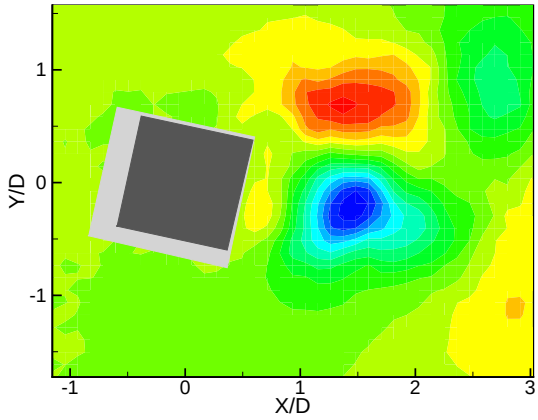

u5

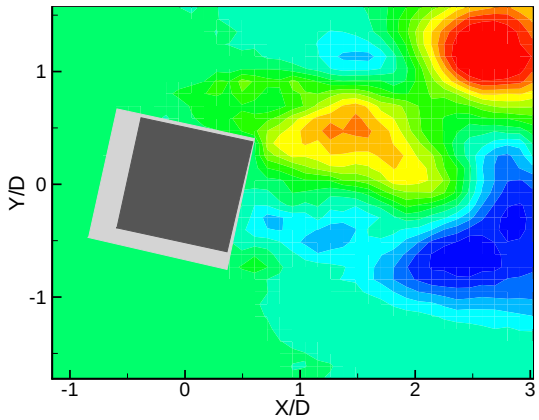

v5

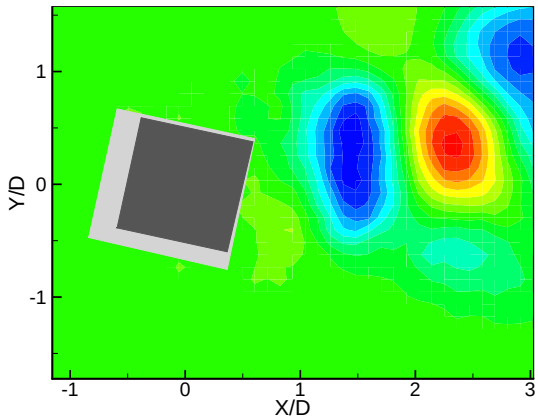

u6

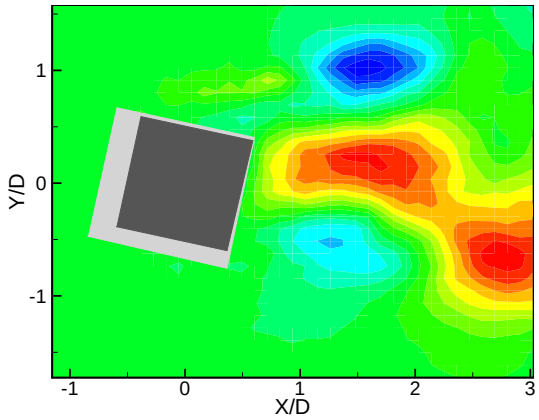

v6

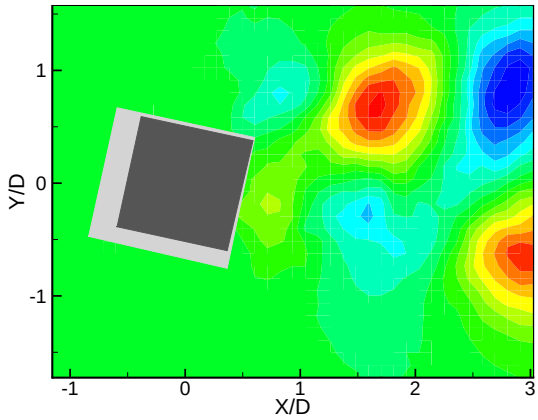

Angle of incidence: 15°

u1

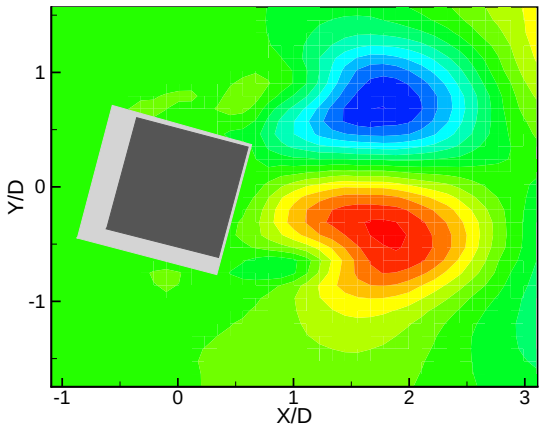

v1

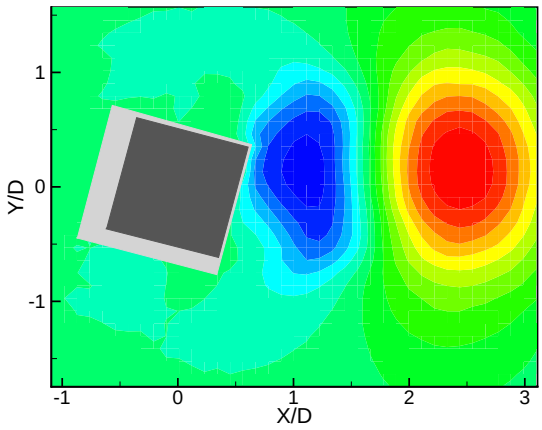

u2

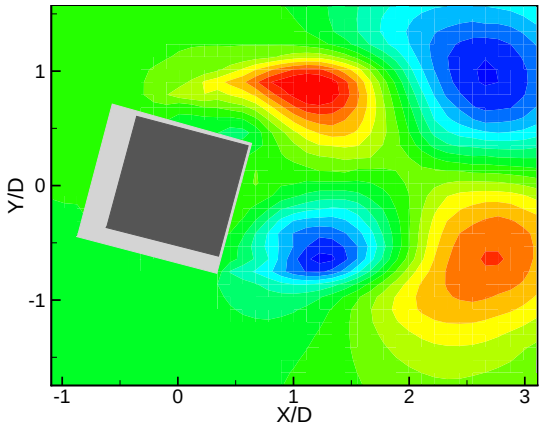

v2

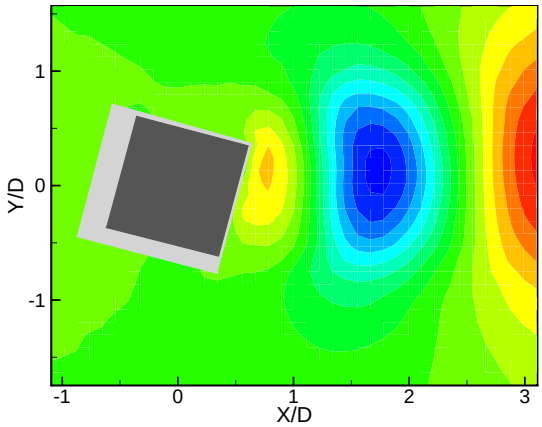

u3

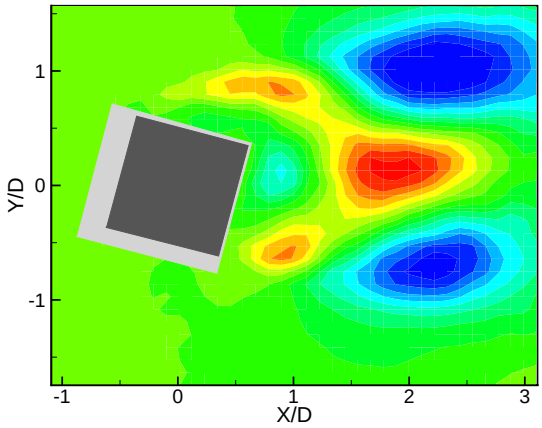

v3

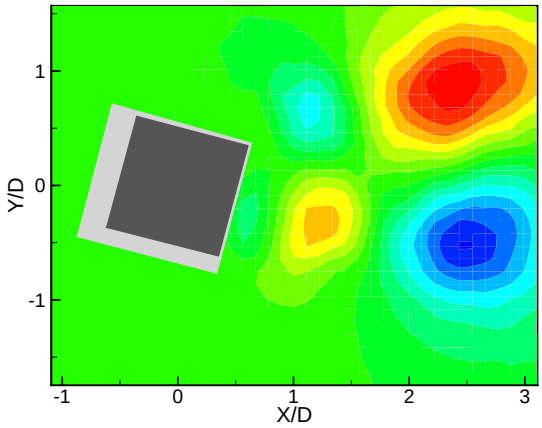

u4

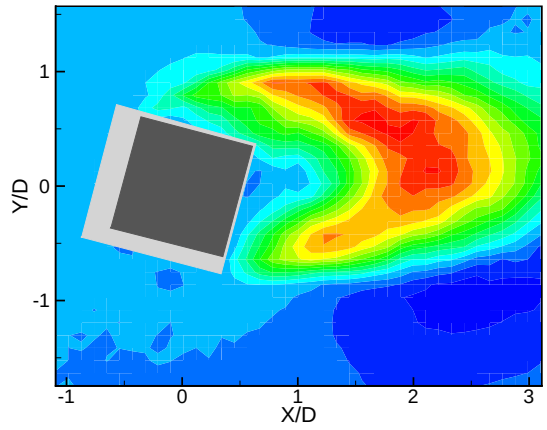

v4

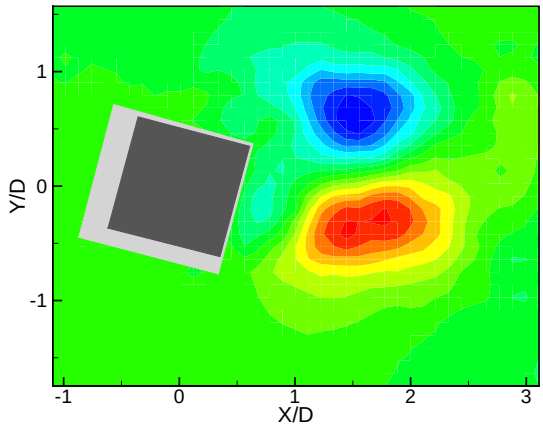

u5

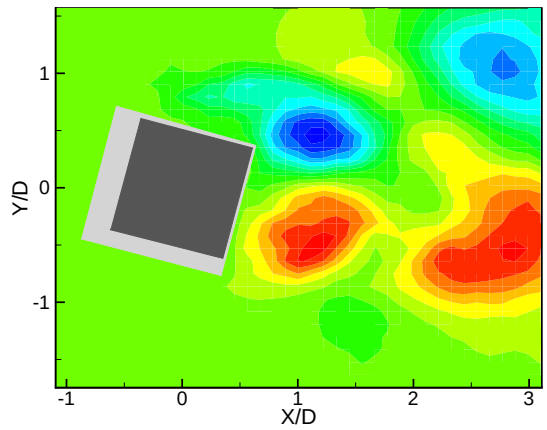

v5

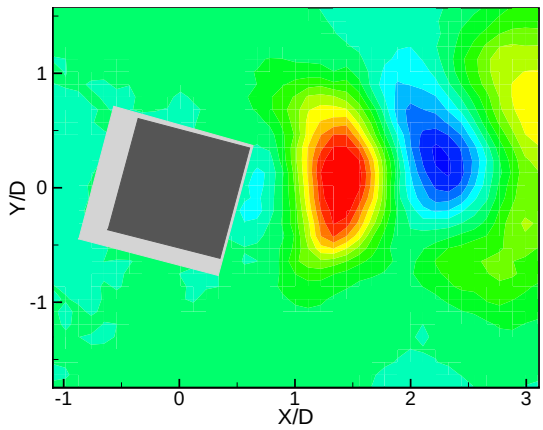

u6

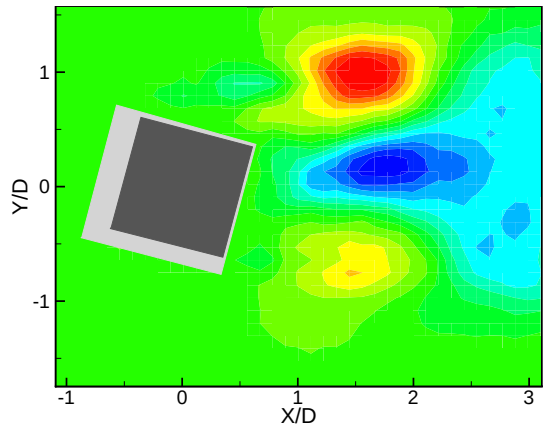

v6

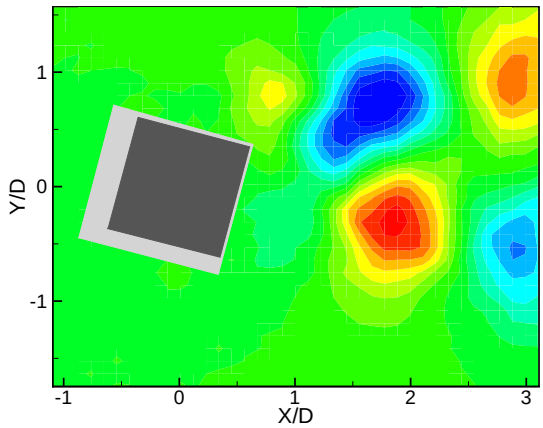

Angle of incidence: 20°

u1

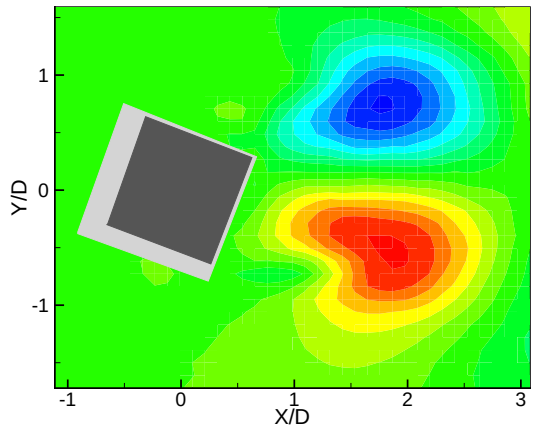

v1

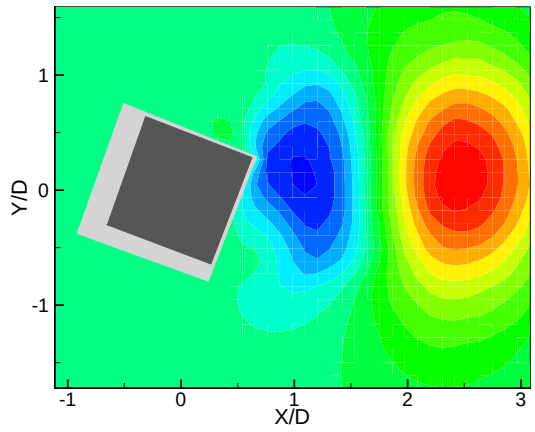

u2

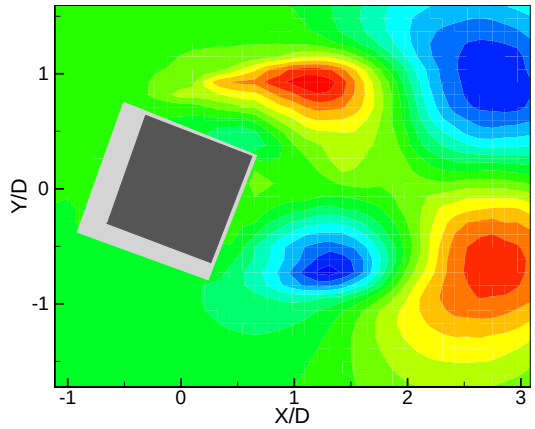

v2

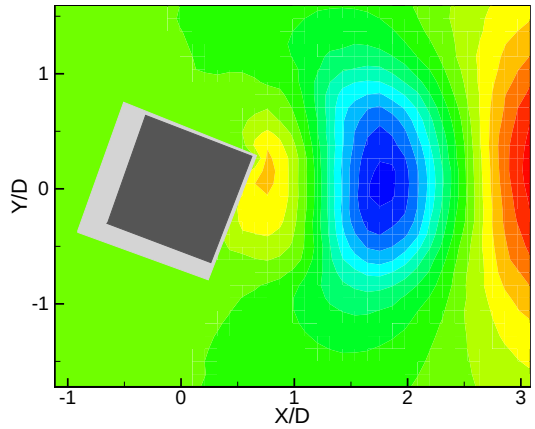

u3

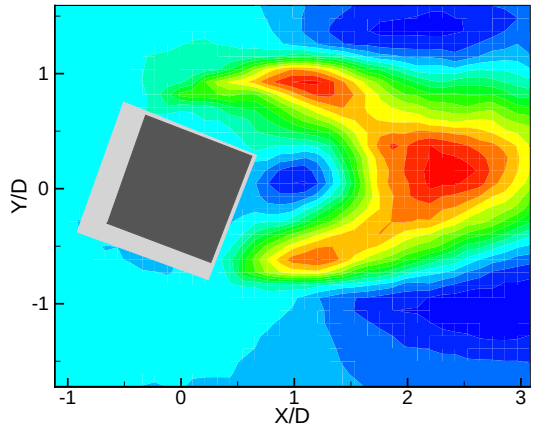

v3

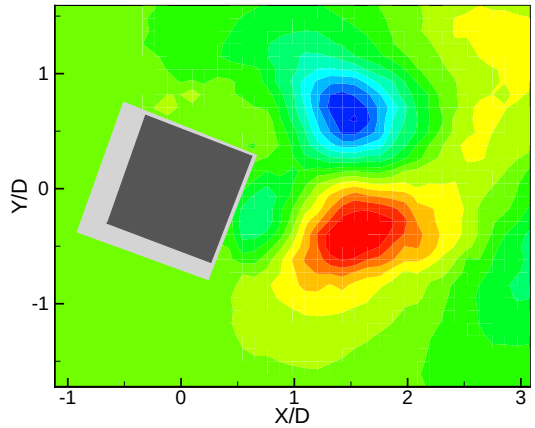

u4

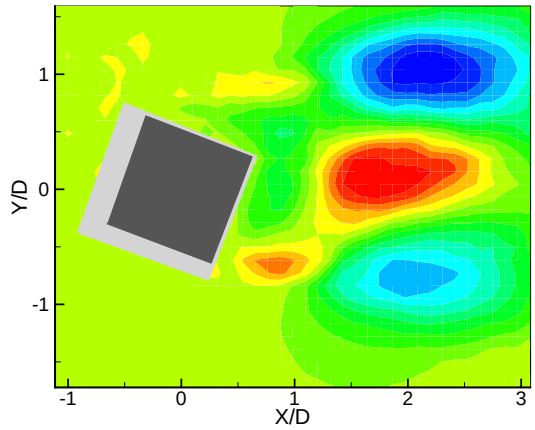

v4

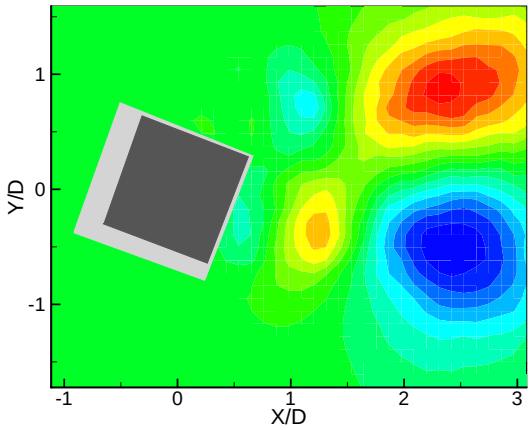

u5

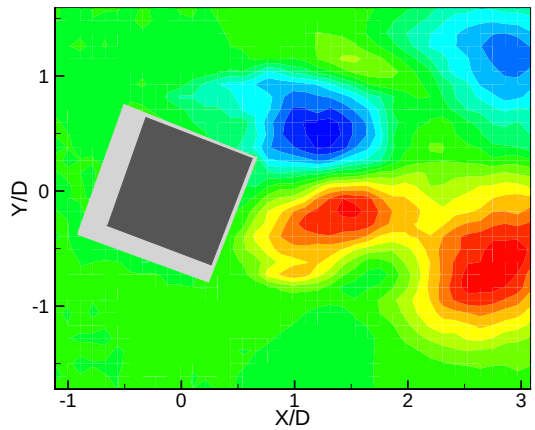

v5

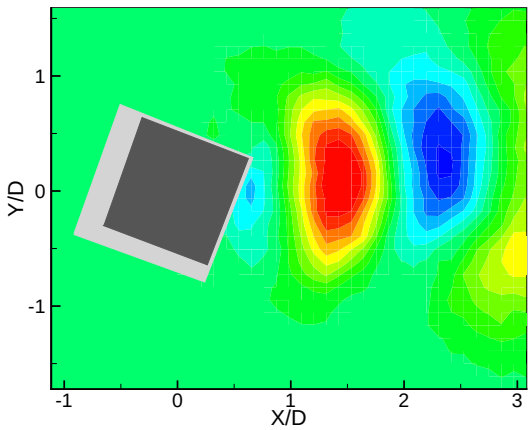

u6

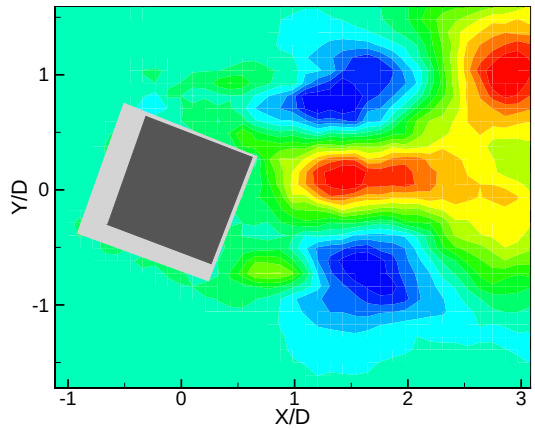

v6

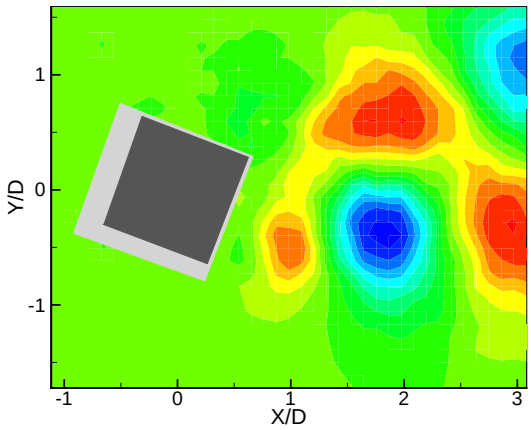

Angle of incidence: 25°

u1

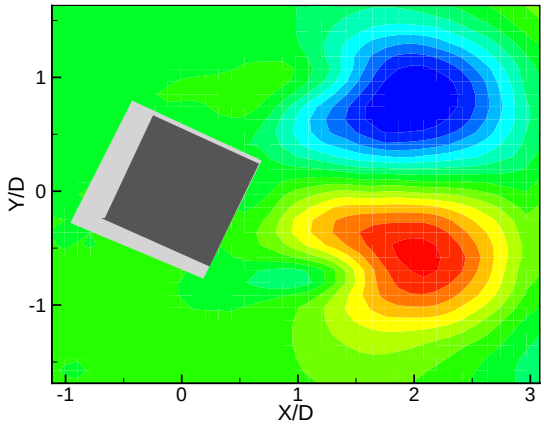

v1

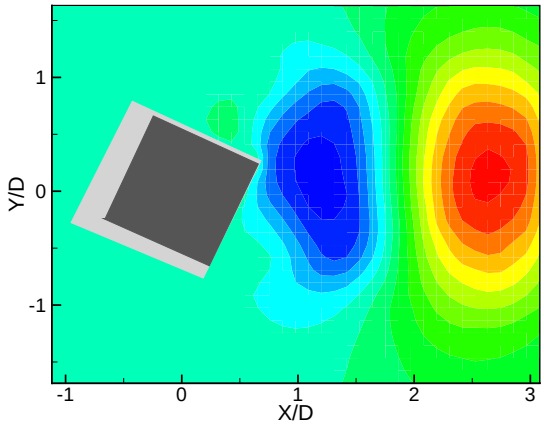

u2

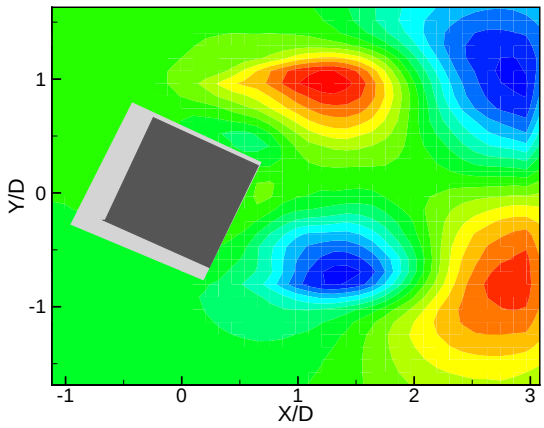

v2

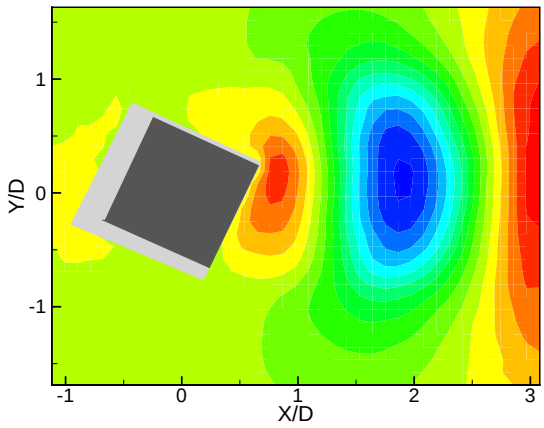

u3

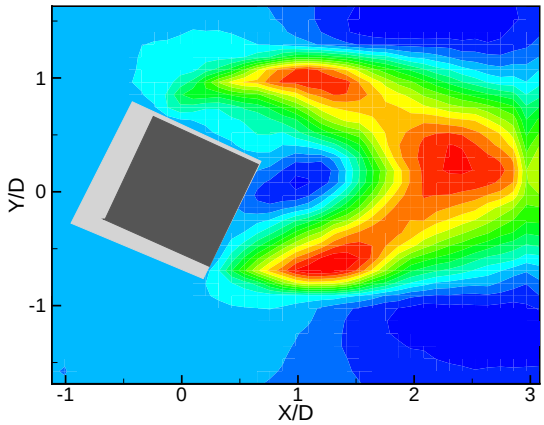

v3

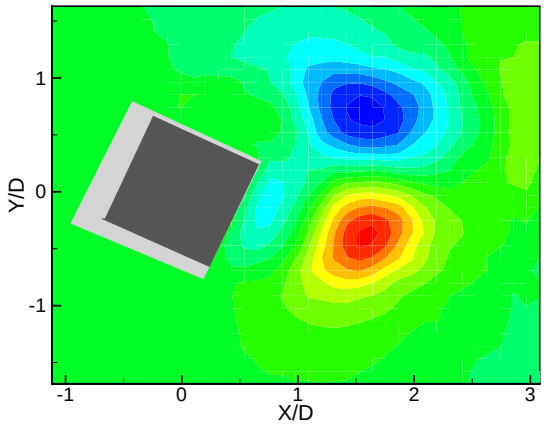

u4

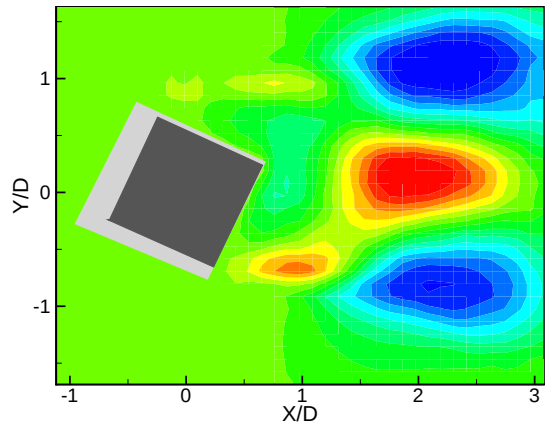

v4

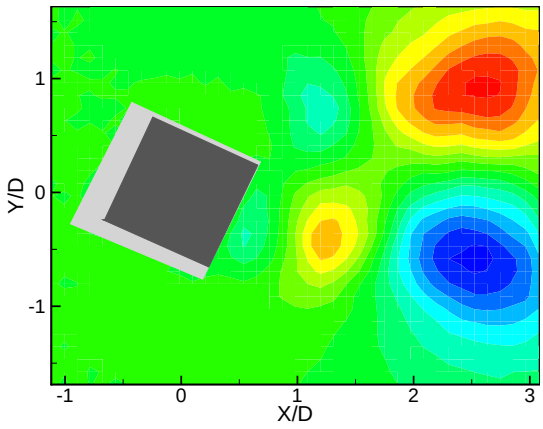

u5

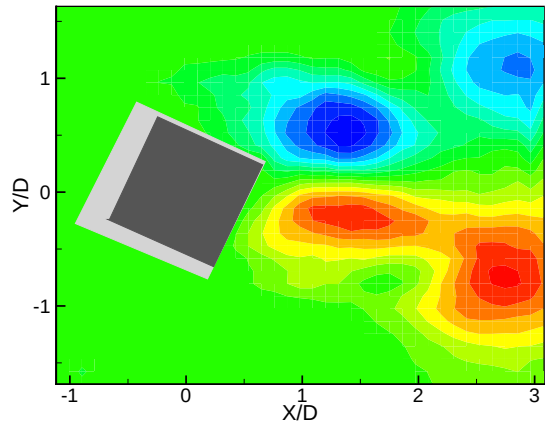

v5

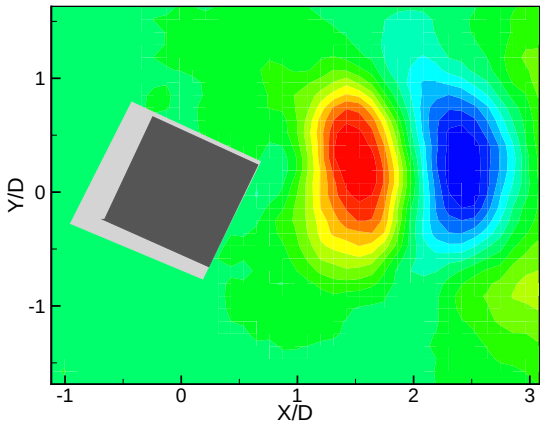

u6

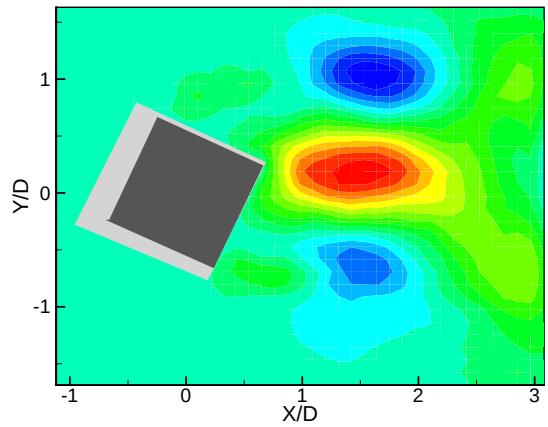

v6

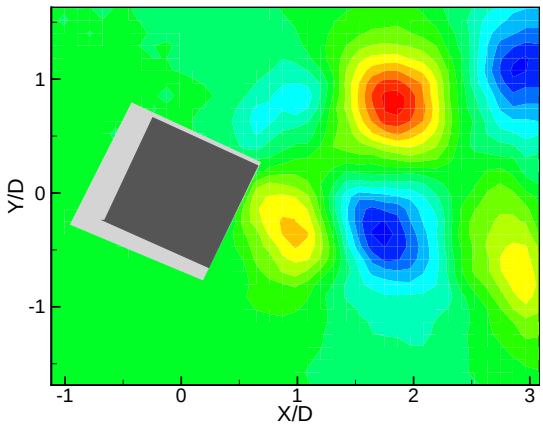

Angle of incidence: 30°

u1

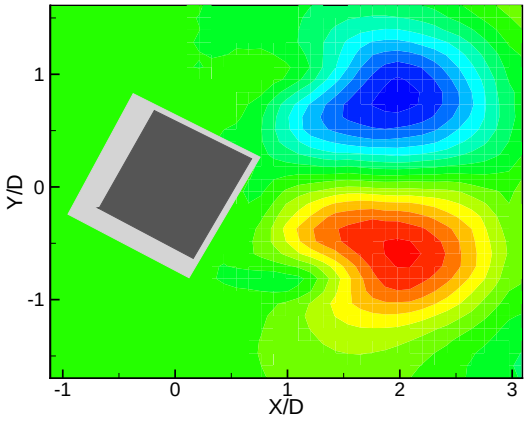

v1

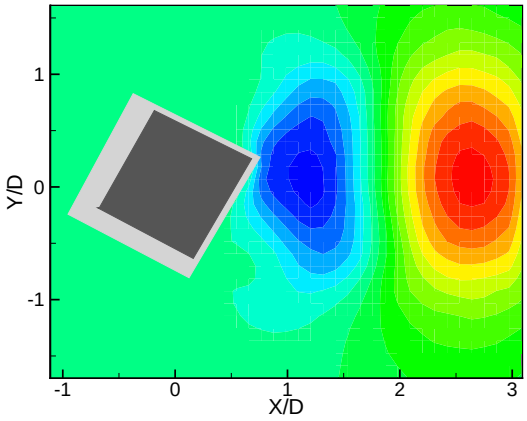

u2

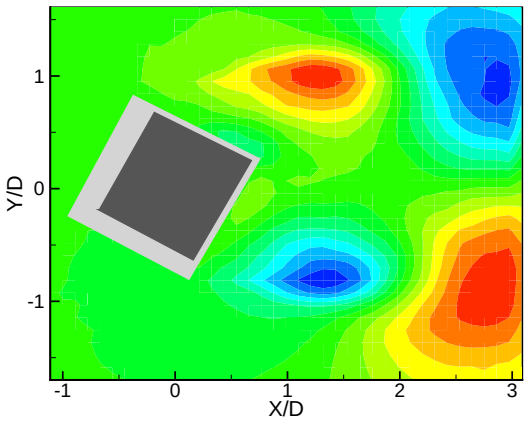

v2

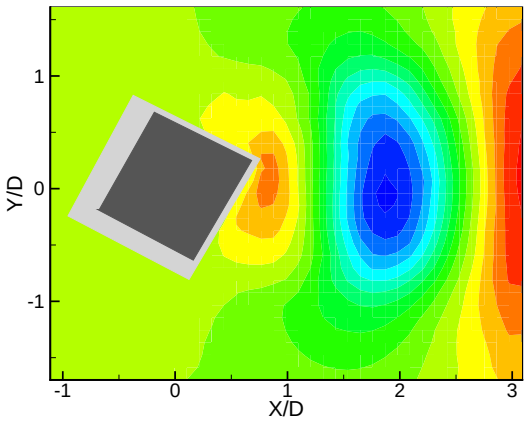

u3

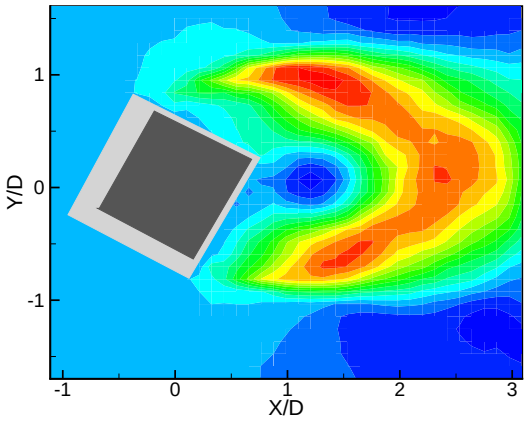

v3

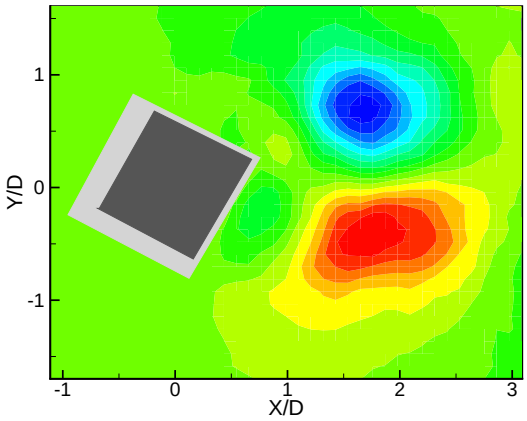

u4

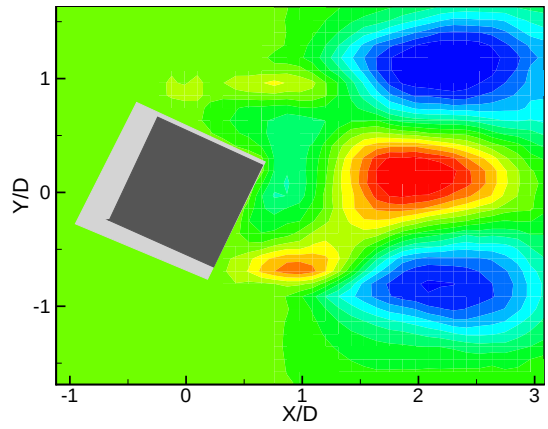

v4

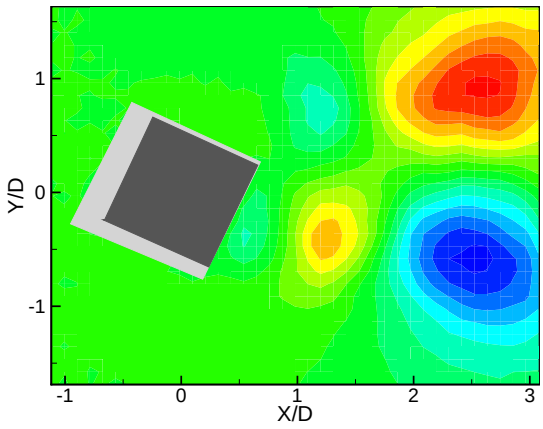

u5

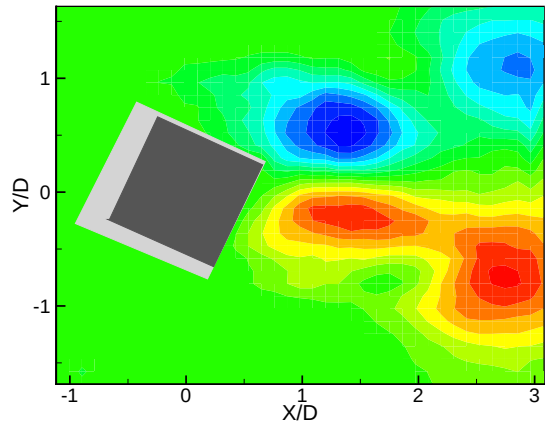

v5

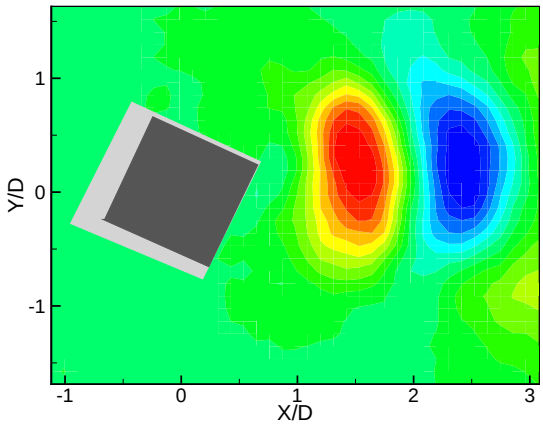

u6

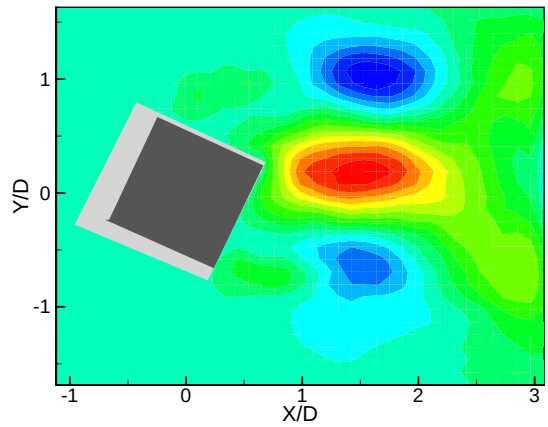

v6

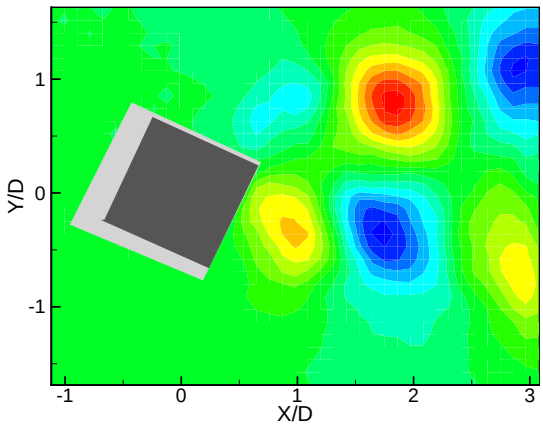

Angle of incidence: 35°

u1

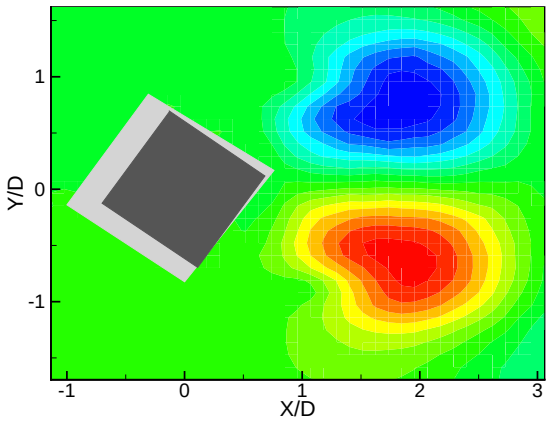

v1

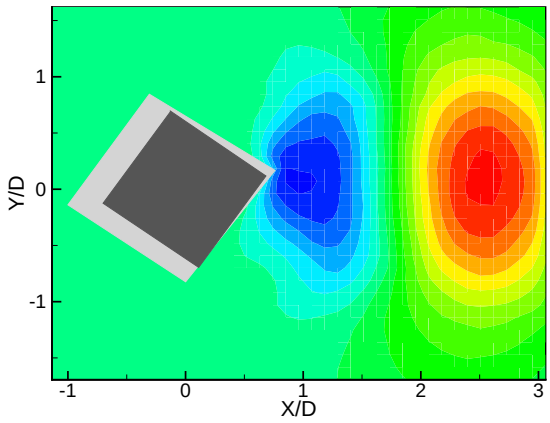

u2

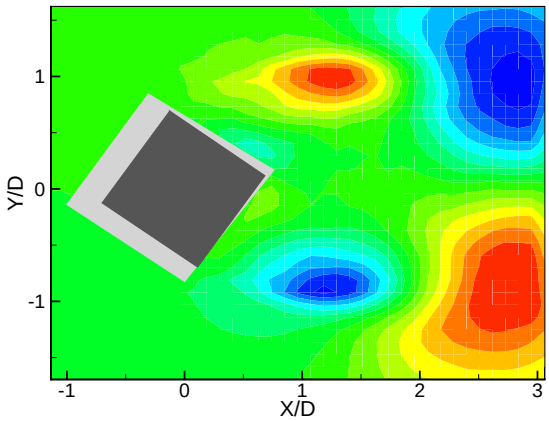

v2

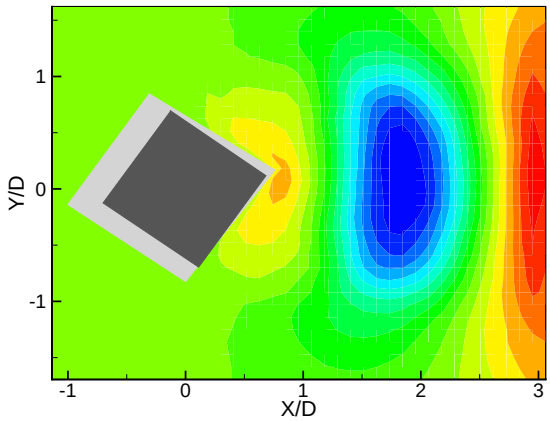

u3

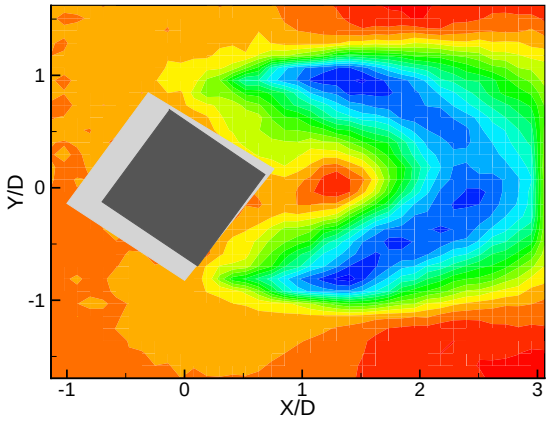

v3

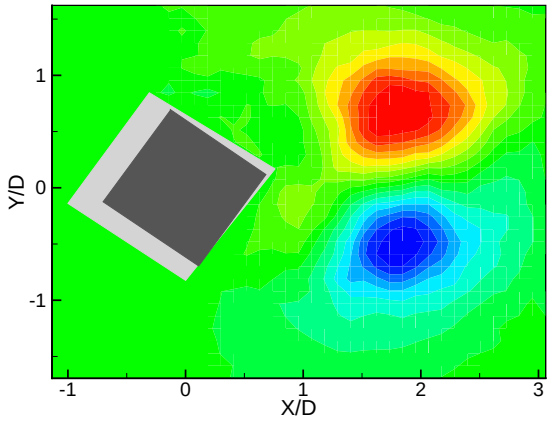

u4

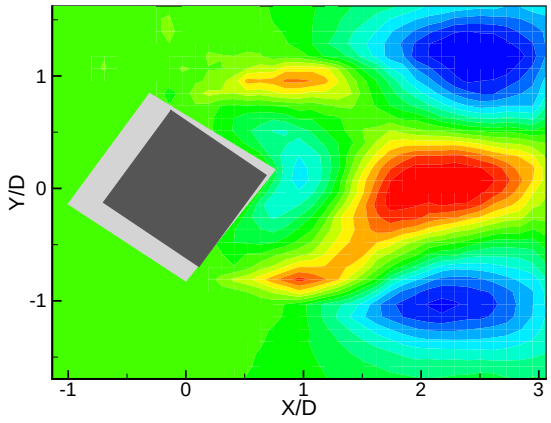

v4

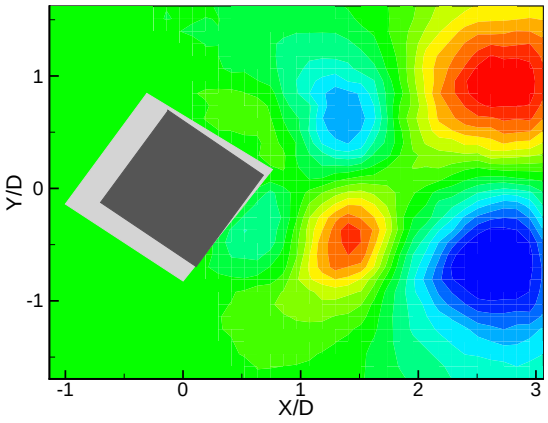

u5

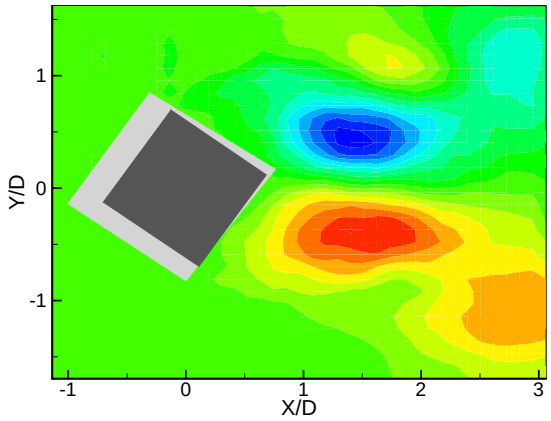

v5

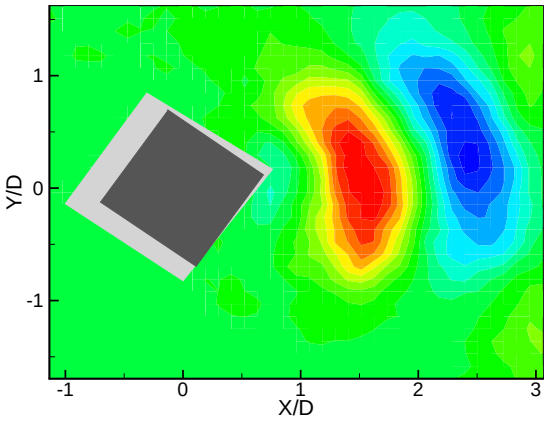

u6

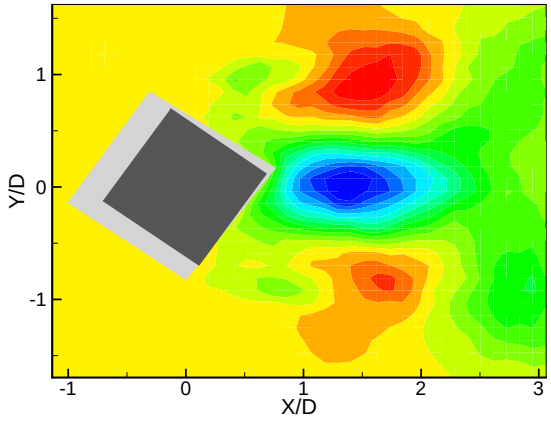

v6

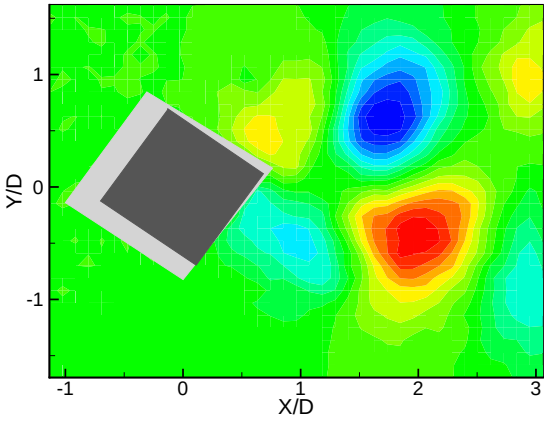

Angle of incidence: 40°

u1

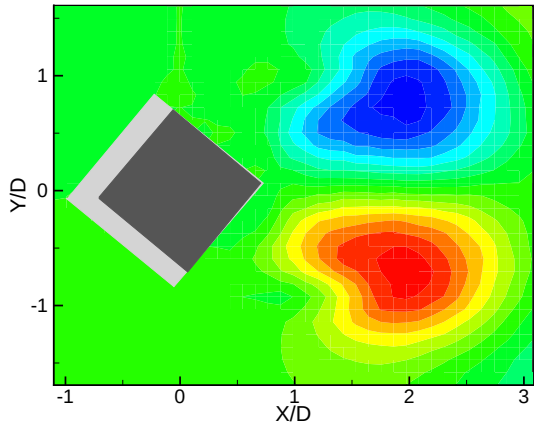

v1

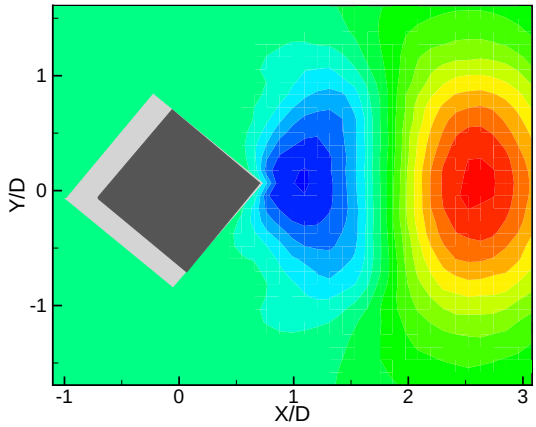

u2

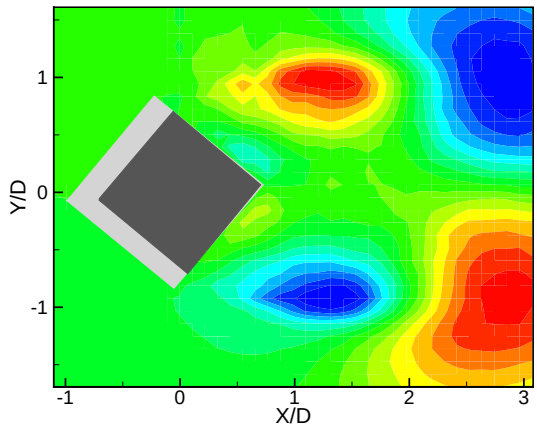

v2

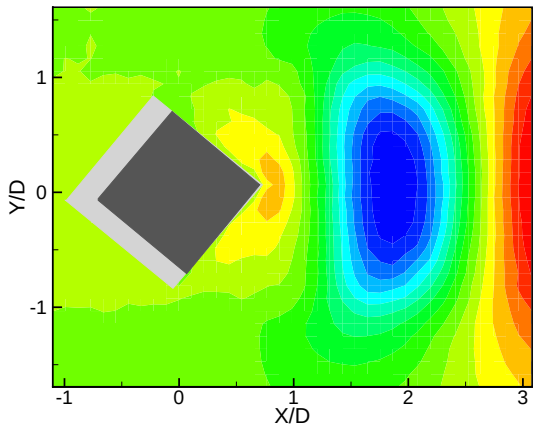

u3

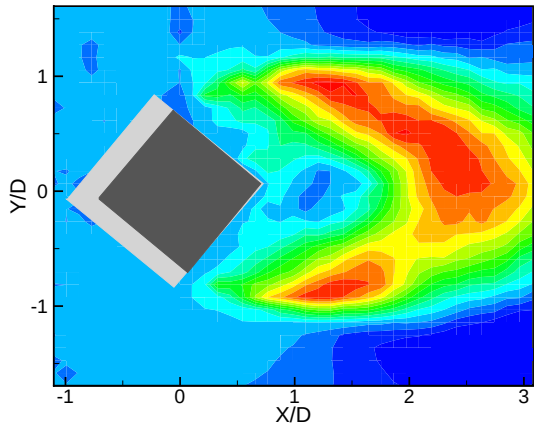

v3

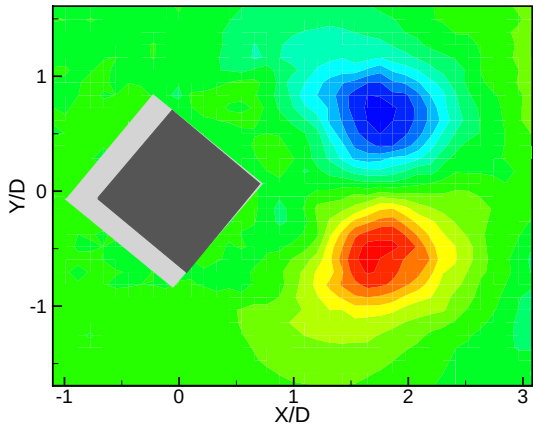

u4

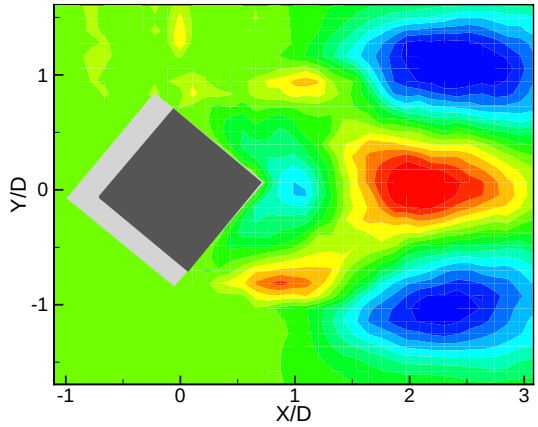

v4

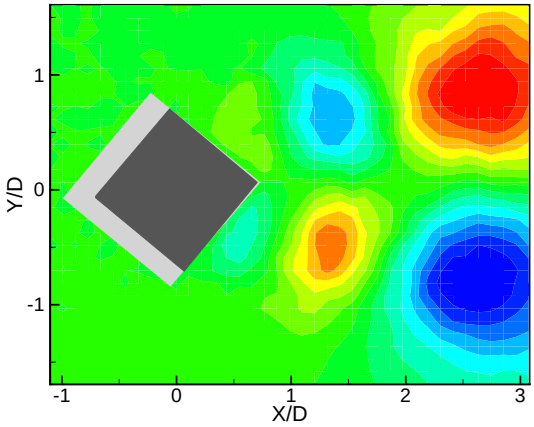

u5

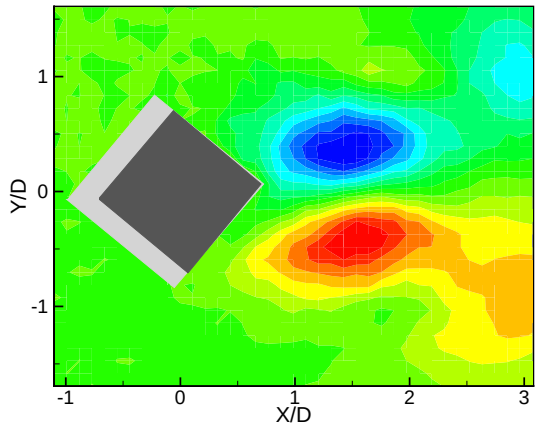

v5

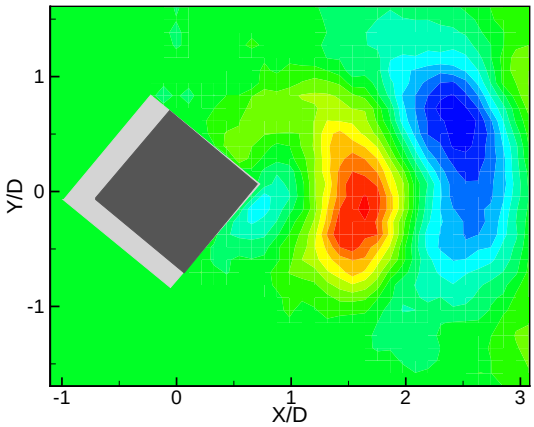

u6

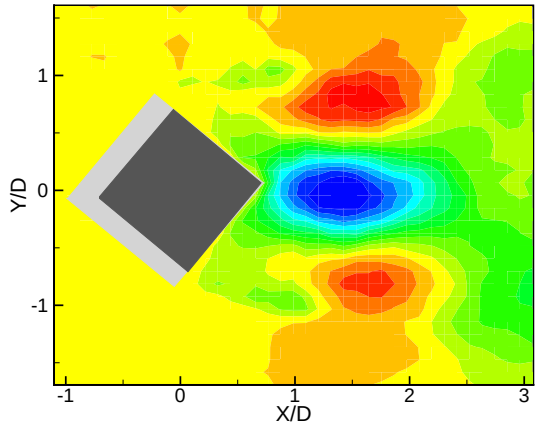

v6

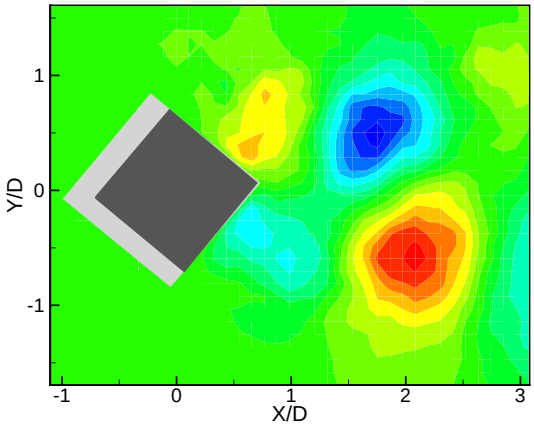

Angle of incidence: 45°

u1

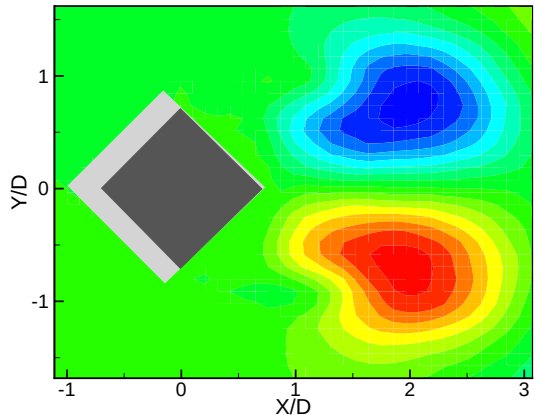

v1

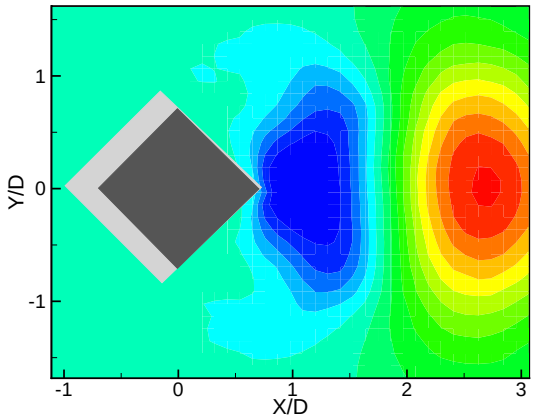

u2

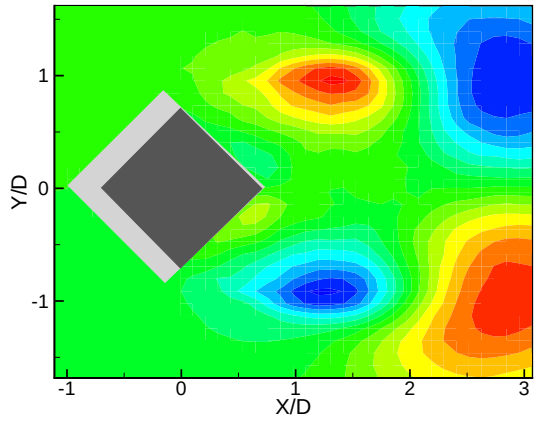

v2

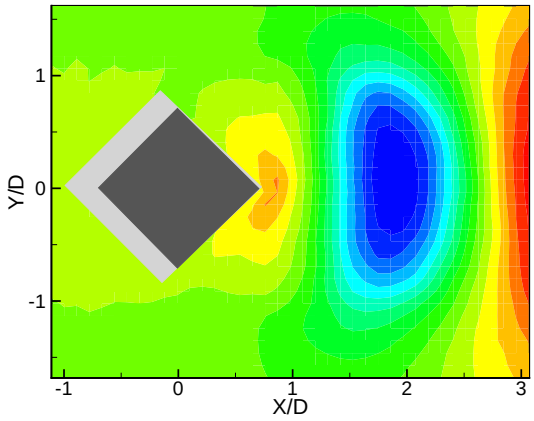

u3

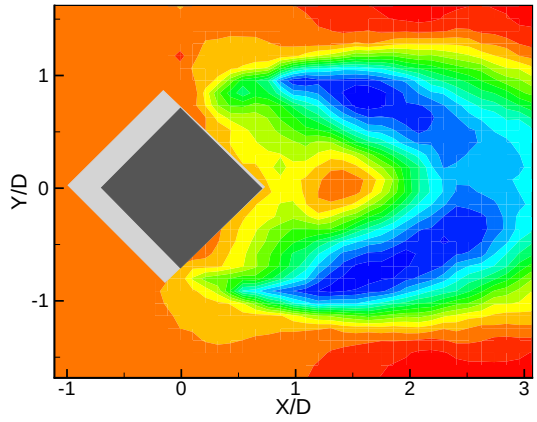

v3

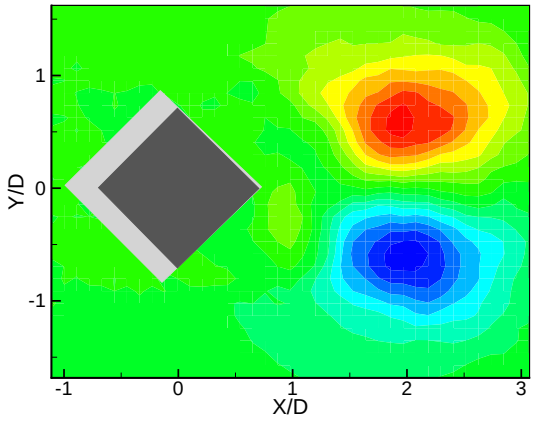

u4

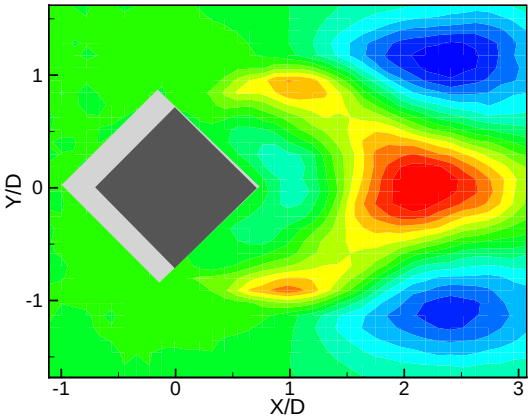

v4

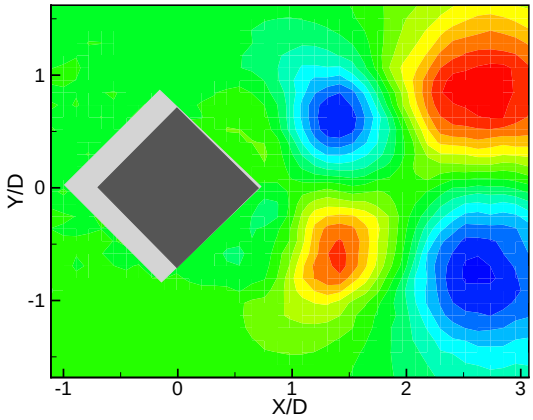

u5

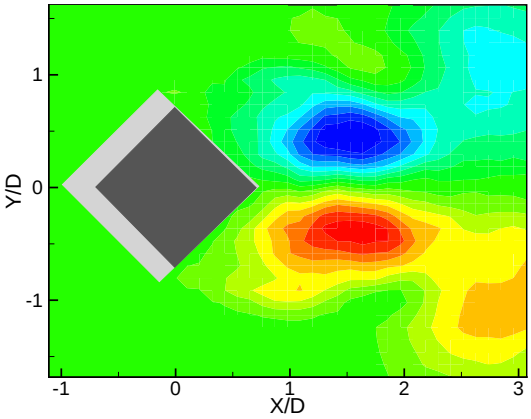

v5

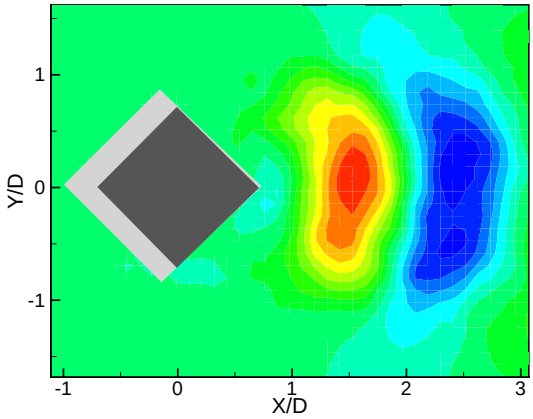

u6

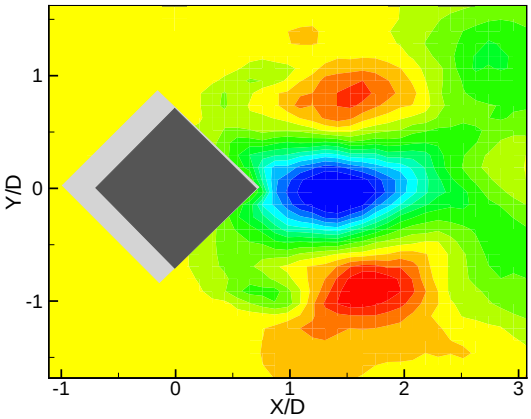

v6

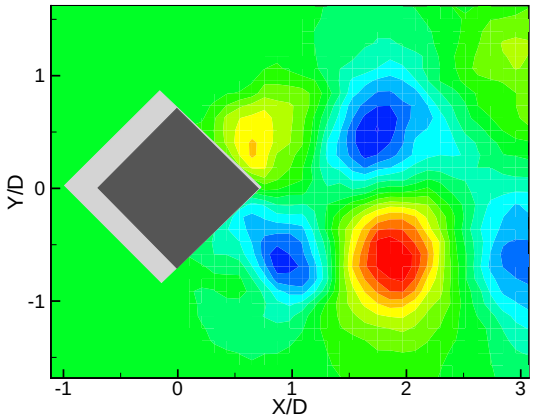

D.2.2 Fluctuating velocities reconstructed from first 6 POD modes

Angle of incidence: 0°, u_{rms}

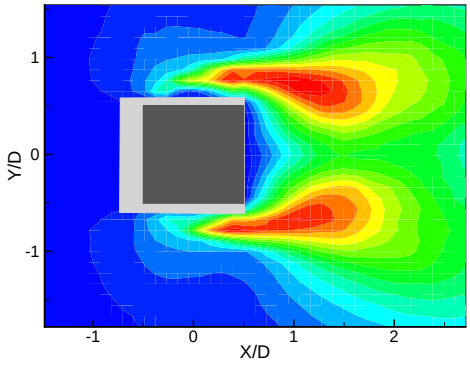

v_{rms}

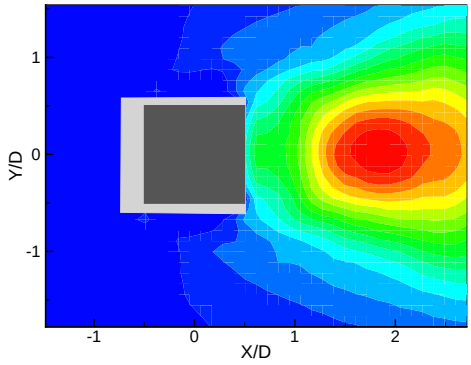

Angle of incidence: 2.5°, u_{rms}

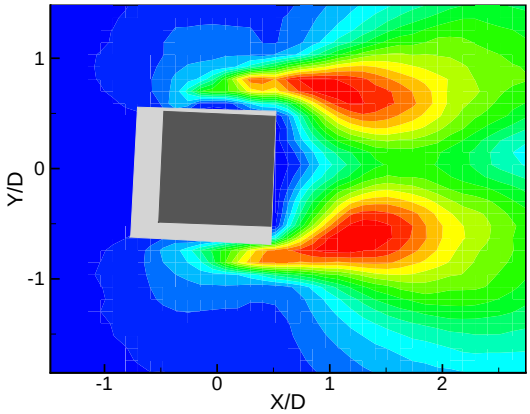

v_{rms}

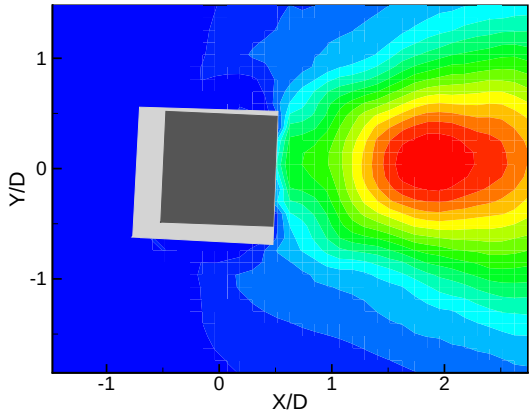

Angle of incidence: 5°, u_{rms}

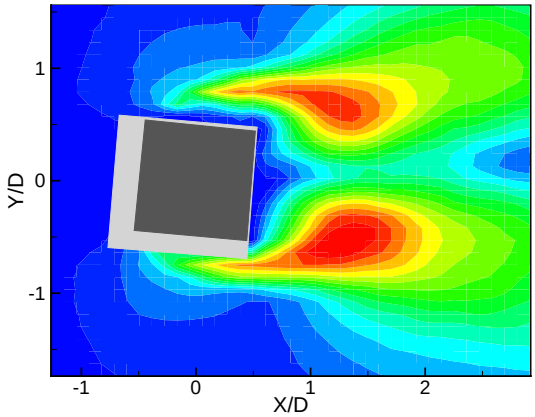

v_{rms}

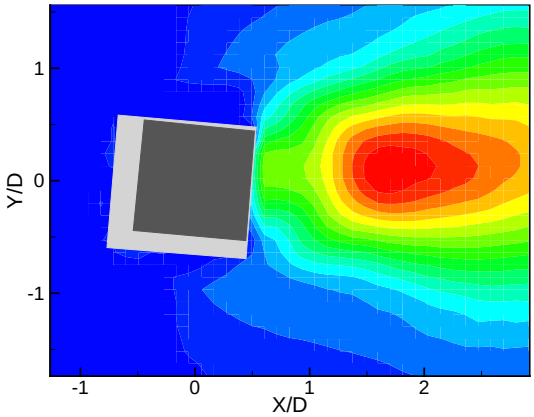

Angle of incidence: 7.5°, u_{rms}

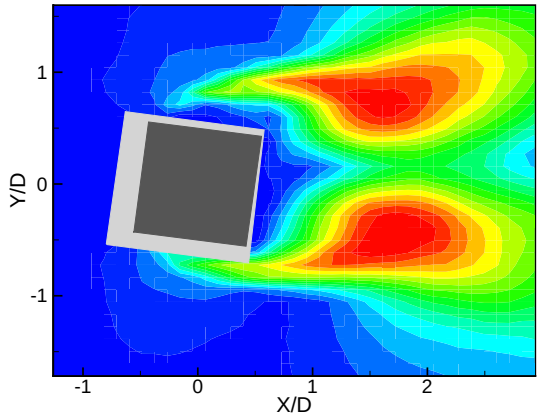

v_{rms}

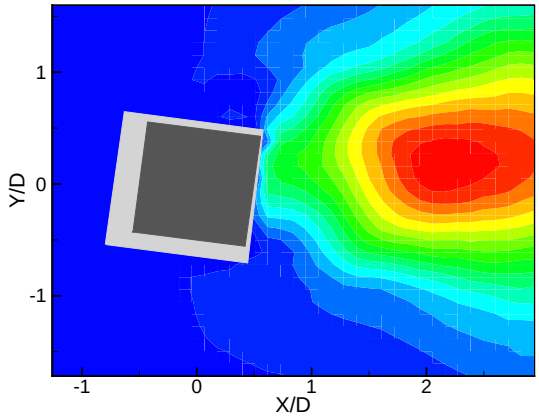

Angle of incidence: 10°, u_{rms}

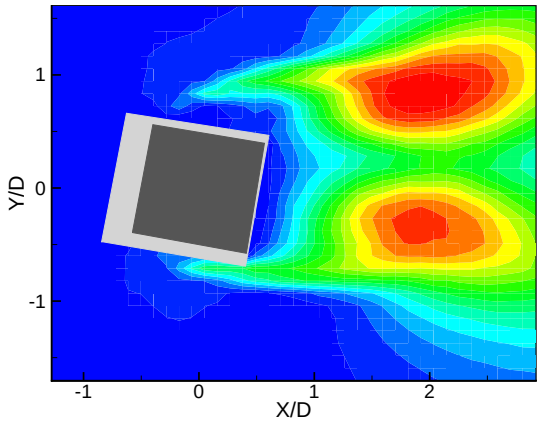

v_{rms}

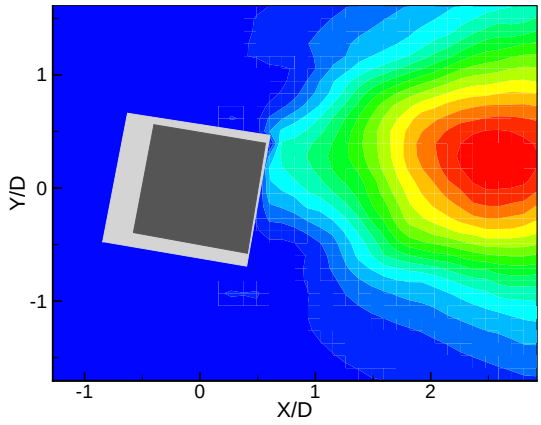

Angle of incidence: 12.5°, u_{rms}

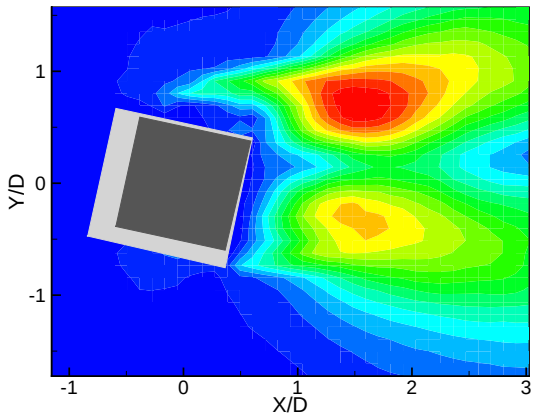

v_{rms}

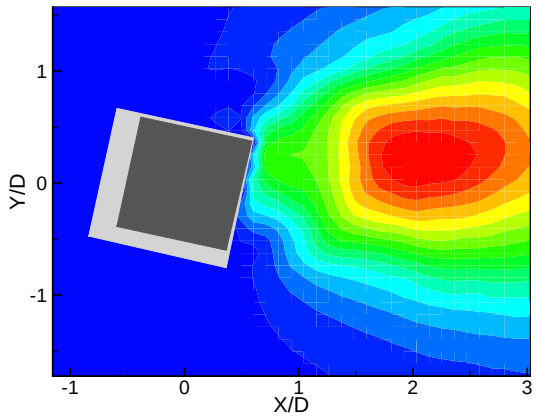

Angle of incidence: 15°, u_{rms}

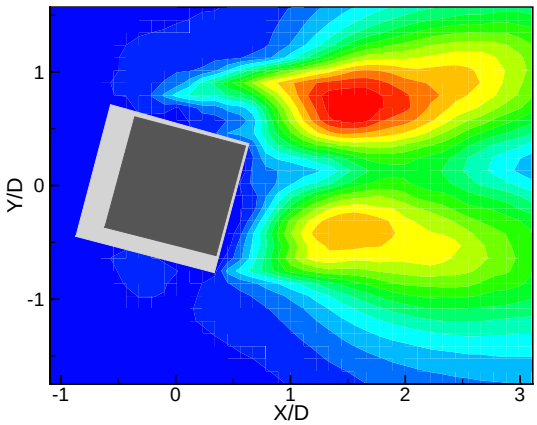

v_{rms}

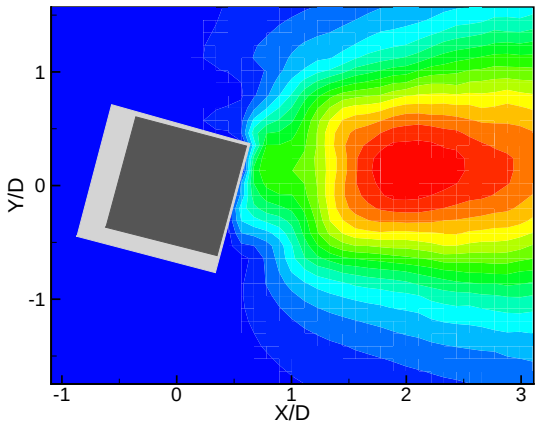

Angle of incidence: 20°, u_{rms}

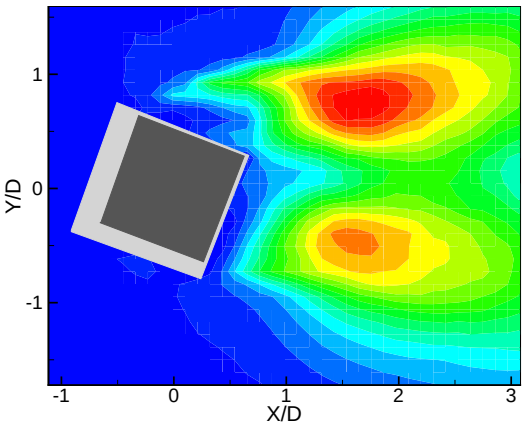

v_{rms}

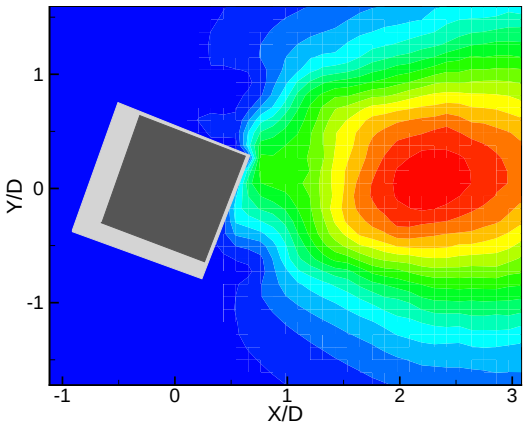

Angle of incidence: 25°, u_{rms}

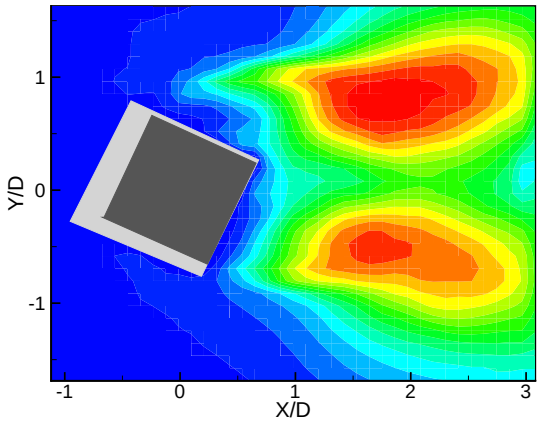

v_{rms}

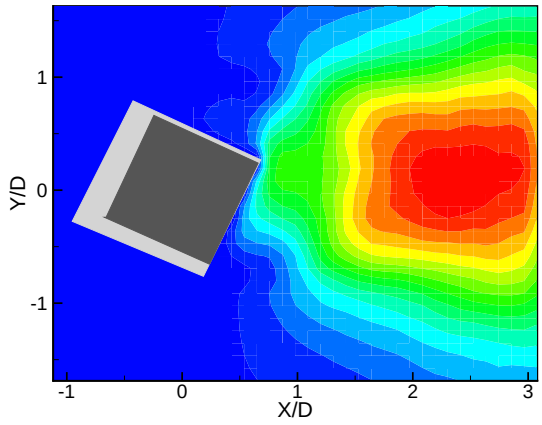

Angle of incidence: 30°, u_{rms}

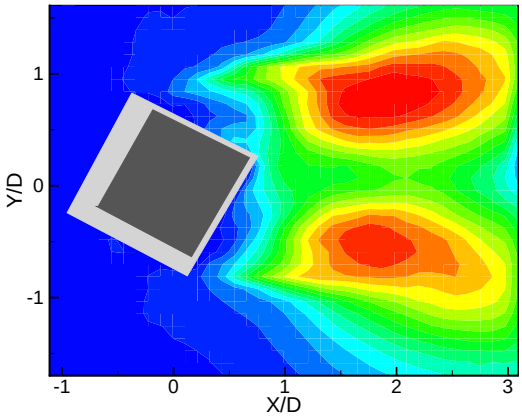

v_{rms}

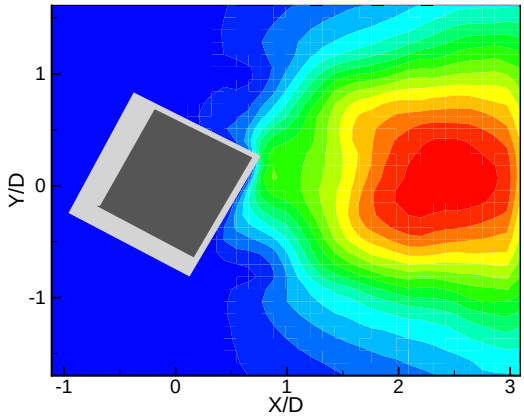

Angle of incidence: 35°, u_{rms}

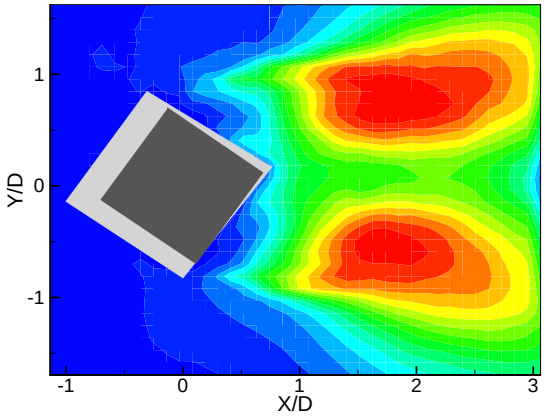

v_{rms}

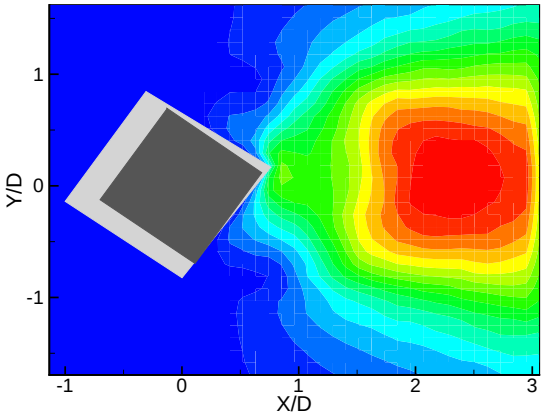

Angle of incidence: 40°, u_{rms}

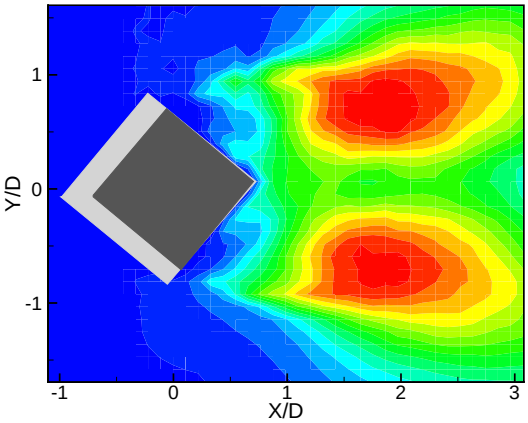

v_{rms}

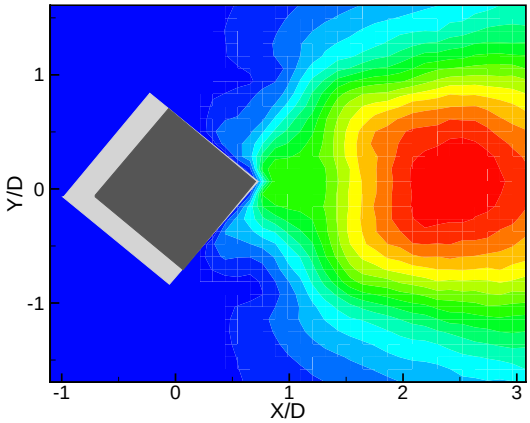

Angle of incidence: 45°, u_{rms}

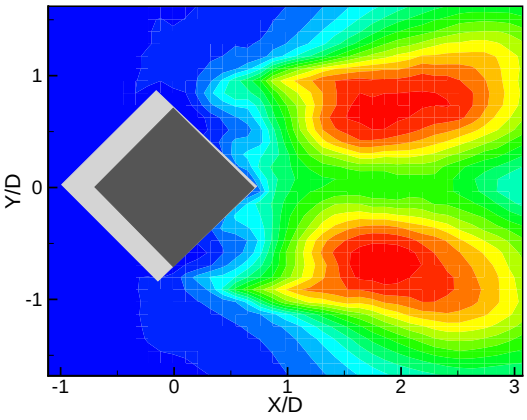

v_{rms}

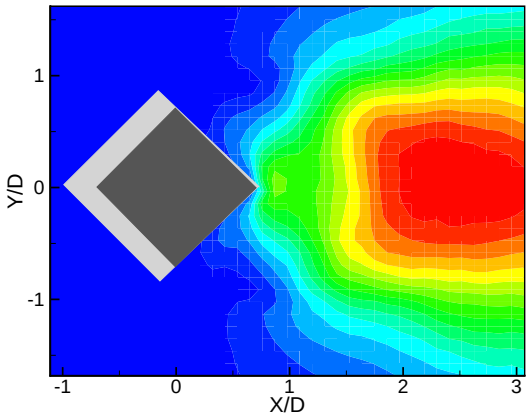

D.2.3 Phase portraits of first two normalized eigenvalues

Angle of incidence: 0°

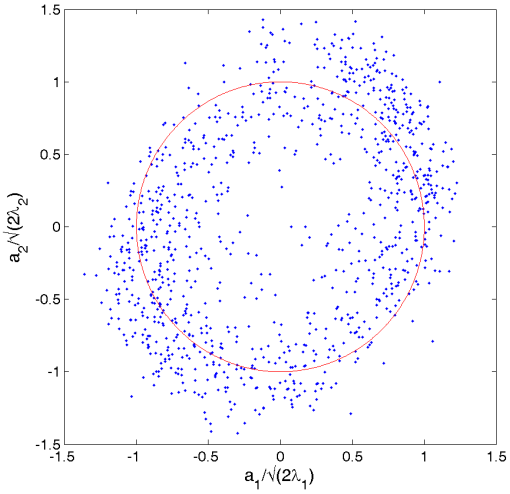

Angle of incidence: 2.5°

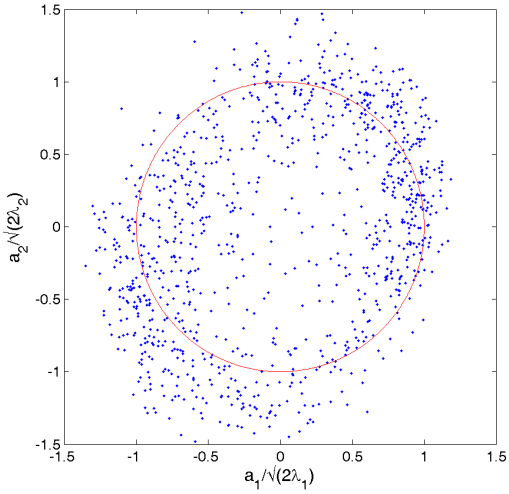

Angle of incidence: 5°

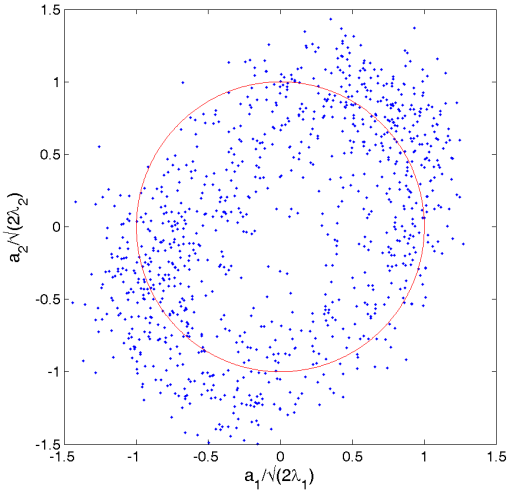

Angle of incidence: 7.5°

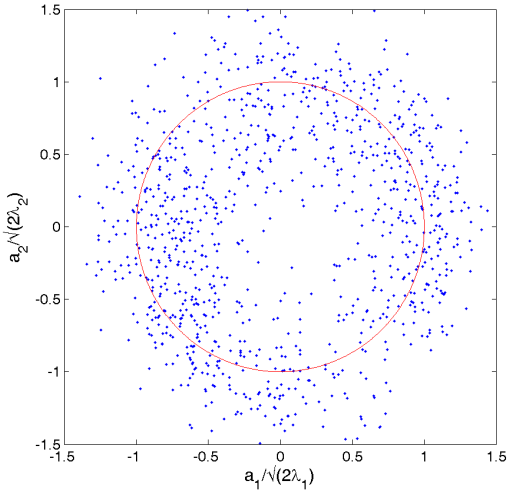

Angle of incidence: 10°

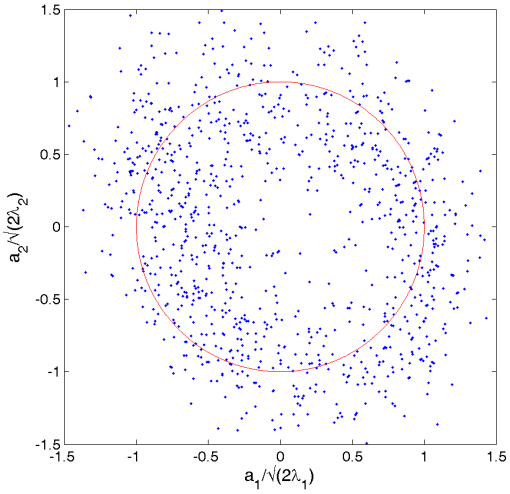

Angle of incidence: 12.5°

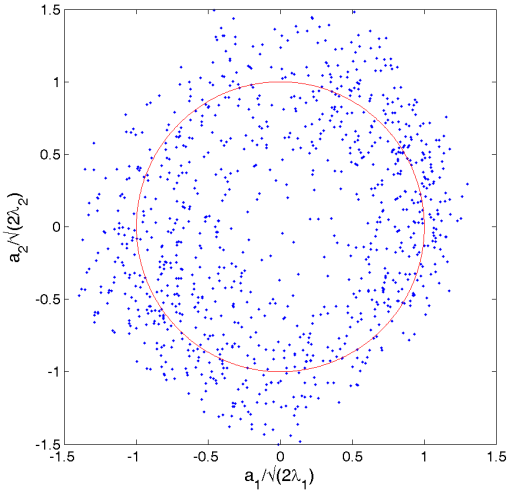

Angle of incidence: 15°

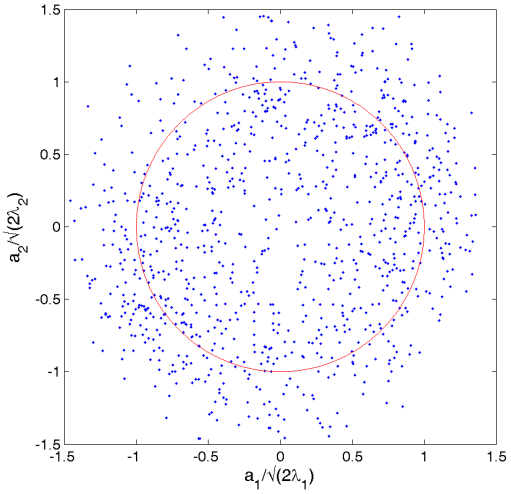

Angle of incidence: 20°

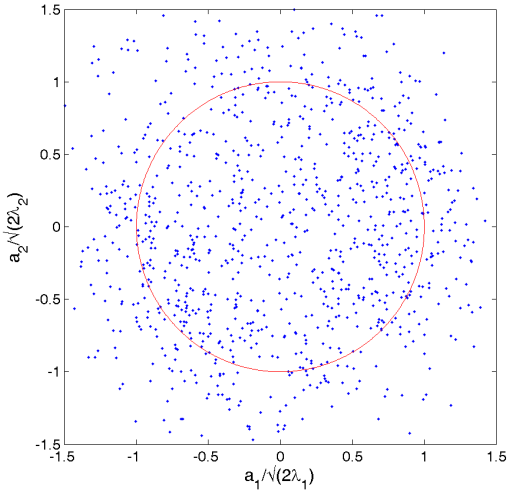

Angle of incidence: 25°

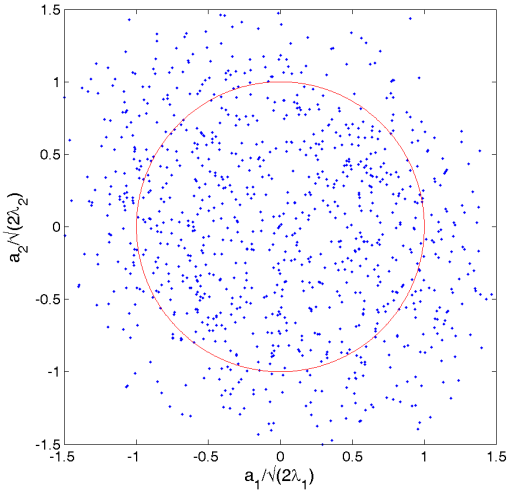

Angle of incidence: 30°

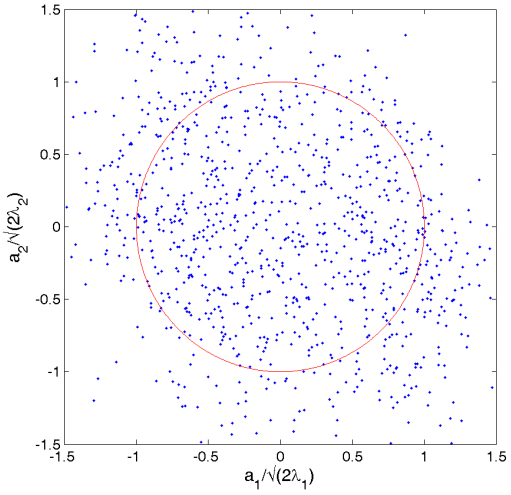

Angle of incidence: 35°

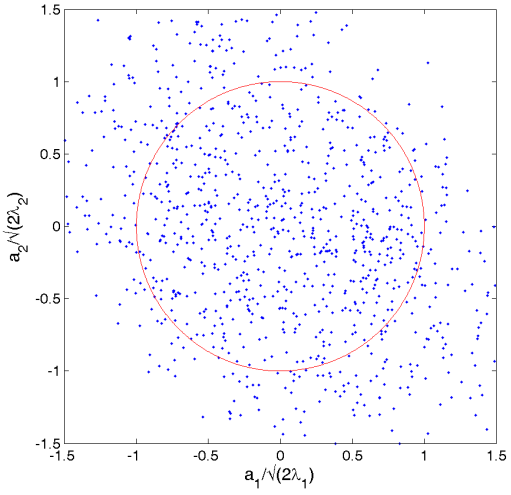

Angle of incidence: 40°

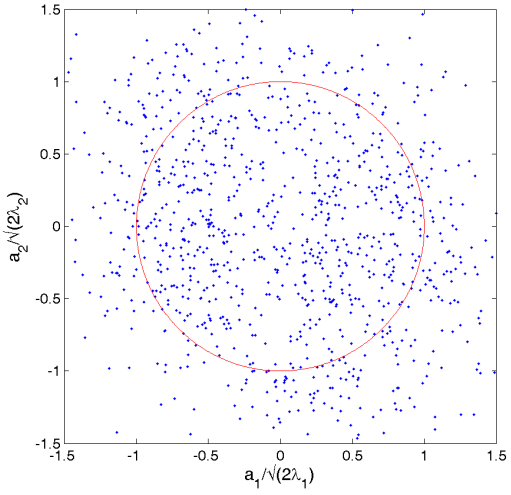

Angle of incidence: 45°

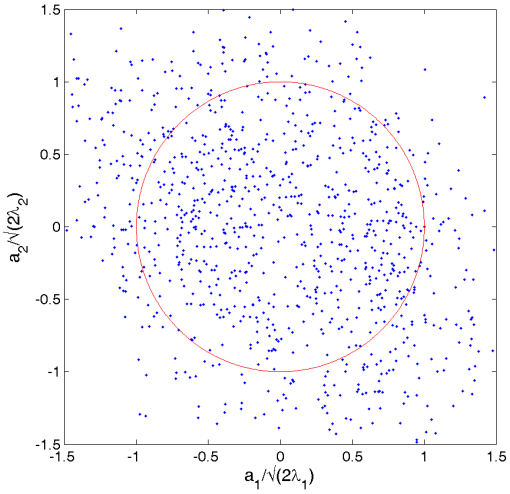

D.2.4 Snapshots of low-order phase reconstructed flow

Angle of incidence: 0°, φ = 0°

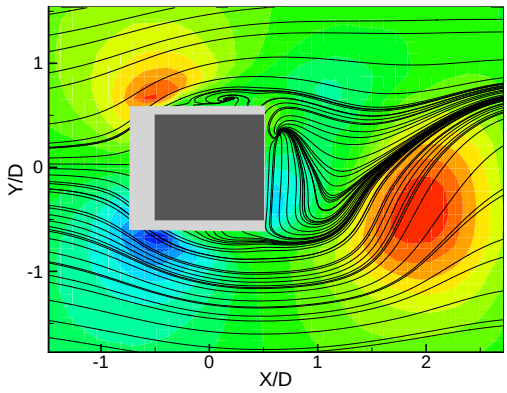

φ = 180°

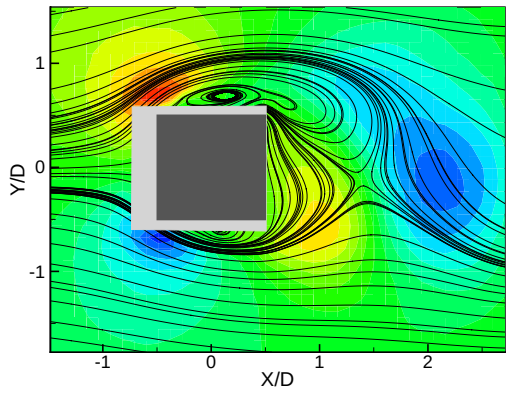

φ = 45°

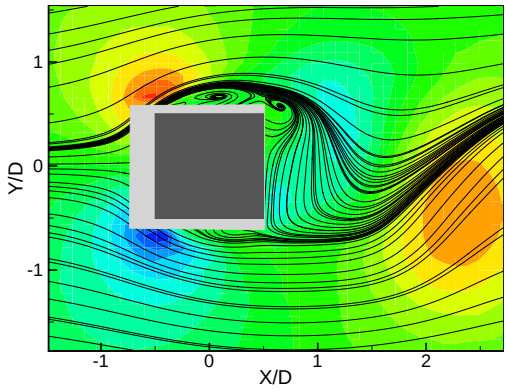

φ = 225°

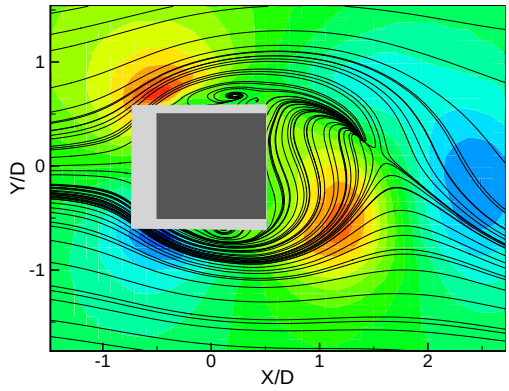

φ = 90°

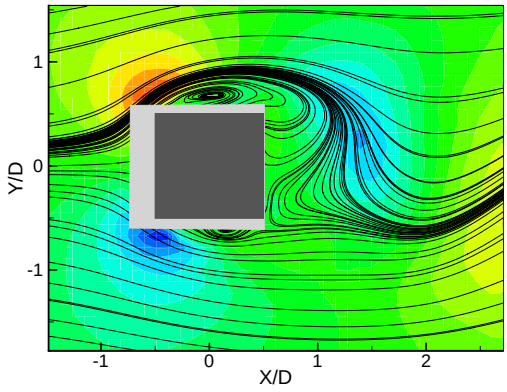

φ = 270°

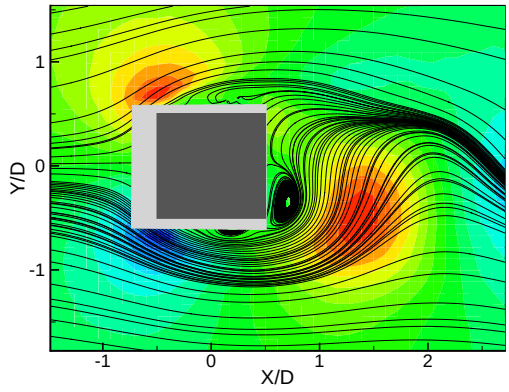

φ = 135°

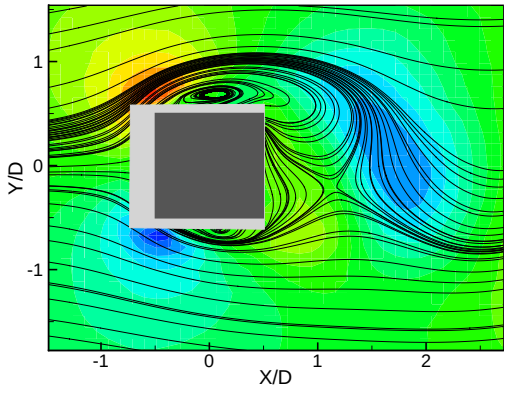

φ = 315°

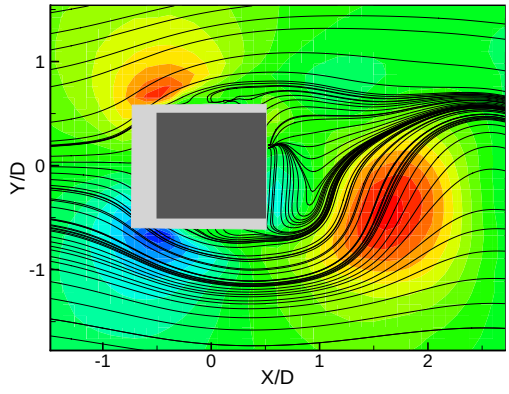

Angle of incidence: 2.5°, φ = 0°

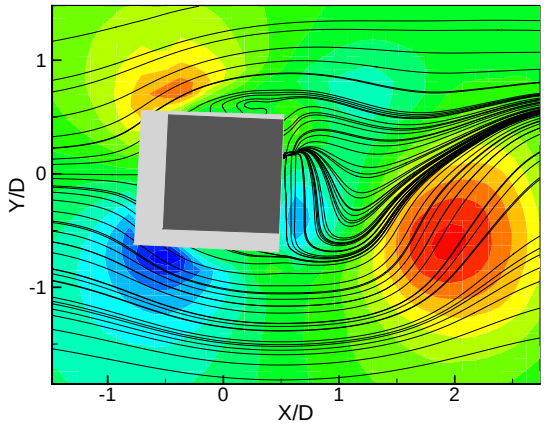

φ = 180°

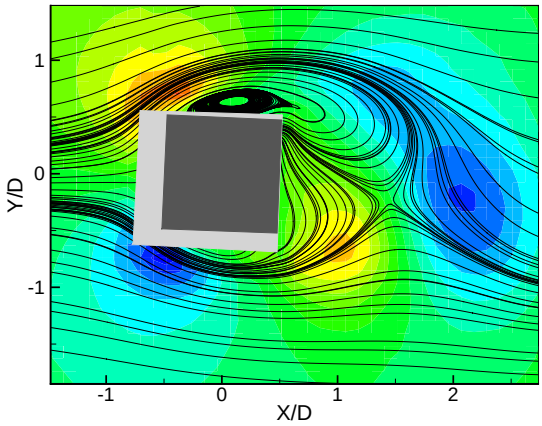

φ = 45°

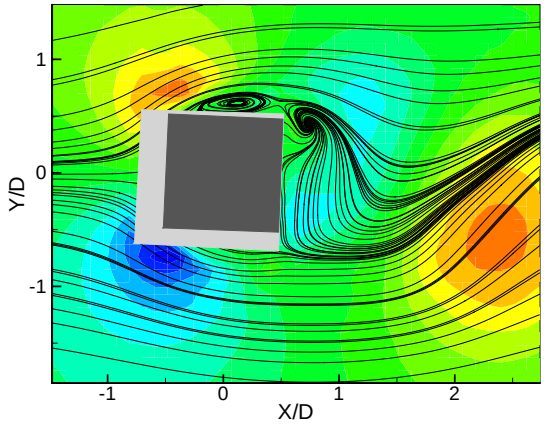

φ = 225°

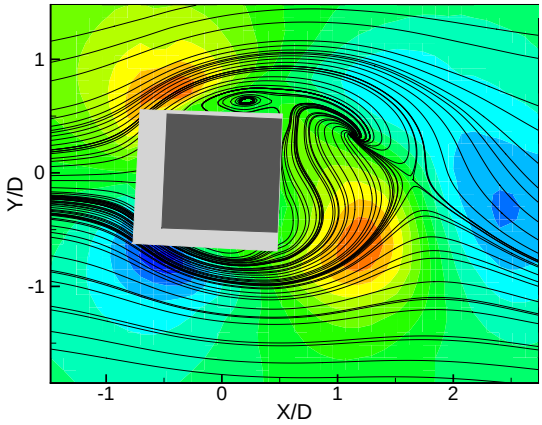

φ = 90°

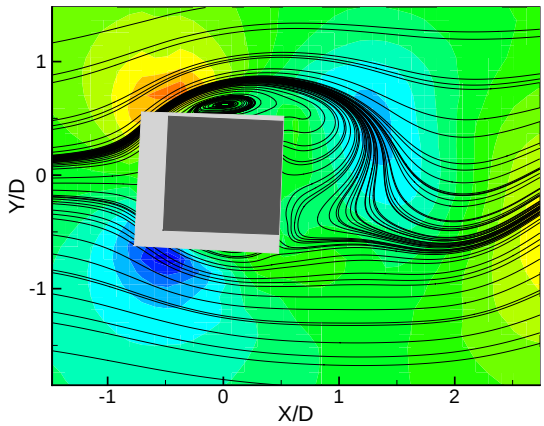

φ = 270°

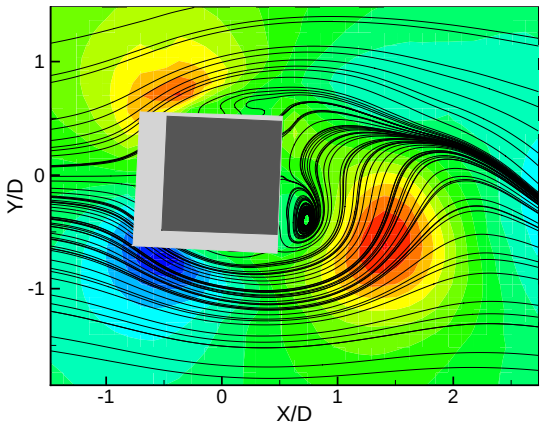

φ = 135°

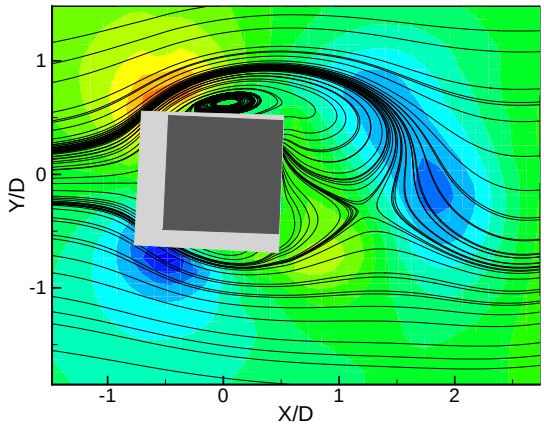

φ = 315°

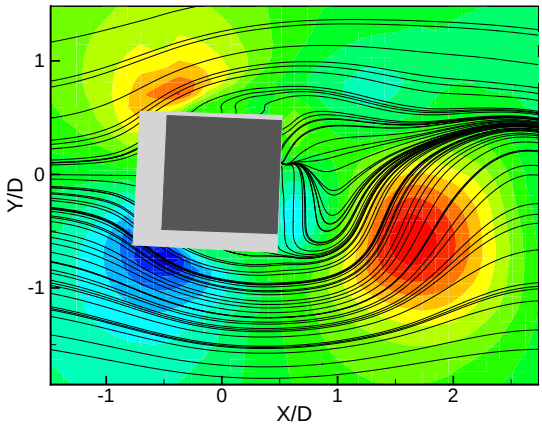

Angle of incidence: 5°, φ = 0°

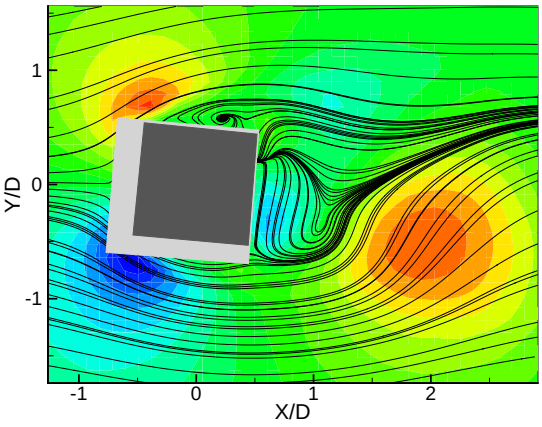

φ = 180°

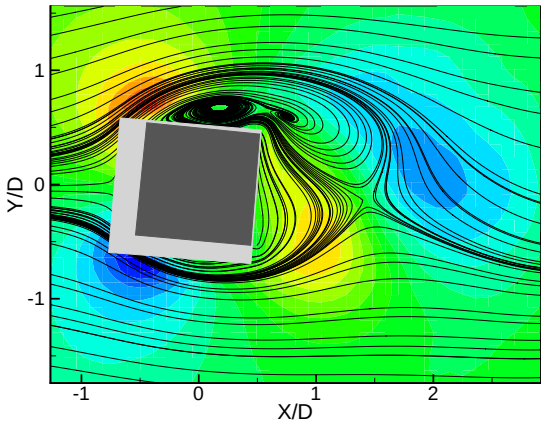

φ = 45°

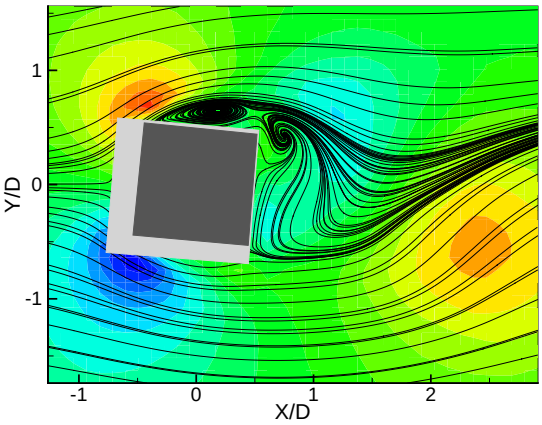

φ = 225°

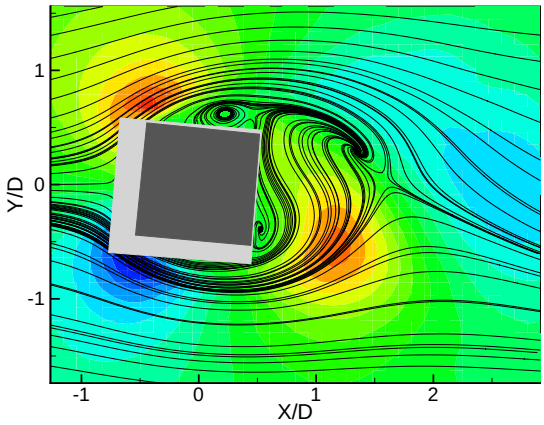

φ = 90°

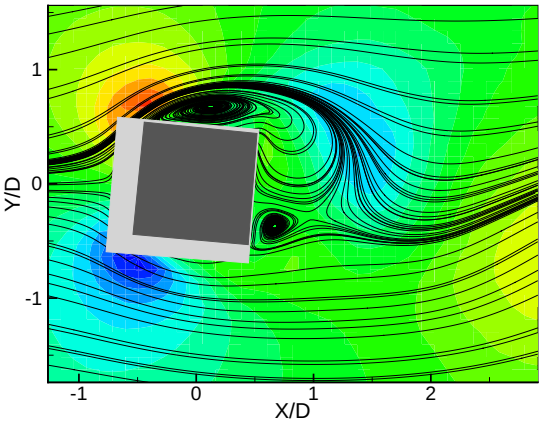

φ = 270°

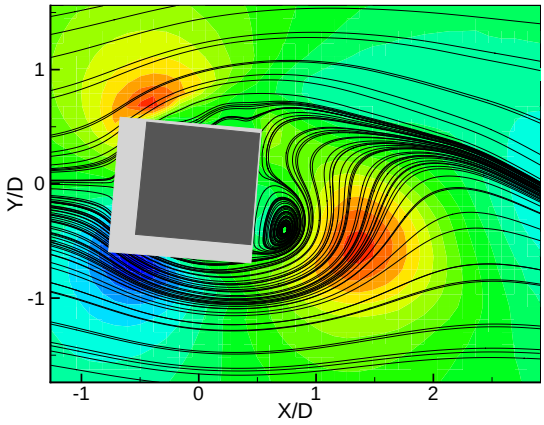

φ = 135°

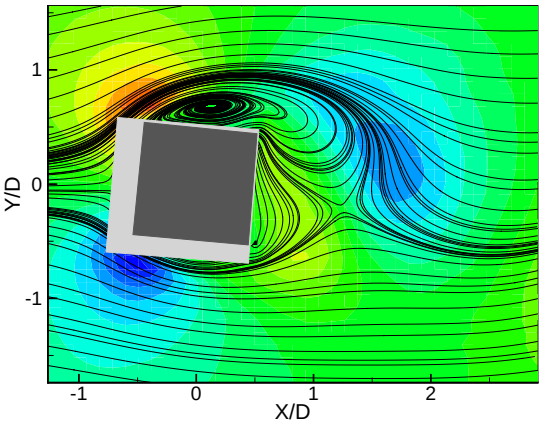

φ = 315°

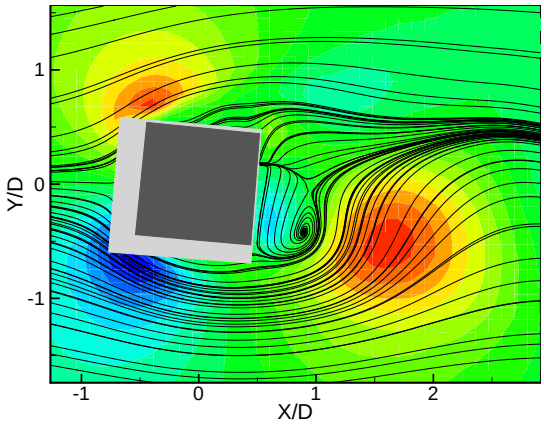

Angle of incidence: 7.5°, φ = 0°

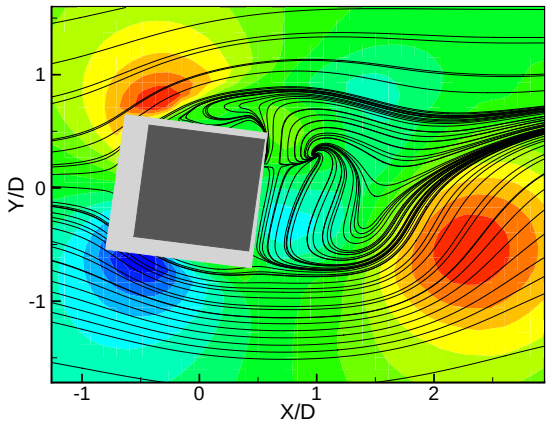

φ = 180°

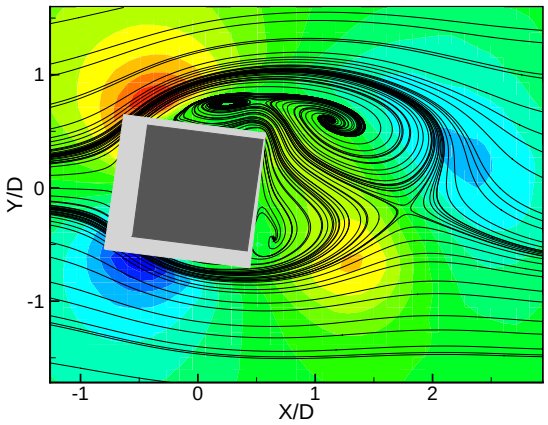

φ = 45°

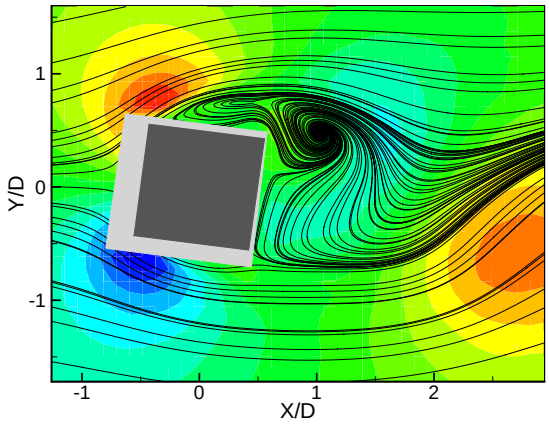

φ = 225°

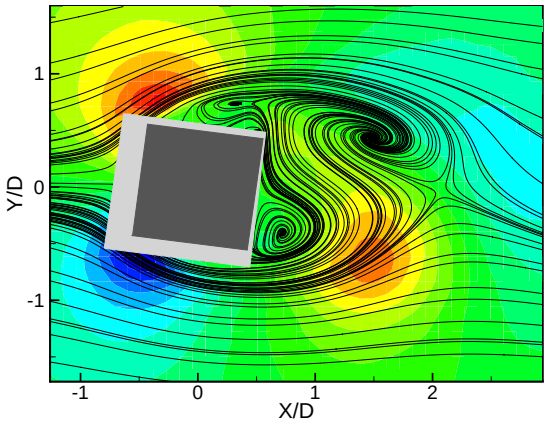

φ = 90°

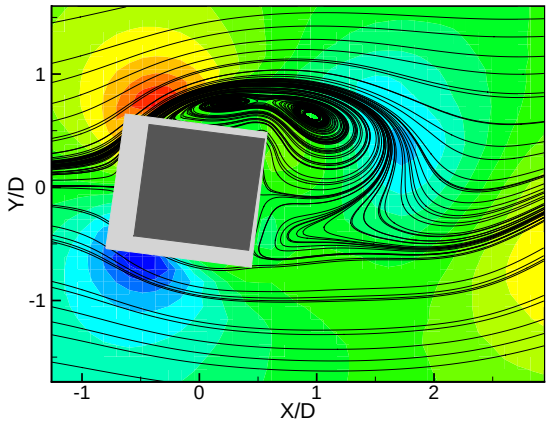

φ = 270°

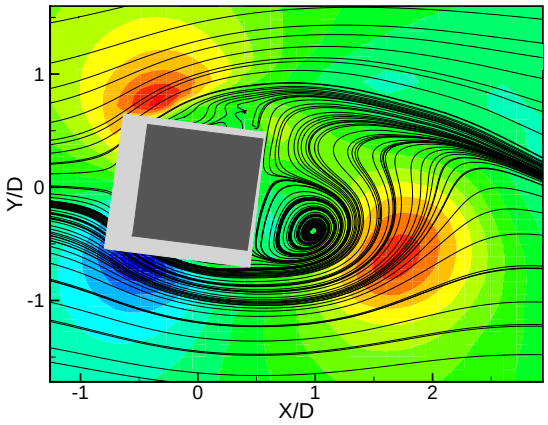

φ = 135°

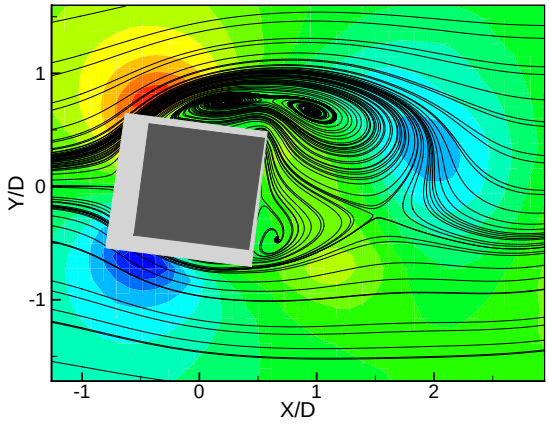

φ = 315°

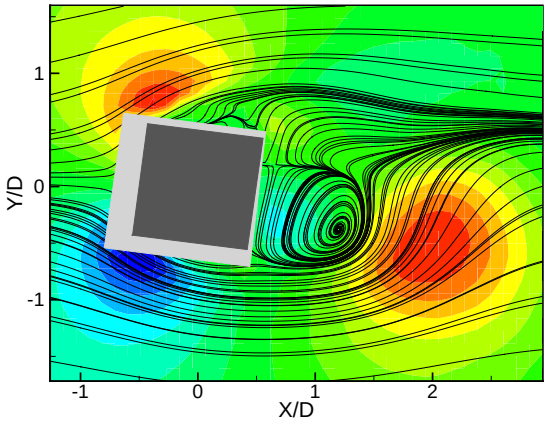

Angle of incidence: 10°, φ = 0°

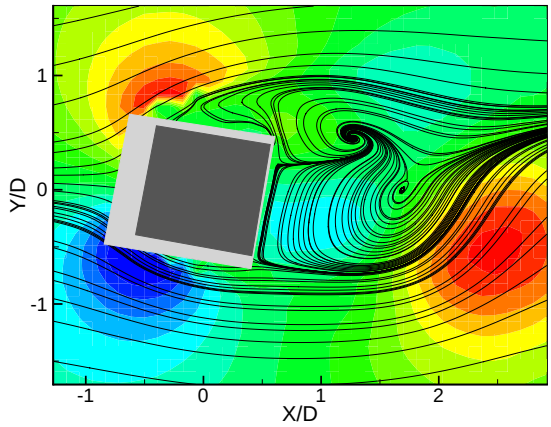

φ = 180°

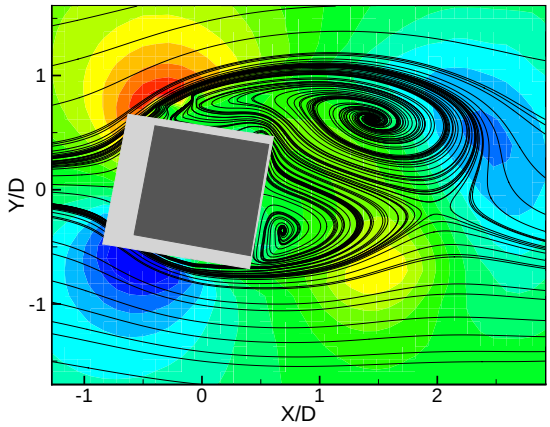

φ = 45°

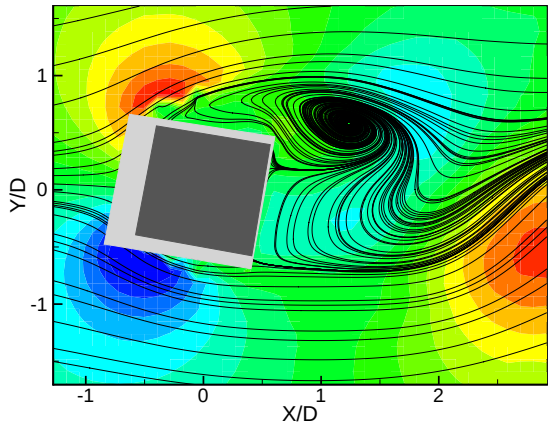

φ = 225°

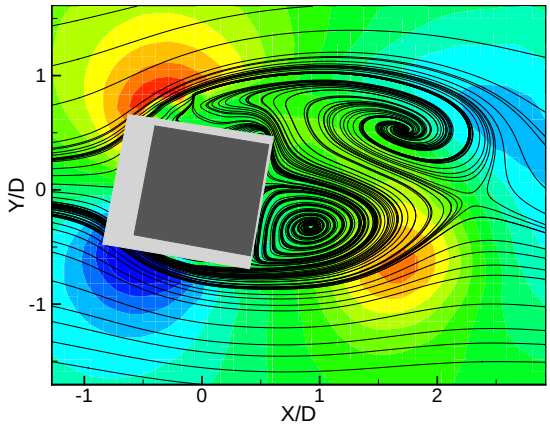

φ = 90°

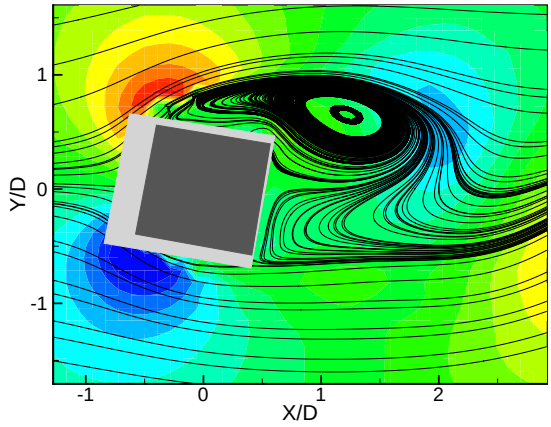

φ = 270°

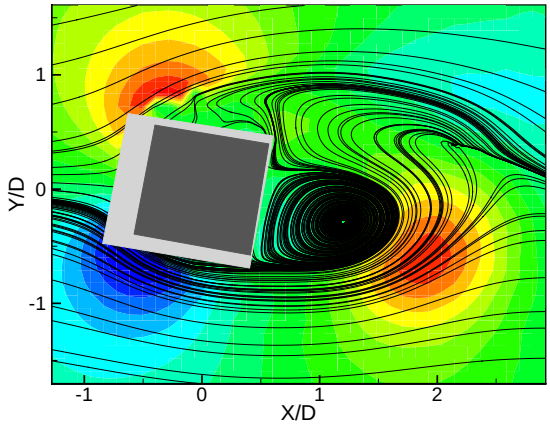

φ = 135°

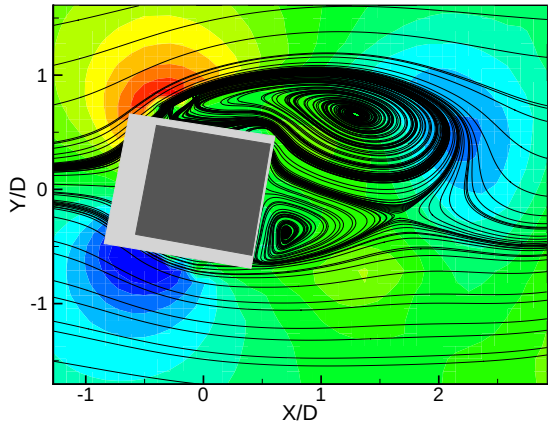

φ = 315°

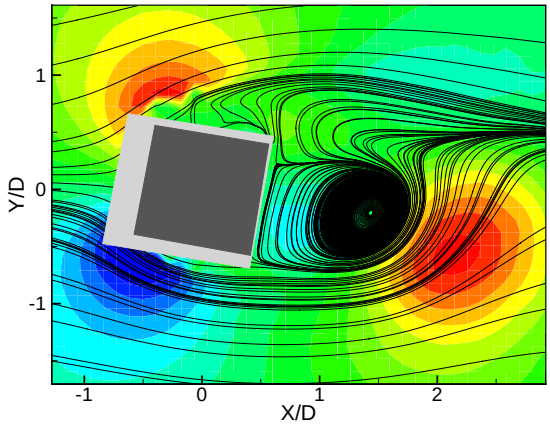

Angle of incidence: 12.5°, φ = 0°

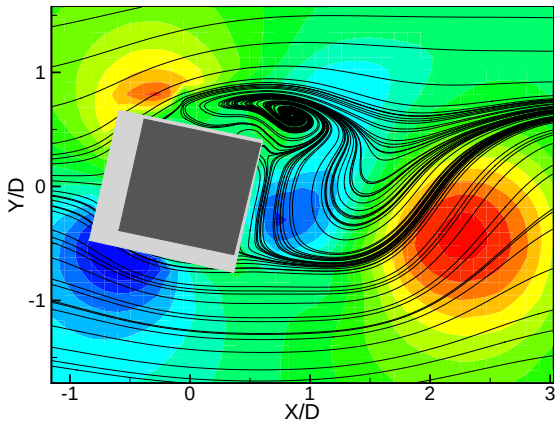

φ = 180°

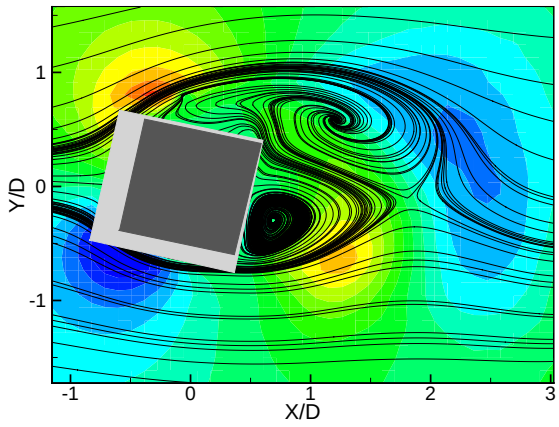

φ = 45°

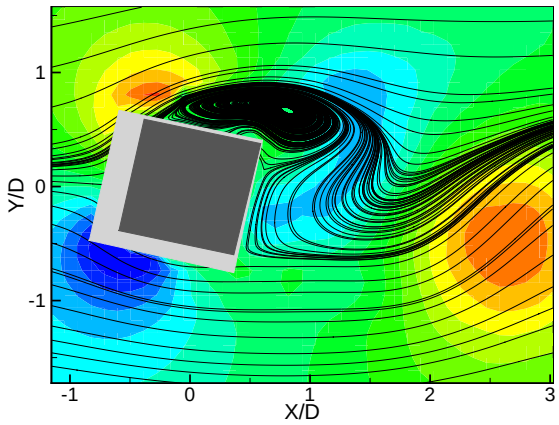

φ = 225°

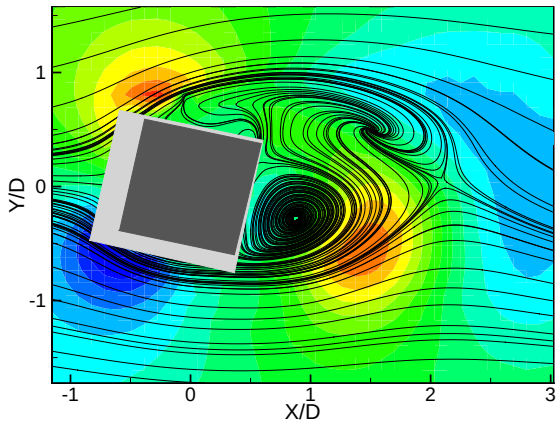

φ = 90°

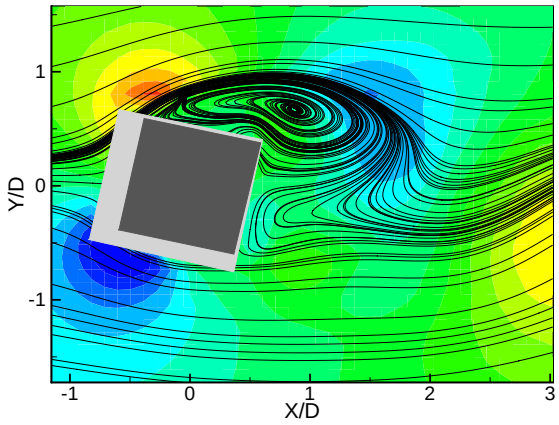

φ = 270°

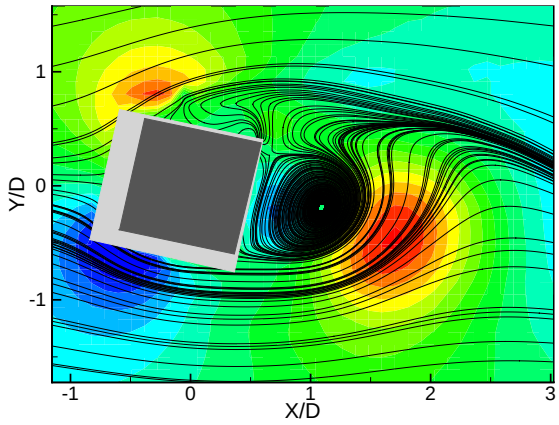

φ = 135°

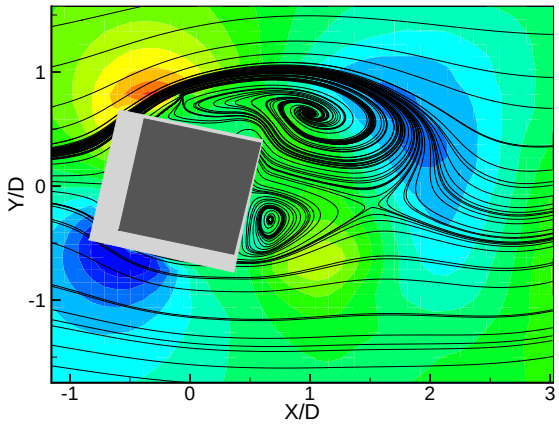

φ = 315°

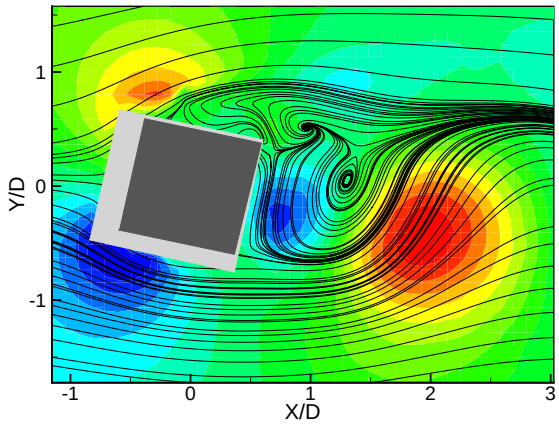

Angle of incidence: 15°, φ = 0°

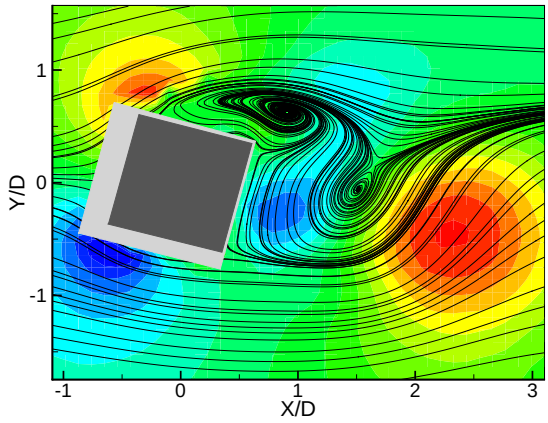

φ = 180°

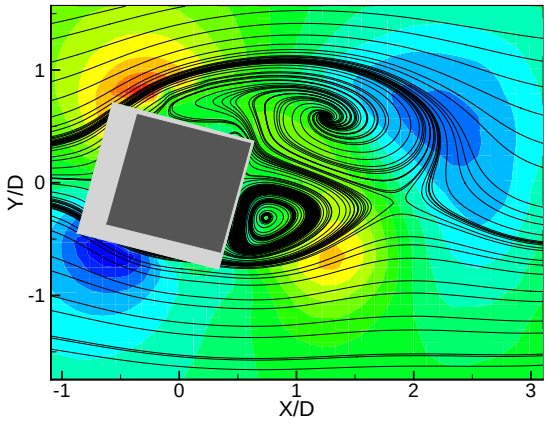

φ = 45°

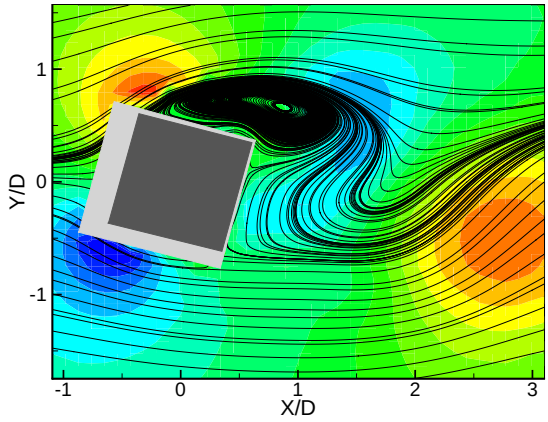

φ = 225°

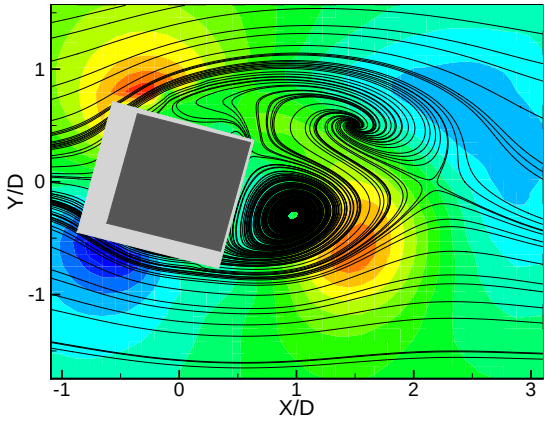

φ = 90°

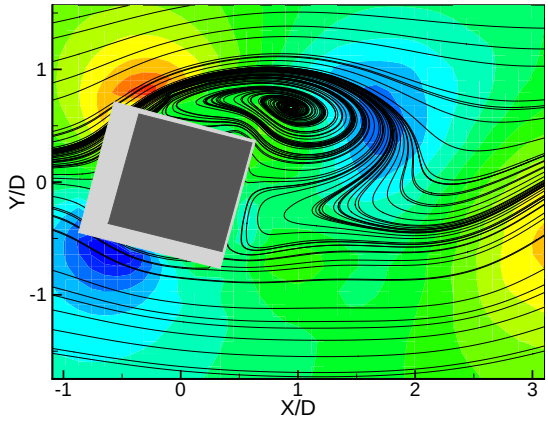

φ = 270°

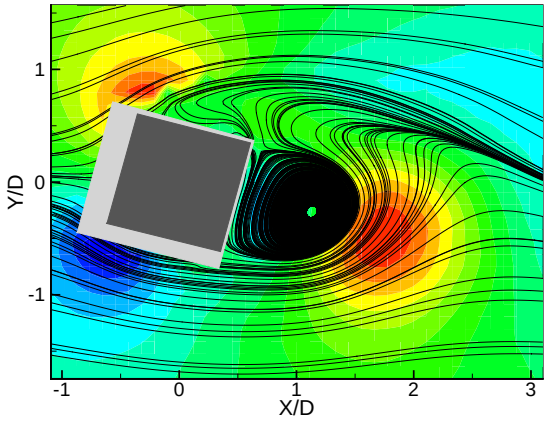

φ = 135°

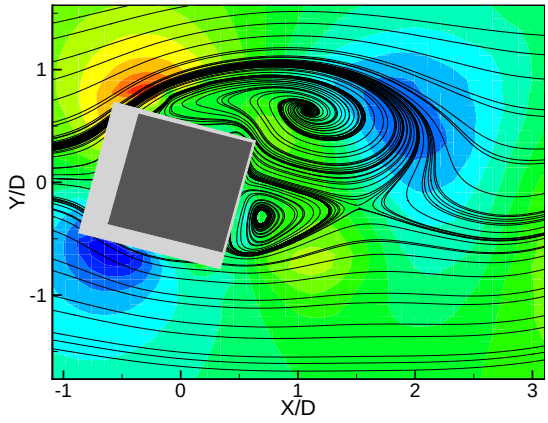

φ = 315°

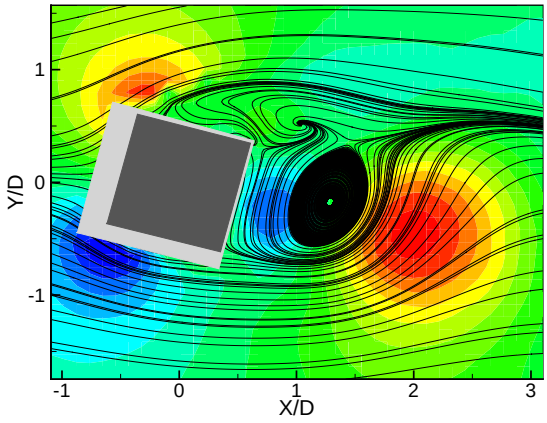

Angle of incidence: 20°, φ = 0°

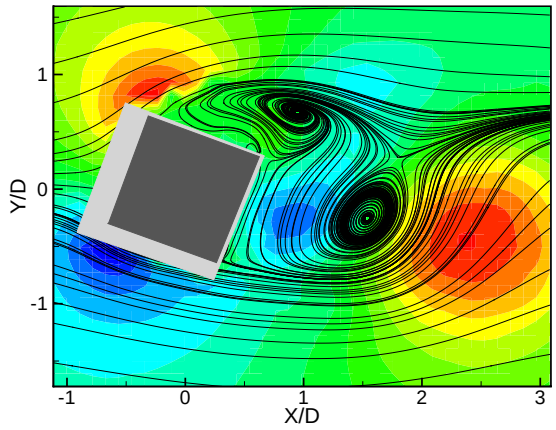

φ = 180°

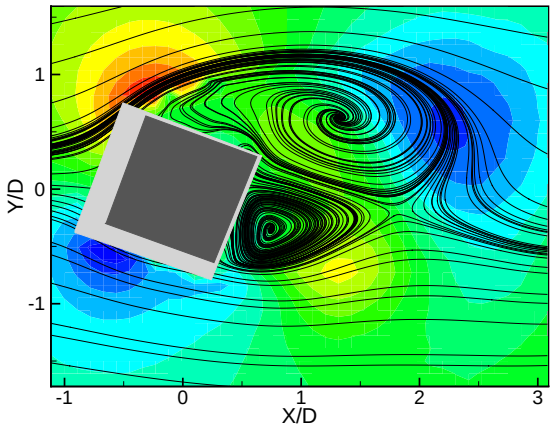

φ = 45°

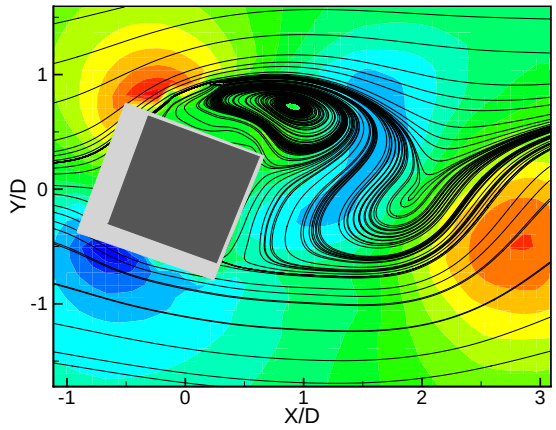

φ = 225°

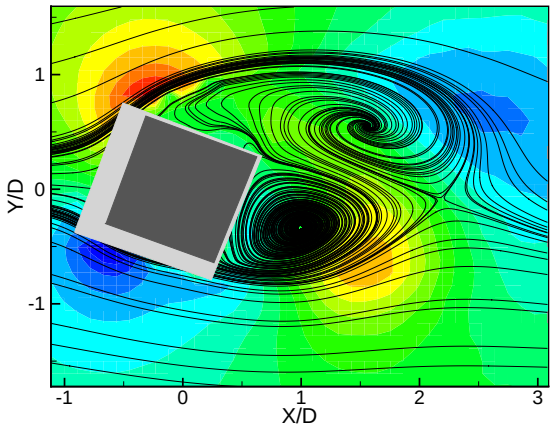

φ = 90°

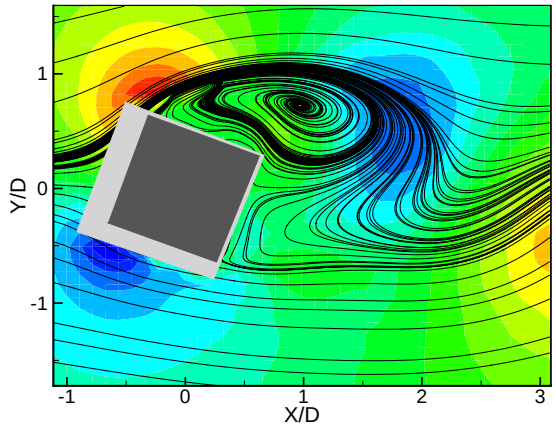

φ = 270°

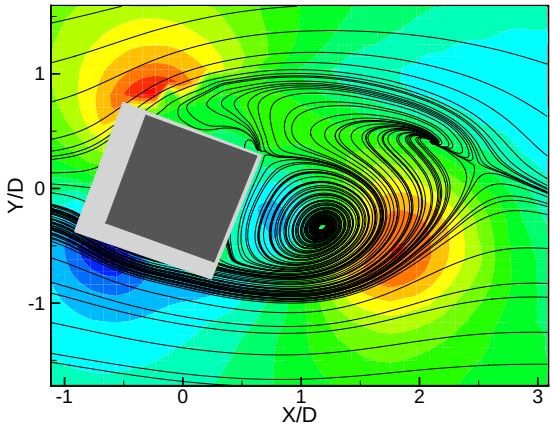

φ = 135°

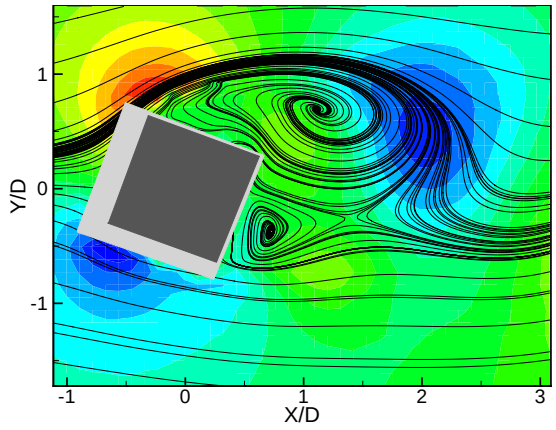

φ = 315°

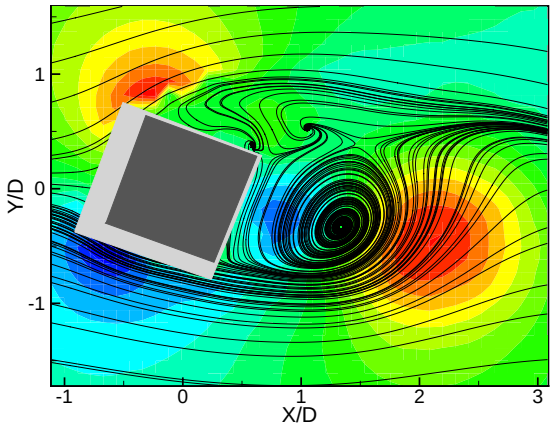

Angle of incidence: 25°, φ = 0°

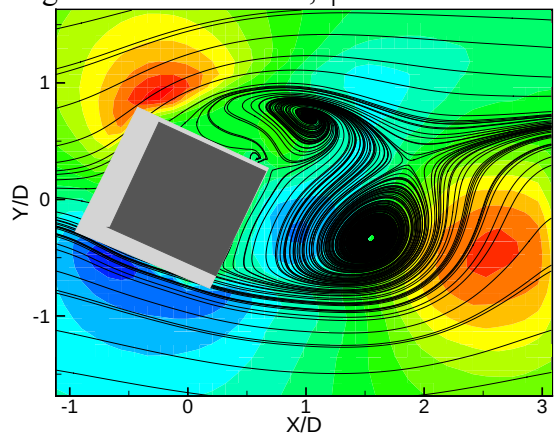

φ = 180°

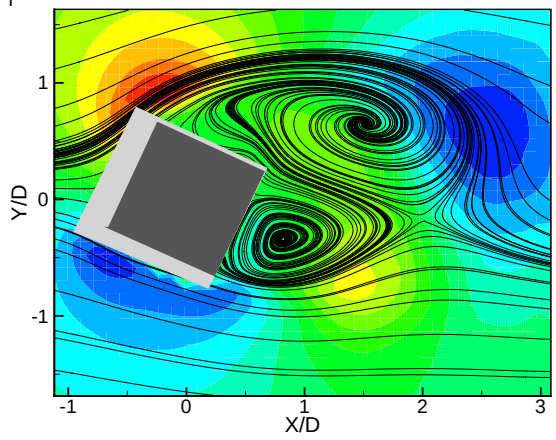

φ = 45°

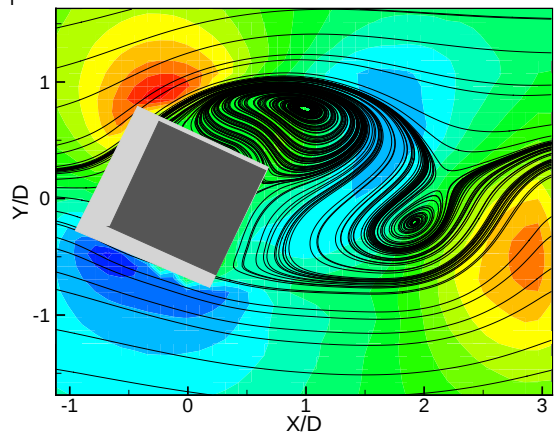

φ = 225°

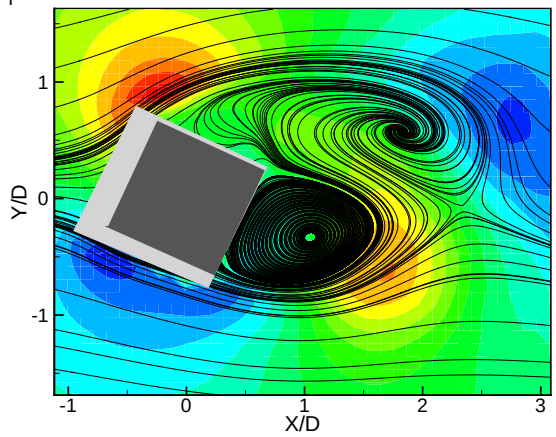

φ = 90°

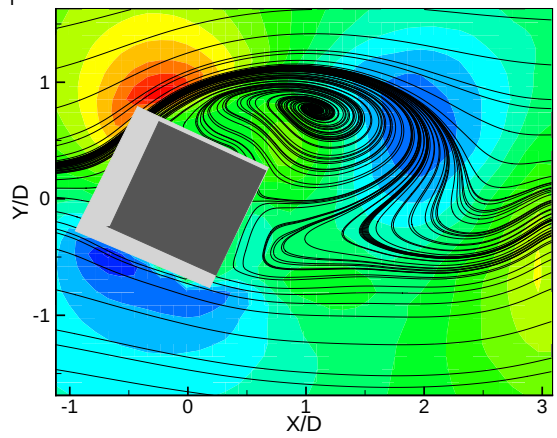

φ = 270°

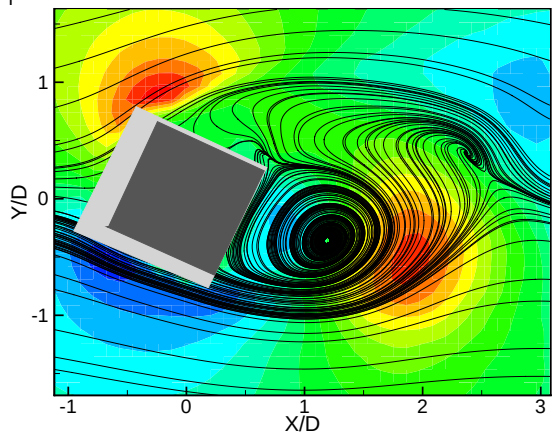

φ = 135°

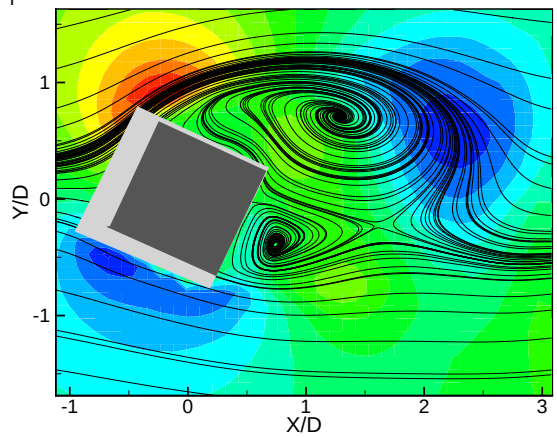

φ = 315°

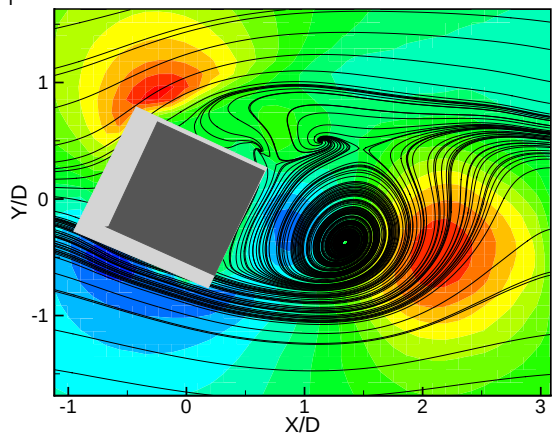

Angle of incidence: 30°, φ = 0°

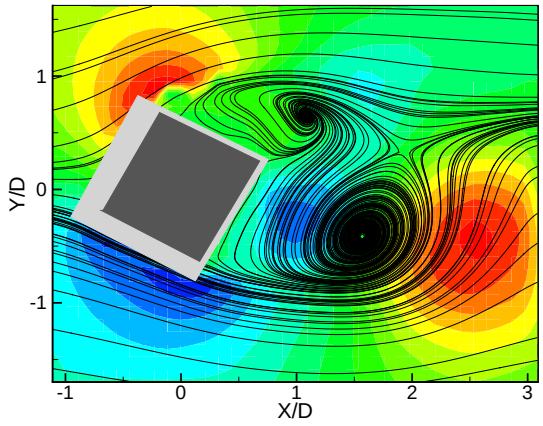

φ = 180°

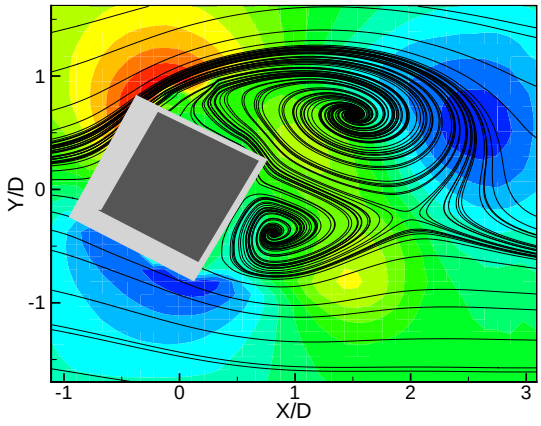

φ = 45°

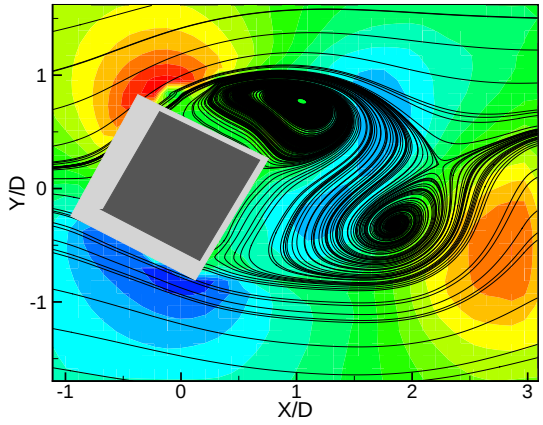

φ = 225°

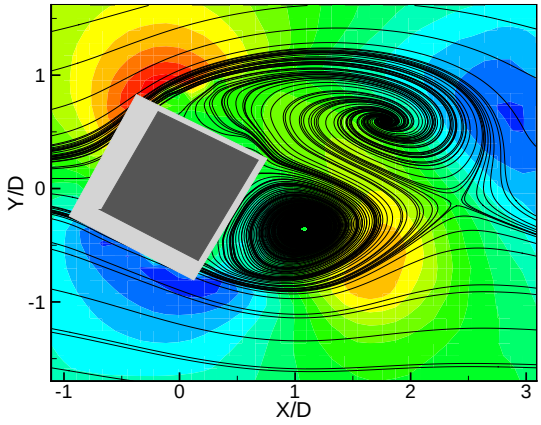

φ = 90°

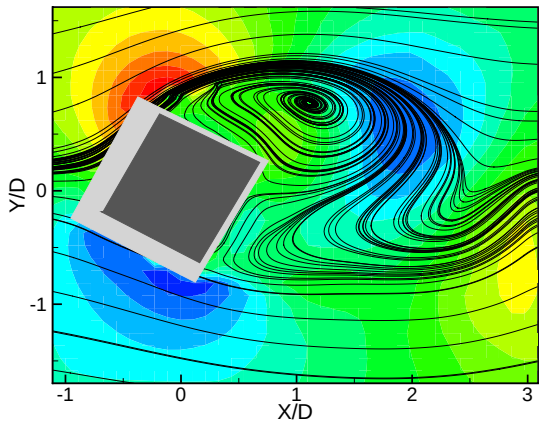

φ = 270°

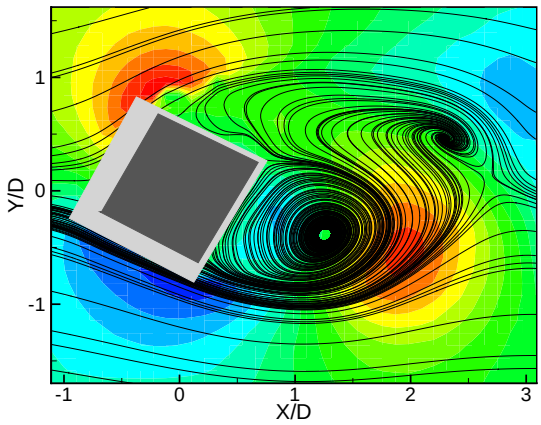

φ = 135°

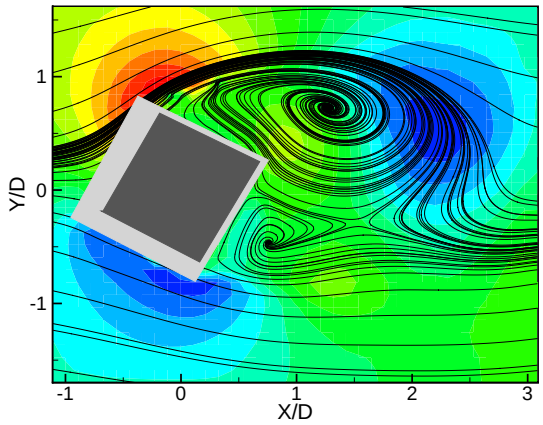

φ = 315°

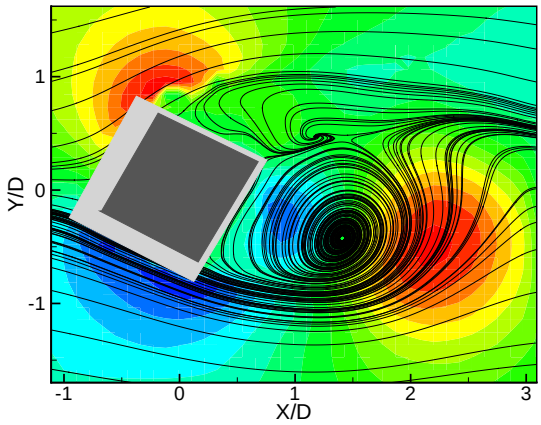

Angle of incidence: 35°, φ = 0°

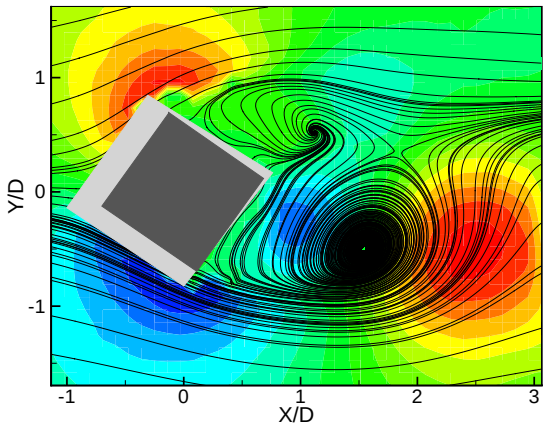

φ = 180°

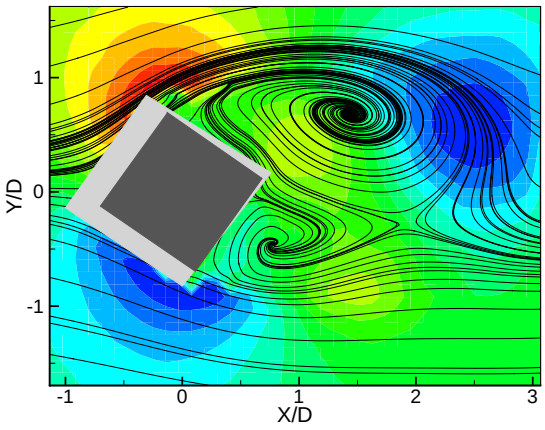

φ = 45°

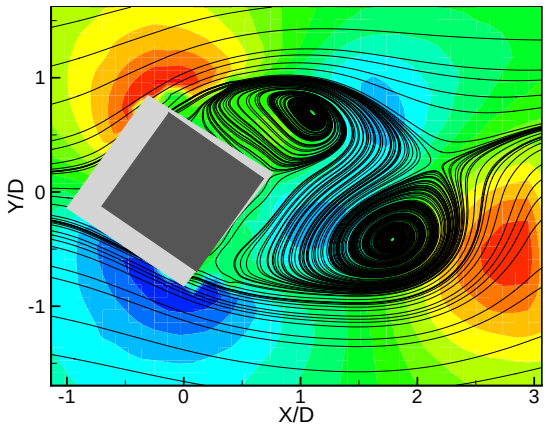

φ = 225°

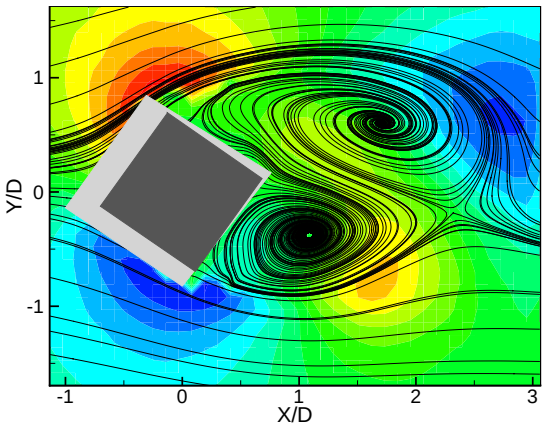

φ = 90°

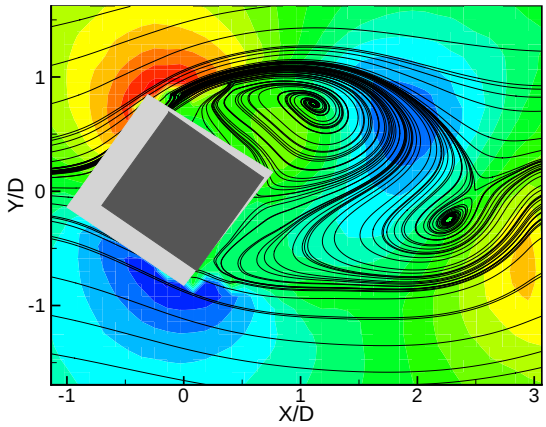

φ = 270°

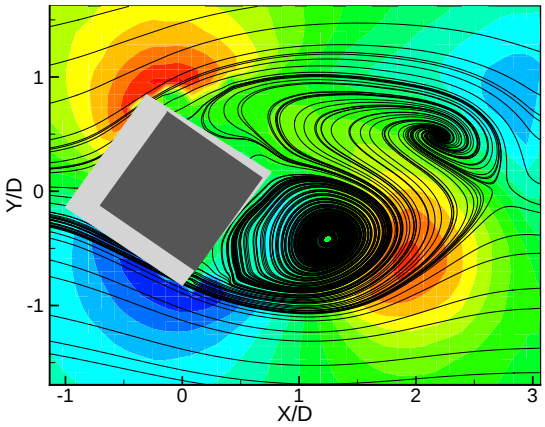

φ = 135°

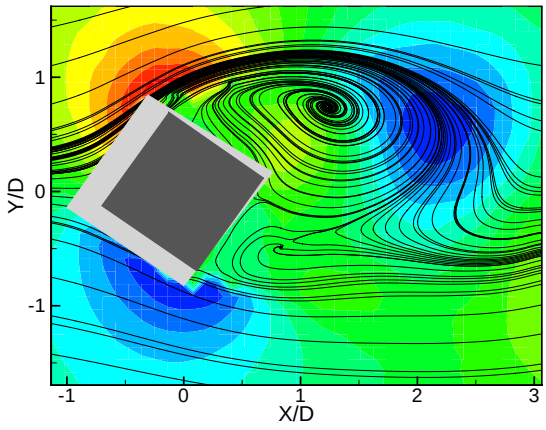

φ = 315°

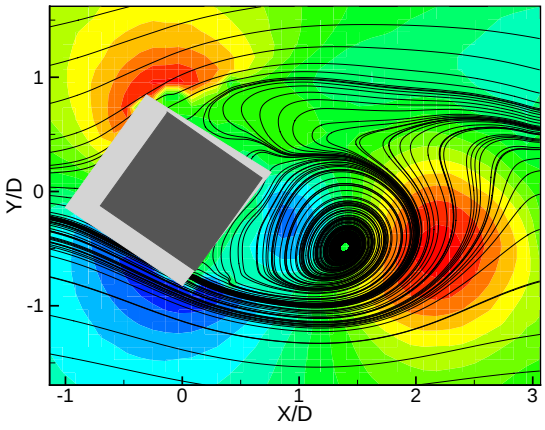

Angle of incidence: 40°, φ = 0°

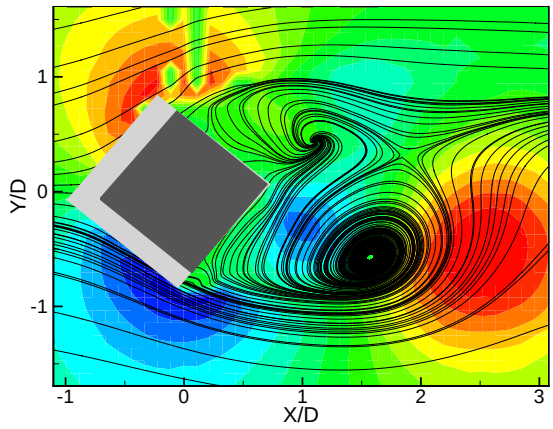

φ = 180°

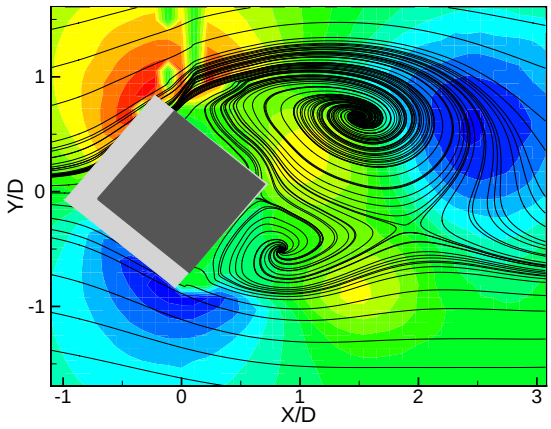

φ = 45°

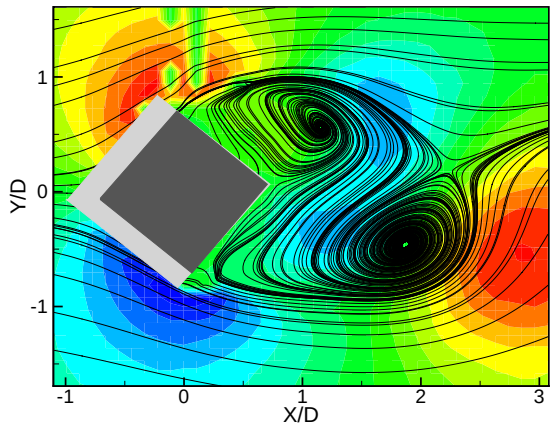

φ = 225°

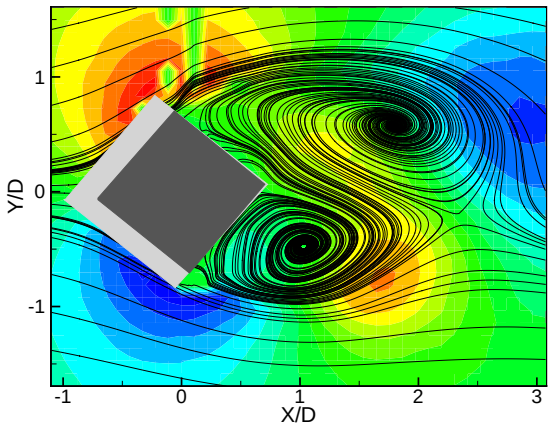

φ = 90°

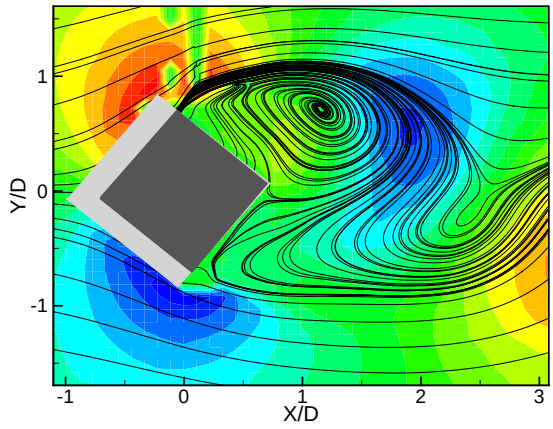

φ = 270°

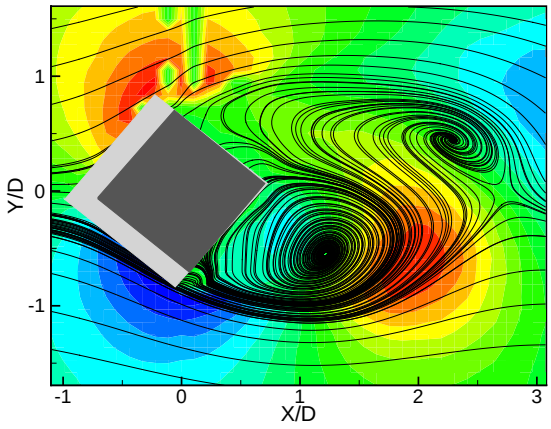

φ = 135°

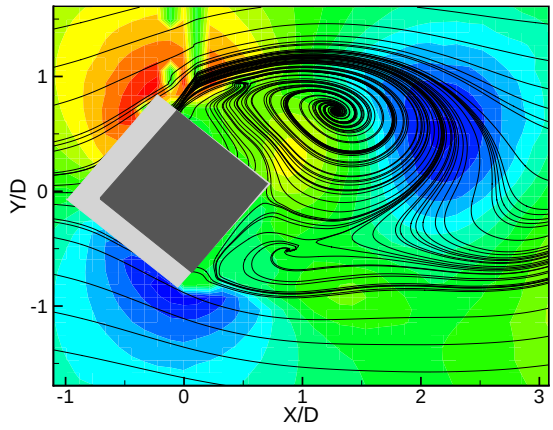

φ = 315°

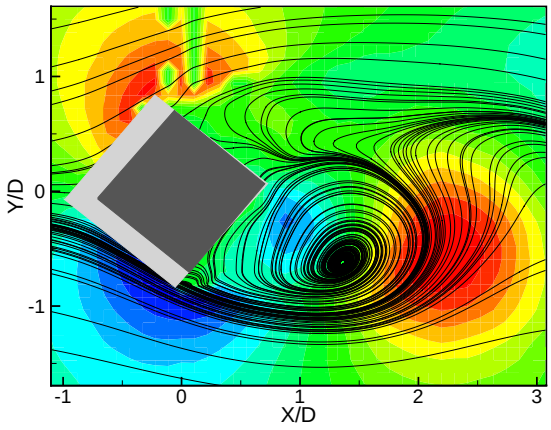

Angle of incidence: 45°, φ = 0°

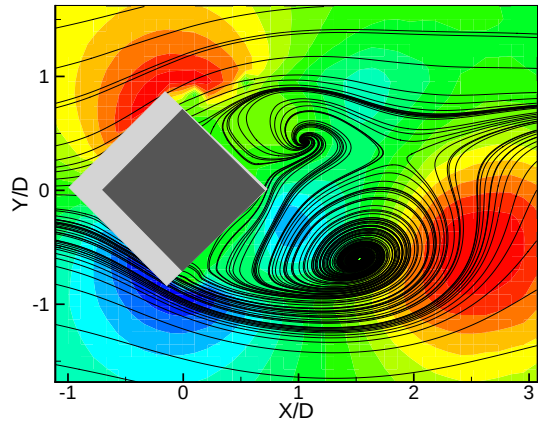

φ = 180°

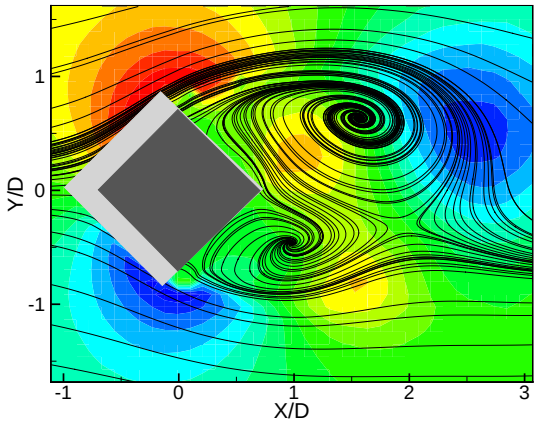

φ = 45°

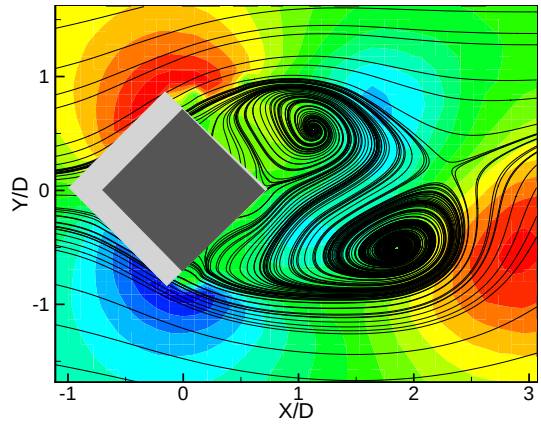

φ = 225°

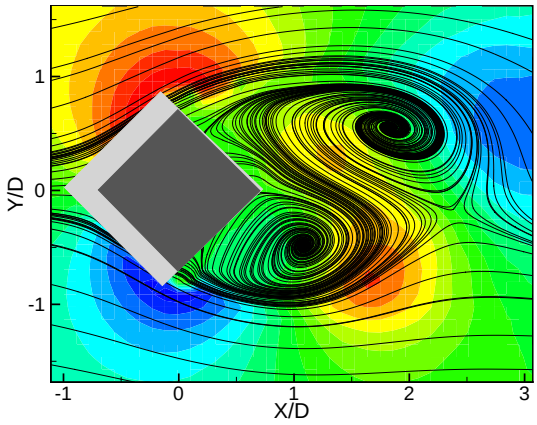

φ = 90°

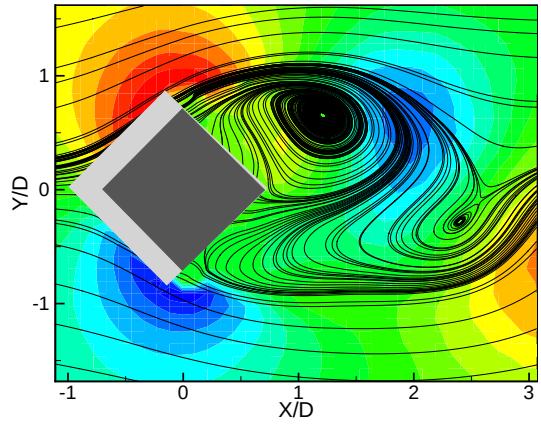

φ = 270°

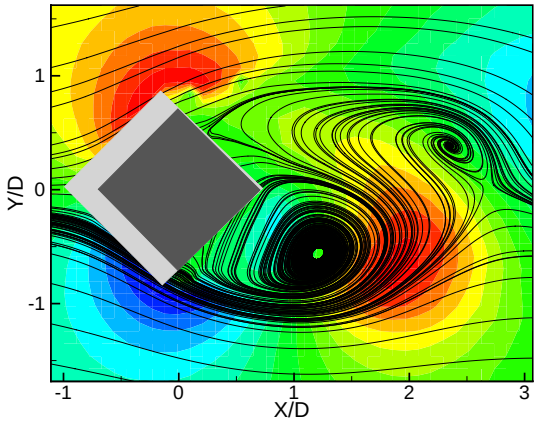

φ = 135°

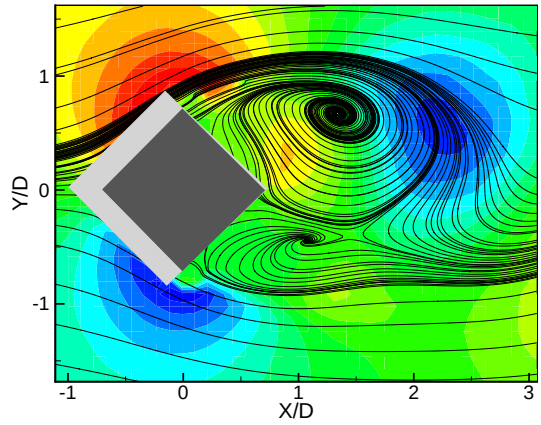

φ = 315°

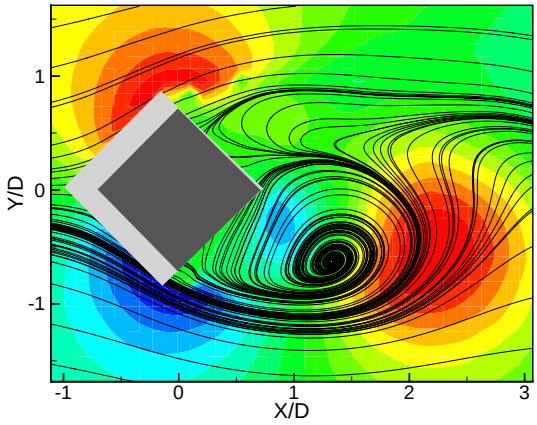

D.3 Pressure coefficients (Case C only)

Angle of incidence: 0°

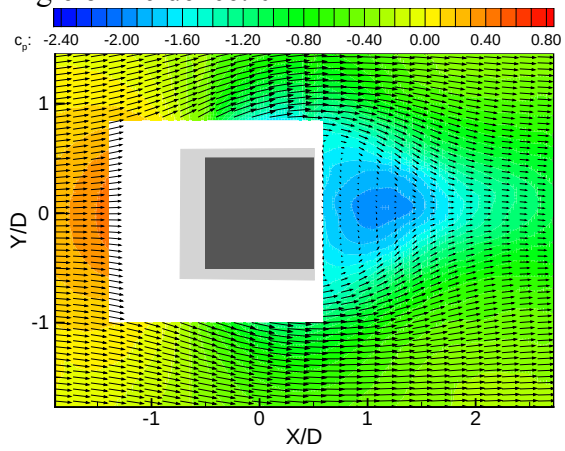

Angle of incidence: 2.5°

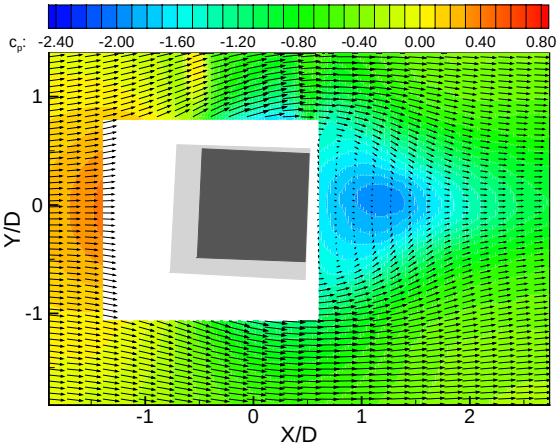

Angle of incidence: 5°

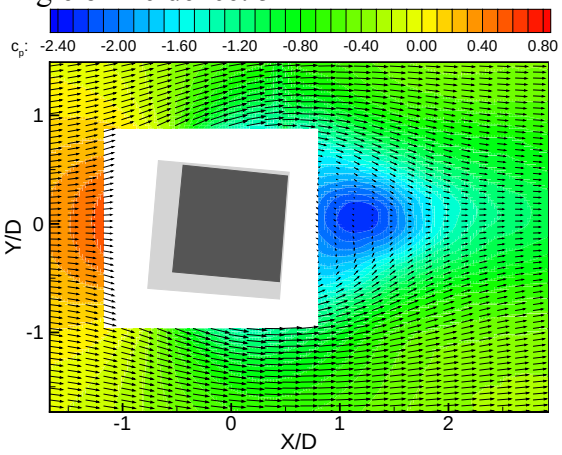

Angle of incidence: 7.5°

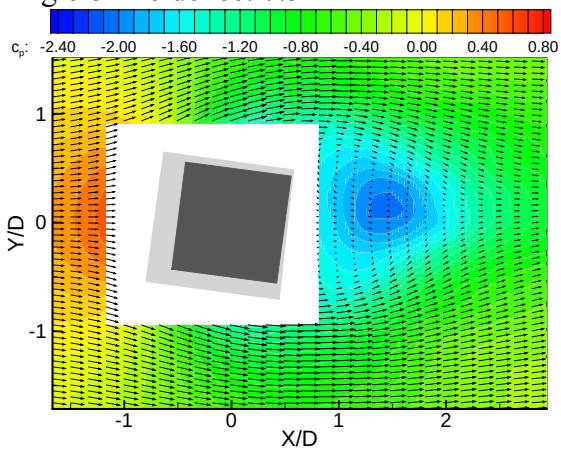

Angle of incidence: 10°

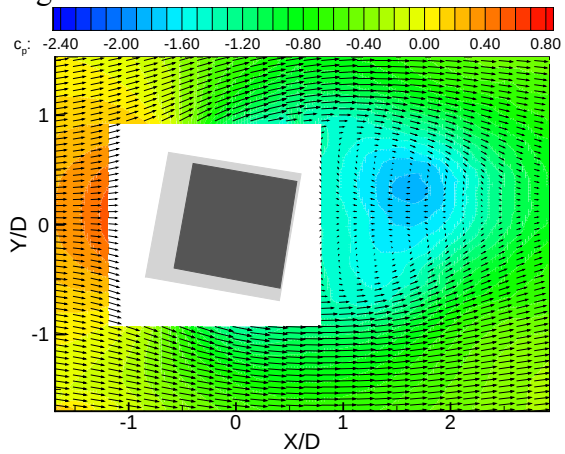

Angle of incidence: 12.5°

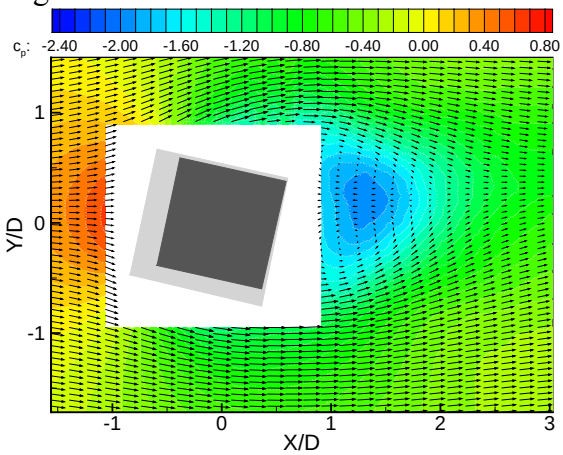

Angle of incidence: 15°

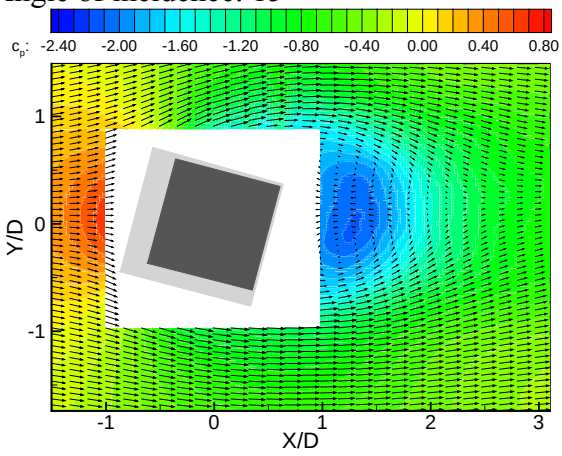

Angle of incidence: 20°

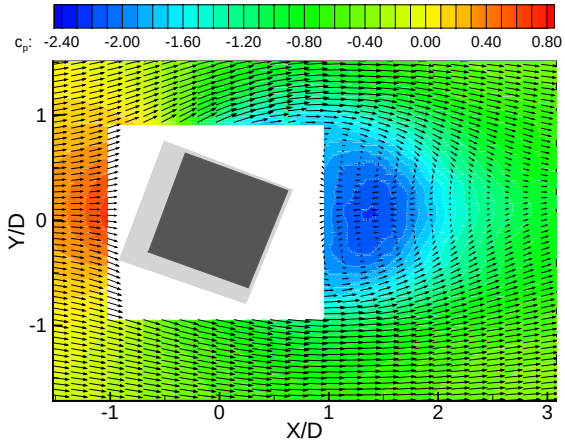

Angle of incidence: 25°

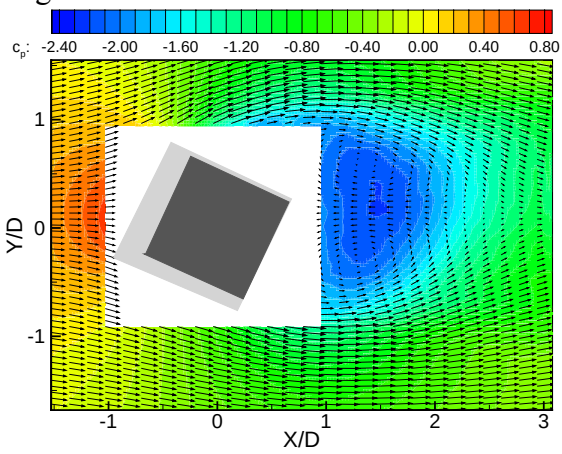

Angle of incidence: 30°

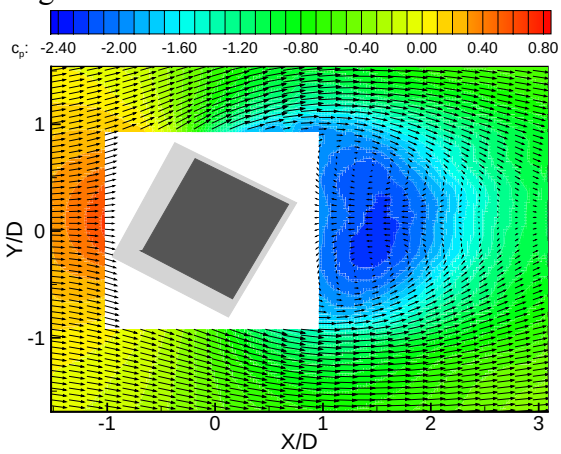

Angle of incidence: 35°

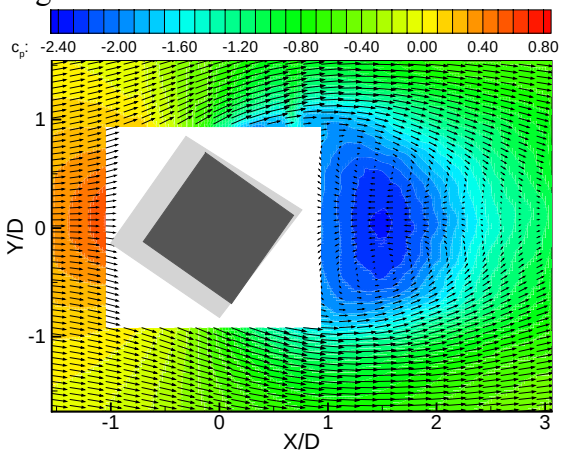

Angle of incidence: 40°

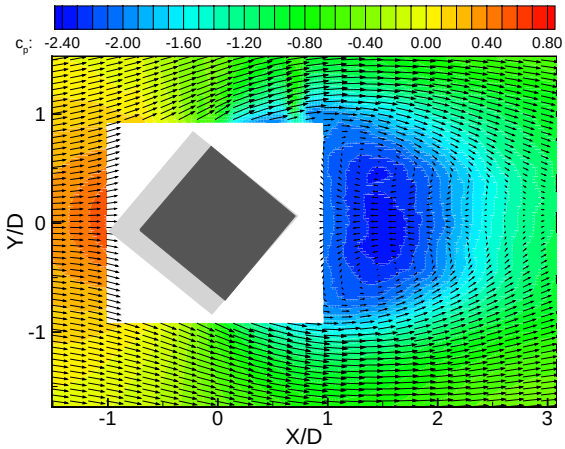

Angle of incidence: 45°